Universität Münster

institut für theoretische physik

Theoretische Physik

# Temporal Localized States and Frequency Combs in Kerr Cavities and Mode-Locked Lasers

Inaugural-Dissertation zur Erlangung des Doktorgrades
der Naturwissenschaften im Fachbereich Physik
der Mathematisch-Naturwissenschaftlichen Fakultät
der Universität Münster

vorgelegt von

Thomas Georg Seidel

aus Göttingen

– 2025 –

Revised version.
June 30, 2025

| | |
|---|---|
| Dekan: | Prof. Dr. Rudolf Bratschitsch |
| Erste Gutachterin: | Prof. Dr. Svetlana Gurevich |
| Zweiter Gutachter: | Prof. Dr. Julien Javaloyes |
| Tag der mündlichen Prüfung: | ............................... |
| Tag der Promotion: | ............................... |

# Abstract

In this thesis, we study in a theoretical framework nonlinear optical systems that can generate frequency combs and temporal localized states (TLSs), which are essential for applications in high-precision metrology, optical communication, and ultrafast signal processing. Specifically, we analyze two different systems capable of producing pulsed emission: injected Kerr resonators and passively mode-locked (PML) lasers. We develop delay differential equation models from first principles, which we study using analytical and numerical techniques.

In the first part of the thesis, we investigate a Kerr–Gires–Tournois interferometer. This recently proposed setup consists of an injected micro-cavity containing a nonlinear Kerr medium, which is coupled to a long external cavity closed by a feedback mirror. Depending on whether the injection is red- or blue-detuned with respect to the micro-cavity resonance, the system operates in the normal or anomalous dispersion regime, respectively. In the normal dispersion regime, TLSs are created by the locking of domain walls that connect the bistable continuous wave (CW) states. Higher-order dispersive effects lead to oscillatory domain wall tails, allowing the fronts to interlock at discrete distances. This enables the formation of both bright and dark TLSs as peaks on the lower or dips on the upper CW state, respectively. While these properties can be explained by employing the Lugiato–Lefever equation, the validity of this mean-field model is limited only to weak injections. On the other hand, our model is not subject to these limitations and hence allows to explore much richer dynamics beyond the mean-field limit.

The second part of the thesis focuses on the interaction of TLSs in PML lasers. When multiple pulses circulate in a cavity, they interact with each other in many ways. Among these, we focus on interactions via carriers, overlapping tails, and satellites induced by time-delayed feedback. These interactions govern the degrees of freedom of the TLSs, particularly their phases and positions. To study their dynamics in more detail, we project the full high-dimensional phase space onto the subspace of the phases and positions. The resulting equations of motion demonstrate important implications regarding the notion of coherence in PML lasers. In short cavities, where the pulses are trapped in an equidistant configuration, the pulses' phases behave like coupled oscillators in the Kuramoto model with nearest neighbor interactions. In longer cavities, where the translational mode is not damped, we describe many interesting dynamical regimes such as periodic states and stable non-equidistant configurations.

# Kurzzusammenfassung

In dieser Arbeit untersuchen wir in einem theoretischen Rahmen nichtlineare optische Systeme, die Frequenzkämme und zeitlich lokalisierte Zustände (TLS) erzeugen können, die für Anwendungen in der hochpräzisen Messtechnik, der optischen Kommunikation und der ultraschnellen Signalverarbeitung unerlässlich sind. Konkret analysieren wir zwei verschiedene Systeme, die gepulste Emission erzeugen können: injizierte Kerr-Resonatoren und passiv modengekoppelte (PML) Laser. Wir entwickeln Modelle basierend auf retardierten Differentialgleichungen, die wir mit analytischen und numerischen Methoden untersuchen.

Im ersten Teil der Arbeit untersuchen wir ein Kerr-Gires-Tournois-Interferometer. Dieser kürzlich vorgeschlagene Aufbau besteht aus einer injizierten Mikrokavität, die ein nichtlineares Kerr-Medium enthält und mit einer langen externen Kavität gekoppelt ist, die durch einen Rückkopplungsspiegel geschlossen wird. Je nachdem, ob die Injektion in Bezug auf die Resonanz der Mikrokavität rot oder blau verstimmt ist, arbeitet das System im normalen oder anomalen Dispersionsbereich. Im normalen Dispersionsbereich werden die TLS durch die Kopplung von Domänenwänden erzeugt, die die bistabilen Dauerstrich-Zustände (CW) verbinden. Dispersionseffekte höherer Ordnung führen zu oszillierenden Ausläufern der Domänenwände, so dass die Fronten in diskreten Abständen ineinandergreifen können. Dies ermöglicht die Bildung sowohl heller als auch dunkler TLS als Spitzen auf dem unteren bzw. Senken auf dem oberen CW-Zustand. Diese Eigenschaften lassen sich zwar mit der Lugiato-Lefever-Gleichung erklären, aber die Gültigkeit dieses Mean-Field Modells ist nur auf schwache Injektionen beschränkt. Unser Modell hingegen unterliegt nicht diesen Einschränkungen und ermöglicht daher die Erforschung einer viel reichhaltigeren Dynamik jenseits der Mean-Field-Grenzen.

Der zweite Teil der Arbeit befasst sich mit der Wechselwirkung von TLS in PML-Lasern. Wenn mehrere Pulse in einer Kavität zirkulieren, interagieren sie auf vielfältige Weise miteinander. Dabei konzentrieren wir uns auf Wechselwirkungen über Ladungsträger, überlappende Ausläufer und Satelliten, die durch zeitverzögerte Rückkopplung entstehen. Diese Wechselwirkungen bestimmen die Freiheitsgrade der TLS, insbesondere ihre Phasen und Positionen. Um ihre Dynamik im Detail zu untersuchen, projizieren wir den gesamten hochdimensionalen Phasenraum auf den Unterraum der Phasen und Positionen. Die sich daraus ergebenden Bewegungsgleichungen zeigen wichtige Implikationen für den

Begriff der Kohärenz in PML-Lasern. In kurzen Kavitäten, in denen die Pulse in einer äquidistanten Konfiguration gehalten werden, verhalten sich die Phasen der Pulse wie gekoppelte Oszillatoren im Kuramoto-Modell mit Wechselwirkungen der nächsten Nachbarn. In längeren Resonatoren, in denen die Translationsmode nicht gedämpft ist, zeigen wir viele interessante dynamische Zustände wie periodische Zustände und stabile nicht-äquidistante Konfigurationen.

# Contents

**Abstract** i

**Kurzzusammenfassung** iii

**1. Introduction** 1

1.1. Mode-Locking . . . 3

1.2. Dispersive Kerr Resonators . . . 6

1.2.1. The Injected Kerr–Gires–Tournois Interferometer . . . 7

1.3. Outline of the Thesis . . . 8

**2. Theoretical Preliminaries** 11

2.1. Dynamical Systems with Time Delay . . . 11

2.1.1. Two-Time Representation . . . 13

2.2. Linear Stability of Steady States in Time-Delayed Systems . . . 14

2.2.1. Pseudo-Continuous Spectrum of Eigenvalues . . . 15

2.2.2. Instantaneous Eigenvalues . . . 16

2.3. From Time-Delayed to Spatially Extended Systems . . . 17

2.3.1. Normal Form via the Multiple Time Scale Approach . . . 18

2.3.2. Normal Form via the Functional Mapping Approach . . . 20

2.3.3. Simple Example via the Multiple Time Scale Approach . . . 23

2.3.4. Simple Example via the Functional Mapping Approach . . . 26

**3. Modeling of Laser Systems** 27

3.1. The Wave Equation . . . 27

3.1.1. Dispersion . . . 28

3.1.2. Nonlinear Polarization . . . 33

3.2. Injected Kerr–Gires–Tournois Interferometer . . . 34

3.2.1. Micro-Cavity with an Embedded Kerr Medium . . . 34

3.2.2. Expanding Around a Micro-Cavity Mode . . . 37

3.2.3. Injected Micro-Cavity . . . 40

3.2.4. The KGTI in Different Reference Frames . . . 42

3.3. Passively Mode-Locked Ring Laser . . . 44

3.3.1. Unidirectional Slowly Varying Traveling Wave . . . 45

3.3.2. Carrier Dynamics . . . 46

3.3.3. Time-delayed Model derived from First Principles . . . 47

3.3.4. Haus Master Equation . . . . . . . . . . . . . . . . . . . . 50
3.3.5. Lasing Threshold . . . . . . . . . . . . . . . . . . . . . . 52
3.3.6. Time-Delayed Feedback . . . . . . . . . . . . . . . . . . 54

**4. The Injected Kerr–Gires–Tournois Interferometer 57**
4.1. Conservative Dynamics . . . . . . . . . . . . . . . . . . . . . . . 57
4.1.1. Towards Dissipative Dynamics . . . . . . . . . . . . . . . . 65
4.2. Steady States of the Injected KGTI . . . . . . . . . . . . . . . . 66
4.2.1. Continuous-Wave Branch . . . . . . . . . . . . . . . . . . . 66
4.2.2. Cavity Response . . . . . . . . . . . . . . . . . . . . . . . 67
4.2.3. Multi-Parameter Study of the Steady State Solution . . . . 71
4.2.4. Instabilities of Steady State Solutions . . . . . . . . . . . . 75
4.2.5. Linear Stability of CW Solutions in the KGTI System . . . 76
4.2.6. Stability Map of the KGTI System . . . . . . . . . . . . . 79
4.3. Formation of Locked Domain Walls in the Normal Dispersion Regime 83
4.3.1. Normal Form at the Onset of Bistability . . . . . . . . . . 86
4.3.2. Spatial Eigenvalues . . . . . . . . . . . . . . . . . . . . . . 89
4.4. Existence-Range of Locked Domain Walls . . . . . . . . . . . . . . 93
4.4.1. Influence of the Feedback Rate . . . . . . . . . . . . . . . 93
4.4.2. Influence of the Detuning . . . . . . . . . . . . . . . . . . 97
4.4.3. Influence of the Cavity Coupling Factor . . . . . . . . . . . 101
4.5. Domain Walls in the Weakly Dissipative Limit . . . . . . . . . . . 103
4.6. Square Waves . . . . . . . . . . . . . . . . . . . . . . . . . . . . 110
4.7. Temporal Localized States Beyond the Mean-Field Limit . . . . . 115
4.8. Influence of Two-Photon Absorption . . . . . . . . . . . . . . . . 122
4.9. Conclusion . . . . . . . . . . . . . . . . . . . . . . . . . . . . . . 123

**5. Dynamics of Pulses in Mode-Locked Lasers 125**
5.1. Introduction . . . . . . . . . . . . . . . . . . . . . . . . . . . . . 125
5.2. Phase Dynamics . . . . . . . . . . . . . . . . . . . . . . . . . . . 129
5.2.1. Measuring Coherence . . . . . . . . . . . . . . . . . . . . . 130
5.2.2. Reciprocal Interaction . . . . . . . . . . . . . . . . . . . . 132
5.2.3. Coherence and Phase Configurations in Harmonic Solutions 140
5.2.4. Measuring Splay States Experimentally . . . . . . . . . . . 149
5.3. Interplay of Positions and Phases . . . . . . . . . . . . . . . . . . 155
5.3.1. Deriving the Amplitude-Functions . . . . . . . . . . . . . . 157

5.3.2. Phase Space Analysis for a Configuration of two Pulses . . 158
5.3.3. Influence of the Feedback Delay . . . . . . . . . . . . . . . 162
5.3.4. Influence of the Feedback Phase . . . . . . . . . . . . . . . 165
5.3.5. Dynamics of a General Multi-Pulse State . . . . . . . . . . 168
5.4. Conclusion . . . . . . . . . . . . . . . . . . . . . . . . . . . . 171

**6. Summary and Outlook 173**

**A. Numerical Methods 177**
A.1. Time Simulations . . . . . . . . . . . . . . . . . . . . . . . . . 177
A.1.1. Semi-Implicit Euler Scheme for the KGTI . . . . . . . . . 177
A.1.2. Split-Step Method for the Haus Master Equation . . . . . 178
A.2. Path Continuation . . . . . . . . . . . . . . . . . . . . . . . . 180

**B. Derivation of Normal Forms for the KGTI 183**
B.1. Normal Form at the Onset of Bistability . . . . . . . . . . . . . 183
B.2. Derivation of the Normal Form in the Mean-Field Limit . . . . . . 190
B.2.1. Normal Form via a Multiple Time Scale Analysis . . . . . 190
B.2.2. Normal Form via a Functional Mapping Approach . . . . . 198
B.2.3. The "Intuitive" Normal Form . . . . . . . . . . . . . . . . 200

**C. Derivation of the Equations of Motion 203**
C.1. The Explicit Form of the EOM . . . . . . . . . . . . . . . . . . 209
C.2. Special Cases and Simplifications . . . . . . . . . . . . . . . . . 212
C.2.1. Nearest Neighbor Interactions . . . . . . . . . . . . . . . . 212
C.2.2. Damped Translational Mode . . . . . . . . . . . . . . . . . 213
C.2.3. Interaction of Two Pulses . . . . . . . . . . . . . . . . . . 214
C.2.4. Linear Stability Analysis of $N$ Equidistant Pulses . . . . . 215
C.3. Analytical Approaches to Carrier Interaction . . . . . . . . . . . 216
C.4. Obtaining the Eigenmodes of the Direct and Adjoint System . . . 217
C.5. Extracting Steady States from Phase Space . . . . . . . . . . . 218
C.6. Extract Phase-Interaction-Parameters via Perturbation Approach 219

**List of Publications 223**

**Bibliography 225**

# 1. Introduction

The invention of the laser marked a turning point in science and technology in the middle of the 20th century. The foundation for the invention was laid by Albert Einstein in 1916 when he proposed the concept of stimulated emission [1]. It took until 1954 that this translated into an experimental realization by Charles Townes and James Gordon [2]. While their device operated in the microwave regime, the first laser in the optical domain was demonstrated in 1960 by Theodore Maiman [3], which lead to the 1964 Nobel Prize in physics. Since then, lasers have found applications in a vast range of fields ranging from telecommunications [4] to medicine (e.g., laser surgery and imaging) [5], as well as manufacturing, including material processing, laser cutting, and welding [6] to name just a few. In these examples, lasers are primarily used as a monomode *continuous-wave* (CW) source, meaning that a single laser mode corresponding to a standing wave, oscillates in the laser cavity. On the other hand, if the other laser modes are not suppressed and the individual modes evolve without a fixed phase relation, the output intensity is a slowly evolving waveform due to the arbitrary interference between the multiple modes. However, by enforcing a fixed phase relation between the modes – a technique known as *mode-locking* (ML) – it is possible to generate extremely short, high-intensity pulses. In the frequency domain, these pulses correspond to an *optical frequency comb*, consisting of a series of equally spaced spectral lines. In 2005, Theodor W. Hänsch and John L. Hall were awarded the Nobel Prize in physics for their contributions to the development of optical frequency comb technology, which revolutionized precision metrology [7]. In the following years, frequency comb technology has expanded into other fields and found applications in, e.g., optical clocks [8], dual-comb spectroscopy [9], and astronomical spectrograph calibration for exoplanet detection [10].

The link between the spectral and temporal representations of frequency combs is visualized in Fig. 1.1. The frequency comb (left) is centered around the carrier frequency $\omega_0$ of the pulse. Each spectral line corresponds to a plane wave of which the real part is shown in different colors in the right panel of the figure. These frequencies correspond to the cavity modes of the laser. Due to the fixed phase relation between the modes, the plane waves can interfere constructively, meaning their maxima align, which leads to the formation of a pulse in the temporal domain. For the rest of the time, the plane waves no longer maintain a fixed phase relation and interfere destructively resulting them to cancel each other

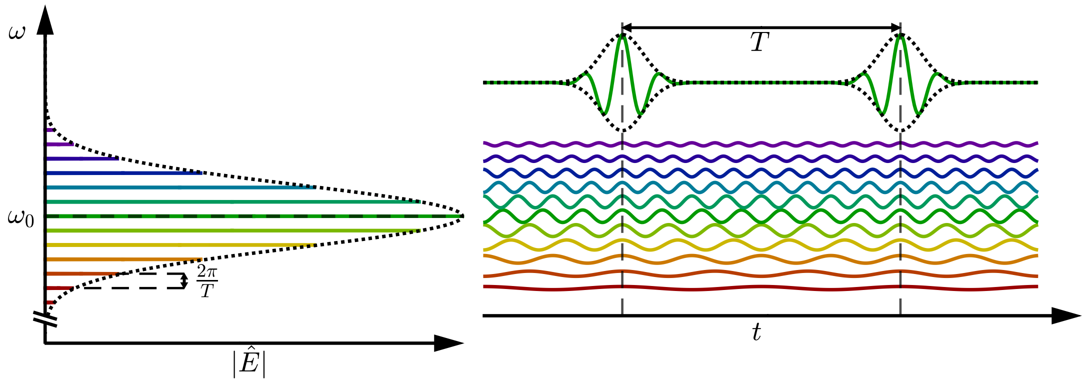


**Figure 1.1:** Schematic of a frequency comb. The pulses in the right panel have a carrier frequency $\omega_0$ and repeat with a period $T$. This corresponds to the frequency comb shown in the left panel. Each peak in the power spectrum $|\hat{E}|$ stands for a plane wave with the given frequency. At the maximum of the wave packet, the plane waves interfere constructively.

out. The pulse repetition rate $T$ is related to the spectral spacing of the comb lines by $\omega_{\text{rep}} = \frac{2\pi}{T}$. Additionally, the pulse duration $T_p$ is inversely proportional to the width frequency comb's envelope. In other words, the shorter the pulse duration, the more modes are locked together, and the higher the peak intensity of the pulse.

The concept of frequency combs is linked to *localized states* (LSs) where certain physical quantities (such as energy or mass) are confined to a specific region rather than spreading uniformly across a system. LSs can be observed in nature in various of systems ranging from vegetation patterns [11] to electronic states in disordered materials [12]. Generally, the localization can occur in space, time, or both. In optical systems, localized states in dispersive and diffractive nonlinear resonators were observed and predicted more than 30 years ago and the resulting structures are termed *cavity solitons* [13–16]. Spatial localization can occur in the transverse plane of optical resonators, where cavity solitons appear as localized intensity peaks across the resonator's aperture [17]. *Temporal localized states* (TLSs) can be used to generate arbitrary patterns in the time domain in the output of a fiber laser and therefore, can be used as bits of information [18–21].

TLSs can be generated in dissipative systems which are paired with an external driving force providing gain to the system. Therefore, optical TLSs form in an interplay of gain and losses and are also termed dissipative solitons [22]. In this thesis, we consider two mechanisms for the creation of TLSs in optical systems, namely *mode-locking* [23] and *dispersive Kerr resonators* [18, 24]. An important differentiation between them is, that mode-locking is a phase-invariant process while the frequency comb of a Kerr resonator is phase-locked to an external injection.

## 1.1. Mode-Locking

The term mode-locking refers to the process in which the cavity modes of a resonator are locked in certain phase relations. Usually, the lasing modes do not phase-lock spontaneously and additional elements are inserted in the laser cavity to promote pulsed operation. These elements provide gain (amplification) and losses (dampening) to the electric field. Here, one differentiates active and passive mode-locked systems. In systems with *active mode-locking*, the losses are modulated with a frequency that is synchronized with the modes of the cavity [25]. The modulation is typically realized using either an electro-optic or an acoustooptic intra-cavity modulator [26–30]. This approach leads to a very regular train of pulses, however, the pulse width is limited by the speed of the external modulator [25].

On the other hand, in *passively mode-locked* (PML) systems, losses are provided by a passive element, generally a saturable absorber. The gain section is electrically or optically pumped, thereby generating an inversion of charge carriers, and the absorber section has a reverse bias applied to it [31]. For the mechanism, it is essential that the gain and absorber are depleted at different rates. This is illustrated in Fig. 1.2. The different depletion rates of the gain (green) and losses (red) open a window of net-amplification around the pulse shown in shaded green. Then, the absorber recovers faster than the gain such that there are net losses (shaded red). Hence, the carriers act as pulse-shaping elements where the width of the pulse is controlled by the ratio of the depletion and recovery rates.

For the experimental implementation of PML, one can employ *Vertical-Cavity Surface-Emitting Lasers* (VCSELs). VCSELs are circular disk lasers emitting by their surface. Their height is only a few micrometers, while their diameter ranges from several micrometers to hundreds of micrometers, with arrays reaching millimeter scales. The short propagation length in VCSELs is compensated by stacked, highly reflective, distributed Bragg mirrors. Further, one can couple a VCSEL to a *semiconductor saturable absorber mirror* (SESAM) in a face-to-face configuration, and thereby create a long external cavity, which can be easily tuned in length from a few centimeters towards several meters [21]. This setup

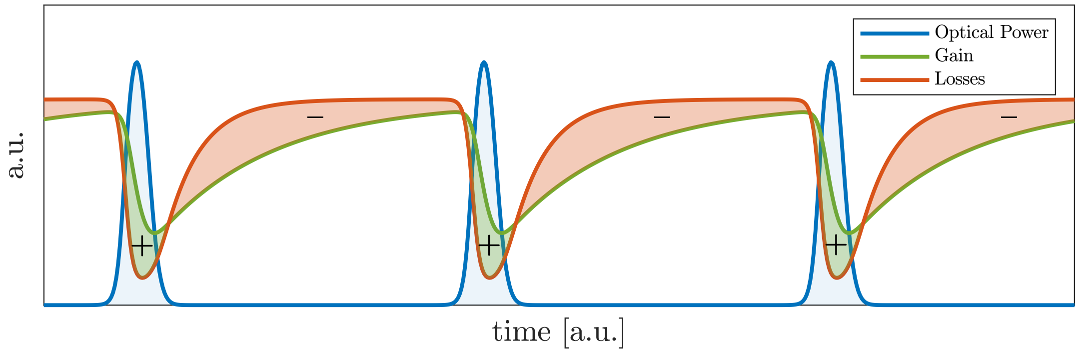


**Figure 1.2:** Schematic illustrating the principle of passive mode-locking. Around a pulse, the absorber is depleted faster than the gain such that a window of net-amplification is opened (shaded green). For the rest of the time, there are net-losses (shaded red) as the losses outweigh the gain.

corresponds to a nonlinear Fabry–Pérot interferometer and is termed *Vertical-External-Cavity Surface-Emitting Laser* (VECSEL). VECSELs have proven to provide excellent performance such that sub-picosecond pulse trains can be realized [32–35]. In VECSELs the interplay between the potentially wide aperture and the thermal lensing, diffraction, and nonlinear refraction index change leads to complex transverse spatial dynamics [36, 37]. Their transverse dynamics, and the consequence of coupling high finesse micro-cavities with a time delay $\tau$, are the source of complex and interesting temporal and spatio-temporal dynamics [38].

A PML can operate in the *fundamental mode-locked* (FML) regime, where a single pulse circulates in the cavity, or in the *harmonic mode-locked* (HML) state, where $N$ equidistant pulses reside within the cavity. An important limit case is the *long-cavity limit* where the cavity size is much larger than all other time scales in the system [39]. When operating a VECSEL in the long-cavity limit and below the lasing threshold, that is, the off-state of the laser is stable, individual pulses become TLSs, which can be independently placed throughout the cavity [21]. Further, we note that frequency combs created by PML lasers are phase-invariant. Studying the interactions of the TLSs – both in position and phase – is one of the focuses of this thesis. For the theoretical modeling, we employ a ring cavity in order to benefit from the broad theoretical background that is present for this simple design [40, 41]. A schematic setup is shown in Fig. 1.3. Here, five pulses circulate in the main cavity of size $\tau$ and each of them possesses a phase and position as indicated by the blue and orange arrows, respectively. The pulses can interact with each other via several mechanisms.

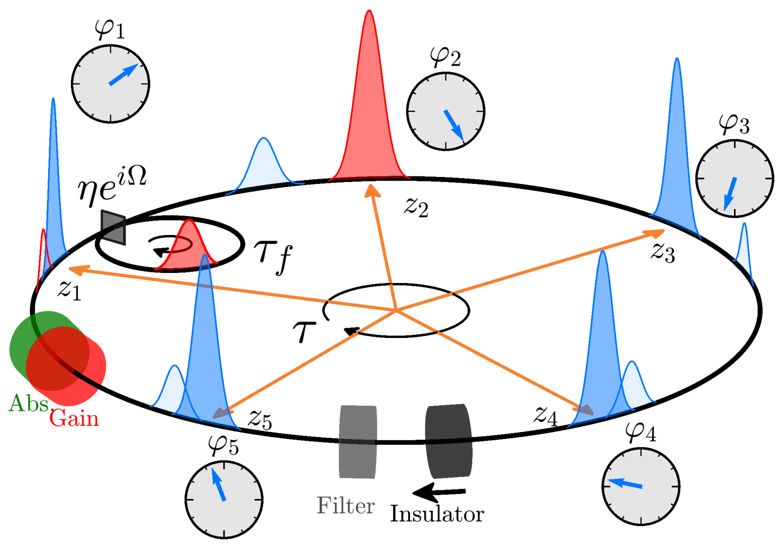


**Figure 1.3:** Schematic of a unidirectional ring cavity of length $\tau$ with five pulses per round-trip. The cavity is mode-locked by a saturable absorber and coupled to a time-delayed feedback loop with round-trip time $\tau_f$, feedback rate $\eta$ and phase $\Omega$. Each pulse circulating possesses a phase $\varphi_i$ and position $z_i$. The pulses are non-equidistant and their respective satellites induced by time-delayed feedback exhibit different amount of overlap with neighboring pulses.

First, each pulse creates a depletion in the gain (cf. Fig. 1.2) that influences the next pulse [42]. Next, the decaying tails of the pulses can overlap, enabling a coherent interaction [42, 43]. Finally, recent work demonstrated the influence of *time-delayed feedback* on the output of a PML laser; see e.g. [44–48]. Here, we take time-delayed feedback into account by introducing a second cavity of size $\tau_f$ (cf. Fig. 1.3), which is coupled to the main cavity by a factor of $\eta e^{i\Omega}$, where $\eta$ represents the strength of the feedback and $\Omega$ introduces an additional phase shift. This leads to the appearance of satellites in the main cavity, cf. the small pulses, which interact with the main pulses and thus, influence their position and phase [44, 45]. We note that all of these interaction are not limited to ring cavities but occur in the same way in VECSELs, as there, the pulses cross in the external cavity in free space such that no additional interaction is added. Hence, it is sufficient to consider a ring cavity to study the pulse interactions in a VECSEL.

For the theoretical and numerical analysis, we employ a model derived from first principles, which is based upon *delay differential equations* (DDEs) [41]. In the uniform field limit, where gain, absorption and losses are small, the DDE model is equivalent to the established *Haus Master Equation* (HME) [25].

## 1.2. Dispersive Kerr Resonators

Another approach to generating frequency combs utilizes dispersive resonators containing nonlinear media, which are pumped with a monomode CW beam. Hence, in contrast to the frequency combs created by PML, these combs are phase-locked to the CW injection. Most commonly, the nonlinear medium is a Kerr medium, which is a material exhibiting a third-order ($\chi_3$) nonlinearity. However, there have also been important demonstrations using materials with second-order ($\chi_2$) nonlinearities for frequency conversion and microwave photonic applications [49, 50]. Depending on the application, the resonator can be a high-Q microring, which ranges from a few micrometers to millimeters in diameter and therefore can be integrated in photonic chips [24, 51, 52], or a fiber loop, which can be several meters long [18, 53]. A Kerr medium exhibits an intensity-dependent index of refraction. This results in a process called *four-wave mixing* [54]. Here, two pump photons are converted into an “idler” and a “signal” photon of frequency $\omega_i$ and $\omega_s$, respectively. These photons are in phase and are positioned symmetrically around the pump frequency $\omega_0$ with an offset $\Delta\omega$. The value of this offset is determined by a phase-matching condition that is fulfilled for the cavity modes. That is, the offset corresponds to the free spectral range $2\pi/\tau$ where $\tau$ is the cavity length. Hence, four-wave mixing describes a process in which energy is transferred between frequency components. Successive four-wave mixing creates the Kerr frequency comb, cf. Fig. 1.1. Finally, the interplay of dispersive properties of the resonator, the nonlinearity of the Kerr medium and the external injection lead to the formation of dissipative cavity solitons that may be used as addressable bits in all-optical information storage and processing [18, 24].

Recently, an alternative setup was proposed that aims to combine the advantages of dispersive Kerr micro-resonators and mode-locked VECSELs while mitigating their limitations [55]. This *Kerr–Gires–Tournois Interferometer* (KGTI) employs a broad micro-cavity like in a VECSEL, which contains a Kerr medium. The maximum achievable power of mode-locked VECSELs is limited by the use of dissipative nonlinearities (gain and saturable absorption), which require a thorough thermal management. On the other hand, Kerr micro-resonators exhibit numerous advantages such as high quality factors (up to $Q = 10^{10}$) and the possibility to integrate them in photonic chips, however, the small transverse size inherently limits the generated optical power and forbids the multiplexing of information in e.g. higher-order transverse or polarization modes. The KGTI is not subject to these limitations and thus, can achieve a high output power while enabling spatio-temporal dynamics leading to applications employing spatial multiplexing [55].

### 1.2.1. The Injected Kerr–Gires–Tournois Interferometer

A *Gires–Tournois Interferometer (GTI)* is essentially an asymmetrical Fabry–Pérot resonator composed of two face-to-face mirrors where one has a very high reflectivity and the other is partially transparent [56]. A GTI induces controllable dispersive effects while typically second-order group velocity dispersion (GVD) is the dominating effect [57]. Its amount is tunable by choosing the operating frequency with respect to the cavity resonance. Using a red or blue detuning, one can achieve either normal or anomalous dispersion. At resonance, GVD vanishes such that higher order effects such as third-order dispersion become dominant.

Here, we consider a GTI in which a thin slice of a nonlinear Kerr medium is embedded and that is coupled to a distant feedback mirror forming an external cavity. A schematic setup is shown in Fig. 1.4. The micro-cavity of length $\tau_c$ containing the Kerr medium is enclosed by two Bragg mirrors with reflectivities $r_1$ and $r_2$, respectively. It is injected by a field $Y$ that circulates in the external cavity of size $\tau \gg \tau_c$. The output $O$ is the difference between the micro-cavity field $E$ and the external field $Y$. The feedback mirror has a reflectivity $\eta$ and exerts a phase shift $\phi$. The whole setup is subject to monomode CW injection of amplitude $Y_0$ and frequency $\omega_0$.

From a modeling perspective, typical Kerr resonators are well modeled by the *Lugiato–Lefever equation* (LLE) or coupled-mode models [24, 58–64] in the limit of a small intracavity power. The LLE is derived by modeling the propagation in the resonator by the *nonlinear Schrödinger equation* (NLS) with boundary conditions defined by the *Ikeda map* that links the output with the input while taking the injection into account [65]. In a mean-field approximation, this results in the LLE [66]. While the LLE captures the fundamental dynamics of Kerr-frequency-comb-generation, many aspects lie beyond its reach and domain of applicability. For instance, the existence of multi-stability and “super cavity solitons” was demonstrated both experimentally and theoretically using the NLS equation with boundary conditions defined by the Ikeda map [67, 68]. On the other hand, the model describing the dynamics in the KGTI is based upon *Delay*

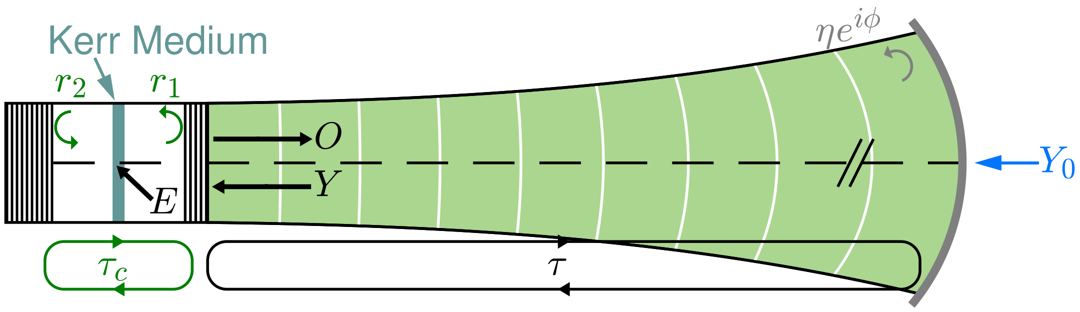


**Figure 1.4:** Schematic of the Kerr–Gires–Tournois interferometer, which is composed of a micro-cavity containing a Kerr medium coupled to a long external cavity of size $\tau$ that is closed by a mirror of reflectivity $\eta$. The setup is driven by a monomode injection field $Y_0$.

*Algebraic Equations* (DAEs) [55], that are not limited in applicability to the mean-field limit. In this thesis, we will theoretically study this model derived from first principles employing analytical and numerical tools, and thus, unveil many aspects of the dynamics in the KGTI. The work lays the foundation for a future experimental realization of this proposed setup.

## 1.3. Outline of the Thesis

The thesis is structured as follows. In Chapter 2, we introduce various theoretical preliminaries and concepts that are used throughout the thesis. Next, in Chapter 3, we derive the dynamical models for the systems under study, namely the KGTI (Section 3.2) and a passively mode-locked ring laser (Section 3.3).

We proceed with studying the dynamical regimes in the KGTI in Chapter 4. First, we consider the conservative case where the external cavity is closed and no injection is present leading to the demonstration of integrability and reversibility in a time-delayed system (Section 4.1). The study of the dissipative KGTI starts with an extended analysis of the steady states and their stability in (multi-dimensional) parameter-space, which gives an overview of the dynamical regimes (Section 4.2). In the following, we explore the complex dissipative patterns that can emerge in the KGTI system. In particular, we study bright and dark TLSs, which consist in the locking of domain walls that connect the bistable steady states. We underline our analysis by deriving a normal form that describes this process as a minimal pattern formation scenario (Section 4.3). Next, we explore the range of existence of the locked domain walls in different parameters and describe interesting dynamics such as chaotic regimes (Section 4.4). Finally, we study their formation in the weakly dissipative limit (Section 4.5). In the last four subsection, we analyze the formation of square waves (Section 4.6), explore temporal localized structures beyond the mean-field limit (Section 4.7) and study the influence of two-photon absorption (Section 4.8), before concluding our results on the KGTI in Section 4.9.

In the next Chapter 5, we study the dynamics of multi-pulse states found in the output of a PML laser. We use a superposition ansatz to describe a solution consisting in $N$ pulses per round-trip, and from that, derive effective *equations of motion* (EOM) for the pulses' $N$ phases and $N$ positions, thus expressing the dynamics of the $2N$ degrees of freedom. From that, we can consider two cases. First in Section 5.2, we study shorter cavities for which the position and phase dynamics are decoupled because the translational mode is damped due to strong carrier interactions. Hence, the dynamics is fully described by the EOM for the $N$ phases, which is equivalent to the *Kuramoto model* with nearest neighbor interactions. This equivalence has important consequences for understanding the phase relation and thus, the coherence of the HML state. The second case in Section 5.3 applies to cavities where phase- and position dynamics occur on the same time scales. Here, one needs to study the full $2N$-dimensional EOM. We perform a detailed bifurcation analysis of the parameters of the time-delayed feedback and explore the vast dynamical regimes. The results of the chapter are then concluded in Section 5.4.

Finally, in Chapter 6, the results of this thesis are summarized, and an outlook towards the possibility of further studies is given. The appendix contains details on the numerical methods and schemes used throughout this thesis (Appendix A), the full derivation of the normal forms for the KGTI (Appendix B) and the complete derivation of the EOM for multi-pulse states PML lasers (Appendix C).

# 2. Theoretical Preliminaries

In this chapter, we introduce important theoretical concepts that are used throughout the thesis. We begin with introducing dynamical systems that include time delays, see Section 2.1. In Section 2.2, we present how to determine the linear stability of steady states in such systems. Finally, in Section 2.3, we clarify the link between time-delayed and spatially extended systems. In particular, we present two schemes to derive a normal form from a time-delayed system.

## 2.1. Dynamical Systems with Time Delay

Dynamical systems describe how state vectors evolve over time based on deterministic rules and are therefore relevant in virtually all fields of natural sciences, as well as in economics and engineering, e.g., for modeling market dynamics or control systems [69]. They are formalized either as iterative maps when considering discrete time-steps, or as differential equations for the case of continuous time evolution. These systems can be nonlinear, which makes their study more involved as they – in general – cannot be solved analytically anymore. Nonlinear dynamical systems where extensively studied and formalized in the last century, such that there is a large framework to build upon and of which we want to mention key aspects relevant for this thesis.

A fundamental aspect of dynamical systems is the classification of their solutions. These can be fixed points, periodic orbits, quasiperiodic orbits (i.e., tori), and even more complex invariant sets (termed *strange attractors*), which all describe invariant manifolds in the respective phase space. The manifolds can either act as attractors or repellers depending on their associated linear stability. Further, the dynamics also depends on system parameters which define the potential landscape in which the trajectories evolve. Here, the nonlinearity of the system plays a crucial role because it allows small shifts in parameters to lead to qualitative changes of the system behavior, which is called a *bifurcation* point. Important bifurcations include saddle-node (SN or fold), Andronov-Hopf (AH), torus, period-doubling, transcritical, and pitchfork bifurcations. All of the mentioned are local bifurcations that can be described by a local *normal form*. That is, any system that exhibits a certain local bifurcation is locally equivalent to the respective normal form. This differentiates them from global bifurcations which cannot be described by a local normal form. Hence, in a global bifurcation, not only the local environment of an equilibrium changes, but the phase space as a whole undergoes a critical transition. Important global bifurcations include homoclinic and saddle-node infinite-period (SNIPER) bifurcations [69].

The simplest form of a dynamical system is given by an *ordinary differential equation* (ODE) of the form $\dot{x}(t) = f(x(t), t)$ where $x \in \mathbb{R}^n$ is the state vector and $t$ is time. Here, the RHS defined by $f$ is time-dependent, making the system *non-autonomous*, whereas a time-independent system is referred to as *autonomous*. While for a dynamical system described by an ODE all action are instantaneous, this is often not the case in real-world scenarios, where the propagation velocity of signals is, in general, finite. Hence, the proper mathematical modeling needs to take this into account, such that the dynamics in these systems do not only depend on the current state of the system, but also its past [70, 71]. Examples for such systems range from applications in economy [72], over climate modeling [73] to active matter [74], just to name a few. Such systems are modeled by *delay differential equations* (DDEs), which can formally be written as

$$M\dot{x} = f(x(t), x(t-\tau), t), \tag{2.1}$$

where $\tau$ is a time delay. In general, also multiple delays $\tau_1, \ldots, \tau_m$, state or time dependent delays and time delays in spatially extended systems are possible [75–77]. Further, $M$ is a *mass matrix*, which defines the time scales of the components of $\dot{x}$. In particular, $M$ can be singular making the evolution instantaneous. Here, some parts in Eq. (2.1) do not contain temporal derivatives but can contain delays. Hence, these equations are not dynamical but rather define an algebraic constraint and are therefore called *delay algebraic equations* (DAEs). Another form of delayed equations are *neutral delay differential equations* (NDDEs). Here, the dynamics also depend on the temporal derivative of a delayed state

$$\dot{x} = f(x(t), x(t-\tau), \dot{x}(t-\tau), t). \tag{2.2}$$

However, one can show that every NDDEs can be written as a DAE. We simply define $y = \dot{x}(t)$, which leads to

$$\dot{x} = f(x(t), x(t-\tau), y(t-\tau), t), \tag{2.3}$$

$$0 = y - f(x(t), x(t-\tau), y(t-\tau), t), \tag{2.4}$$

which is a DAE for the new state vector $v = (x, y)$. Hence, NDDEs are a subset of DAEs. It must be noted that this equivalence does not go in both direction. A DAE cannot always be translated into a NDDE.

An important consequence of systems containing a delay is that they are infinite dimensional [78]. This can be easily seen, when considering Eq. (2.1) as an initial value problem. Here, the initial state needs to be defined over and interval $[-\tau, 0)$ and thus, exhibits infinitely many degrees of freedom.

Due to the difficulties to obtain analytical solutions in nonlinear dynamical systems, numerical methods play an important role in their analysis. In particular, one can use numerical schemes for time-integration and, therefore, perform direct numerical simulations (DNS). On the other hand, numerical path continuation techniques offer a powerful tool for a more cohesive analysis. For more details on the numerical schemes used in this thesis, see Appendix A.

### 2.1.1. Two-Time Representation

An important limit for systems with time delays occurs, when the delay becomes much larger than all other time scales in the system and, therefore, forms its own independent time scale. This is referred to as the *long-delay limit*. Mathematically this means, that we can consider a time trace $x(t)$ as $x(t) = x(\xi\tau + z)$ where $\xi \in \mathbb{N}$ counts the round-trip number and $z \in [0, \tau]$ is defines the dynamics within one round-trip [79, 80]. This property is visualized in Fig. 2.1. The signal in panel (a) can be cut into pieces of length $\tau$, that can be stacked next to each other, see panel (b). There. we can observe that the signal exhibits a drift. The drift stems from the fact that a physical system has a finite causal response time. Hence, the actual period of the solutions $T$ is slightly larger than the time delay $\tau$ in the long-delay limit. This is visualized in Fig. 2.1 (c), where we cut the trace in pieces of length $T > \tau$ such that the drift vanishes.

The visualization represented in Fig. 2.1 (b),(c) allows to observe the dynamics of a DDE over many round-trips, which is a useful tool to study the long-term behavior of a system. Further, it reveals that time-delayed systems exhibit a fundamental similarity to spatially extended systems [79, 81]. In this context, Fig. 2.1 (b) is referred to as a *two-time* (or *space-time*) diagram as it visualizes the dynamics of a “space-like” variable $z$ along a slow time $\xi$, that counts the round-trip number. Further, using $T$ instead of the natural time scale $\tau$ as the folding parameter, corresponds to going into the co-moving reference frame.

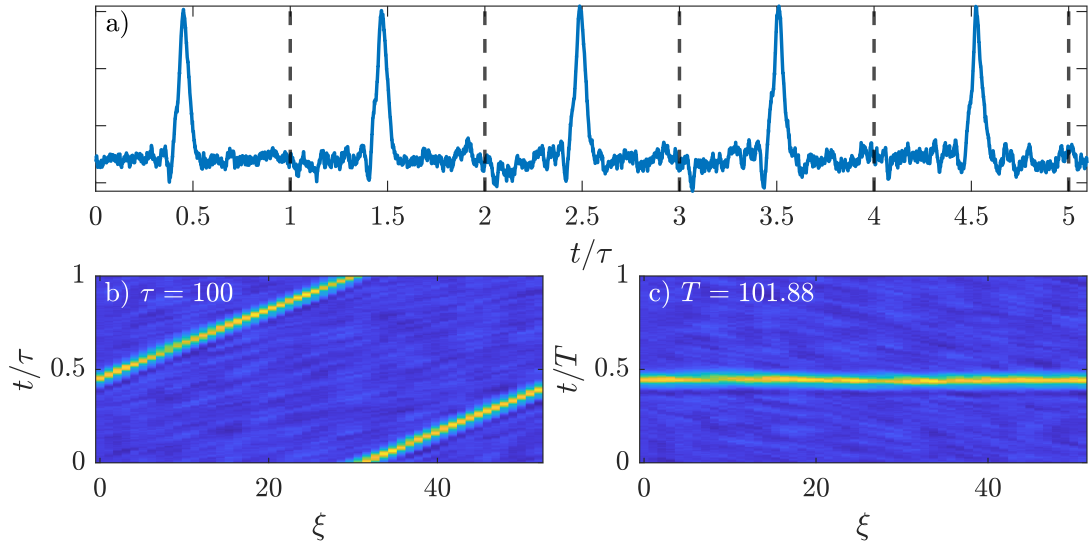


**Figure 2.1:** The signal in (a) stemming from the simulation of a time-delayed system with time delay $\tau$ can be cut into pieces of length (b) $\tau$ and (c) $T > \tau$ to observe the long-term dynamics.

However, one has to remember that the "space" in Fig. 2.1 is not periodic but rather connects the end of one round-trip to the beginning of the next round-trip. Denoting $x(\xi, z) = x(\xi\tau + z)$, this property can be written as

$$x(\xi, \tau) = x(\xi + 1, 0) \,. \tag{2.5}$$

For the comparison of this type of boundary condition to a standard periodic boundary condition, it is instructive to consider the respective time traces as ways to fill the surface of a cylinder. While the trajectory of a spatially extended system with periodic boundaries forms rings that are stacked on top of each other, the time trace of a time-delayed systems is a single string that curls around the cylinder.

## 2.2. Linear Stability of Steady States in Time-Delayed Systems

Determining the linear stability of steady states in a time-delayed system needs a more refined approach compared to ODEs. We consider a general non-autonomous time-delayed system $M\dot{x} = f(x(t), x(t-\tau))$. Here, a steady state $\tilde{x}$ satisfies $f(\tilde{x}, \tilde{x}) = 0$. To determine its stability, two different cases need to be differentiated. First, there are eigenvalues stemming from the delayed part of the equation.

In fact, there is an infinite number of these eigenvalues [70]. In Section 2.2.1 it is shown, that these discrete eigenvalues lay on a continuous curve in the long-delay limit. Hence, this spectrum is called the *pseudo-continuous spectrum of eigenvalues* [70, 82]. On the other hand, there are eigenvalues stemming from the instantaneous part of the equation, cf. Section 2.2.2.

### 2.2.1. Pseudo-Continuous Spectrum of Eigenvalues

To determine the pseudo-continuous spectrum of eigenvalues of a steady state, we consider small perturbations $\delta$ to the state vector and linearize the system

$$M\frac{d}{dt}\left(\tilde{x}+\delta\right) = f\left(\tilde{x}+\delta,\tilde{x}+\delta_\tau\right) \tag{2.6}$$

$$\Leftrightarrow \dot{\delta} = \underbrace{f\left(\tilde{x},\tilde{x}\right)}_{=0} + A\delta + B\delta_\tau, \tag{2.7}$$

where $A = \frac{\partial f\left(x,x_\tau\right)}{\partial x}\Big|_{x=\tilde{x}}$, $B = \frac{\partial f\left(x,x_\tau\right)}{\partial x_\tau}\Big|_{x=\tilde{x}}$ and the index $\tau$ refers to the delay state. We consider perturbations $\delta\left(t\right) = \delta_0 e^{\lambda t}$, $\lambda \in \mathbb{C}$, which yields the following equation

$$\left(M\lambda - A - Be^{-\lambda\tau}\right)\delta = 0, \tag{2.8}$$

where the solutions for the eiqenvalues $\lambda$ are defined by the characteristic equation

$$\det\left[-M\lambda + A + Be^{-\lambda\tau}\right] = 0. \tag{2.9}$$

This equation is transcendental, i.e., in general it posses an infinite number of solutions for the eigenvalues $\lambda$. However, according to the general theory [83], the eigenvalues are bound to the right and accumulate solely at $\mathrm{Re}\lambda \to -\infty$ such that only a finite number of eigenvalues determines the stability [70]. It is shown in [84] that the major part of the solution of Eq. (2.9) falls on the following curve:

$$\lambda = \frac{\gamma}{\tau} + i\mu \text{ with } \gamma,\mu \in \mathbb{R}. \tag{2.10}$$

This ansatz makes sense intuitively, as any perturbation induced by the time-delayed nature of the system can only grow as fast as the delay. Hence, we can assume that the growth rate ($\mathrm{Re}\left(\lambda\right)$) is inversely proportional to the time delay. Further, in the long-delay limit, where $\tau$ is large compared to other time scales in the system, all terms proportional to $\tau^{-1}$ vanish. Using this and the scaling Eq. (2.10) in Eq. (2.9) gives

$$\det\left[iM\mu - A - Be^{-\gamma}e^{-i\mu\tau}\right] = 0. \tag{2.11}$$

Defining $g = e^{-\gamma}e^{-i\mu\tau}$ leads to

$$\det\left[-iM\mu + A + Bg\right] = 0, \tag{2.12}$$

which has possibly multiple solutions $g = g_j(\mu) \in \mathbb{C}$. Taking the absolute value of $g_j$ and solving for the real part $\gamma_j$ yields

$$\gamma_j = -\ln\left|g_j(\mu)\right|. \tag{2.13}$$

This equation defines the (multiple) branches of the pseudo-continuous spectrum of eigenvalues $\lambda_j = -\frac{\ln|g_j(\mu)|}{\tau} + i\mu$, which are parametrized by $\mu$. To find explicitly the position of the eigenvalues on the pseudo-continuous spectrum, we need to find the discrete values $\mu_k$ for which eigenvalues exist. We restart with the definition of $g_j(\mu) = e^{-\gamma_j}e^{-i\mu\tau}$ and rearrange for the imaginary part of the eigenvalues

$$\Rightarrow e^{i\mu\tau} = \frac{1}{e^{\gamma_j}g_j(\mu)} = \left(\frac{g_j(\mu)}{|g_j(\mu)|}\right)^{-1} = e^{-i\arg(g_j(\mu))}. \tag{2.14}$$

This equation defines the positions of the eigenvalues on the pseudo-continuous spectrum as the imaginary part needs to satisfy

$$\mu_k\tau = -\arg\left(g_j(\mu_k)\right) + 2\pi k, \quad k \in \mathbb{Z}. \tag{2.15}$$

In general, the solutions $\mu_k$ need to be found numerically. An important consequence of Eqs. (2.10) and (2.15) is, that the distances of the imaginary and real parts of two neighboring eigenvalues both scale with $\tau^{-1}$. That is, the spectrum becomes denser for longer delays.

### 2.2.2. Instantaneous Eigenvalues

The instantaneous eigenvalues stem from the immediate response of the system to a perturbation [70, 85]. Therefore, we neglect the time-delayed part of the equation and simply consider the characteristic equation

$$\det\left[-M\lambda + A\right] = 0, \tag{2.16}$$

where $A = \frac{\partial f\left(x, x_\tau\right)}{\partial x}\Big|_{x=\tilde{x}}$. Because of this, there are $\operatorname{rank}\left(M\right)$ instantaneous eigenvalues to the generalized eigenvalue problem in Eq. (2.16). Hence, there is only a finite number of instantaneous eigenvalues.

## 2.3. From Time-Delayed to Spatially Extended Systems

We already introduced the similarities between time-delayed and spatially extended systems in Section 2.1.1, in particular by the two-time representation presented in Fig. 2.1. Further, the pseudo-continuous spectrum of eigenvalues described in Section 2.2.1 can be understood as a dispersion relation. In this section, we aim to exploit these similarities in order to directly translate a time-delayed into a spatially extended system. That is, we want to find a *normal form* in form of a *partial differential equation (PDE)* describing the dynamics of a time-delayed system in some specific limit. Normal forms are a minimal set of equations that exhibits a certain dynamics [86]. That is, for every dynamical system undergoing a local bifurcation, the dynamics on a suitable invariant manifold is captured by the normal form of that bifurcation.

For the analysis of time-delayed systems the derivation of normal forms is a powerful tool because many physical properties such as diffusion and dispersion are hidden in the time-delayed representation, while in a PDE, they have a one-to-one correspondence to specific terms. For instance, the coefficient of first derivative in space is the drift velocity, the second order derivative in space controls diffusion and so on. Therefore, we can unveil how the parameters in a time-delayed system control the physical phenomena that can be observed.

To summarize, our goal is to approximate a DDE such as

$$M\dot{v} = f\left(v, v\left(t-\tau\right), p\right) \tag{2.17}$$

by a PDE normal form

$$\partial_\xi y = f\left(v, \partial_z v, \partial_z^2 v, \ldots, p\right) \tag{2.18}$$

around a critical value $p_c$ of the control parameter $p$. In order to derive the normal form, we make use of the separation of time scales occurring in delayed equations in the long-delay limit (cf. Section 2.1.1). That is, there is a fast time controlling the evolution within a round-trip and a slow time scale controlling the evolution from round-trip to round-trip [79]. This allows us to define a smallness parameter as

$$\epsilon = \frac{1}{\tau} \ll 1. \tag{2.19}$$

Next, we normalize the time delay in Eq. (2.17), which yields

$$\epsilon M \dot{v} = f\left(v, v\left(t-1\right), p\right). \tag{2.20}$$

This equation is our starting point to derive a normal form equation. In the following, two derivation schemes are presented. These are a derivation via a multiple-time scale approach (cf. Section 2.3.1) and via a functional mapping approach (cf. Section 2.3.2). Finally, a normal form for a simple example is calculated using both schemes, cf. Sections 2.3.3 and 2.3.4.

### 2.3.1. Normal Form via the Multiple Time Scale Approach

First, it is necessary to define an expansion point around which the delayed equation is approximated. Generally, this is a critical parameter value $p_c$. For that we define a deviation from the critical parameter value in orders of $\epsilon$, i.e., $p = p_c + \epsilon \Delta p_1 + \epsilon^2 \Delta p_2 + \ldots$. The same is done for the fields $v$, i.e., $v = v_c + \epsilon v_1 + \epsilon^2 v_2 + \ldots$. Further, we define new time scales in orders of $\epsilon$, which later can be identified with $\xi$ and $z$. In particular, the fastest time scale corresponds to the "space-like" variable $z$ and a combination of the others corresponds to the slow time $\xi$. As a convenient choice, we can use the fact that a solution's period $T$ is slightly larger than the time delay $\tau$. That is, if we properly scale the space-like variable, we can remove the drift. Hence, we define

$$t_0 = \omega t, \quad t_1 = 0, \quad t_2 = \epsilon^2 t, \quad t_3 = \epsilon^3 t, \tag{2.21}$$

where small changes in $\omega$ account for the difference between delay time and period: $\omega = 1 + \epsilon\omega_1 + \epsilon^2\omega_2 + \epsilon^3\omega_3 + \ldots$. This technique is known as the Poincaré–Lindstedt method and allows us to set the $t_1$ scale to 0 [69]. Note that this choice is optional, one could also include the $t_1$ scale and not scale $t_0$, but instead remove the drift in the end by going into the co-moving reference frame. According to the scaling, the time derivative in Eq. (2.20) needs to be separated into orders of $\epsilon$:

$$\begin{aligned}\frac{d}{dt} &= \mathcal{T}_0 + \epsilon\mathcal{T}_1 + \epsilon^2\mathcal{T}_2 + \epsilon^3\mathcal{T}_3 + \dots \\ \text{where } \mathcal{T}_0 &= \partial_0, \mathcal{T}_1 = \omega_1\partial_0, \mathcal{T}_2 = \omega_2\partial_0 + \partial_2, \mathcal{T}_3 = \omega_3\partial_0 + \partial_3.\end{aligned} \tag{2.22}$$

Here, we defined $\partial_j = \frac{\partial}{\partial t_j}$. Next, we express the delayed state $v\,(t-1)$ in the new time scales. For that, we need to evaluate the new time scales for the delayed state $t-1$, i.e, $t_j(t-1)$. We find

$$\begin{aligned} t_0(t-1) &= \omega(t-1) = t_0 - \omega, & t_1(t-1) &= 0, \\ t_2(t-1) &= \epsilon^2(t-1) = t_2 - \epsilon^2, & t_3(t-1) &= \epsilon^3(t-1) = t_3 - \epsilon^3. \end{aligned}$$

That is, the delayed state is $v\,(t-1) = v\,(t_0 - \omega, t_2 - \varepsilon^2, t_3 - \varepsilon^3)$. This expression can be expanded for small $\epsilon$, i.e.,

$$v\,(t-1) = v\left(t_0 - 1 - \epsilon\omega_1 - \epsilon^2\omega_2 - \epsilon^3\omega_3, t_2 - \epsilon^2, t_3 - \epsilon^3\right) \tag{2.23}$$

$$= \left[1 + \epsilon\partial_\epsilon + \frac{\epsilon^2}{2}\partial_\epsilon^2 + \frac{\epsilon^3}{6}\partial_\epsilon^3 + \dots\right] v\left(t_0 - \omega, t_2 - \epsilon^2, t_3 - \epsilon^3\right)\bigg|_{\epsilon=0}. \tag{2.24}$$

The first derivative with respect to $\epsilon$ reads

$$\partial_\epsilon v\left(t_0 - \omega, t_2 - \epsilon^2, t_3 - \epsilon^3\right) = \left[\left(-\omega_1 - 2\epsilon\omega_2 - 3\epsilon^2\omega_3\right)\partial_0 - 2\epsilon\partial_2 - 3\epsilon^2\partial_3\right] v\left(t_0 - \omega, t_2 - \epsilon^2, t_3 - \epsilon^3\right).$$

Analogously, we compute the higher derivatives to finally obtain

$$\begin{aligned} v\,(t-1) &= \left[\mathcal{S}_0 + \epsilon\mathcal{S}_1 + \epsilon^2\mathcal{S}_2 + \epsilon^3\mathcal{S}_3 + \mathcal{O}\left(\epsilon^4\right)\right] v\,(t_0 - 1, t_2, t_3)\,, \\ \text{where} \quad & \mathcal{S}_0 = 1, \quad \mathcal{S}_1 = -\omega_1\partial_0, \quad \mathcal{S}_2 = -\omega_2\partial_0 - \partial_2 + \frac{\omega_1^2}{2}\partial_0^2, \\ & \mathcal{S}_3 = -\omega_3\partial_0 - \frac{\omega_1^3}{6}\partial_0^3 + \omega_1\omega_2\partial_0^2 + \omega_1\partial_0\partial_2 - \partial_3. \end{aligned} \tag{2.25}$$

In the next step, all expansions (time scales, parameters, fields) are plugged into Eq. (2.20) and sorted in orders of $\epsilon$. Each order must be fulfilled separately, such that from the coefficients of the order of $\epsilon$, we derive a solvability condition, i.e., a specific equation that fulfills that order. Such a solvability condition can be obtained for higher dimensional systems by employing the Fredholm alternative.

Next, we combine the results from the different orders to obtain the normal form. For that, we define an effective slow time scale that includes all time scales up to the expanded order without the zeroth order. For instance, when expanding up to third order, the effective time scale reads $\partial_\xi = \epsilon^2 \partial_2 + \epsilon^3 \partial_3$. The zeroth-order time scale turns into the spatial variable $z$, which we define as $t_0 = \epsilon z$ such that $z \in [0, T]$. Hence, the resulting PDE normal form and the original delayed equation are in the same order of magnitude and are directly comparable.

Finally, it is important to remember that the following derivations are not unique. One can define the deviation of parameters and fields as one likes (including fractional scaling), however, each different ansatz leads to terms appearing in different orders. In the end, the range of validity of the normal form is limited by the given constraints (i.e., the way the deviation are defined at the beginning). For instance, if the initial scalings are not appropriate some physical effect might not be captured by the normal form. Hence, the goal is to find the "good" scaling giving a rich normal form.

### 2.3.2. Normal Form via the Functional Mapping Approach

An alternative to the multiple time scale analysis presented in the previous section is to consider the delayed equation as a map [87, 88]. This approach makes it particularly easy to find the linear operator of the normal form, but also the nonlinearity can be computed analytically by again assuming a scaling of the nonlinearity in the smallness parameter $\epsilon$. We consider a general NDDE of the form

$$\dot{v}(t) = f\left(v(t), v(t-\tau), \dot{v}(t-\tau), \dots\right). \tag{2.26}$$

First, we normalize the time delay and denote the profile at time $t$ with $v_t$

$$\epsilon \dot{v}_t = f\left(v_t, v_{t-1}, \epsilon \dot{v}_{t-1}, \dots\right). \tag{2.27}$$

Next, we separate the right hand side into a linear and nonlinear part, which we assume to be order $\epsilon^\alpha$

$$\epsilon \dot{v}_t = \mathcal{A} v_t + \mathcal{B} v_{t-1} + \epsilon^\alpha \tilde{N}\left(v_t, v_{t-1}, \epsilon \dot{v}_{t-1}, \dots\right). \tag{2.28}$$

We can express the derivative in Fourier space as $\dot{v}_t \to -i\omega\hat{v}_t$ where $\hat{v}_t$ is the Fourier transform of $v_t$. Using this and solving Eq. (2.28) for $\hat{v}_t$ yields

$$\hat{v}_t = \mathcal{M}\hat{v}_{t-1} + \epsilon^\alpha N\left(\hat{v}_t, \hat{v}_{t-1}, i\epsilon\omega\hat{v}_{t-1}, \dots\right), \tag{2.29}$$

where $\mathcal{M} = -\left(i\omega\epsilon + \mathcal{A}\right)^{-1}\mathcal{B}$ and $N = -\left(i\omega\epsilon + \mathcal{A}\right)^{-1}\tilde{N}$. The goal is to derive the corresponding PDE, which has the form

$$\partial_\xi v\left(\xi, z\right) = \mathcal{L}\left(\partial_z\right) v\left(\xi, z\right) + \epsilon^\alpha \mathcal{N}\left[v\left(\xi, z\right)\right], \tag{2.30}$$

where we have to find the linear operator $\mathcal{L}$ and the nonlinear operator $\mathcal{N}$. Again, we go into Fourier space, use the shortcuts $v_\xi = v\left(\xi, z\right)$ & $\mathcal{N}_\xi = \mathcal{N}\left[v\left(\xi, z\right)\right]$ and integrate this equation from round-trip $\xi = n-1$ to $\xi = n$:

$$\begin{aligned}
\int_{n-1}^{n} \partial_\xi \hat{v}_\xi d\xi &= \int_{n-1}^{n} \left(\mathcal{L}\hat{v}_\xi + \epsilon^\alpha \mathcal{N}_\xi\right) d\xi && (2.31)\\
\Leftrightarrow \quad \int_{\hat{v}_{n-1}}^{\hat{v}_n} \frac{d\hat{v}_\xi}{\hat{v}_\xi} &= \int_{n-1}^{n} \left(\mathcal{L} + \epsilon^\alpha \frac{\mathcal{N}_\xi}{\hat{v}_\xi}\right) d\xi && (2.32)\\
\Rightarrow \hat{v}_n &= \exp\left[\mathcal{L} + \epsilon^\alpha \int_{n-1}^{n} \frac{\mathcal{N}_\xi}{\hat{v}_\xi} d\xi\right] \hat{v}_{n-1} && (2.33)\\
&= e^{\mathcal{L}}\left[1 + \epsilon^\alpha \int_{n-1}^{n} \frac{\mathcal{N}_\xi}{\hat{v}_\xi} d\xi\right] \hat{v}_{n-1} + \mathcal{O}\left(\epsilon^{2\alpha}\right) && (2.34)\\
&= e^{\mathcal{L}}\hat{v}_{n-1} + \epsilon^\alpha e^{\mathcal{L}} \int_{n-1}^{n} \frac{\hat{v}_{n-1}}{\hat{v}_\xi} \mathcal{N}_z d\xi + \mathcal{O}\left(\epsilon^{2\alpha}\right) && (2.35)\\
&= e^{\mathcal{L}}\hat{v}_{n-1} + \epsilon^\alpha \int_{n-1}^{n} e^{\mathcal{L}(n-\xi)} \mathcal{N}_\xi d\xi + \mathcal{O}\left(\epsilon^{2\alpha}\right). && (2.36)
\end{aligned}$$

In the last steps, we used first order approximation for the step: $e^{\mathcal{L}}\hat{v}_{n-1} = \hat{v}_n + \mathcal{O}\left(e^\alpha\right)$ (cf. Eq. (2.34)). Further, we used $\frac{\hat{v}_n}{\hat{v}_\xi} = e^{\mathcal{L}(n-\xi)} + \mathcal{O}\left(e^\alpha\right)$, which results from applying the first order approximation for the step $(n-\xi)$ times. Comparing Eq. (2.36) to Eq. (2.29) defines the linear operator $\mathcal{L}$ as

$$\mathcal{L} = \ln \mathcal{M}. \tag{2.37}$$

In the next step, we need to find the nonlinearity $\mathcal{N}$. For this, we make another first order step to find an approximation of the nonlinearity in Eq. (2.29):

$$N_{t-1} := N\left(e^{\mathcal{L}} v_{t-1}, v_{t-1}, \epsilon\dot{v}_{t-1}, \dots\right) + \mathcal{O}\left(\epsilon^\alpha\right). \tag{2.38}$$

And consequently, we obtain again from comparing Eq. (2.36) to Eq. (2.29)

$$N_{n-1} = \int_{n-1}^{n} e^{\mathcal{L}(n-\xi)} \mathcal{N}_\xi d\xi. \tag{2.39}$$

This integral can be solved in different precisions using the rectangle, midpoint, Simpson, etc. approximation methods. These methods are based upon evaluating the integrand at different positions in the interval $[n-1, n]$ and weighting these results (while the weights add up to unity):

- Zeroth order: rectangle method; evaluate the integrand at $\xi = n-1$

$$\int_{n-1}^{n} e^{\mathcal{L}(n-\xi)} \mathcal{N}_\xi d\xi = e^{\mathcal{L}} \mathcal{N}_{n-1} + \mathcal{O}(\epsilon); \tag{2.40}$$

- First order: midpoint or trapezoid method; evaluate the integrand at $\xi = n - \frac{1}{2}$ or $\xi = n, n-1$

$$\begin{aligned} \int_{n-1}^{n} e^{\mathcal{L}(n-\xi)} \mathcal{N}_\xi d\xi &= e^{\mathcal{L}/2} \mathcal{N}_{n-\frac{1}{2}} + \mathcal{O}\left(\epsilon^2\right) &(2.41)\\ &= \frac{1}{2}\left[e^{\mathcal{L}} \mathcal{N}_{n-1} + \mathcal{N}_n\right] + \mathcal{O}\left(\epsilon^2\right); &(2.42) \end{aligned}$$

- Second order: Simpsons method; evaluate the integrand at $\xi = n, n-\frac{1}{2}, n-1$

$$\int_{n-1}^{n} e^{\mathcal{L}(n-\xi)} \mathcal{N}_\xi d\xi = \frac{1}{6}\left[e^{\mathcal{L}} \mathcal{N}_{n-1} + 4e^{\mathcal{L}/2} \mathcal{N}_{n-\frac{1}{2}} + \mathcal{N}_n\right] + \mathcal{O}\left(\epsilon^3\right). \tag{2.43}$$

In the next step, all nonlinearities that are not evaluated at $n-1$ need to be transformed into that, in order to being able to solve for the searched nonlinearity $\mathcal{N}_{n-1}$. For that, we expand the linear operator as $\mathcal{L} = \mathcal{L}_0 + \epsilon\mathcal{L}_1 + \epsilon^2\mathcal{L}_2 + \ldots$

$$\begin{aligned} \mathcal{N}_{n-1+a} &= \mathcal{N}\left(y_{n-1+a}\right) = \mathcal{N}\left(e^{\mathcal{L}a} y_{n-1} + \mathcal{O}\left(\epsilon^\alpha\right)\right) &(2.44)\\ &= \mathcal{N}\left[e^{i\mathcal{L}_0}\left(1 + \epsilon a\mathcal{L}_1 + \epsilon^2\left(\frac{(a\mathcal{L}_1)^2}{2} + a\mathcal{L}_2\right) + \ldots\right) y_{n-1}\right] + \mathcal{O}\left(\epsilon^\alpha\right). &(2.45) \end{aligned}$$

In particular, if we have $\mathcal{L}_0 = 0$, we obtain

$$\mathcal{N}_{n-1+a} = \mathcal{N}_{n-1} + \epsilon a \left(\mathcal{L}_1 y_{n-1}\right) \mathcal{N}'_{n-1} + \cdots + \mathcal{O}\left(\epsilon^\alpha\right) \tag{2.46}$$

Here, to find the derivatives of the nonlinearity, we compute the action of the linear operator on it. For instance, if $\mathcal{L}_1 \sim \partial_z$, we have

$$\mathcal{L}_1 \mathcal{N}_{n-1} = \left(\mathcal{L}_1 y_{n-1}\right) \mathcal{N}'_{n-1}. \tag{2.47}$$

With this, Eq. (2.46) reads

$$\mathcal{N}_{n-1+a} = \mathcal{N}\left(e^{\mathcal{L}a} y_{n-1}\right) = \mathcal{N}_{n-1} + \epsilon a \mathcal{L}_1 \mathcal{N}_{n-1} = e^{\mathcal{L}a} \mathcal{N}_{n-1} + \mathcal{O}\left(\epsilon^2\right). \tag{2.48}$$

As a consequence, with this special case, both first order methods Eqs. (2.41) and (2.42) are equivalent to the rectangle method but hold to a higher order such that the searched nonlinearity reads

$$\mathcal{N}_{n-1} = e^{-\mathcal{L}} N_{n-1} + \mathcal{O}\left(\epsilon^2\right). \tag{2.49}$$

### 2.3.3. Simple Example via the Multiple Time Scale Approach

To better illustrate the steps to achieve a normal form PDE from a time-delayed system, we consider the following simple example

$$\dot{E} = -E + \eta E\left(t - \tau\right). \tag{2.50}$$

We define the smallness parameter $\epsilon = \tau^{-1}$ and expand the field in orders of $\epsilon$: $E = E_0 + \epsilon E_1 + \epsilon^2 E_2 + \ldots$. The critical parameter value is $\eta = 1$ such that we define $\eta = 1 - \epsilon\Delta\eta_1 - \epsilon^2\Delta\eta_2 + \ldots$. Next, we use the time scales defined in Eq. (2.22) and the expression for the delayed state in Eq. (2.25) and plug them into Eq. (2.50). Then we obtain

$$\begin{aligned} &\epsilon\left(\mathcal{T}_0 + \epsilon\mathcal{T}_1 + \epsilon^2\mathcal{T}_2 + \epsilon^3\mathcal{T}_3 + \ldots\right)\left(E_0 + \epsilon E_1 + \epsilon^2 E_2 + \ldots\right) = \\ &-\left(E_0 + \epsilon E_1 + \epsilon^2 E_2 + \ldots\right) + \left[\mathcal{S}_0 + \epsilon\mathcal{S}_1 + \epsilon^2\mathcal{S}_2 + \epsilon^3\mathcal{S}_3 + \ldots\right] \\ &\times\left[1 - \epsilon\Delta\eta_1 - \epsilon^2\Delta\eta_2 + \ldots\right]\left[E_0\left(t_0 - 1\right) + \epsilon E_1\left(t_0 - 1\right) + \epsilon^2 E_2\left(t_0 - 1\right) + \ldots\right]. \end{aligned} \tag{2.51}$$

#### Zeroth Order

Collecting all terms of zeroth order from Eq. (2.51), we find the condition for periodic solutions

$$E_0 = E_0\left(t_0 - 1\right). \tag{2.52}$$

### First Order

Collecting all terms of order $\epsilon$ from Eq. (2.51), we find

$$\mathcal{T}_0 E_0 = -E_1 + \mathcal{S}_0 E_1 (t_0 - 1) + \mathcal{S}_1 E_0 (t_0 - 1) - \Delta\eta_1 E_0 \tag{2.53}$$

$$\Leftrightarrow \; E_1 = E_1 (t_0 - 1) - (1 + \omega_1)\, \partial_0 E_0 - \Delta\eta_1 E_0, \tag{2.54}$$

where we used the condition from Eq. (2.52). Next, we can choose $\omega_1 = -1$ in order to cancel the drift term such that we remain with

$$E_1 = E_1 (t_0 - 1) - \Delta\eta_1 E_0. \tag{2.55}$$

We require $E_1$ to be a periodic solutions, i.e., $E_1 = E_1 (t_0 - 1)$. Consequently, we find that $\Delta\eta_1 = 0$.

### Second Order

Collecting all terms of order $\epsilon^2$ from Eq. (2.51), we find

$$\mathcal{T}_0 E_1 + \mathcal{T}_1 E_0 = - E_2 + \mathcal{S}_0 E_2 (t_0 - 1) + \mathcal{S}_1 E_1 + \mathcal{S}_2 E_0 - \Delta\eta_2 E_0 \tag{2.56}$$

$$\begin{aligned} \Leftrightarrow \; \partial_2 E_0 + E_2 =& E_2 (t_0 - 1) - (1 + \omega_1)\, \partial_0 E_1 + (-\omega_2 - \omega_1)\, \partial_0 E_0 \\ &+ \frac{\omega_1^2}{2} \partial_0^2 E_0 - \Delta\eta_2 E_0. \end{aligned} \tag{2.57}$$

The coefficient of the $\partial_0 E_1$-term cancels due to the choice of $\omega_1$ from the previous order. Further, we can choose $\omega_2 = -\omega_1 = 1$ in order to cancel the coefficient of the $\partial_0 E_0$-term. Finally, we require a periodic solution also for $E_2$, i.e., $E_2 = E_2 (t_0 - 1)$, such that we remain with

$$\partial_2 E_0 = \frac{\omega_1^2}{2} \partial_0^2 E_0 - \Delta\eta_2 E_0. \tag{2.58}$$

In fact, we could already build the normal form from this step. Then the effective time scale reads $\partial_\xi = \epsilon^2 \partial_2$ and we find

$$\partial_\xi E = \frac{1}{2} \partial_x^2 E - (1 - \eta)\, E. \tag{2.59}$$

In order to capture higher order effects in the normal form, we can also proceed to the third order.

### Third Order

Collecting all terms of order $\epsilon^3$ from Eq. (2.51), we find

$$\begin{aligned}\mathcal{T}_0 E_2 + \mathcal{T}_1 E_1 + \mathcal{T}_2 E_0 = & - E_3 + \mathcal{S}_0 E_3 (t-1) + \mathcal{S}_1 E_2 + \mathcal{S}_2 E_1 + \mathcal{S}_3 E_0 \\ & + \mathcal{S}_0 \Delta\eta_3 E_0 + \mathcal{S}_0 \Delta\eta_2 E_1 + \mathcal{S}_1 \Delta\eta_2 E_0 .\end{aligned} \tag{2.60}$$

Plugging in all values for the $\mathcal{T}_i$ and $\mathcal{S}_i$ gives

$$\begin{aligned}\partial_3 E_0 + \partial_2 E_1 = & \left(-\omega_2 - \omega_3\right) \partial_0 E_0 + \left(-\omega_1 - \omega_2\right) \partial_0 E_1 + \left(-1 - \omega_1\right) \partial_0 E_2 \\ & + \left(-1 + \omega_1 \partial_0\right) \partial_2 E_0 + \frac{\omega_1^2}{2} \partial_0^2 E_1 + \left(-\frac{\omega_1^3}{6} \partial_0^3 + \omega_1 \omega_2 \partial_0^2\right) E_0 \\ & - \Delta\eta_2 E_1 - \Delta\eta_3 E_0 + \omega_1 \Delta\eta_2 \partial_0 E_0 ,\end{aligned} \tag{2.61}$$

where we already used $E_3 = E_3 (t-1)$. Further, we use the solvability condition from the previous order in Eq. (2.58) to replace the $\partial_2 E_0$-term. Then, the coefficient of the $\partial_0 E_1$- and $\partial_0 E_2$-terms cancel due to the choice of $\omega_1$ and $\omega_2$ from the previous orders. Further, we can choose $\omega_3 = -\omega_2 = -1$ in order to cancel the coefficient of the $\partial_0 E_0$-term. We remain with

$$\begin{aligned}\partial_3 E_0 + \partial_2 E_1 = & \frac{\omega_1^2}{2} \partial_0^2 E_1 + \frac{\omega_1^3}{3} \partial_0^3 E_0 - \frac{3\omega_1^2}{2} \partial_0^2 E_0 \\ & - \Delta\eta_2 E_1 - \Delta\eta_3 E_0 + \Delta\eta_2 E_0 .\end{aligned} \tag{2.62}$$

### Building the Normal Form

To find the final normal form, we define the effective slow time scale $\partial_\xi = \epsilon^2 \partial_2 + \epsilon^3 \partial_3$ and obtain

$$\partial_\xi E = \left(\epsilon^2 \partial_2 + \epsilon^3 \partial_3\right) \left(E_0 + \epsilon E_1\right) + \mathcal{O}\left(\epsilon^4\right) \tag{2.63}$$

$$= \epsilon^2 \partial_2 E_0 + \epsilon^3 \left(\partial_3 E_0 + \partial_2 E_1\right) + \mathcal{O}\left(\epsilon^4\right) . \tag{2.64}$$

The two terms correspond to the solvability conditions from the second and third order in Eqs. (2.58) and (2.62). With this, we obtain

$$\begin{aligned}\partial_\xi E = & \epsilon^2 \frac{\omega_1^2}{2} \partial_0^2 \left(E_0 + \epsilon E_1\right) + \epsilon^3 \frac{\omega_1^3}{3} \partial_0^3 E_0 - \left(\epsilon^2 \Delta\eta_2 + \epsilon^3 \Delta\eta_3\right) \left(E_0 + \epsilon E_1\right) \\ & - \epsilon^3 \frac{3\omega_1^2}{2} \partial_0^2 E_0 + \epsilon^3 \Delta\eta_2 E_0 + \mathcal{O}\left(\epsilon^4\right) .\end{aligned} \tag{2.65}$$

Next, we rebuild the parameter $\eta$ and the field from the deviations, i.e., $\epsilon^2 \Delta\eta_2 + \epsilon^3 \Delta\eta_3 = 1 - \eta + \mathcal{O}\left(\epsilon^4\right)$ and $E_0 + \epsilon E_1 = E + \mathcal{O}\left(\epsilon^2\right)$. Further, we define the space variable $z = \epsilon t_0$.

This cancels all $\epsilon$ in Eq. (2.65) except for the last two terms (which remain $\mathcal{O}(\epsilon)$) and we find the final normal form as

$$\partial_\xi E = \frac{1}{2}\partial_z^2 E - \frac{1}{3}\partial_z^3 E_0 - (1-\eta) E + \mathcal{O}(\epsilon) . \tag{2.66}$$

Further, we can approximate the period $T$ by considering the stretching of the $t_0$-scale by the $\omega_i$. We found that

$$\omega = 1 - \epsilon + \epsilon^2 - \epsilon^3 + \mathcal{O}\left(\epsilon^4\right) = \frac{1}{1+\epsilon} + \mathcal{O}\left(\epsilon^4\right) . \tag{2.67}$$

Hence, the (normalized) period reads $T = \frac{1}{\omega} = 1 + \epsilon$. Reversing the normalization yields the period

$$T_\tau = \frac{T}{\epsilon} = \tau + 1 \tag{2.68}$$

where we used that $\tau = \epsilon^{-1}$.

### 2.3.4. Simple Example via the Functional Mapping Approach

We consider again the linear delayed equation Eq. (2.50). Following Section 2.3.2, we find the coefficients as $\mathcal{A} = -1$ and $\mathcal{B} = \eta$. Hence, we find the linear operator according to Eq. (2.37):

$$\mathcal{L} = \ln\left[\frac{\eta}{1 - i\omega\epsilon}\right] = \ln\eta - \ln[1 - i\omega\epsilon] \tag{2.69}$$

$$= -(1-\eta) + i\omega\epsilon + \frac{1}{2}(-i\omega\epsilon)^2 - \frac{1}{3}(-i\omega\epsilon)^3 + \ldots , \tag{2.70}$$

where we used that $1 - \eta$ scales as $\epsilon^2$. Then the PDE normal form reads

$$\partial_\xi E = -(1-\eta) E - \partial_z E + \frac{1}{2}\partial_z^2 E - \frac{1}{3}\partial_z^3 E + \mathcal{O}\left(\epsilon^4\right) , \tag{2.71}$$

which is in accordance with Eq. (2.66). Removing the drift term by going into the comoving frame also yields $T_\tau = \tau + 1$. For an example that includes a nonlinearity, see Appendix B.2.2.

# 3. Modeling of Laser Systems

In this section, we present the derivation of the different laser models used throughout this thesis. We begin with Maxwell's equation to formalize the light-matter interaction in dielectric media, see Section 3.1. From that, we derive the dynamical equations for the KGTI (cf. Section 3.2) and a PML ring laser (cf. Section 3.3).

In the course of the derivation, we go back and forth between the time/spatial domain and the frequency space. We define the corresponding Fourier transformation as

$$\mathcal{F}_t\left[f\left(t\right)\right] = \int_{-\infty}^{\infty} f\left(t\right) e^{i\omega t} dt = \hat{f}\left(\omega\right), \tag{3.1}$$

$$\mathcal{F}_t^{-1}\left[f\left(t\right)\right] = \frac{1}{2\pi}\int_{-\infty}^{\infty} \hat{f}\left(\omega\right) e^{-i\omega t} d\omega = f\left(t\right), \tag{3.2}$$

such that a derivative can be expressed as $\mathcal{F}\left[\partial_t^n f\left(t\right)\right] = \left(-i\omega\right)^n \hat{f}\left(\omega\right)$.

## 3.1. The Wave Equation

The starting point of the derivation are Maxwell's equations describing the evolution of the electric field[1] $\mathbf{E}\left(\mathbf{r},t\right)$ and the magnetic field $\mathbf{B}\left(\mathbf{r},t\right)$ where $\mathbf{r}\in\mathbb{R}^3$ is the position vector. Considering that the used materials are non-magnetizable and do not contain free charges or currents, they read

$$\nabla\cdot\mathbf{D} = 0, \tag{3.3}$$

$$\nabla\cdot\mathbf{B} = 0, \tag{3.4}$$

$$\nabla\times\mathbf{E} = -\dot{\mathbf{B}}, \tag{3.5}$$

$$\nabla\times\mathbf{H} = \dot{\mathbf{D}}, \tag{3.6}$$

where the electric displacement field $\mathbf{D}$ and the magnetic field $\mathbf{H}$ are defined as

$$\mathbf{D} = \epsilon_0\mathbf{E} + \mathbf{P}, \tag{3.7}$$

$$\mathbf{H} = \frac{\mathbf{B}}{\mu_0}. \tag{3.8}$$

Here, the constants $\epsilon_0$ and $\mu_0$ are the vacuum permittivity and permeability, respectively, and the polarization $\mathbf{P}$ describes the response of the material to an electric field. In particular, the polarization has a linear part $\mathbf{P}_l$ and a nonlinear part $\mathbf{P}_{nl}$.

First, we want to transform Maxwell's equations into a wave equation. For that, we

[1] We use the complex exponential notation for the electric and magnetic fields. The physical electric and magnetic fields are the real parts of these quantities.

calculate the curl of Eq. (3.5)

$$\nabla \times (\nabla \times \mathbf{E}) = -\mu_0 \nabla \times \dot{\mathbf{H}}. \tag{3.9}$$

Using the vector calculus identity $\nabla \times (\nabla \times \mathbf{v}) = \nabla (\nabla \cdot \mathbf{v}) - \nabla^2 \mathbf{v}$ for the left hand side, and linearity of the curl (i.e., $\nabla \times \dot{\mathbf{v}} = \partial_t (\nabla \times \mathbf{v})$) for the right hand side together with Eq. (3.6), we obtain

$$\nabla (\nabla \cdot \mathbf{E}) - \nabla^2 \mathbf{E} = -\mu_0 \ddot{\mathbf{D}}. \tag{3.10}$$

### 3.1.1. Dispersion

Before we start to take the nonlinear effects of the polarization into account, we explore the implications of the linear polarization $\mathbf{P}_l$. It is defined as the convolutions of the linear part of the electric susceptibility $\chi_l$ and the electric field $\mathbf{E}$:

$$\mathbf{P}_l (\mathbf{r}, t) = \epsilon_0 \chi_l (t) * \mathbf{E} (\mathbf{r}, t') = \epsilon_0 \int_{-\infty}^{t} \chi_l (t - t') \, \mathbf{E} (\mathbf{r}, t') \, dt'. \tag{3.11}$$

Going to Fourier space, the convolution turns into a multiplication, such that

$$\hat{\mathbf{P}}_l (\mathbf{r}, \omega) = \epsilon_0 \hat{\chi}_l (\omega) \, \hat{\mathbf{E}} (\mathbf{r}, \omega) \, . \tag{3.12}$$

As a result, the Fourier-transformed electric displacement is linear in $\hat{\mathbf{E}}$

$$\hat{\mathbf{D}} (\mathbf{r}, \omega) = \epsilon_0 \left(1 + \hat{\chi}_l (\omega)\right) \hat{\mathbf{E}} (\mathbf{r}, \omega) \, , \tag{3.13}$$

and hence, Eq. (3.3) reveals $\nabla \cdot \mathbf{E} = 0$ for a linear homogeneous medium. Using these insight in Eq. (3.10) (and using $\partial_t^2 \to -\omega^2$), leads to the wave equation

$$\nabla^2 \hat{\mathbf{E}} (\mathbf{r}, \omega) + \frac{\omega^2 n_l^2 (\omega)}{c^2} \hat{\mathbf{E}} (\mathbf{r}, \omega) = 0, \tag{3.14}$$

where the speed of light in vacuum is $c = 1/\sqrt{\epsilon_0 \mu_0}$ and the frequency-dependent refractive index $n_l$ is defined as

$$n_l (\omega) = \sqrt{1 + \chi_l (\omega)}. \tag{3.15}$$

The fundamental solutions of the wave equation (3.14) are plane waves of the form

$$\mathbf{u} (\mathbf{r}, t) = \mathbf{u}_0 e^{i(\mathbf{q} \cdot \mathbf{r} - \omega t)}, \tag{3.16}$$

where $\mathbf{q} \in \mathbb{R}^3$ is the wavevector. Plugging this ansatz into the wave equation leads to the dispersion relation

$$|\mathbf{q}|(\omega) = \frac{n_l(\omega)}{c}\omega. \tag{3.17}$$

That is, dispersion describes the phenomenon that the index of refraction $n_l$ of a medium depends on the angular frequency of the wave and the dispersion relations tells us how the angular frequency and the wavenumber are related.

In the following, we visualize the implication of the dispersion relation in Eq. (3.17) on *wave packets*, which are superpositions of plane waves centered around a wavevector $\mathbf{q}_0$ with an corresponding frequency $\omega_0$. For simplicity, we consider a one-dimensional system in $\mathbf{e}_z$-direction, i.e., $\mathbf{q} = q\mathbf{e}_z$. The amplitudes of the individual plane waves are defined by a weight function $\hat{b}(\omega)$ such that the wave packet reads[2]

$$H(z,t) = \int_{-\infty}^{\infty} \hat{b}(\omega - \omega_0)\, e^{i[q(z-z_0)-\omega(t-t_0)]} d\omega. \tag{3.18}$$

The wave packet usually has its maximum where all phases align, i.e., at position $z_0$ at time $t_0$. Note that for $z = z_0$, Eq. (3.18) corresponds to an inverse Fourier transformation (cf. Eq. (3.2)), i.e.

$$H(z_0,t) = 2\pi b(t-t_0)\, e^{-i\omega_0(t-t_0)}, \tag{3.19}$$

such that $H(z_0,t)$ is a a plane wave with wavenumber $\omega_0$ with modulated amplitude defined by $b(t)$. A visualization of a wave packet is shown in Fig. 3.1. The plane waves in panel (b) are weighted with a Gaussian distribution $\hat{b}(\omega)$ and each has a maximum at $t_0$. They sum up to the wave packet in panel (a), which therefore has its maximum at $t_0$ as well. For simplicity, we set $t_0 = 0$ and $z_0 = 0$ in the following without loss of generality.

Now we let the wave packet propagate in the medium and measure again the temporal profile after some propagation length $z > z_0$. Here, we can define two important quantities, namely the *phase and group velocity.* First, the phase velocity is the velocity in time of each individual plane wave (i.e., the velocity of each orange dot in Fig. 3.1 (b)). It is defined as

$$\text{phase velocity: } v_p = \frac{c}{n_l(\omega)} = \frac{\omega}{q}. \tag{3.20}$$

Hence, one can also define dispersion as the phenomena where the phase velocity is different for different frequencies $\omega$. Second, the group velocity $v_g$ is the velocity of the wave packet, i.e., the velocity of the green cross in Fig. 3.1 (a), which marks the

[2] Note that one could equivalently define a weight function for the wavenumbers $\hat{b}(q)$.

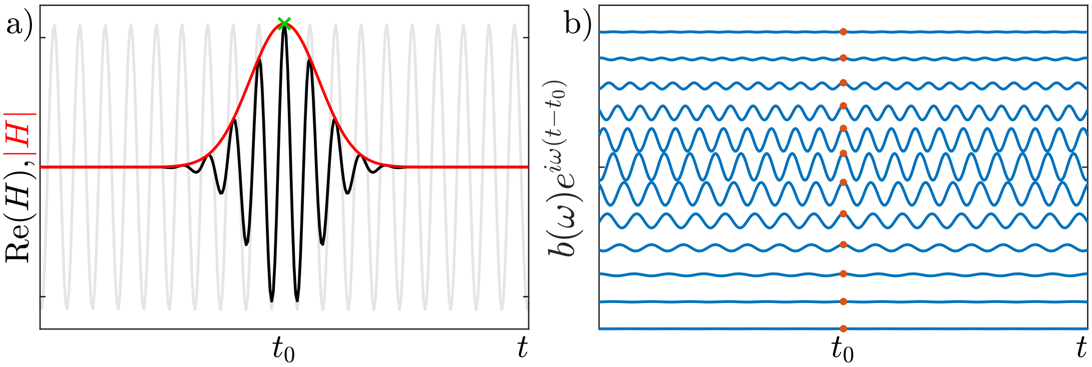


**Figure 3.1:** Initial state at $z = z_0$ of a Gaussian wave packet centered around $\omega_0$. (a) Real part (black) and absolute value (red) of wave packet. The opaque gray oscillation of frequency $\omega_0$ shall help to guide the eye. The green cross is located at the maximum of the wave packet at $t_0$. (b) Individual plane waves with different frequencies $\omega$ weighted by a Gaussian distribution centered around $\omega_0$. The plane waves sum up to the wave packet in (a) (i.e., we show the discrete version of Eq. (3.18)). The orange dots in (b) at $t_0$ mark maxima of the individual plane waves. This figure is intended as a reference for Fig. 3.2.

maximum of the wave packet. In the simplest case, when no dispersion is present and the index of refraction is frequency-independent, the phase velocity is the same for all phases and consequently $v_g = v_p$. In the dispersive case, we can expand $q(\omega)$ around $\omega_0$ and obtain:

$$q(\omega) = q_0 + \sum_{n=1}^{\infty} \frac{1}{n!} \frac{\partial^n q}{\partial \omega^n}\bigg|_{\omega_0} (\omega - \omega_0)^n, \tag{3.21}$$

where $q_0 = q(\omega_0)$. Expanding $q$ up to first order yields the following relation for a plane wave

$$e^{i(qz-\omega t)} = e^{i(q_0 z - \omega_0 t)} \exp\left[i\bar{\omega}\left(\frac{\partial q}{\partial \omega}\bigg|_{\omega_0} z - t\right)\right], \tag{3.22}$$

where $\bar{\omega} = \omega - \omega_0$. Plugging this into the definition of the wave packet in Eq. (3.18) leads to

$$H(z,t) = e^{i(q_0 z - \omega_0 t)} \underbrace{\int_{-\infty}^{\infty} \hat{b}(\bar{\omega}) \exp\left[i\bar{\omega}\left(\frac{\partial q}{\partial \omega}\bigg|_{\omega_0} z - t\right)\right] d\bar{\omega}}_{=b\left(t - \frac{\partial q}{\partial \omega}|_{\omega_0} z\right)}. \tag{3.23}$$

That is, the wave packet corresponds to a plane wave with frequency $\omega_0$ and wavenumber $q_0$ with a modulated amplitude defined by the shifted weight function $b\left(t - \frac{\partial q}{\partial \omega}|_{\omega_0} z\right)$.

Hence, the speed (in time) of this amplitude function $b$ is the group velocity:

$$\text{group velocity: } v_g = \frac{1}{\left.\frac{\partial q}{\partial \omega}\right|_{\omega_0}} = \left.\frac{\partial \omega}{\partial q}\right|_{q_0}. \tag{3.24}$$

Expanding the dispersion relation in Eq. (3.21) to higher orders allows us to define the higher-order contributions as the

$$\text{group velocity dispersion (GVD): } \beta_2 = \left.\frac{\partial^2 q}{\partial \omega^2}\right|_{\omega_0}, \tag{3.25}$$

$$\text{and third-order dispersion (TOD): } \beta_3 = \left.\frac{\partial^3 q}{\partial \omega^3}\right|_{\omega_0}. \tag{3.26}$$

To study the effect of GVD, we again consider the wave packet defined in Eq. (3.18) with the dispersion relation Eq. (3.21) expanded up to second order. We obtain for the temporal evolution of the wave packet

$$H(z,t) = e^{i(q_0 z - \omega_0 t)} \int_{-\infty}^{\infty} \hat{b}(\bar{\omega})\, e^{i\frac{\beta_2}{2}\bar{\omega}^2 z} e^{i\bar{\omega}\left(\frac{z}{v_g} - t\right)} d\bar{\omega} \tag{3.27}$$

For the example of a Gaussian distribution, we have $b(\omega) = A\exp\left(-\alpha\omega^2\right)$, where $A, \alpha \in \mathbb{R}^+$, such that

$$H(z,t) = A e^{i(q_0 z - \omega_0 t)} \sqrt{\frac{\pi}{\alpha - i\frac{\beta_2}{2}z}} \exp\left[-\frac{\left(t - \frac{z}{v_g}\right)^2}{4\left(\alpha - i\frac{\beta_2}{2}z\right)}\right] \tag{3.28}$$

$$\sim e^{i(q_0 z - \omega_0 t)} \exp\left[-\frac{\left(t - \frac{z}{v_g}\right)^2}{4} \frac{\alpha + i\frac{\beta_2}{2}z}{\alpha^2 + \left(\frac{\beta_2}{2}z\right)^2}\right], \tag{3.29}$$

where in the last line we left out the constant and normalization coefficients for clarity. Looking at this equation in detail (in particular the last exponential), we can observe two effects. First, the distribution spreads out in time when increasing $z$ and second, the frequency is not solely driven by $\omega_0$ but changes along the temporal domain (because the last exponential has an imaginary part). This effect is called the *chirp* of a wave packet.

The presented effects are summarized and visualized in Fig. 3.2. We show the state of the Gaussian wave packet depicted in Fig. 3.1 after it traveled through different media defined by the dispersion relations in the last row of Fig. 3.2. Here, we show both $q(\omega)$ (black) and $n(\omega)$ (green). The phases of the individual plane waves are marked by orange dots in the second row and the center of the wave packet according to the group velocity is indicated by a green cross in the first row. When no dispersion is

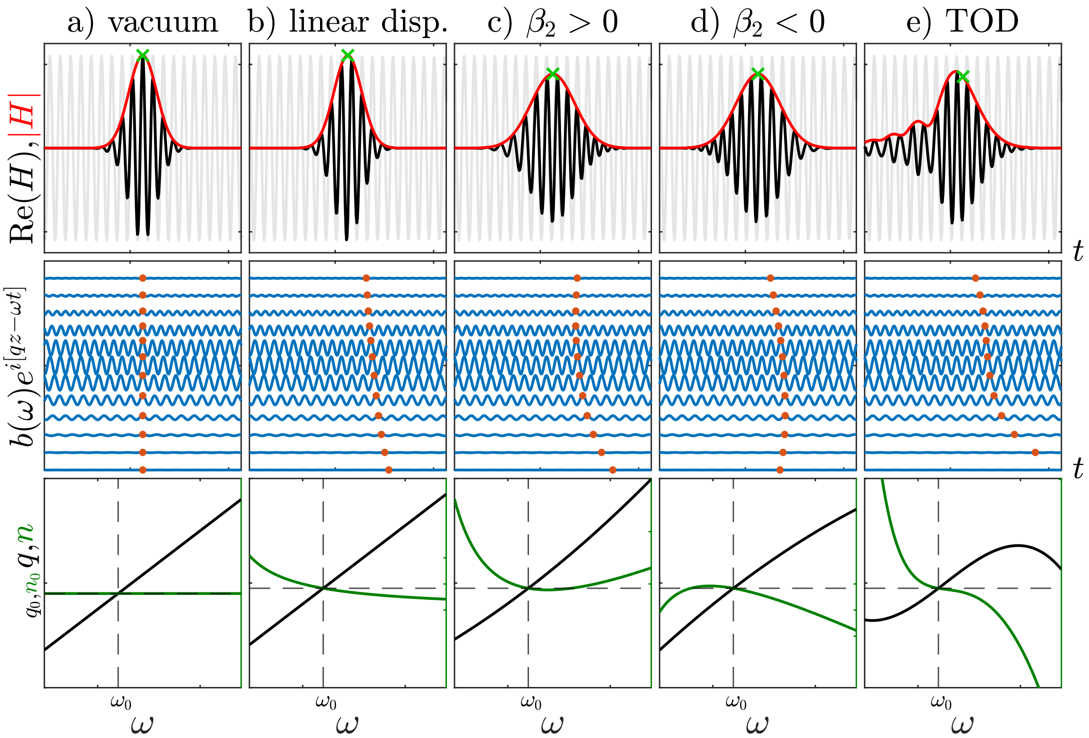


**Figure 3.2:** State of Gaussian wave packet shown in Fig. 3.1 after traveling through media with different dispersion relations defined in the third row, where we show both $q(\omega)$ (black) and $n(\omega)$ (green). First row: real part and absolute value of wave packet. The green cross is located at the position corresponding to the group velocity. Second row: individual plane waves with different frequencies $\omega$ weighted by a Gaussian distribution centered around $\omega_0$. The plane waves sum up to the wave packet above. The orange dots mark $t_0 + \frac{z}{v_p}$. Third row: dispersion relation.

present (panels (a)/first column), the phase velocity is the same for all plane waves and therefore also corresponds to the group velocity. For panels (b) (second column), the dispersion relation $q(\omega)$ is still linear in $\omega$, however, here $\omega_0$ is such that Eq. (3.21) has a constant part, i.e., there is a common phase shift and therefore $n(\omega)$ is not a constant. This results in different phase velocities for different wavenumbers in accordance to Eq. (3.20), yet the group velocity remains the same as before. Next, in panels (c) (third column) GVD is also present resulting in a parabolic dispersion relation. Here, the temporal evolution is governed by Eq. (3.29). Hence, we can observe the broadening of the pulse. Further, the wave packet is now not simply a weighted plane wave anymore but exhibits different frequencies. This can be seen when comparing the wave packet in black with the gray background corresponding to the plane wave with frequency $\omega_0$. On the left edge of the wave packet the frequency is lower than $\omega_0$ and on the right edge it is higher (which visualizes the chirp of the pulse). Importantly, we differentiate two cases of GVD depending on whether $\beta_2$ is positive or negative. The case $\beta_2 > 0$ is referred to as *normal dispersion*. Here, the refractive index increases with increasing frequencies. On the other hand, if $\beta_2 < 0$, we have *anomalous dispersion* where the refractive index decreases with increasing frequencies (cf. panels (d)). While the wave packet have the same amplitude envelope in the two cases, they exhibit an opposite chirp. In the normal dispersion case, the frequency of the wave packet increase with time, while in the anomalous case, it decreases (which can be seen when comparing the left and right tails of the wave packets). Finally, in panels (e) (fifth column), the dispersion relation also has cubic part, i.e., there is an influence of TOD. Hence, the amount of GVD changes for different wavenumbers, which results in promoted asymmetry of the wave packet envelope.

### 3.1.2. Nonlinear Polarization

While the dispersive effects in the previous section can describe many interesting phenomena in nature from rainbows to splitting of light in prisms, nonlinear media are essential for application in lasers. That is, the nonlinear part of the polarization $\mathbf{P}_{nl}$ models the interaction with carriers in mode-locked lasers and the Kerr effect in Kerr resonators.

We assume waves that propagates in the longitudinal $z$-direction, such that the electric field only has components in the transversal plane. Further, we consider a quasi-monochromatic field around a carrier frequency $\omega_0$. This lets us define the slowly evolving envelope of the electric field $\hat{\mathbf{E}}\left(\mathbf{r},\omega\right)$ via

$$\hat{\mathbf{E}}\left(\mathbf{r},\omega\right) = \hat{E}\left(\mathbf{r},\omega\right) e^{-i\omega_0 t}\mathbf{e}_\perp, \tag{3.30}$$

where $\mathbf{e}_\perp$ is a unit vector in the transversal (i.e., radial) direction. Accordingly, the polarization can be defined as

$$\mathbf{P} = \mathbf{P}_l + \mathbf{P}_{nl} = \left(P_l + P_{nl}\right) e^{-i\omega_0 t}\mathbf{e}_\perp + \text{h.o.t.} \tag{3.31}$$

where the higher order terms are non-resonant frequencies[3]. From assuming that the nonlinear effects are small compared to the linear contributions of the polarization ($P_{nl} \ll P_l$) and using the first Maxwell equation (3.3), follows that $\nabla \cdot \hat{E} \approx 0$. Hence, we can rewrite Eq. (3.10) to obtain the nonlinear wave-equation

$$\nabla^2 \hat{E} + \frac{\omega^2 n_l^2\left(\omega\right)}{c^2}\hat{E} = -\mu_0\omega^2\hat{P}_{nl}. \tag{3.32}$$

[3]The polarization can be expanded in powers of $E$ from which the higher frequencies stem.

## 3.2. Injected Kerr–Gires–Tournois Interferometer

In the following, we derive the dynamical equations that describe an injected Kerr–Gires–Tournois interferometer as depicted in Fig. 1.4. The derivation roughly follows the steps presented in [89], which are based on a technique first introduced in [90].

### 3.2.1. Micro-Cavity with an Embedded Kerr Medium

We begin with the description of the micro-cavity, which is detailed in Fig. 3.3. Our starting point is the nonlinear wave-equation in Eq. (3.32). First, we need to define the nonlinear polarization $P_{nl}$ induced by the Kerr medium. A Kerr medium has an intensity dependent index of refraction such that the nonlinear polarization reads

$$P_{nl} = \frac{3}{4}\epsilon_0 \chi_3 (\mathbf{r}) |E|^2 E, \tag{3.33}$$

where $\chi_3(\mathbf{r})$ described the amplitude and spatial dependence of the medium [59]. We consider a thin slice of a Kerr medium of width $W$ located at $z = z_0$. Hence, the susceptibility reads

$$\chi_3 (\mathbf{r}) = \tilde{\chi}_3 W \delta (z - z_0), \tilde{\chi} \in \mathbb{C}. \tag{3.34}$$

We consider the Fourier transform in the transverse direction of Eq. (3.32) and integrate

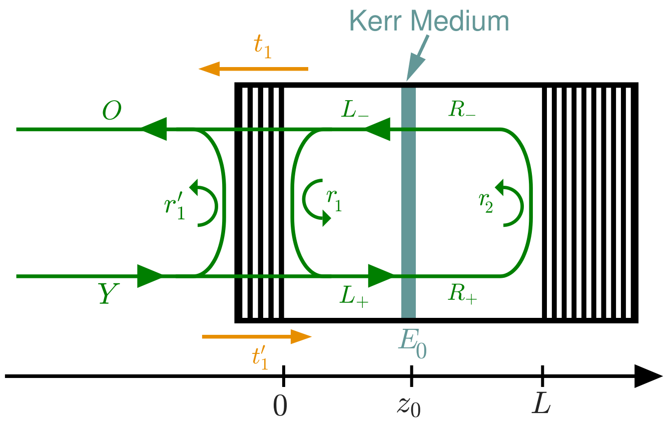


**Figure 3.3:** Close-up of the micro-cavity shown in Fig. 1.4. The micro-cavity is enclosed by two Bragg mirrors with reflectivities $r_{1,2}$ with a thin slice of a Kerr medium located at $z_0$. The outside reflectivity of the top Bragg mirror is $r_1'$, while the transmission coefficients are $t_1$ and $t_1'$, respectively. The ingoing and outgoing fields are $Y$ and $O$, and the micro-cavity field can be split into four parts $L_\pm, R_\pm$, respectively. Here, the index denotes forward and backwards propagating waves, respectively. The field at the nonlinear medium is $E_0$.

over a small range of $2\epsilon$ around $z_0$. This gives

$$-\frac{3\tilde{\chi}_3}{4c^2}\omega^2 W\mathcal{F}_{t,\perp}\left[|E|^2 E\right] = \int_{z_0-\epsilon}^{z_0+\epsilon}\left[\frac{\omega^2}{v_p^2} - \mathbf{q}_\perp^2\right]\hat{E}dz + \left[\partial_z\hat{E}\right]_{z_0-\epsilon}^{z_0+\epsilon}. \tag{3.35}$$

To the left and right of the nonlinear region, the electric field is simply a propagating wave, i.e., it is proportional to $e^{\pm iqz}$ where $\pm$ denotes forward and backward propagation, respectively, and the longitudinal wavevector $q$ is defined by the dispersion relation

$$q\left(\mathbf{q}_\perp,\omega\right) = \sqrt{\frac{\omega^2}{v_p^2} - \mathbf{q}_\perp^2}. \tag{3.36}$$

Hence, the electric field is a piecewise function to the left and right of the Kerr slice (cf. Fig. 3.3):

$$\hat{E}\left(\mathbf{q}_\perp,z,\omega\right) = \begin{cases}\hat{L}\left(\mathbf{q}_\perp,z,\omega\right) = \hat{L}_+\left(\mathbf{q}_\perp,\omega\right)e^{iqz} + \hat{L}_-\left(\mathbf{q}_\perp,\omega\right)e^{-iqz}, & 0 < z < z_0\\ \hat{R}\left(\mathbf{q}_\perp,z,\omega\right) = \hat{R}_+\left(\mathbf{q}_\perp,\omega\right)e^{iqz} + \hat{R}_-\left(\mathbf{q}_\perp,\omega\right)e^{-iqz}. & z_0 < z < L\end{cases} \tag{3.37}$$

These fields must connect continuously at $z_0$, i.e., we can define the field $\hat{E}_0$ as

$$\begin{aligned}\hat{E}_0\left(\mathbf{q}_\perp,\omega\right) &:= \hat{E}\left(\mathbf{q}_\perp,z_0,\omega\right) = \hat{L}\left(\mathbf{q}_\perp,z_0,\omega\right) = \hat{R}\left(\mathbf{q}_\perp,z_0,\omega\right)\\ &= \hat{L}_+\left(\omega\right)e^{iqz_0} + \hat{L}_-\left(\omega\right)e^{-iqz_0} \qquad (3.38)\\ &= \hat{R}_+\left(\omega\right)e^{iqz_0} + \hat{R}_-\left(\omega\right)e^{-iqz_0}. \qquad (3.39)\end{aligned}$$

Plugging this ansatz into Eq. (3.35) and considering the limit $\epsilon \to 0$ gives another boundary condition (where all fields are evaluated at $(\mathbf{q}_\perp, z_0, \omega)$)

$$\begin{aligned}-\frac{3\tilde{\chi}_3}{4c^2}\omega^2 W\mathcal{F}_{t,\perp}\left[|E_0|^2 E_0\right] &= \partial_z\hat{R} - \partial_z\hat{L} \qquad (3.40)\\ \overset{(3.37)}{\Leftrightarrow} -\frac{3\tilde{\chi}_3}{4iqc^2}\omega^2 W\mathcal{F}_{t,\perp}\left[|E_0|^2 E_0\right] &= \left(\hat{R}_+ - \hat{L}_+\right)e^{iqz_0} - \left(\hat{R}_- - \hat{L}_-\right)e^{-iqz_0}. \qquad (3.41)\end{aligned}$$

Next, we need to find the amplitudes of the forward and backward propagating waves $\hat{L}_\pm$ and $\hat{R}_\pm$. These can be obtained from conditions induced by the boundaries of the micro-cavity at the distributed Bragg mirrors (DBR). Here, $r_1$ and $r_2$ are the reflectivities of the top and bottom mirrors inside the micro-cavity, respectively, while $r_1'$ is the reflectivity at the outside of the top of the micro-cavity (cf. Fig. 3.3). The corresponding transmission coefficients are $t_1$ and $t_1'$. Note that – in general – the reflectivities can be frequency-dependent. However, we assume that the DBRs have a wide bandwidth such that the moduli of the reflection coefficients do not depend on the frequency, i.e., $r_{1,2}(\omega) = |r_{1,2}| e^{i\phi_{1,2}(\omega)}$. Summing up the influx and efflux at each of the three boundaries, we can establish the following conditions:

$$\hat{R}_- e^{-iqL} = r_2 \hat{R}_+ e^{iqL}, \tag{3.42}$$

$$\hat{L}_+ = r_1 \hat{L}_- + t_1' \hat{Y}, \tag{3.43}$$

$$\hat{O} = r_1' \hat{Y} + t_1 \hat{L}_-. \tag{3.44}$$

Solving Eq. (3.42) for $\hat{R}_\pm$ and inserting that into Eq. (3.39) gives

$$\hat{R}_+ = \frac{e^{-iqz_0}}{1 + r_2 e^{2iq(L-z_0)}} \hat{E}_0, \tag{3.45}$$

$$\hat{R}_- = \frac{r_2 e^{iqz_0} e^{2iq(L-z_0)}}{1 + r_2 e^{2iq(L-z_0)}} \hat{E}_0. \tag{3.46}$$

Further, we solve Eq. (3.43) for $\hat{L}_\pm$ and plug that into Eq. (3.38)

$$\hat{L}_+ = \frac{r_1 e^{iqz_0} \hat{E}_0 + t_1' \hat{Y}}{1 + r_1 e^{2iqz_0}}, \tag{3.47}$$

$$\hat{L}_- = \frac{e^{iqz_0} \hat{E}_0 - t_1' e^{2iqz_0} \hat{Y}}{1 + r_1 e^{2iqz_0}}. \tag{3.48}$$

Plugging the definitions of the amplitudes $\hat{L}_\pm$ and $\hat{R}_\pm$ (cf. Eqs. (3.45)–(3.48)) into the condition at the Kerr slice in Eq. (3.41) (and simplify) gives

$$F_1(q,\omega)\hat{E}_0 = -\frac{3\tilde{\chi}_3}{8iqc^2}\omega^2 W \Gamma(q,\omega) \mathcal{F}_{t,\perp}\left[|E_0|^2 E_0\right] + F_2(q,\omega)\hat{Y}, \tag{3.49}$$

where we introduce the confinement factor $\Gamma$ and functions $F_{1,2}$ that are characteristic of the Fabry-Pérot resonator

$$\Gamma(q,\omega) = \left(1 + r_1 e^{2iqz_0}\right)\left(1 + r_2 e^{2iq(L-z_0)}\right), \tag{3.50}$$

$$F_1(q,\omega) = 1 - r_1 r_2 e^{2iqL}, \tag{3.51}$$

$$F_2(q,\omega) = t_1' e^{iqz_0}\left(1 + r_2 e^{2iq(L-z_0)}\right). \tag{3.52}$$

In the next step, we consider the modes of the micro-cavity. A resonant micro-cavity mode $q_m$ fulfills

$$2q_m L + \phi_1(\omega_m) + \phi_2(\omega_m) = 2\pi m, \; m \in \mathbb{Z}. \tag{3.53}$$

Note, that this corresponds to the minima of $|F_1|$. Further, we choose to place the Kerr slice such that there are resonances to both sides of it:

$$2q_m z_0 + \phi_1(\omega_m) = 2\pi n_1, \ n_1 \in \mathbb{Z}, \tag{3.54}$$

$$2q_m(L - z_0) + \phi_2(\omega_m) = 2\pi n_2, \ n_2 \in \mathbb{Z}. \tag{3.55}$$

These conditions maximize the confinement factor $\Gamma$. We notice that building the sum of Eqs. (3.54) and (3.55) leads to Eq. (3.53).

### 3.2.2. Expanding Around a Micro-Cavity Mode

Next, we expand Eq. (3.49) around a micro-cavity mode $q_m$. But we only take terms into account where the corresponding functions $F_{1,2}$ and $\Gamma$ change significantly. That is, we compare the rate of change of a function (i.e., its derivative) to its value and the characteristic length scale ($L$). Here, we consider the good cavity limit, where the reflectivities of the DBRs are close to unity ($|r_{1,2}| \to 1$) such that $\Gamma \to 4$, $F_2 \to 2t_1'$ and $F_1 \to 1 - |r_1 r_2| \ll 1$. We find the following scalings

$$\left.\frac{1}{LF_1}\frac{dF_1}{dq}\right|_{q_m} \sim \frac{1}{1 - |r_1 r_2|} \gg 1, \tag{3.56}$$

$$\left.\frac{1}{LF_2}\frac{dF_2}{dq}\right|_{q_m} \sim 1, \tag{3.57}$$

$$\left.\frac{1}{L\left(\frac{\Gamma}{q}\right)}\frac{d\left(\frac{\Gamma}{q}\right)}{dq}\right|_{q_m} \sim 1. \tag{3.58}$$

Consequently, we expand $F_1$ to first order (small changes in $q$ change the value significantly) while we remain with zeroth order for $\Gamma$ and $F_2$. We have

$$F_1(q_m, \omega_m) = 1 - |r_1 r_2|, \tag{3.59}$$

$$\left.\frac{dF_1}{dq}\right|_{q_m} = -i|r_1 r_2|\left[2L + \partial_q(\phi_1 + \phi_2)|_{q_m}\right], \tag{3.60}$$

$$F_2(q_m, \omega_m) = t_1' e^{iq_m z_0}(1 + |r_2|), \tag{3.61}$$

$$\Gamma(q_m, \omega_m) = (1 + |r_1|)(1 + |r_2|), \tag{3.62}$$

where we used $\omega_m$, which is the angular frequency corresponding to wavevector $q_m$ (cf. dispersion relation in Eq. (3.36)).

Next, we assume shallow transverse dynamics (i.e., $\mathbf{q}_\perp \ll 1$) such that, we can expand the dispersion relation in Eq. (3.36) as[4]

$$q\left(\mathbf{q}_\perp, \omega_m + \delta\omega\right) = q\left(0, \omega_m + \delta\omega\right) - \frac{\mathbf{q}_\perp^2}{2q_m} \tag{3.63}$$

$$= q_m + \frac{1}{v_g^{(m)}}\delta\omega - \frac{\mathbf{q}_\perp^2}{2q_m}, \tag{3.64}$$

where we used the definition of the group velocity (corresponding to the mode $\omega_m$) $v_g^{(m)}$ from Eq. (3.24). Finally, we define $\delta q$, which follows from Eq. (3.64) and reads

$$\delta q = q\left(\mathbf{q}_\perp, \omega_m + \delta\omega\right) - q_m = \frac{\delta\omega}{v_g^{(m)}} - \frac{\mathbf{q}_\perp^2}{2q_m}. \tag{3.65}$$

Now, we can write down the expansion of $F_1\left(q, \omega\right)$ around $\left(q_m, \omega_m\right)$:

$$F_1\left(q_m + \delta q, \omega + \delta\omega\right) = F_1\left(q_m, \omega_m\right) + \left.\frac{dF_1}{dq}\right|_{q_m} \delta q \tag{3.66}$$

$$= F_1\left(q_m, \omega_m\right) - F_1'\left(q_m, \omega_m\right)\frac{\mathbf{q}_\perp^2}{2q_m} - i\tau_e\left|r_1 r_2\right|\delta\omega, \tag{3.67}$$

$$\text{where } \tau_e = \frac{2L_e}{v_g^{(m)}} = \frac{2L + \partial_q\left(\phi_1 + \phi_2\right)|_{q_m}}{v_g^{(m)}}$$

is an effective round-trip time, that is defined via the effective length $L_e$, that takes the effects of the DBRs into account.

After all this build-up, we go back to the equation at the Kerr slice (3.49) and plug in the expansions for $F_{1,2}$ and $\Gamma$:

$$\left[1 + iL_\perp^2\mathbf{q}_\perp^2 - i\frac{\delta\omega}{\kappa}\right]\hat{E}_0 = i\tilde{s}\mathcal{F}_{t,\perp}\left[\left|E_0\right|^2 E_0\right] + \tilde{h}\hat{Y}. \tag{3.68}$$

Here, we introduced the following shortcuts

$$\kappa = \frac{1}{\tau_e}\frac{1 - |r_1 r_2|}{|r_1 r_2|}, \qquad \tilde{s} = \frac{3\tilde{\chi}_3\omega_m^2 W}{8q_m c^2}\frac{\left(1 + |r_1|\right)\left(1 + |r_2|\right)}{1 - |r_1 r_2|},$$

$$\tilde{h} = \frac{F_2\left(q_m, \omega_m\right)}{F_1\left(q_m, \omega_m\right)}, \qquad L_\perp = \sqrt{\frac{|r_1 r_2|}{1 - |r_1 r_2|}\frac{L}{q_m}},$$

where $L_\perp$ is the diffraction length dressed by the cavity confinement and defines the lengthscale of the transverse space, $\kappa$ is the amplitude of the photon decay rate, $\tilde{h}$ is the coupling parameter and $\tilde{s}$ is the amplitude of the Kerr nonlinearity. Using that $\delta\omega = \omega - \omega_m$, we can transform back into the time and (normalized) transverse space

[4] Expanding to higher orders in $\mathbf{q}_\perp^2$ takes higher order effects such as aberration into account.

domains ($-i\delta\omega \rightarrow \partial_t$, $-L_\perp^2 \mathbf{q}_\perp^2 \rightarrow \Delta_\perp$)

$$\frac{1}{\kappa}\partial_t E_0 = -\left(1 + i\frac{\omega_m}{\kappa}\right) E_0 + i\Delta_\perp E_0 + i\tilde{s}\left|E_0\right|^2 E_0 + \tilde{h}Y \tag{3.69}$$

In the next steps, we introduce scalings in Eq. (3.69) in order to obtain a minimal model. First, we rescale time such that $\kappa^{-1}\partial_t \rightarrow \partial_{t'}$. Further, we define the scaled micro-cavity resonance $\omega_c = \kappa^{-1}\tilde{\omega}_m$. With that, we obtain

$$\dot{E}_0 = -\left(1 + i\omega_c\right) E_0 + i\Delta_\perp E_0 + i\tilde{s}\left|E_0\right|^2 E_0 + \tilde{h}Y. \tag{3.70}$$

To have $E_0$ and $Y$ in the same order of magnitude, we apply rescalings. For that, we consider again the output relation $O = r_1'Y + t_1L_-$ (cf. Eq. (3.44)) and use the definition of $L_-$ found in Eq. (3.48) to obtain

$$\begin{aligned} O\left(t\right) &= \frac{t_1 e^{iq_m z_0}}{1 + r_1 e^{2iq_m z_0}} E_0\left(t\right) + \left(r_1' - \frac{t_1 t_1' e^{2iq_m z_0}}{1 + r_1 e^{2iq_m z_0}}\right) Y\left(t\right) && (3.71) \\ &=: \alpha E_0\left(t\right) + \beta Y\left(t\right). && (3.72) \end{aligned}$$

We assume lossless DBRs such that we can use relations that link the reflectivities and transmissivity on both sides of a mirror: $r = -r'$ and $t't = 1 + r'r = 1 - r^2$. Further, using Eq. (3.54), we can simplify the complex exponential as $e^{2iq_m z_0} = e^{-i\phi_1(q_m)}$ and consequently $r_1\left(q_m\right) e^{2iq_m z_0} = |r_1|$. With that, the coefficients in the output relation Eq. (3.72) read

$$\begin{aligned} \alpha &= \frac{t_1 e^{iq_m z_0}}{1 + |r_1|}, && (3.73) \\ \beta &= -\frac{r_1\left(1 + |r_1|\right) + \left(1 - r_1^2\right) e^{-i\phi_1(q_m)}}{1 + |r_1|}. && (3.74) \end{aligned}$$

The spacing in the DBRs shall be tuned with respect to the micro-cavity resonance, such that at resonance, there is no phase shift, i.e., $\phi_1\left(q_m\right) = 0$. This allows us to simplify Eq. (3.74) to $\beta = -1$. Further, we can define a new coupling coefficient as

$$h = \alpha\tilde{h} = \frac{\left(1 + |r_2|\right)\left(1 - |r_1|\right)}{1 - |r_1 r_2|}. \tag{3.75}$$

Note that in the limit of a perfectly reflective bottom mirror, where $|r_2| \rightarrow 1$, the coupling factor is $h = 2$. In this limit the micro-cavity identifies as a Gires–Tournois interferometer (GTI) [56] and hence $|r_2| \rightarrow 1$ is denoted the GTI limit. Finally, we rescale the micro-cavity fields as $E = \alpha E_0$ such that the output relation Eq. (3.72) simply reads

$$O(t) = E(t) - Y(t). \tag{3.76}$$

With this, we simplify the micro-cavity equation in Eq. (3.70)

$$\dot{E} = -(1 + i\omega_c) E + i\Delta_\perp E + is|E|^2 E + hY, \tag{3.77}$$

where we define the scaled Kerr-coefficient $s = \alpha^{-2}\tilde{s}$.

### 3.2.3. Injected Micro-Cavity

So far, we only described the dynamics in the micro-cavity by the ODE Eq. (3.77). To complete the model of the injected KGTI, we need to define the external cavity field $Y$ and the injection $Y_0$, cf. Fig. 3.4 (a). The output of the micro-cavity $O$ is re-injected into the micro-cavity after a round-trip time $\tau$ and after being reflected from an mirror with reflectivity $\eta$ and phase $\phi$, that closes the external cavity. Further, the setup is subject to an external injection. Here, we consider a monomode injection beam of amplitude $Y_0$ and frequency $\omega_0$, i.e., the injection reads $Y_0 e^{-i\omega_0 t}$. Due to the mirror, the injection experiences a transmission coefficient $|t| = \sqrt{1-\eta^2}$ (the phase can be absorbed in the definition of $Y_0$). Consequently, we arrive at the following description of the external cavity field $Y$

$$Y(t) = \eta e^{i\phi} O(t-\tau) + \sqrt{1-\eta^2} Y_0 e^{-i\omega_0 t}. \tag{3.78}$$

In order to avoid the explicit time-dependence in Eq. (3.78), we transform $E$ and $Y$ into the reference frame of the injection, i.e.,

$$E \to E e^{-i\omega_0 t}, \quad Y \to Y e^{-i\omega_0 t}. \tag{3.79}$$

With this, Eq. (3.77) reads

$$\dot{E} = \left[-1 + i\left(s|E|^2 - \omega_c + \omega_0\right)\right] E + i\Delta_\perp E + hY. \tag{3.80}$$

Here, we can define the detuning

$$\delta = \omega_c - \omega_0 \tag{3.81}$$

between the micro-cavity resonance and the injection. Another consequence of the transformation in Eq. (3.79) is that the output $O = E - Y$ is re-injected with an effective phase of

$$\varphi = \phi + \omega_0 \tau. \tag{3.82}$$

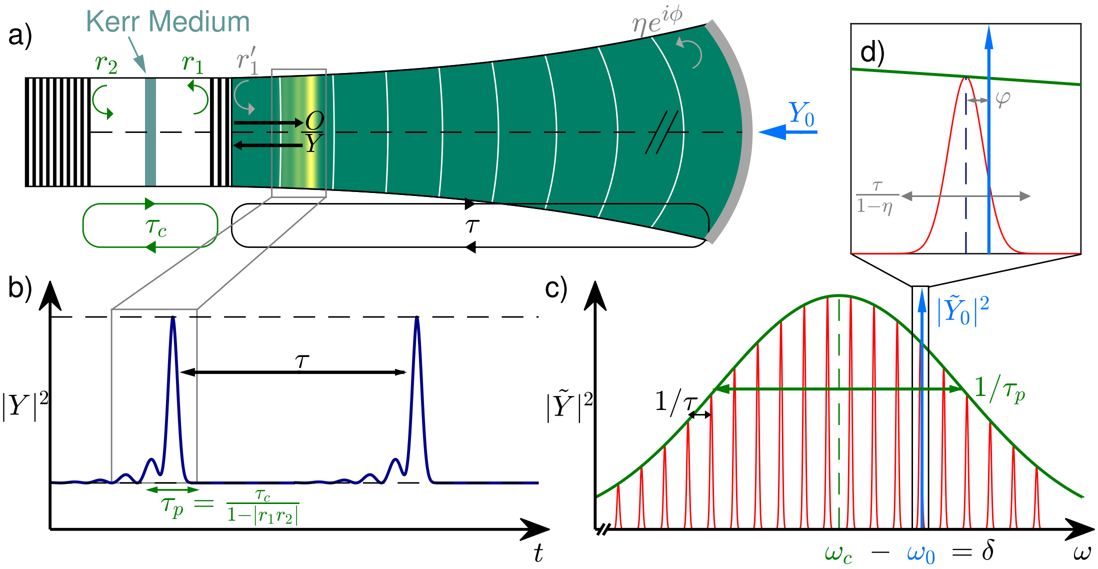


**Figure 3.4:** (a) Schematic of the KGTI. A single TLS circulates in the external cavity, which is detailed in (b). It corresponds to the comb depicted in (c). The injection field with amplitude $Y_0$ and frequency $\omega_0$ is, at the same time, detuned from the micro-cavity resonance with parameter $\delta = \omega_c - \omega_0$ but also from the nearest external cavity mode with detuning $\varphi$ (see close-up in inset (d)) whose width is controlled by the external cavity reflectivity $\eta$.

As both, the injection frequency $\omega_0$ and the delay time $\tau$ are large, small changes in the cavity size lead to large changes the effective phase $\varphi$, which makes this parameter easily accessible in an experimental realization.

We note, that in this thesis, we focus on the temporal dynamics. Therefore, in the following, we neglect the transversal contributions introduced by $\Delta_\perp$ (and possible higher order spatial terms). These effects are studied in detail in [91].

The relations between the physical quantities and the system parameters are summarized in Fig. 3.4. Panel (a) shows the KGTI with a single TLS circulating in the external cavity. The TLS is detailed in panel (b), where we note that the pulse width is given by $\tau_p = \frac{\tau_c}{1-|r_1 r_2|}$. In the frequency spectrum, the TLS corresponds to the frequency comb shown in panel (c), where we also indicate the detuning $\delta$ between the micro-cavity resonance $\omega_c$, around which the comb is centered, and frequency of the injection $\omega_0$. The inset in panel (d) details that the injection is also detuned by $\varphi$ from the nearest resonant external cavity mode.

Finally, with the definitions of the detuning in Eq. (3.81) and the effective phase in

Eq. (3.82), we obtain

$$\dot{E} = \left[-1 + i\left(s\left|E\right|^2 - \delta\right)\right]E + hY, \tag{3.83}$$

$$Y = \eta e^{i\varphi}\left[E\left(t-\tau\right) - Y\left(t-\tau\right)\right] + \sqrt{1-\eta^2}Y_0. \tag{3.84}$$

These equations are composed of two parts: a dynamical equation (Eq. (3.83)) for the micro-cavity field and a DAE (Eq. (3.84)) for the external cavity field. The equation is called to be algebraic as it does not contain a temporal derivative, cf. Section 2.1. The algebraic constraint allows to capture all external cavity reflections as Eq. (3.84) can be successively plugged into itself, such that one obtains a single equation with an infinite number of delays. Defining $\rho = \eta e^{i\varphi}$ and $\bar{Y}_0 = \sqrt{1-\eta^2}Y_0$, we obtain

$$Y = \rho\left(E_\tau - \left(\rho\left(E_{2\tau} - (\dots)\right) + \bar{Y}_0\right)\right) + \bar{Y}_0 \tag{3.85}$$

$$= \rho E_\tau - \rho^2 E_{2\tau} + \rho^3 E_{3\tau} + \dots + \left[1 - \rho + \rho^2 + \dots\right]\bar{Y}_0 \tag{3.86}$$

$$= \sum_{k=1}^{\infty}\left(-\rho\right)^{k-1}\left[\rho E_{k\tau} + \bar{Y}_0\right] = \sum_{k=1}^{\infty}\left(-\rho\right)^{k-1}\rho E_{k\tau} + \frac{1}{1+\rho}\bar{Y}_0. \tag{3.87}$$

For small feedback values $\eta = |\rho|$, this series can be truncated after the first iteration as then $\eta \ll \eta^2 \ll \eta^3 \ll \dots$. This allows, to approximate Eqs. (3.83) and (3.84) by a corresponding DDE. However, for feedback values closer to unity, all contributions are in the same order of magnitude, such that all multiple delays need to considered. Next, as Eqs. (3.83) and (3.84) are derived from first principles, GVD and TOD are naturally captured [57]. While the sign of the GVD is defined by the detuning $\delta$, the description of TOD is more involved as will be apparent from later sections.

Finally we note, that in general, the coefficient of the nonlinearity $s$ can be complex resulting in a complex index of refraction, which describes the effect of *two-photon absorption* (TPA). On the other hand, the real part of $s$ describes the Kerr effect, where negative $\mathrm{Re}(s)$ model the defocusing and positive $\mathrm{Re}(s)$ the focusing Kerr effect, respectively. In this work, mainly focus on the focusing Kerr effect. In this case ($s > 0 \in \mathbb{R}$), the parameter can be removed by a scaling of the field: $E \to \sqrt{s}E$ (same for $Y$ and $Y_0$). Hence, if not stated differently, we use $s = 1$. The influence of TPA is studied briefly in Section 4.8.

### 3.2.4. The KGTI in Different Reference Frames

It is possible to consider the system equations (3.83) and (3.84) in different reference frames, namely the injection and micro-cavity frames. While the transformations between the reference frames are in no way complicated, it is important to remember the implications on the injection term and the effective phase. We summarize the system equation in the different reference frames in Table 3.1. For most use cases, it it preferable to use the reference frame of the injection as here, the system equations become autonomous.

**Table 3.1:** Equations (3.83),(3.84) in different reference frames.

| | |
|---|---|
| no reference frame | $\dot{E} = \left[-1 + i\left(s\left\|E\right\|^2 - \omega_c\right)\right] E + hY$ <br> $Y = \eta e^{i\phi}\left[E\left(t-\tau\right) - Y\left(t-\tau\right)\right] + \sqrt{1-\eta^2} Y_0 e^{-i\omega_0 t}$ |
| injection | $\dot{E} = \left[-1 + i\left(s\left\|E\right\|^2 - \delta\right)\right] E + hY$ <br> $Y = \eta e^{i(\phi+\omega_0\tau)}\left[E\left(t-\tau\right) - Y\left(t-\tau\right)\right] + \sqrt{1-\eta^2} Y_0$ |
| micro-cavity | $\dot{E} = \left[-1 + is\left\|E\right\|^2\right] E + hY$ <br> $Y = \eta e^{i(\phi+\omega_c\tau)}\left[E\left(t-\tau\right) - Y\left(t-\tau\right)\right] + \sqrt{1-\eta^2} Y_0 e^{i\delta t}$ |

## 3.3. Passively Mode-Locked Ring Laser

In this section, we derive a mathematical description for a passively mode-locked laser. We consider a ring geometry for the laser cavity as depicted in Fig. 3.5 following the approach in [41]. In addition to the main cavity of length $\tau$, we also model a time-delayed feedback loop of length $\tau_f$ (cf. Section 3.3.6 for details). Both cavities are confined by mirrors (M). In the main cavity a gain section and a saturable absorber section are placed, which act as pulse shaping elements. The unidirectional optical isolator ensures that the pulses only propagate in one direction and the bandwidth limiting element enables that only certain laser modes are amplified as others are suppressed. The markers $z_1$-$z_5$ denote end and starting points of different section which are referenced during the derivation of the model. The detector is behind a semitransparent mirror (SM) with reflectivity $\sqrt{\kappa}$. The time-delayed feedback cavity is connected to the main cavity by a SM which transmits a fraction of $\eta$ of the electric field, i.e., a fraction of $\eta$ of the electrical field is fed back into the main cavity.

In the first step in Section 3.3.1, we motivate the ansatz of a traveling wave. Next, in Section 3.3.2, we mathematically describe the carrier dynamics. From that we derive a first principle model based upon delay differential equations (DDE) in Section 3.3.3 while at first neglecting the time-delayed feedback loop. Based on DDE model, we derive a normal form PDE in Section 3.3.4. Finally, we include the effects of the time-delayed feedback in Section 3.3.6.

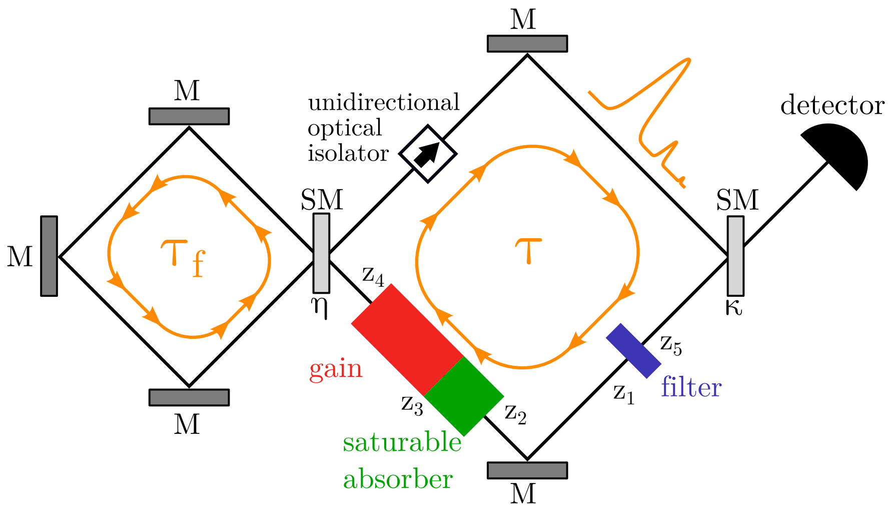


**Figure 3.5:** Schematic sketch of a PML laser employing a ring geometry. The main cavity of size $\tau$ is coupled to a secondary cavity of size $\tau_f$ providing time-delayed feedback. Adapted from [45].

### 3.3.1. Unidirectional Slowly Varying Traveling Wave

The starting point is the nonlinear wave equation in Eq. (3.32) that was derived for a slowly varying envelope around a carrier frequency $\omega_0$. Here, we consider only the dynamics along the longitudinal direction while the transverse mode leads to a confinement factor $\gamma_\perp$ in the RHS of Eq. (3.32). For the longitudinal direction, we also make the ansatz of a slowly varying envelope $\hat{E}_0$ which is defined as the amplitude of the electric field around the wavevector $q_0$

$$\hat{E}\left(z,\omega\right) = \hat{E}_0\left(z,\omega\right) e^{iq_0 z}. \tag{3.88}$$

Note that we assume that propagation only occurs in the $+z$-direction (which is ensured by the unidirectional optical insulator in Fig. 3.5). Further, we expand $q = \frac{n_e}{c}\omega$ around $\omega_0$:

$$q\left(\omega\right) = \underbrace{q\left(\omega_0\right)}_{=q_0} + \frac{1}{v_g}\delta\omega, \tag{3.89}$$

where $\delta\omega = \omega - \omega_0$. Then we obtain for the LHS of the nonlinear wave equation (3.32):

$$\begin{aligned}\left[\partial_z^2 + q^2\left(\omega\right)\right]\hat{E}_0\left(z,\omega\right)e^{iq_0 z} &= e^{iq_0 z}\left[\partial_z^2 + 2iq_0\partial_z - q_0^2 + \left(q_0 + \frac{1}{v_g}\delta\omega\right)^2\right]\hat{E}_0\left(z,\omega\right) \\ &= e^{iq_0 z}\left[2iq_0\left(\partial_z - i\frac{\delta\omega}{v_g}\right) + \partial_z^2 + \frac{\left(\delta\omega\right)^2}{v_g^2}\right]\hat{E}_0\left(z,\omega\right).\end{aligned} \tag{3.90}$$

We assume a slowly evolving envelope in both space and time such that the respective derivatives are small. This allows us to neglect the second order derivatives in Eq. (3.90), i.e., $\partial_z^2\hat{E}_0 = \left(-i\delta\omega\right)^2\hat{E}_0 \approx 0$. With that, we can simplify Eq. (3.90) to obtain

$$e^{iq_0 z}\left(\partial_z - i\frac{\delta\omega}{v_g}\right)\hat{E}_0\left(z,\omega\right) = i\gamma_\perp\frac{\omega_0}{2cn_0\epsilon_0}\hat{P}_{nl}, \tag{3.91}$$

where $n_0 = n\left(\omega_0\right)$ and the coefficient of the nonlinear polarization is $\omega^2 \approx \omega_0^2$. In free space, this equation corresponds to the traveling wave (or advection) equation and describes simple propagation.

### 3.3.2. Carrier Dynamics

Because we assumed a slowly evolving envelope for the electric field in both space and time, we use the same assumption for the nonlinear polarization $\hat{P}_{nl}$

$$\hat{P}_{nl}(z,\omega) = \epsilon_0 \hat{\chi}_{nl} \hat{E}_0 e^{iq_0 z}. \tag{3.92}$$

Now we have to characterize the nonlinear susceptibility. We assume a parabolic band structure in the semiconductor and the carrier distribution to follow a Fermi distribution[92]. Further, we assume a broad gain/absorption spectrum such that the susceptibility remains constant in the active regions: $\chi(\omega) = \chi(\omega_0)$, which is also assured by introducing a spectral filter. The carrier density $\mathcal{N}$ has a critical value $\mathcal{N}^{(tr)}$ where the material becomes transparent. Linearizing the susceptibility around this point gives

$$\chi_{nl} = \left.\frac{\partial \chi_{nl}}{\partial \mathcal{N}}\right|_{\mathcal{N}^{(tr)}} \left(\mathcal{N} - \mathcal{N}^{(tr)}\right). \tag{3.93}$$

Separating this equation into real and imaginary parts and defining the differential gain coefficient $g_r = -\frac{\partial \mathrm{Im}(\chi_{nl})}{\partial \mathcal{N}}|_{\mathcal{N}^{(tr)}}$ and the linewidth enhancement factor describing the amplitude-phase coupling

$$\alpha = \left.\frac{\frac{\partial \mathrm{Re}(\chi_{nl})}{\partial \mathcal{N}}}{\frac{\partial \mathrm{Im}(\chi_{nl})}{\partial \mathcal{N}}}\right|_{\mathcal{N}^{(tr)}}, \tag{3.94}$$

we find that the susceptibility reads

$$\chi_{nl} = -g_r(\alpha + i)\left(\mathcal{N} - \mathcal{N}^{(tr)}\right). \tag{3.95}$$

This equation therefore characterizes the gain (or absorption) and the corresponding change in the relative refractive index of the nonlinear medium. Finally, we have to model the dynamics of the carriers which can be done with the rate equation

$$\frac{\partial \mathcal{N}}{\partial t} = J_r - \Gamma_r \mathcal{N} + \mathrm{Im}(\chi_{nl})|E|^2, \tag{3.96}$$

where $\Gamma_r$ is the rate of spontaneous emission, $J_r$ is the gain current and the last term proportional to the intensity stands for the stimulated emission. Plugging Eq. (3.95) in the susceptibility from Eq. (3.95) yields

$$\frac{\partial \mathcal{N}}{\partial t} = J_r - \Gamma_r \mathcal{N} - g_r\left(\mathcal{N} - \mathcal{N}^{(tr)}\right)|E|^2. \tag{3.97}$$

### 3.3.3. Time-delayed Model derived from First Principles

We follow the derivation presented in [41] to find model derived from first principles in form of a set of DDEs. At first, the additional feedback loop is neglected. First, we split the main cavity in Fig. 3.5 into five sections: the gain element ($z_3 < z < z_4$), the absorber element ($z_2 < z < z_3$), the bandwidth limiting element ($z_5 < z < z_1 + L$ where $L = v_g \tau$ is the length of the cavity and $v_g$ is the group velocity) and the parts between the bandwidth limiting element and gain ($z_4 < z < z_5$) and absorber elements ($z_1 < z < z_2$), respectively. The last two mentioned sections are passive such that we find (following Eq. (3.91) where we apply an inverse Fourier transform)

$$\left(\partial_z + \frac{1}{v_g}\partial_t\right) E_0\left(t, z\right) = 0. \tag{3.98}$$

For the active sections, we use the nonlinear wave equation (3.32) together with the nonlinear susceptibility from Eq. (3.95). Employing Eq. (3.91), we obtain

$$\left(\partial_z + \frac{1}{v_g}\partial_t\right) E_0 = g_r \gamma_r \frac{\omega_0}{c n_0} \frac{1 - i\alpha_r}{2} \left(\mathcal{N}_r - \mathcal{N}_r^{(tr)}\right) E_0, \tag{3.99}$$

$$\frac{\partial \mathcal{N}_r}{\partial t} = J_r - \Gamma_r \mathcal{N}_r - g_r \left(\mathcal{N}_r - \mathcal{N}_r^{(tr)}\right) \left|E_0\right|^2, \tag{3.100}$$

where the subscript $r$ stands for the gain ($r = g$) and absorber ($r = q$) sections, respectively, $\gamma_r$ is the transverse confinement factor for the corresponding sections, and we note that the absorber gain is $J_q = 0$. Next, we consider the co-moving reference frame by applying the following parameters transformation

$$(t, z) \to (t', z') \quad \text{where } t' = t - \frac{z}{v_g}, \quad z' = \frac{z}{v_g}. \tag{3.101}$$

Naturally, the field is now static in the passive sections with respect to the transformed time, i.e., Eq. (3.98) transforms to

$$\frac{\partial E_0(t', z')}{\partial z'} = 0. \tag{3.102}$$

Further, in order to nondimensionalize the quantities, we introduce the following scalings

$$g_r' = g_r \gamma_r v_g \frac{\omega_0}{c n_0}, \qquad n_r = g_r' \left(\mathcal{N}_r - \mathcal{N}_r^{(tr)}\right), \qquad A\left(t', z'\right) = E_0\left(t, z\right)\sqrt{g_g},$$
$$j_g = g_g' \frac{J_g - \Gamma_g \mathcal{N}_g^{tr}}{\Gamma_g}, \qquad j_q = g_q' \mathcal{N}_q^{(tr)}.$$

With these transformations, Eqs. (3.99) and (3.100) become

$$\frac{\partial_{z'} A(t', z')}{\partial z'} = \frac{1 - i\alpha_{g,q}}{2} n_{g,q}(t', z') A(t', z'), \tag{3.103}$$
$$\frac{\partial n_g(t', z')}{\partial t'} = \Gamma_g (j_g - n_g(t', z')) - n_g(t', z') |A(t', z')|^2, \tag{3.104}$$
$$\frac{\partial n_q(t', z')}{\partial t'} = \Gamma_q (-j_q - n_q(t', z')) - n_q(t', z') s |A(t', z')|^2. \tag{3.105}$$

Here, the parameter $s = g_q/g_g$ is the ratio of the saturation intensities in the gain and absorber sections. Next, we integrate the optical field over the separate sections $z'_1, \ldots, z'_5$ where $z'_k = \frac{z_k}{v_g}, k = 1, ..., 5$ to relate the fields at the beginning and end of each section (cf. Fig. 3.5). We start with the passive sections, i.e., we integrate Eq. (3.102) from $z'_{1,4}$ to $z'_{2,5}$, which gives the (rather trivial) relations

$$A(t', z'_2) = A(t', z'_1), \quad A(t', z'_5) = A(t', z'_4), \tag{3.106}$$

For the gain and absorber sections, we integrate Eq. (3.103) from $z'_{2,3}$ to $z'_{3,4}$ which yields

$$A(t', z'_4) = \exp\left(\frac{1 - i\alpha_g}{2} G(t')\right) A(t', z'_3), \tag{3.107}$$
$$A(t', z'_3) = \exp\left(-\frac{1 - i\alpha_q}{2} Q(t')\right) A(t', z'_2), \tag{3.108}$$
$$\text{where } G(t') := \int_{z'_3}^{z'_4} n_g(t', z')\, dz', \text{ and } Q(t') := -\int_{z'_2}^{z'_3} n_q(t', z')\, dz'. \tag{3.109}$$

Here, the dimensionless quantities $G(t')$ and $Q(t')$ describe the integrated (over space and time) gain and loss introduced by the absorber and gain sections [93]. Next, we multiply Eq. (3.103) with $A^*$ and add its complex conjugated. Integrating the result from $z'_{2,3}$ to $z'_{3,4}$ gives the following useful relation

$$\int_{z'_{2,3}}^{z'_{3,4}} n_{g,q}(t', z') |A(t', z')|^2 dz' = \left|A\left(t', z'_{3,4}\right)\right|^2 - \left|A\left(t', z'_{2,3}\right)\right|^2. \tag{3.110}$$

Using this, we also integrate the carrier equations (3.104,(3.105) from $z'_{2,3}$ to $z'_{3,4}$ to obtain dynamical equations for $G$ and $Q$, respectively:

$$\frac{\partial G(t')}{\partial t'} = \Gamma_g (G_0 - G) - |A(t', z'_4)|^2 + |A(t', z'_3)|^2, \tag{3.111}$$
$$\frac{\partial Q(t')}{\partial t'} = \Gamma_q (Q_0 - Q) + s |A(t', z'_3)|^2 - s |A(t', z'_2)|^2, \tag{3.112}$$
$$\text{where } G_0 := \int_{z'_3}^{z'_4} j_g dz', \text{ and } Q_0 := \int_{z'_2}^{z'_3} j_q dz'. \tag{3.113}$$

The optical field $A(t', z')$ is evaluated at different positions $z'_{2-4}$. However, we can successively use the relations found in Eqs. (3.106)–(3.108) and plug them into Eqs. (3.111) and (3.112) such that we find the dynamical carrier equations

$$\frac{\partial G(t')}{\partial t'} = \Gamma_g (G_0 - G) - e^{-Q}\left(e^G - 1\right)\left|A(t', z'_1)\right|^2, \tag{3.114}$$
$$\frac{\partial Q(t')}{\partial t'} = \Gamma_q (Q_0 - Q) - s\left(1 - e^{-Q}\right)\left|A(t', z'_1)\right|^2, \tag{3.115}$$

which are now both expressed in terms of $A(t', z'_1)$. Finally, we have to account for the action of the filter. In Fourier space, the fields in front of and behind the filter are related as

$$\hat{A}(\omega', z'_1 + \tau) = \hat{f}(\omega')\,\hat{A}(\omega', z'_5), \tag{3.116}$$

where $\tau = \frac{L}{v_g}$ and $\hat{f}(\omega')$ is the frequency response function of the filter. When transforming Eq. (3.116) into the time domain, the multiplication turns into a convolution

$$A(t', z'_1 + \tau) = f(t') * A(t', z'_5) = \int_{-\infty}^{t'} f(t' - \theta)\, A(\theta, z'_5)\, d\theta, \tag{3.117}$$

where the upper boundary corresponds to $t'$ due to causality[5]. Again, we want all fields to be evaluated at the same positions. That is, to calculate $A(\theta, z'_5)$ we successively use the relations found in Eqs. (3.106)–(3.108) which gives

$$A(\theta, z'_5) = R(\theta)\, A(\theta, z'_1), \tag{3.118}$$
$$\text{where } R(\theta) = \exp\left(\frac{1 - i\alpha_g}{2} G(\theta) - \frac{1 - i\alpha_q}{2} Q(\theta)\right). \tag{3.119}$$

Further, we use the periodic boundaries of the ring cavity. That is, we add $L$ to $z$ such that the transformation defined by Eq. (3.101) gives: $(t, z + L) \to (t' - \tau, z' + \tau)$. Hence, we find $A(t', z'_1 + \tau) = A(t' + \tau, z'_1)$. With that, we can rewrite Eq. (3.117) and find

$$A(t' + \tau, z'_1) = \int_{-\infty}^{t'} f(t' - \theta)\, R(\theta)\, A(\theta, z'_1)\, d\theta. \tag{3.120}$$

We can observe that all fields are evaluated at $z'_1$, such that we can define $A(t') :=$ $A(t', z'_1)$. In order to evaluate the integral in Eq. (3.120), we need to characterize the filter by defining its frequency response function. Here, we employ a Lorentzian filter with a bandwidth $\gamma$ and central frequency $\omega_0$, which in the time domain reads

$$f(t') = \sqrt{\kappa}\gamma \exp\left[(-\gamma + i\omega_0)\, t'\right], \tag{3.121}$$

[5] A causal filter cannot act on future optical fields.

where we also included the effect of the cavity output, i.e., after every round-trip a fraction of $\kappa$ of the optical intensity remains in the cavity. Using the frequency response function defined in Eq. (3.121), we derive Eq. (3.120) with respect to $t'$ to obtain

$$\begin{aligned}\frac{\partial A\left(t'+\tau\right)}{\partial t'} &= \frac{\partial}{\partial t'}\left[\int_{-\infty}^{t'} f\left(t'-\theta\right) R\left(\theta\right) A\left(\theta\right) d\theta\right] \\ &= f\left(0\right) R\left(t'\right) A\left(t'\right) + \left(-\gamma + i\omega_0\right)\int_{-\infty}^{t'} f\left(t'-\theta\right) R\left(\theta\right) A\left(\theta\right) d\theta \\ &= \sqrt{\kappa}\gamma R\left(t'\right) A\left(t'\right) + \left(-\gamma + i\omega_0\right) A\left(t'+\tau\right), \end{aligned} \tag{3.122}$$

where we employed Leibniz's integral rule and, in the last step, used the definition of $A\left(t'+\tau\right)$ given in Eq. (3.120). Finally, we shift Eq. (3.122) by $\tau$ and go into the co-rotating frame ($A \to Ae^{i\omega_0 t}$) which gives the following DDE model

$$\frac{\dot{A}}{\gamma} = \sqrt{\kappa}\exp\left(\frac{1-i\alpha_g}{2}G_\tau - \frac{1-i\alpha_q}{2}Q_\tau - i\varphi\right)A_\tau - A, \tag{3.123}$$

$$\dot{G} = \Gamma_g\left(G_0 - G\right) - e^{-Q}\left(e^G - 1\right)|A|^2, \tag{3.124}$$

$$\dot{Q} = \Gamma_q\left(Q_0 - Q\right) - s\left(1 - e^{-Q}\right)|A|^2, \tag{3.125}$$

where $\varphi = \omega_0\tau$ and the index $\tau$ stands for the delayed variable (i.e., $A_\tau \coloneqq A\left(t'-\tau\right)$).

### 3.3.4. Haus Master Equation

In the next step, we want to transform the DDE ring model in Eqs. (3.123)–(3.125) into a normal form PDE using the schemes presented in Section 2.3. First, we normalize the time delay and go into the long-delay limit where $\epsilon = \tau^{-1}$ is small. Next, we use the functional mapping approach (cf. Section 2.3.2) and expand in the uniform field limit where the gain, absorption and losses are small (i.e., they are $\mathcal{O}\left(\epsilon^2\right)$). Then we go into Fourier space where $\partial_t \to -i\omega$ and solve Eq. (3.123) for $A_t \coloneqq A\left(t\right)$

$$A_n = \frac{\sqrt{\kappa}\exp\left[\frac{1-i\alpha_g}{2}G_{n-1} - \frac{1-i\alpha_q}{2}Q_{n-1} - i\varphi\right]}{1 - \frac{i\epsilon\omega}{\gamma}}A_{n-1}. \tag{3.126}$$

Expanding the exponential and separating into linear and nonlinear terms yields

$$A_n = \frac{\sqrt{\kappa}e^{-i\varphi}}{1-\frac{i\epsilon\omega}{\gamma}}A_{n-1} + \sqrt{\kappa}e^{-i\varphi}\left(\frac{1-i\alpha_g}{2}G_{n-1} - \frac{1-i\alpha_q}{2}Q_{n-1}\right)A_{n-1} + \mathcal{O}\left(\epsilon^3\right). \tag{3.127}$$

Then the linear operator in the PDE normal form reads

$$\mathcal{L} = \ln\left[\frac{\sqrt{\kappa}e^{-i\varphi}}{1-\frac{i\epsilon\omega}{\gamma}}\right] = \sqrt{\kappa} - 1 - i\varphi - \frac{-i\epsilon\omega}{\gamma} + \frac{1}{2}\left(\frac{-i\epsilon\omega}{\gamma}\right)^2 + \mathcal{O}\left(\epsilon^3\right). \tag{3.128}$$

To find the nonlinearity, we use a zeroth order approximation for the integral Eq. (2.39) such as the rectangular method (cf. Eq. (2.40)). Hence, we find

$$\mathcal{N}_{n-1} = e^{-\mathcal{L}} N_{n-1} + \mathcal{O}(\epsilon) = e^{-\mathcal{L}_0} N_{n-1} + \mathcal{O}(\epsilon), \tag{3.129}$$

where $\mathcal{L}_0 = -i\varphi$. Here, the phases cancel out and we obtain

$$\mathcal{N}_{n-1} = \sqrt{\kappa}\left(\frac{1-i\alpha_g}{2}G_{n-1} - \frac{1-i\alpha_q}{2}Q_{n-1}\right)A_{n-1} + \mathcal{O}(\epsilon). \tag{3.130}$$

Lastly, we need to consider the PDE versions of the carriers defined in Eqs. (3.124) and (3.125). However, as they do not contain a time delay they can only evolve on the fast time scale. Further, using the above scaling for the gain and absorber simplifies the nonlinearities in these terms:

$$e^{-Q}\left(e^{G} - 1\right) = G + \mathcal{O}\left(\epsilon^3\right), \tag{3.131}$$

$$\left(1 - e^{-Q}\right) = Q + \mathcal{O}\left(\epsilon^3\right). \tag{3.132}$$

Finally, the PDE normal form derived up to $\mathcal{O}\left(\epsilon^2\right)$ reads

$$\partial_\xi A = \left[v\partial_z + \frac{1}{2\gamma^2}\partial_z^2 + \sqrt{\kappa} - 1 - i\varphi + \sqrt{\kappa}\left(\frac{1-i\alpha_g}{2}G - \frac{1-i\alpha_q}{2}Q\right)\right]A, \tag{3.133}$$

$$\partial_z G = \Gamma_g\left(G_0 - G\right) - G\left|A\right|^2, \tag{3.134}$$

$$\partial_z Q = \Gamma_q\left(Q_0 - Q\right) - sQ\left|A\right|^2, \tag{3.135}$$

which corresponds to the *Haus master equation* [25]. Often, a different scaling of this equation is used, where we define $k = 1 - \sqrt{\kappa}$ and absorb $\kappa$ in the carriers: $g = \sqrt{\kappa}G$, $g_0 = \sqrt{\kappa}G_0$, $q = \sqrt{\kappa}Q$ and $q_0 = \sqrt{\kappa}Q_0$. Further, the common phase can be removed by transforming $A \to Ae^{-i\varphi\xi}$ and the drift is removed by going into the comoving frame.

$$\partial_\xi E = \left[\frac{1}{2\gamma^2}\partial_z^2 - k + \frac{1-i\alpha_g}{2}g - \frac{1-i\alpha_q}{2}q\right]E \tag{3.136}$$

$$\partial_z g = \Gamma_g\left(g_0 - g\right) - g\left|E\right|^2 \tag{3.137}$$

$$\partial_z q = \Gamma_q\left(q_0 - q\right) - sq\left|E\right|^2. \tag{3.138}$$

Another common scaling normalizes time with respect to the absorber recovery rate $\Gamma_q$ (sometimes also called $\gamma_q$).

Finally, we have to make remarks on the boundary conditions. The easiest choice are obviously period boundaries. However, in Section 2.1.1, we detail that while time-delayed systems are similar to PDEs, their boundaries are not periodic but connect the end of one round-trip to the beginning of the next one. This property corresponds to preserving the carrier memory between round-trips and can be implemented in Eqs. (3.136)–(3.138) by introducing dynamic boundaries for the carriers, see [94–96]. This allows for the description of complex pulse trains such as Q-switched transitions. However, in our application, we study the phase and position dynamics of pulses that do not change (significantly) in shape. Therefore, the dynamic boundaries introduce small corrections, which are on much faster time scales compared to the slow phase and position dynamics. Hence, we chose to use periodic boundary conditions as it simplifies the numerical effort. However, we cross-checked some findings using the approach presented in [95] and obtained identical results.

### 3.3.5. Lasing Threshold

Below a certain threshold value for the gain pump rate, a semiconductor laser remains in the off-state as the losses cannot be compensated. The off-state is the trivial steady state solution, where the optical field vanishes such that the gain $g$ corresponds to its pumping rate $g_0$ and the absorber $q$ is the value of the unsaturated losses $q_0$. At the lasing threshold, the off-solution becomes unstable and the continuous-wave state emerges. In the following, we calculate the lasing threshold first for the DDE model in Eqs. (3.123)–(3.125) and in the second step, show that the PDE model Eqs. (3.136)–(3.138) exhibits the same threshold.

Substituting the plane-wave ansatz $A(t') = A_0 e^{-i\omega t'}$ into the dynamical equation describing the evolution of the field defined in Eq. (3.123) leads to

$$\frac{i\omega}{\gamma} = \sqrt{\kappa}\exp\left[\frac{1-i\alpha_g}{2}G - \frac{1-i\alpha_q}{2}Q - i\varphi + \omega\tau\right] - 1. \tag{3.139}$$

Here, the gain $G = G_0 + \delta G$ and absorber $Q = Q_0 + \delta Q$ still fulfill the carrier equations Eqs. (3.124) and (3.125), and $\delta G$ and $\delta Q$ account for deviations from the off-state. At the lasing threshold, the amplitude of the plane-wave $A_0$ is small such that $\delta G$ and $\delta Q$ are small as well. Expanding Eq. (3.139) gives

$$\frac{i\omega}{\gamma} = \sqrt{\kappa}\exp\left[\frac{1-i\alpha_g}{2}G_0 - \frac{1-i\alpha_q}{2}Q_0 - i\varphi + \omega\tau\right] - 1 + \mathcal{O}\left(\delta G, \delta Q\right). \tag{3.140}$$

Now, we simply need to solve for the gain $G_0$ which can be achieved by taking the modulus-square of Eq. (3.140) such that we obtain

$$1+\frac{\omega^2}{\gamma^2}=\kappa e^{G_0-Q_0} \tag{3.141}$$

$$\Leftrightarrow \quad G_0(\omega)=Q_0-\ln\kappa+\ln\left(1+\frac{\omega^2}{\gamma^2}\right). \tag{3.142}$$

However, the frequency $\omega$ must still fulfill Eq. (3.140). We can derive an equation defining the possible frequencies $\omega$ by taking the imaginary part of Eq. (3.140) which gives

$$\frac{\omega}{\sqrt{\kappa}\gamma}=\sin\left(\frac{\alpha_q Q_0-\alpha_g G_0}{2}-\varphi+\omega\tau\right). \tag{3.143}$$

As this equation is transcendental, it has an infinite number of solutions for $\omega$ that correspond to the external cavity modes. However, here we are interested in the long-delay limit where $\tau \gg 1$. Hence, the term $\omega\tau$ in Eq. (3.143) is a rapidly oscillating phase such that an arbitrary small value of $\omega=\omega_c\to 0$ can cancel the other terms in the sine and therefore, solve Eq. (3.143). This is important because the lasing threshold is then the minimum of $G_0(\omega)$, i.e.

$$G_{\mathrm{th}}\coloneqq G_0(0)=Q_0-\ln\kappa. \tag{3.144}$$

We note that increasing the frequency by adding $\frac{2\pi}{\tau}$, i.e.

$$\omega_k=\omega_c+\frac{2\pi k}{\tau},\ \ k\in\mathbb{Z} \tag{3.145}$$

still solves Eq. (3.143) due to $\tau\gg 1$. Here, the $\omega_k$ correspond to the external cavity modes.

Similarly, for the PDE model in Eqs. (3.136)–(3.138), we use a plane-wave ansatz $E(\xi,z)=E_0e^{(ik_z z+\lambda\xi)}$, which leads to

$$\lambda=-\frac{k_z^2}{2\gamma}+\frac{1-i\alpha_g}{2}g_0-\frac{1-i\alpha_q}{2}q_0-k. \tag{3.146}$$

As we are looking for the point, where the off-solution becomes unstable, we set $\mathrm{Re}(\lambda)=0$ such that we obtain

$$g_0(k_z)=q_0+2k+\frac{k_z}{\gamma^2}. \tag{3.147}$$

This function has a minimum for[6] $k_z = 0$, such that the lasing threshold reads

$$g_{\mathrm{th}} = q_0 + 2k. \tag{3.148}$$

In order to compare with the previous result from the DDE model, we can revert the scaling of the parameters:

$$\begin{aligned} g_{\mathrm{th}} &= \sqrt{\kappa} Q_0 + 2\left(1 - \sqrt{\kappa}\right) && (3.149) \\ &= \sqrt{\kappa}\left(Q_0 + 1 - \kappa\right) + \mathcal{O}\left(\epsilon^4\right) && (3.150) \\ &= \sqrt{\kappa}\left(Q_0 - \ln \kappa\right) + \mathcal{O}\left(\epsilon^4\right), && (3.151) \end{aligned}$$

where we used that $\kappa - 1 \sim \epsilon^2$ such that we find, as it should be, the same result as in Eq. (3.144) (remember that $g_{\mathrm{th}} = \sqrt{\kappa} G_{\mathrm{th}}$).

### 3.3.6. Time-Delayed Feedback

Time-delayed feedback (TDF) refers to a process in which the output of the system is fed back into itself after a certain delay. This concept can influence the dynamics of the system and can have significant effects on its stability, behavior, and performance, see e.g. [44–48]. While TDF can be used to actively control the output of a laser, it can also stem from (parasitic) reflections of lenses making it almost unavoidable in an experimental setup. Hence, TDF can have both, stabilizing and destabilizing, effects.

We denote the feedback time delay $\tau_f$ and the portion of the field that is re-injected $\eta$, cf. the setup in Fig. 3.5. Further, the optical field can experience a relative phase when being re-injected, which we denote $\Omega$. Hence, TDF can be modeled by simply adding a term $\eta e^{i\Omega} E\left(t - \tau_f\right)$ to the field equation in the DDE model (3.123) and the PDE model (3.136).

In a part of our analysis, we carry out a statistical study under the influence of noise, which stems from the spontaneous emission fluctuations and the mechanical vibrations in the cavity. We model this noise for simplicity with a (normalized) white Gaussian stochastic process $\zeta$, that is added to the field equation with an amplitude of $\sigma$. This

[6] Remember that the PDE model was derived in the long-delay limit such that the the discussion about the external cavity modes defined in Eq. (3.143) applies here as well.

leads to the following equations for the DDE model

$$\begin{aligned}\frac{\dot{A}}{\gamma} =& \sqrt{\kappa}\exp\left(\frac{1-i\alpha_g}{2}G_\tau - \frac{1-i\alpha_q}{2}Q_\tau - i\varphi\right)A_\tau - A \\ & + \eta e^{i\Omega}A\left(t-\tau_f\right) + \sigma\zeta,\end{aligned} \tag{3.152}$$

$$\dot{G} = \Gamma_g\left(G_0 - G\right) - e^{-Q}\left(e^G - 1\right)|A|^2, \tag{3.153}$$

$$\dot{Q} = \Gamma_q\left(Q_0 - Q\right) - s\left(1 - e^{-Q}\right)|A|^2, \tag{3.154}$$

and for the PDE model we obtain[7]

$$\partial_\xi E = \left[\frac{1}{2\gamma^2}\partial_z^2 - k + \frac{1-i\alpha_g}{2}g - \frac{1-i\alpha_q}{2}q\right]E + \eta e^{i\Omega}E\left(z-\tau_f\right) + \sigma\zeta, \tag{3.155}$$

$$\partial_z g = \Gamma_g\left(g_0 - g\right) - g\,|E|^2, \tag{3.156}$$

$$\partial_z q = \Gamma_q\left(q_0 - q\right) - sq\,|E|^2. \tag{3.157}$$

Note that the presence of TDF has an influence on the lasing threshold [97], however, as we consider only small feedback amplitudes, this effect can be neglected. In Appendix A.1, we present how Eqs. (3.155)–(3.157) can be numerically integrated.

[7]For simplicity, we use the same symbols for the noise terms in the PDE and DDE models. However, they are not identical but are linked via the derivation of the normal form PDE, cf. Section 3.3.4.

# 4. The Injected Kerr–Gires–Tournois Interferometer

In the first part of the thesis, we study the injected Kerr–Gires–Tournois interferometer (KGTI) introduced in Section 1.2.1. The KGTI is modeled by the DAEs (3.83),(3.84), which were derived from first principles, see Section 3.2.

This chapter is structured as follows. First, in Section 4.1, we consider the conservative case of the KGTI, i.e., in the absence of external injection and with a closed cavity ($\eta = 1$). Next, in Section 4.2, we make the first step in investigating the dissipative case and study in detail the steady state solution in its (multi-dimensional) parameter space. There, we also compute analytically its linear stability which allows us to get an overview over the different dynamical regimes in the KGTI system. In Section 4.3, we present the regime of locked domain walls found for normal dispersion and unveil the mechanism in which these structures are formed. Next, in Section 4.4, we perform a detailed parameter study of the domain walls regime. An important limit case, the weakly dissipative limit, is described in Section 4.5. We explore further dynamical regimes in the KGTI, namely square waves (cf. Section 4.6) and TLSs beyond the mean-field limit (cf. Section 4.7). Finally, in Section 4.8, we briefly study the influence of two-photon absorption, before concluding the finding in Section 4.9.

Parts of this chapter are based on the publications [98–100], as indicated at the beginning of the corresponding sections.

## 4.1. Conservative Dynamics

The current Section 4.1, including the figures, is based on the publication:

[98] T. G. Seidel, S. V. Gurevich, and J. Javaloyes. "Conservative Solitons and Reversibility in Time Delayed Systems". In: *Phys. Rev. Lett.* 128 (2022), p. 083901. DOI: `10.1103/PhysRevLett.128.083901`

TGS carried out the analytical and numerical work under the supervision of SVG and JJ. All figures were created by TGS. A first draft of the text was created by TGS and gradually refined by all authors.

In the first step of studying the KGTI, we consider the case of no external injection (i.e., $Y_0 = 0$). This allows us to describe the system in the reference frame of the micro-cavity (cf. Table 3.1) such that the system equations read

$$\dot{E}\left(t\right) = \left(-1 + i|E|^2\right)E + hY, \tag{4.1}$$

$$Y\left(t\right) = \eta e^{i\bar{\varphi}}\left[E\left(t-\tau\right) - Y\left(t-\tau\right)\right], \tag{4.2}$$

where[8] $\bar{\varphi} = \phi + \omega_c \tau$. This dynamical system is based on the setup shown in Fig. 4.1 (a). The algebraic nature of Eq. (4.2) captures all the multiple reflections in the external cavity, cf. Eq. (3.87). Here, we want to consider the conservative limit, where $\eta = 1$, and all the multiple reflections are conserved. For a perfectly lossless bottom mirror $|r_2| = 1$ the coupling efficiency parameter is $h = 2$, which corresponds to the Gires–Tournois interferometer regime [56].

Due to the time delay, the system composed of Eqs. (4.1) and (4.2) possesses infinitely many degrees of freedom. Hence, its eigenvalue spectrum is a countably infinite set and in the long-delay limit $\tau \to \infty$ it becomes pseudo-continuous. In order to compute the spectrum, we use a scaling ansatz for the eigenvalues $\lambda = \frac{\gamma}{\tau} + i\mu$ and follow the deviation in Section 2.2.1 for the steady state solution $(E, Y) = (0, 0)$. Linearizing the system in Eqs. (4.1) and (4.2), it is characterized by the matrices (cf. Eq. (2.7))

$$A = \begin{pmatrix} -1 & h \\ 0 & -1 \end{pmatrix} \quad \text{and} \quad B = \eta \begin{pmatrix} 0 & 0 \\ e^{i\bar{\varphi}} & -e^{-i\bar{\varphi}} \end{pmatrix}. \tag{4.3}$$

The solution of the characteristic equation (cf. Eq. (2.12)) reads

$$g = -\frac{1}{\eta} \frac{1 + i\mu}{1 + i\mu - h} e^{-i\bar{\varphi}} \tag{4.4}$$

such that the real part $\gamma$ of the eigenvalue spectrum is (cf. Eq. (2.13))

$$\gamma = -\ln|g| = \ln\eta + \frac{1}{2}\ln\left(1 + h\frac{h-2}{1+\mu^2}\right) \tag{4.5}$$

$$\overset{h\to 2}{\approx} \ln\eta + \frac{h-2}{1+\mu^2}. \tag{4.6}$$

Then, the imaginary part $\mu$ of the eigenvalues is defined by (cf. Eq. (2.15))

$$\mu\tau = -\arg(g) + 2\pi k \tag{4.7}$$

$$= -\arctan\left[\frac{(1+\mu^2-h)\sin(\bar{\varphi}) - h\mu\cos(\bar{\varphi})}{(1+\mu^2-h)\cos(\bar{\varphi}) + h\mu\sin(\bar{\varphi})}\right] + 2\pi k \tag{4.8}$$

$$\overset{h\to 2}{\approx} -\arctan\left[\frac{(\mu^2-1)\sin(\bar{\varphi}) - 2\mu\cos(\bar{\varphi})}{(\mu^2-1)\cos(\bar{\varphi}) + 2\mu\sin(\bar{\varphi})}\right] + \frac{h-2}{1+\mu^2}\mu + 2\pi k \tag{4.9}$$

$$\overset{\mu\to 0}{\approx} -2\mu - \bar{\varphi} + \frac{h-2}{1+\mu^2}\mu + 2\pi k \tag{4.10}$$

with $k \in \mathbb{Z}$, see the red dots in Fig. 4.1 (b).

Note that for $h = 2$ the real part $\gamma$ does not depend on $\mu$ yielding a vertical, yet

[8]To be consistent with the notation in the rest of this thesis, we here use $\bar{\varphi}$ instead of $\varphi$ as it was done in the corresponding paper [98].

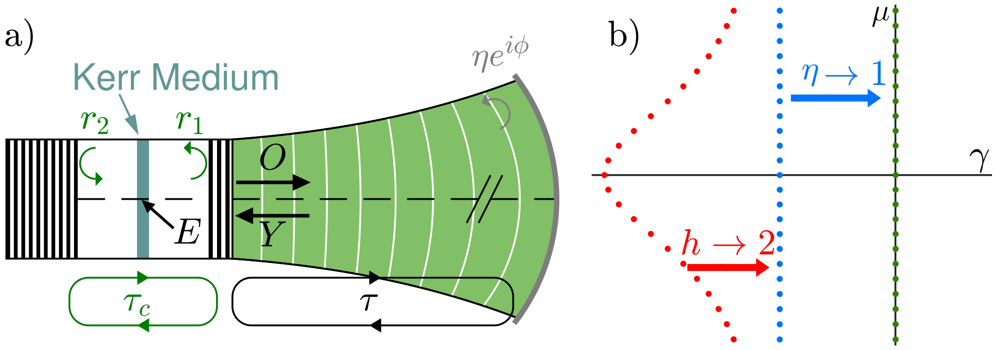


**Figure 4.1:** (a) Setup of the KGTI in absence of external injection, cf. Fig. 1.4. (b) The eigenvalue spectrum of defined in Eqs. (4.6) and (4.10) for different values of $h$ and $\eta$. For $h < 2$ and $\eta < 1$ (red dots) the spectrum resemble an inverted parabola. When $h \to 2$ (blue dots) it flattens as $\gamma = \ln \eta$. For $\eta \to 1$, the spectrum converges to the imaginary axis (green dots).

lossy, spectrum which is shifted from zero by $\ln \eta/\tau$ (blue dots). In the limit of a lossless cavity, where additionally $\eta \to 1$, $\lambda$ converges towards the unitary spectrum presented in green in Fig. 4.1 (b).

In itself, a unitary spectrum is rather surprising in the context of time-delayed systems since it implies the possibility to integrate backward in time without any difficulty. This statement is incompatible with the dynamics of the most widespread time-delayed systems that are based upon DDEs, cf. Eq. (2.1) for non-singular $M$. The so-called method of steps [101] shows that an initial condition $\phi(t)$ must be given over an interval of duration $\tau$ in order to perform the forward integration over a time $\tau$. Then, this newly propagated segment can be reused as a new initial condition in order to perform the next step. That is, if $\phi(t)$ is a $C^p$ function, integrating this function over $n$ steps results in a smoother $C^{p+n}$ profile. Conversely, a $C^p$ initial condition can only be integrated backward during $p$ steps before reaching a discontinuity. All the models based upon DDEs suffer from this difficulty, even in photonics where the latter are based upon the reversible Maxwell equations; the approximations made during their derivation set limits over their time-reversed evolution. We note however, that the delay algebraic models given by Eqs. (4.1),(4.2) or in [36, 55, 102, 103] do not suffer from this difficulty. This can be understood by combining Eq. (4.1) with itself evaluated at $t-\tau$ and using Eqs. (4.2) to eliminate the field $Y$. Noting $E_\tau = E(t-\tau)$, we obtain

$$E + \dot{E} - i\left|E\right|^2 E = \left(E_\tau - \dot{E}_\tau + i\left|E_\tau\right|^2 E_\tau\right) e^{i\bar{\varphi}}. \tag{4.11}$$

Equation (4.11) is a neutral delay differential equation (NDDE) (cf. Section 2.1), where both the delayed value of the field $E_\tau$ and its derivative $\dot{E}_\tau$ appear. Since the right hand side of Eq. (4.11) contains $\dot{E}_\tau$, at each step, the initial condition is both

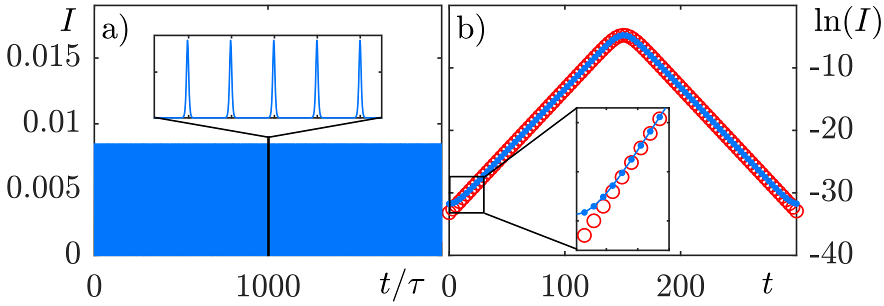


**Figure 4.2:** (a) Temporal trace obtained by integrating Eqs. (4.1,4.2) for $\tau = 300$. The period of the solution is $T = 301.5$ and the inset presents a zoom over five round-trips. The energy of the pulses is $\mu = 0.0063$. (b) Comparison between the intensity profile of a single pulse of (a) (blue dots) and the analytical solution of the NLS equation (red circles, Section 4.1) on a logarithmic scale. The only discrepancy can be seen at the interval boundaries (see inset).

derived and integrated. One understands intuitively that, at variance with DDEs, a $C^p$ initial condition remains $C^p$ and that forward and backward integration do not create asymmetry in the smoothness of the solution profile. Following Kamenskii's classification [101], Eq. (4.11) is an example of a bilateral NDDE; as it preserves its type under time inversion. The general theory of these equations appears to be rich and has not been fully developed yet. From Eq. (4.11), the associated linear evolution operator $\varphi_\tau$ propagating the field over a step reads

$$\varphi_\tau : E\left(t\right) = \left(1 + \frac{d}{dt}\right)^{-1} \left(1 - \frac{d}{dt}\right) e^{i\bar{\varphi}} E\left(t - \tau\right) \tag{4.12}$$

while the adjoint operator $\varphi_\tau^\dagger$ is defined as

$$\varphi_\tau^\dagger : W\left(t\right) = \left(1 - \frac{d}{dt}\right)^{-1} \left(1 + \frac{d}{dt}\right) e^{-i\bar{\varphi}} W\left(t + \tau\right). \tag{4.13}$$

Since $\varphi_\tau^\dagger \varphi_\tau = \mathrm{Id}$, $\varphi_\tau$ is a unitary operator, which explains the purely imaginary spectrum of Fig. 4.1 (b). Consequently, the inverse operator $\varphi_\tau^{-1}$, that corresponds to backward time integration, is $\varphi_\tau^{-1} = \varphi_\tau^\dagger$.

Remarkably, the nonlinear Eqs. (4.1) and (4.2) possess, in the long-delay limit $\tau \gg 1$, periodic orbits with period $T = \tau + \Delta$ and $\Delta > 0$ [82] that correspond to solitary wave trains, see Fig. 4.2(a). The temporal profile of a single pulse coincides extremely well, even on a logarithmic scale, with a hyperbolic secant, a typical solution of the nonlinear Schrödinger equation (NLS) over an infinite domain [104], see Fig. 4.2 (b). The small discrepancy at the tails is due to the fact that solitary solutions in time-delayed systems are periodic orbits, which imposes a smooth reconnection of the solution with itself. An identical discrepancy would be observed if the NLS equation was solved over a periodic domain.

The link between the NDDE (4.11) and the NLS equation can be clarified by performing a multi-scale analysis up to third order or using the functional mapping method, cf. Sections 2.3.1 and 2.3.2. We introduce the two-time representation by defining $z \in [0, \tau]$ and $\xi \in \mathbb{N}$ so that time can be expressed as $t[z, \xi] = z + \xi\tau$. Assuming a field with carrier frequency[9] $\omega_0$, we can transform Eqs. (4.1) and (4.2) into the reference frame of $\omega_0$ and introduce the detuning $\delta = \omega_c - \omega_0$ by using the ansatz $E(t) = A(t)\exp(i\delta t)$. Then one obtains the following amplitude equation (for details on the derivation, see Appendix B.2)

$$i\left(\partial_\xi + \upsilon\partial_z\right)A + \tilde{\varphi}A - \frac{\beta_2}{2}\partial_z^2 A - i\frac{\beta_3}{6}\partial_z^3 A + \gamma\left|A\right|^2 A = 0, \tag{4.14}$$

that is, the NLS equation with third-order dispersion with $\upsilon = 2/\left(1+\delta^2\right)$, $\beta_2 = 4\delta/\left(1+\delta^2\right)^2$, $\beta_3 = 4\left(3\delta^2-1\right)/\left(1+\delta^2\right)^3$ and $\gamma = 2/\left(1+\delta^2\right)$. The effective round-trip phase is $\tilde{\varphi} = \bar{\varphi} - \delta\tau - 2\arctan(\delta) = \varphi - 2\arctan(\delta) \mod (2\pi)$. The second order dispersion coefficient $\beta_2$ cancels at resonance $\delta = 0$, which corresponds to the transition from anomalous to normal dispersion while third-order dispersion $\beta_3$ vanishes for $\delta = \pm\delta_c$ where $\delta_c = 1/\sqrt{3}$. In this case Eq. (4.14) is equivalent to the classical NLS equation up to fourth order. In the anomalous dispersion regime where $\delta = -\delta_c$, $\beta_2 < 0$, $\gamma > 0$ and $\beta_3 = 0$, we obtain the bright hyperbolic secant solitons [104]. The latter can be expressed as a one-parametric family

$$A(z, \xi; \mu) \quad = \quad \sqrt{\frac{2\mu}{\gamma}}\frac{\exp\left[i\left(\mu+\tilde{\varphi}\right)\xi\right]}{\cosh\left[\sqrt{\frac{2\mu}{|\beta_2|}}\left(z-\upsilon\xi\right)\right]}, \tag{4.15}$$

where we defined $\mu$ as the soliton energy, which together with the effective round-trip phase $\tilde{\varphi}$ contributes to the soliton frequency shift. The expression in Eq. (4.15) was given as an initial condition with parameters $(\mu, \varphi) = (0.005, 0)$, times a carrier frequency $\exp(-i\delta_c z)$, to the periodic orbit solver of `DDE-BIFTOOL` [105] which resulted in the exact periodic orbit shown in Fig. 4.2. The superposition in Fig. 4.2(b) using Eq. (4.15) was obtained without fit.

The existence of a unitary, hence reversible, differential operator for small amplitude solutions as well as the normal form (4.14) leading to the NLS equation indicates that Eq. (4.11) may possess a more general symmetry. In particular, one observes that Eq. (4.11) relates the field one step in the future $E_+(t)$ to the initial condition $\phi(t)$ as

$$E_+ + \dot{E}_+ - i\left|E_+\right|^2 E_+ \quad = \quad \left(\phi - \dot{\phi} + i\left|\phi\right|^2\phi\right)e^{i\bar{\varphi}}. \tag{4.16}$$

[9]In the corresponding paper, the carrier frequency was denoted with $\delta$.

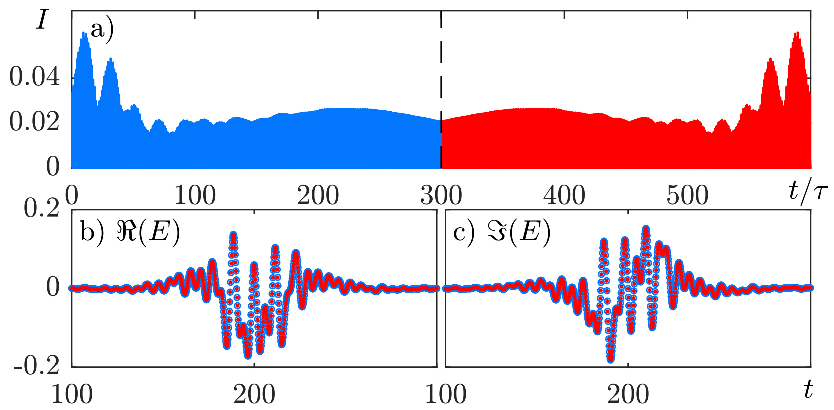


**Figure 4.3:** Numerical simulation showing the reversibility of Eq. (4.11). An asymmetric initial condition (blue circles in (b),(c)) is propagated 300 steps (blue part). Next, at the black dashed line in (a), the operator $R$ is applied. After 300 steps (red part), the final profile shown in (b),(c) with red dots perfectly matches the initial condition after applying $R$ a second time.

Exchanging the left and right hand sides of Eq. (4.11) defines the field one step in the past $E_-$ as

$$E_- - \dot{E}_- + i\,|E_-|^2\,E_- \quad = \quad \left(\phi + \dot{\phi} - i\,|\phi|^2\,\phi\right) e^{-i\bar{\varphi}}. \tag{4.17}$$

Following [106], we denote the nonlinear evolution operator over a step as $\Phi_\tau$ and the mirror-conjugating involution $R$ defined as $R\,[E\,(t)] = E^*\,(-t)$. Reversibility is demonstrated since $R \circ \Phi_\tau \circ R^{-1} = \Phi_{-\tau}$, i.e., performing one step backward in time with the initial condition $\phi\,(t)$ is equivalent to one step forward for another initial condition $\phi^*\,(-t)$ while mirror-conjugating the end result, i.e., $E_+\,(t) = E_-^*\,(-t)$. A demonstration of this property is depicted in Fig. 4.3(a). Starting from a complex, non-solitonic initial condition, we integrate Eq. (4.11) forward 300 steps, see Fig. 4.3(a). Then the operator $R$ is applied to the resulting field profile. Further forward integration over 300 steps followed by the application of $R^{-1} = R$ leads to the perfect superposition with the initial condition shown in Fig. 4.3(b,c). We note that the mirror-conjugate symmetry is present in the NLS equation (4.14); it consists in setting $A\,(z,\xi) \to A^*\,(-z,-\xi)$. While NLS is only an approximation of Eq. (4.11), the time reversal symmetry of Eq. (4.11) is an exact property.

The higher-order terms, that were neglected in deriving Eq. (4.14), scale as $\mathcal{O}\,(\mu^2)$. Hence, Eq. (4.11) is only integrable for sufficiently small amplitude and smooth solutions. In this case, we launched two solitons of equal amplitudes but slightly different carrier frequencies; this leads to different drift velocities thereby allowing for collisions. We notice that the in-phase Fig. 4.4(a,b) and the anti-phase Fig. 4.4(c,d) solitons re-

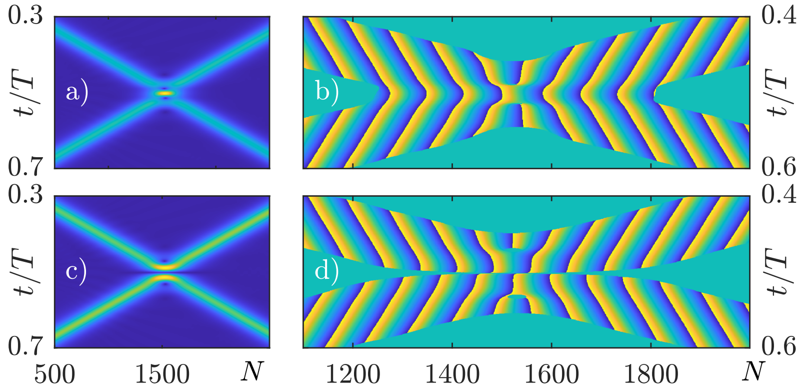


**Figure 4.4:** Two-time representation of two colliding solitons of Eqs. (4.1,4.2) in-phase (a,b) and anti-phase (c,d) as a function of the round-trip number $N$. Panels (a) and (c) show the absolute value of the profile while (b) and (d) show their phase. Each pulse has an energy of $\mu = 0.005$ and $\delta_{1,2} = -\delta_c \pm 0.1$ while $\varphi = 1.95$. The mean carrier frequency $e^{-i\delta_c t}$ was factored out for clarity in (b,d).

produce exactly the elastic behavior expected from an integrable equation [104].

We finally turn our attention to the existence of conserved quantities. For this, we remember that we can split the time $t$ into a slow and fast component such that $t = z + \xi\tau$ where $z \in [0, \tau]$ and $\xi \in \mathbb{N}$. With that, we can define $E_\xi(z)$ as

$$E_\xi(z) = E(z + \xi\tau) = E(t) \tag{4.18}$$

$$\text{where } E_\xi(\tau) = E_{\xi+1}(0)\,. \tag{4.19}$$

Next, we transform Eqs. (4.1) and (4.2) into equations for intensities. For Eq. (4.1), we obtain

$$\frac{\partial I_\xi}{\partial z} = \frac{\partial\left(E_\xi E_\xi^*\right)}{\partial z} = E_\xi^* \frac{\partial E_\xi}{\partial z} + E_\xi \frac{\partial E_\xi^*}{\partial z} \tag{4.20}$$

$$= E_\xi^*\left[\left(-1 + iI_\xi\right)E_\xi + 2Y_\xi\right] + E_\xi\left[-\left(1 + iI_\xi\right)E_\xi^* + 2Y_\xi^*\right] \tag{4.21}$$

$$= -2I_\xi + 4\Re\left(Y_\xi E_\xi^*\right). \tag{4.22}$$

Analogously, we yield for Eq. (4.2)

$$|Y_\xi|^2 = \left(E_{\xi-1} - Y_{\xi-1}\right)\left(E_{\xi-1}^* - Y_{\xi-1}^*\right) \tag{4.23}$$

$$= I_{\xi-1} + |Y_{\xi-1}|^2 - 2\Re\left(Y_{\xi-1}E_{\xi-1}^*\right). \tag{4.24}$$

Next, we combine Eqs. (4.22) and (4.24) to obtain

$$\frac{\partial I_{\xi-1}}{\partial z} = -2\,|Y_\xi|^2 + 2\,|Y_{\xi-1}|^2\,. \tag{4.25}$$

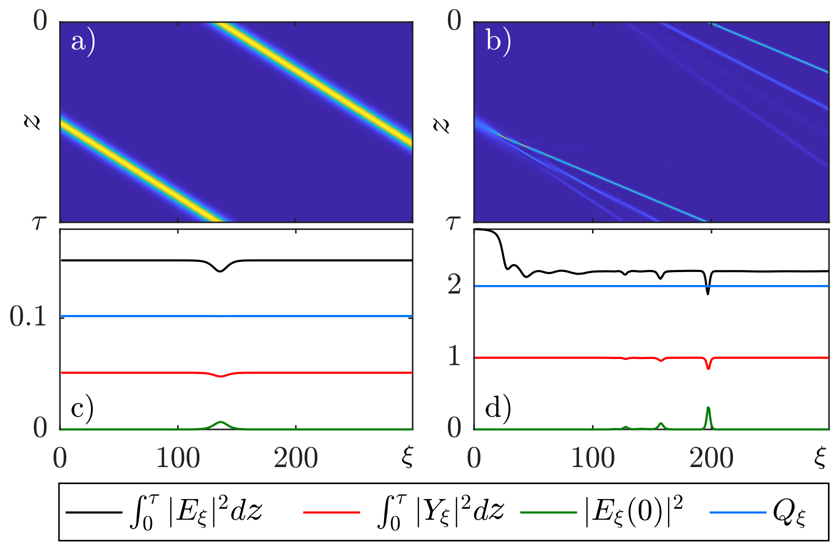


**Figure 4.5:** (a),(b) Evolution of Eqs. (4.1) and (4.2) for different initial conditions. Note that the folding factor for these plots is $\tau$, instead of $T$ as in Fig. (4.4), leading to the drift of the soliton. The initial conditions are (a) a hyperbolic secant (4.15) with $\mu = 0.005$ and (b) a condition which is far away from a steady state. (c),(d) Evolution of different measures to visualize the conservation properties[10]. In (c) all quantities are conserved unless the pulse reaches the edge of the cavity. Then only $Q_\xi$ is conserved. (d) The norm $\int_0^\tau |E_\xi|^2 dz$ is not conserved and $\int_0^\tau |Y_\xi|^2 dz$ as well as $|E_\xi(0)|^2$ show the same imperfections when a soliton exits the cavity. However, $Q_\xi$ is conserved.

We integrate this equation over the length of one delay

$$\int_0^\tau \frac{\partial I_{\xi-1}}{\partial z} dz = I_{\xi-1}(\tau) - I_{\xi-1}(0) \overset{(4.19)}{=} I_\xi(0) - I_{\xi-1}(0) \tag{4.26}$$

$$= -2\int_0^\tau |Y_\xi|^2 dz + 2\int_0^\tau |Y_{\xi-1}|^2 dz \tag{4.27}$$

$$\Leftrightarrow 2\int_0^\tau |Y_\xi|^2 dz + I_\xi(0) = 2\int_0^\tau |Y_{\xi-1}|^2 dz + I_{\xi-1}(0)\,. \tag{4.28}$$

Equation (4.28) defines the discrete conserved quantity $Q_\xi$ at each round-trip as

$$Q_\xi = 2\int_0^\tau |Y_\xi(z)|^2 dz + |E_\xi(0)|^2\,. \tag{4.29}$$

We interpret $Q_\xi$ as the soliton mass that contains the integral of the field intensity in the external cavity $|Y_\xi|^2$, while $|E_\xi(0)|^2$ is the intra-cavity field value. When the cavity snapshot is taken at a particular step $\xi$, the pulse energy can either reside in the external cavity and be contained in the $Y$ field, but it can also lay within the micro-cavity field $E$. We clarify the role of the conserved quantity in Fig. (4.5). The left panels (a,c) depict the smooth evolution of a single soliton in the $(z,\xi)$ representation. We notice that the nominal soliton mass in NLS $q_\xi = \int^\tau |E_\xi|^2 dz$ (black) is conserved up to the point where the soliton exits at $z = \tau$ and reenters at $z = 0$ at round-trip $\xi \simeq 130$.

We notice that $\int^{\tau} |Y_\xi|^2 \, dz$ also shows a downward kink, however, as $|E_\xi(0)|^2$ has an opposed spike, $Q_\xi$ is conserved. For a more complex initial condition with higher energy, one can observe a quick decomposition into multiple spikes after $\xi \simeq 40$ steps, cf. Fig. 4.5(b). Here, and even if the field remains well-localized within the time delay until $\xi \simeq 120$ one already notices that $Q_\xi$ is not conserved anymore, cf. Fig. 4.5(d). This high amplitude transient with fast temporal variations breaks the multi-scale analysis leading to Eq. (4.14) and the high order terms like, e.g., self-steepening, result in a non-integrable normal form. Yet, $Q_\xi$ still remains conserved in this case, too.

### 4.1.1. Towards Dissipative Dynamics

Finally, we perform the link between Eqs. (4.1),(4.2) and another paradigm of dissipative pattern formation that is the Lugiato–Lefever equation [58, 66]. The latter can be understood as a weakly dissipative version of the NLS equation in which the phase symmetry is broken by the presence of monochromatic injection with amplitude $Y_0$ and frequency offset $\delta$ with respect to the micro-cavity resonance. In order to introduce this forcing, the external cavity should be open and one has to simultaneously introduce cavity losses by setting $\eta < 1$. This amounts to adding to the right hand side of Eq. (4.2) a term[11] $Y_0\sqrt{1-\eta^2}e^{i\delta t}$, cf. Table 3.1. A similar multi-scale analysis performed for small cavity losses, small phases and weak injection (cf. Appendix B.2 for details) yields the Lugiato–Lefever equation with third-order dispersion

$$\left(i\partial_\xi + \varphi + iv\partial_z - \frac{\beta_2}{2}\partial_z^2 - i\frac{\beta_3}{6}\partial_z^3 + \gamma |A|^2\right) A = F(A), \tag{4.30}$$

where $F(A) = i(\eta - 1)A + iY_0\sqrt{8(1-\eta)/(1+\delta^2)}$ contains both the effects of losses and injection. Note that here, the fields are rescaled such that the injection has a real coefficient. The limit in which Eq. (4.30) is valid, is studied in more detail in Section 4.5 in the case of normal dispersion where $\delta > 0$. The case of anomalous dispersion is analyzed in details in [107].

[10] In the corresponding paper [98] there was a misplaced factor of 2 for the red line.
[11] The term $e^{i\delta t}$ is missing in the corresponding paper [98].

## 4.2. Steady States of the Injected Kerr–Gires–Tournois Interferometer

After the excursion to conservative systems in the previous section, we turn our attention to the dissipative case. We begin with analyzing the steady states of the KGTI system defined by Eqs. (3.83) and (3.84) – the so-called continous wave (CW) solutions. First, in Section 4.2.1, we provide an analytical solution of the CW branch as a function of the injection parameter $Y_0$. Then, in Section 4.2.2, we consider input-output relations for the different parts of the KGTI in order to describe its cavity response. In Section 4.2.3, we analyze the CW solution in multi-parameter spaces. Next, we analyze the linear stability of the system. First, in Section 4.2.4 possible instabilities are categorized giving insight to what kind of periodic solutions can be expected. Next, in Section 4.2.5, we compute analytically the pseudo-continuous spectrum of eigenvalues of the CW state in the long-delay limit following the approach described in Section 2.2 and discuss the possible frequencies of emerging period solutions. Finally, in Section 4.2.6, we connect the different parts of this section in order to create a stability map that summarizes the CW states and their stability in a single diagram.

### 4.2.1. Continuous-Wave Branch

We begin with calculating the steady states $E_s$ and $Y_s$ of the system in Eqs. (3.83) and (3.84). This can be done analytically by first solving Eq. (3.83) for $Y_s$

$$Y_s = -\frac{1}{h}\left[-1 + i\left(I_s - \delta\right)\right] E_s, \tag{4.31}$$

where $I_s = |E_s|^2$ is the steady state intensity. Then we plug the result into Eq. (3.84) which the can be solved for $Y_0$. Taking the modulus square yields

$$Y_0^2 = \frac{1}{h^2}\frac{\left|1+\eta e^{i\varphi}\right|^2}{1-\eta^2}\left|\frac{1-(h-1)\,\eta e^{i\varphi}}{1+\eta e^{i\varphi}} - i\left(I_s - \delta\right)\right|^2 I_s. \tag{4.32}$$

This is an implicit equation for the CW intensity, however, it is an explicit expression for the injection as a function of the CW intensity. Importantly, Eq. (4.32) contains a cubic nonlinearity in the intensity. This leads to the possibility of a bistable response, i.e., for a certain injection value, there exists multiple CW states. If bistability exists depends on the other system parameters. In particular, one can find critical values for the parameters at which the onset of bistability occurs. For instance, one can set fixed values of $\eta$, $\varphi$ and $h$ to find a critical detuning $\delta_c$ and injection $Y_0^c$. This is shown in Fig. 4.6 where three exemplary CW branches are shown for detunings below, at and above the critical value. Mathematically, the point $(\delta_c, Y_0^c)$ corresponds to a cusp

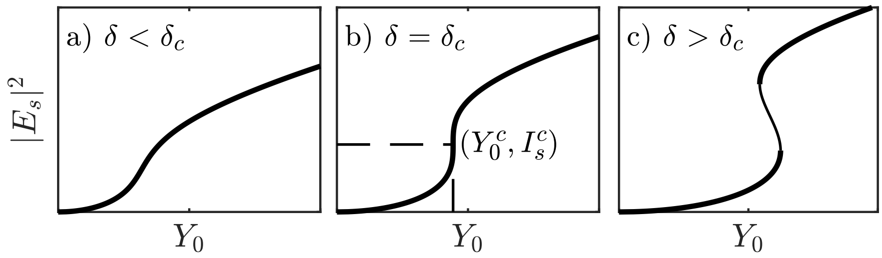


**Figure 4.6:** Branch of the CW solution represented by the constant microcavity field intensity $I_s = |E_s|^2$ as a function of the injection amplitude $Y_0$ for the detuning values below (a), at (b) and above (c) the onset of the optical bistability located at ($Y_0^c$, $I_s^c$). Stable (unstable) solutions are indicated with thick (thin) lines. Adapted from [99].

bifurcation. More details on how to compute the critical parameter values and the unfolding of CW solution are provided in Section 4.2.3. Further, in Section 4.3, the onset of bistability is used as an expansion point for a normal form.

### 4.2.2. Cavity Response

Another way to analyze the steady states is to consider the response curve of the system, i.e., to compute the output $O_s = E_s - Y_s$ of the KGTI system in Eqs. (3.83) and (3.84) for a given input $Y_0$. For that, we define an effective detuning $\theta = \delta - I_s$ such that we obtain from Eq. (3.83)

$$E_s = \frac{hY_s}{1 + i\theta}. \tag{4.33}$$

Plugging this in Eq. (3.84) yields

$$Y_s = \eta e^{i\varphi} \frac{h - 1 - i\theta}{1 + i\theta} Y_s + \sqrt{1 - \eta^2} Y_0, \tag{4.34}$$

which in the GTI limit, where $h = 2$, simplifies to

$$Y_s = \frac{\sqrt{1 - \eta^2} Y_0}{1 - \eta e^{i(\varphi - 2 \arctan \theta)}}. \tag{4.35}$$

Here, we used that $\frac{1-i\theta}{1+i\theta} = e^{-i2 \arctan \theta}$. As a side note, we want to mention, that one can use Eqs. (4.32), (4.33) and (4.35) to calculate the injection as well as explicitly $E_s$ and $Y_s$ for a given intensity value $I_s$ which can be useful when, e.g., searching an initial guess for a continuation. Finally, we can compute the cavity output

$$O_s = E_s - Y_s \overset{(4.33)}{=} e^{-2i \arctan \theta} Y_s \overset{(4.35)}{=} e^{-2i \arctan \theta} \frac{\sqrt{1 - \eta^2} Y_0}{1 - \eta e^{i(\varphi - 2 \arctan \theta)}}. \tag{4.36}$$

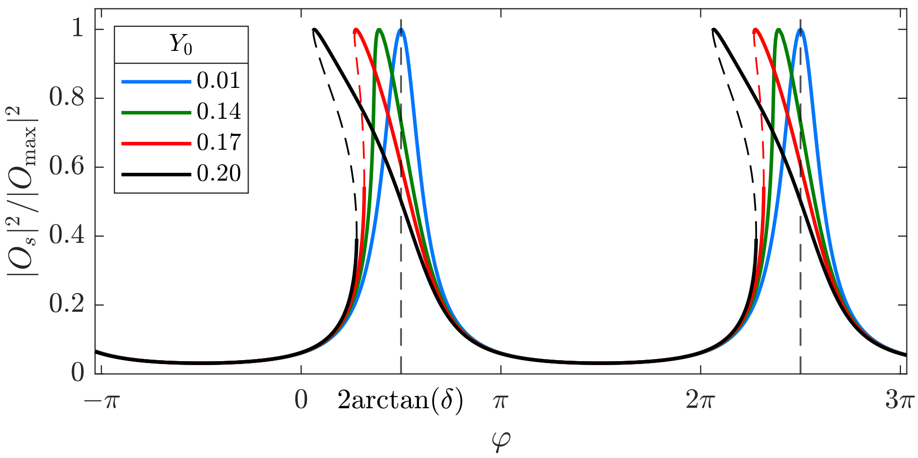


**Figure 4.7:** The response curve in $\varphi$ for different injection values. Other parameters are $(h, \eta, \delta) = (2, 0.7, 1)$. The response becomes more nonlinear for increasing injection. Solid thick and dashed thin lines correspond to stable and unstable solutions, respectively.

For the intensity, we take the modulus square and obtain

$$|O_s|^2 = \frac{(1-\eta^2)\, Y_0^2}{\left|1 - \eta e^{i(\varphi - 2\arctan\theta)}\right|^2}. \tag{4.37}$$

Equation (4.37 defines the input-output relation of the KGTI system and corresponds to the Airy distribution of the optical resonators. In particular, we can see that the transmission coefficient $|T| = 1 - \eta^2$ and the reflection coefficient $|R| = \eta^2$ fulfill $|R| + |T| = 1$. For small injection values, the output is also small such that $I_s$ vanishes and the effective detuning $\theta$ is just the detuning $\delta$. Hence, understanding the right-hand-side of Eq. (4.37) as a function of the phase $\varphi$, it is a resonance curve centered around $\varphi = 2\arctan\delta$, see blue curve centered around the vertical black dashed line in Fig. 4.7. Due to the periodicity in the phase parameter $\varphi$, the resonance reappears for $\varphi = 2\arctan\delta + 2\pi k, k \in \mathbb{Z}$. However, increasing the injection leads to contributions of $I_s$ to the effective detuning resulting in nonlinear response curve (see green, red, black in Fig. 4.7), i.e., close to the resonance, the intensity contribution towards the effective detuning become relevant such that the response curve slants. However, the base of the resonance curve is still centered around $2\arctan\delta$. Note, that in Fig. 4.7, the output intensity is normalized with respect to its maximum such that the curves for different injection values become easily comparable. On the other hand, one can also consider a resonance curve in the detuning $\delta$. This curve is centered around $\delta = \tan\left(\frac{\varphi}{2}\right)$, cf. Fig. 4.8.

Here, it is important to mention a difference in how the nonlinearity effects the sys-

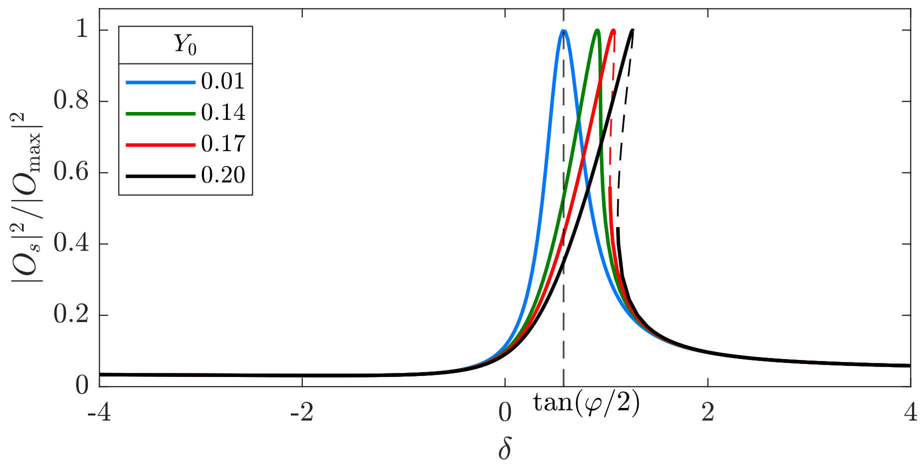


**Figure 4.8:** The response curve in $\delta$ for different injection values. Other parameters are $(h, \eta, \varphi) = (2, 0.7, \pi/3)$. The response gets more and more nonlinear for increasing injection. Solid thick and dashed thin lines correspond to stable and unstable solutions, respectively.

tem in the KGTI compared to the Ikeda map, where the additional phase contribution is directly proportional to the intensity [108]. This allows – when considering larger intensities – the tilted cavity resonance to eventually overlap with the adjacent one which creates multi-stability between multiple solitonic regimes and allows for the formation of "super cavity solitons"[67]. We note, that this aspect is not captured by the LLE as it is derived for weak injections and an overall cavity detuning that remains small during propagation.

In our case, however, the nonlinearity is embedded in the arctangent which is asymptotic to $\pm\frac{\pi}{2}$ for large positve/negative arguments. Considering the factor of 2 in front of the arctangent reveals that the resonance curve can extend maximally to a value of $-\pi$ for large nonlinearities and to $\pi$ for large detuning and therefore can never overlap, which prevents the aforementioned coexistence of more than two stable solutions. This property is visualized in Fig. 4.9 (a),(b). In Fig. 4.9 (a), we show the same response curves as in Fig. 4.7 in addition to one for a very large injection value (yellow). Due to the strong nonlinear contribution of the intensity towards the effective detuning $\theta$ this curve converges towards $-\pi$. Further, Fig. 4.9 (b) shows a response curve for a large detuning $\delta$. While the base of the response curve is centered around $\varphi = 2 \arctan \delta \approx 0.97\pi$ for $\delta = 20$, the upper part of the resonance curve converges towards $-\pi$ such that there is no overlap between neighboring resonance curves. Finally, there exists an interesting intermediate regime, see Fig. 4.9 (c). Here, for lower injection values (blue), the resonance curves is split into multiple branches such that an isola is formed. Increasing the injection (orange, yellow), the isola reconnects with

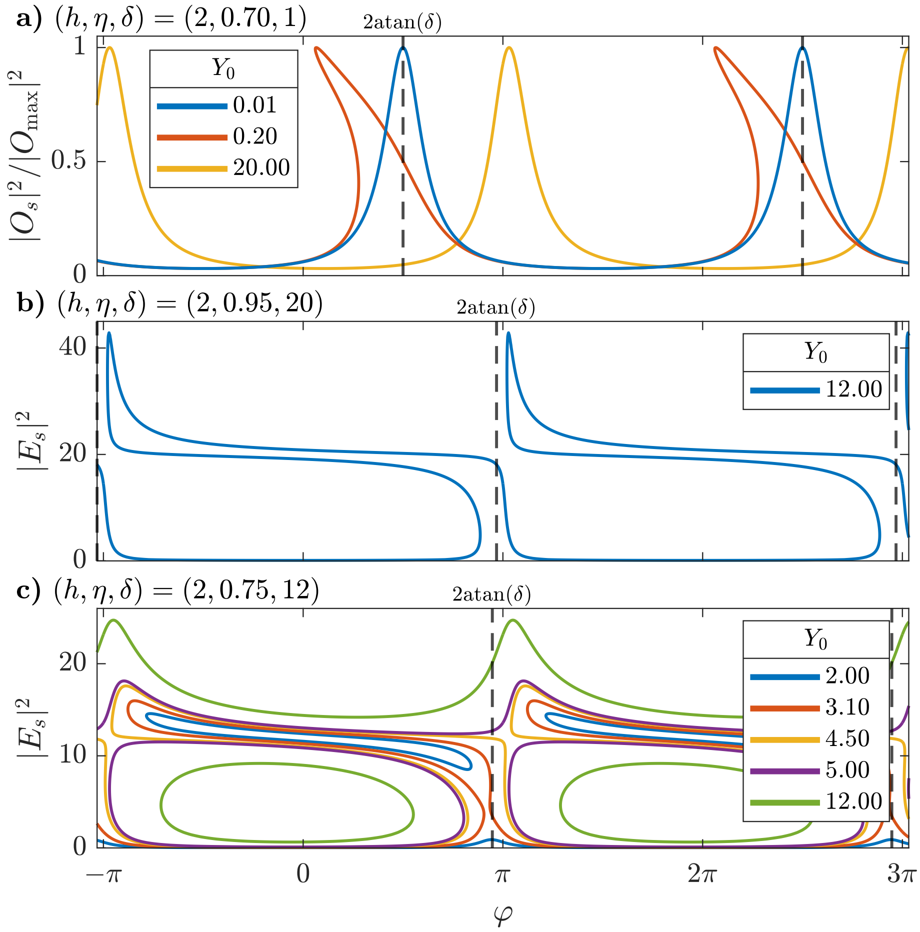


**Figure 4.9:** The response curve in $\varphi$ for several extreme cases (where the stability is omitted for clarity). (a) Towards very large injections $Y_0$, where the effective detuning $\theta$ is dominated by the high intensity. (b) Large detuning $\delta$ and large injection $Y_0$ showing that overlap between neighboring resonance curves cannot be achieved. (c) Large detuning and various injections values showing that the resonance curve can split into multiple branches.

the base of the curve forming a single branch. Eventually, for even larger injections (purple, green), neighboring curves recombine in a transcritical bifurcation (cf. yellow and purple curves close to $\varphi = \pi$), which results again in separated branches.

### 4.2.3. Multi-Parameter Study of the Steady State Solution

While in the previous two subsections, we studied the steady state solution under the influence of a single control parameter, it can be instructive to consider higher dimensional parameter spaces to quickly obtain an overview over possible regimes. Our starting point is the analytical expression of the CW solution in Eq. (4.32). First, we calculate the position of the folds in the bistable regime which correspond to extrema of Eq. (4.32). For that, we differentiate Eq. (4.32) with respect to $I_s$ and find the critical values $I_{s,\pm}$ for which $\frac{dY_0^2}{I_s}|_{I_s=I_{s,\pm}} = 0$. The resulting expressions are lengthy and unintuitive and were therefore obtained using the computer algebra program `Mathematica` [109]:

$$\begin{aligned}
I_{s,\pm} =& \frac{-b \pm \sqrt{b^2-4ac}}{2a}. && (4.38)\\
\text{where}\quad a =& \delta^2+\eta^2\left(\delta^2+(h-1)^2\right)+2\eta\left(\delta^2-h+1\right)\cos(\varphi)-2\delta h\eta\sin(\varphi)+1,\\
b =& 4h\eta\sin(\varphi)-4\delta\left(1+\eta^2+2\eta\cos(\varphi)\right),\\
c =& 3\left(1+\eta^2+2\eta\cos(\varphi)\right).
\end{aligned}$$

The injection at the folds is then defined as

$$Y_\pm = Y_0\left(I_{s,\pm},\delta,\eta,\varphi,h\right). \tag{4.39}$$

With this equation, one can analytically compute the position of the folds of the steady state in different two parameter diagrams. This is shown in Fig. 4.10 (a)–(c) for the $(Y_0,\delta)$-, $(Y_0,\eta)$- and $(Y_0,\varphi)$-planes, respectively. Going one step further, we can analytically compute the cusp points $I_s^c$ as the point where the $I_{s,\pm}$ coincide, i.e., $b^2-4ac=0$ in Eq. (4.38). We obtain the following critical value for the detuning

$$\delta_c = \frac{\sqrt{3}\left(1-(1-h)\eta^2\right)+h\eta\sin(\varphi)-\sqrt{3}(h-2)\eta\cos(\varphi)}{1+2\eta\cos(\varphi)+\eta^2}. \tag{4.40}$$

An exemplary CW branch for a critical detuning was shown in Fig. 4.6 (b). Further, Eq. (4.40) allows us to analytically compute the cusp points in Fig. 4.10, which are highlighted by red circles, crosses and triangles. The critical values $\eta_c$ and $\varphi_c$ can be obtained by solving Eq. (4.40) for $\eta$ and $\varphi$, respectively.

Next, we can analyze how the cusp points evolve in an additional control parameter. We consider, e.g., Fig. 4.10 (c) for different values of $\delta$ and follow the cusps marked by the red crosses. The result of this is shown in Fig. 4.11 (a) where Fig. 4.10 (c) is marked by a horizontal black dashed line. Analogously, we can visualize the cusp lines in the $(\varphi,\eta)$- and $(\eta,\delta)$-planes, cf. Fig. 4.11 (b),(c).

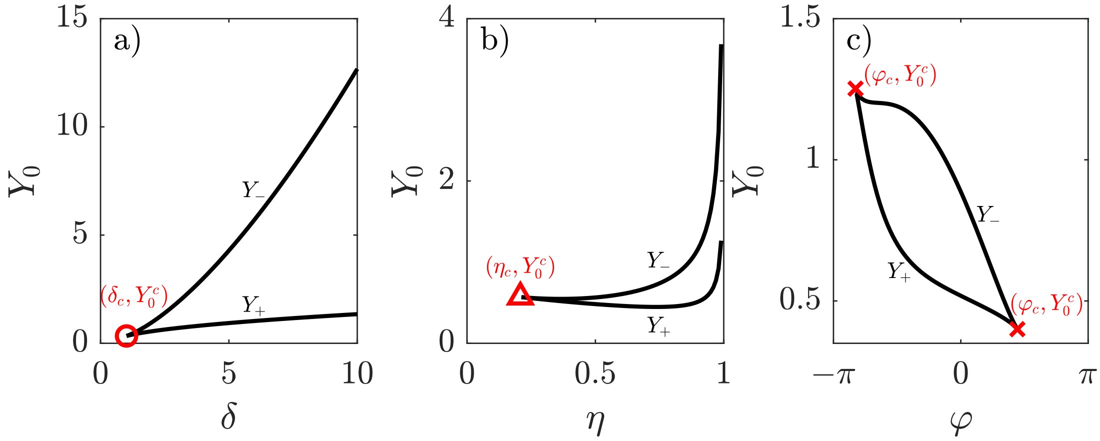


**Figure 4.10:** Two-parameter bifurcation diagrams of the folds (black) of the steady state computed from Eq. (4.39) in different two-parameter spaces. Each point on the lines corresponds to a fold. The cusp point is marked by a red circle, triangle, cross in panels (a), (b), (c), respectively, and is calculated from Eq. (4.40). Other parameters $(h, \eta, \delta, \varphi) = (1.7, 0.6, 1.5, \pi/4)$.

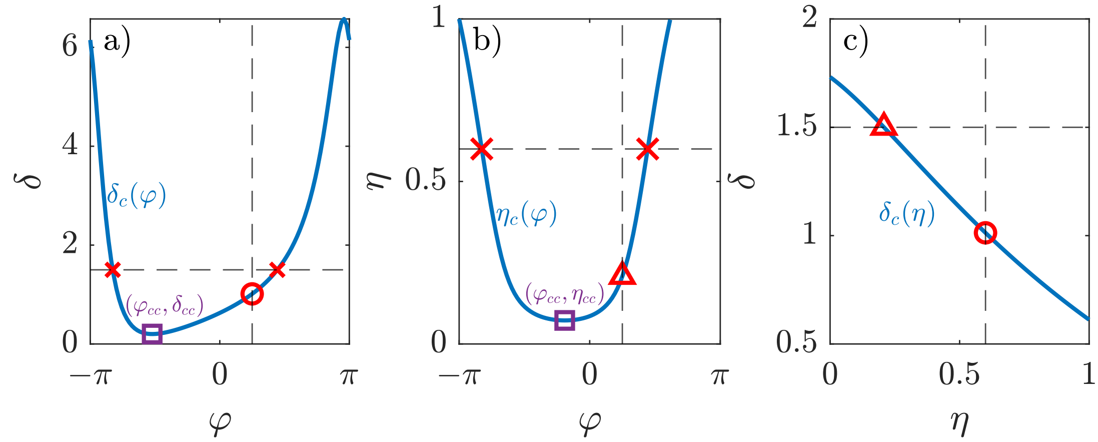


**Figure 4.11:** Cusp lines (blue) in the three-parameter spaces $(Y_0, \varphi, \delta)$, $(Y_0, \varphi, \eta)$ and $(Y_0, \eta, \delta)$ projected onto two dimensions for better readability. The cusp lines are calculated using Eq. (4.40). The black dashed lines and red markers correspond to the two-parameter diagrams and the according cusps in Fig. 4.10. The purple squares in (a) & (b) represent the critical points $(\varphi_{cc}, \delta_{cc})$ and $(\varphi_{cc}, \eta_{cc})$, respectively, defined by Eq. (4.41).

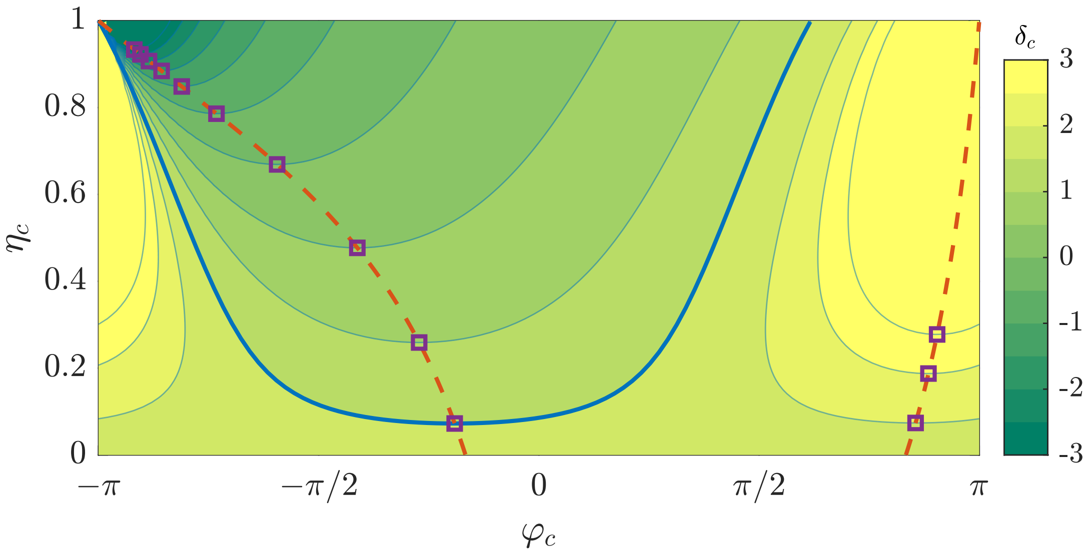


**Figure 4.12:** The critical detuning $\delta_c$ in the $(\eta, \varphi)$-plane calculated from Eq. (4.40) for $h = 1.7$. The thick blue contour line corresponds to Fig. 4.11 (b). The red dashed line connect the extrema of the contour lines marked by purple squares, i.e., it represents the onset of the cusp according to Eq. (4.41).

Here, we note other critical points, which are the extrema of the cusp lines marked by purple squares in Fig. 4.11. These mark the critical points $(\varphi_{cc}, \delta_{cc})$ and $(\varphi_{cc}, \eta_{cc})$ for which the two cusps coincide. This means, that, e.g., in Fig. 4.11 (b), there are no folds for $\eta < \eta_{cc}$ for any phase $\varphi$ in a $(Y_0, |E|^2)$-diagram. The points, where the cusps coincide, can be calculated analytically. For this, we compute for the extrema of Eq. (4.40) with respect to $\varphi$:

$$\delta_{cc} = \frac{\sqrt{3}(2-h)}{2} - \frac{h}{2}\cot(\varphi) \quad \Leftrightarrow \quad \varphi_{cc} = \operatorname{acot}\left(\frac{\sqrt{3}(2-h) - 2\delta}{h}\right). \tag{4.41}$$

In the next step, we can follow the cusp lines in another parameter. For that, we consider Fig. 4.11 (b) for different values of $\delta$. The result is shown in Fig. 4.12, where the color now encodes $\delta_c$. Each point in this diagram stands for a cusp point with coordinates $(\varphi_c, \eta_c, \delta_c, Y_0^c)$, where $Y_0^c = Y_0(\delta_c, \eta_c, \varphi_c, h)$. Consequently, the contour lines of the colormap correspond to the cusp lines. The cusp line from Fig. 4.11 (b) is plotted in thick blue as a reference. Further, for each contour line we can compute the critical point $(\varphi_{cc}, \eta_{cc})$ using Eq. (4.41). These points are plotted as purple squares in Fig. 4.12. The red dashed line connecting them shows the critical points in between the displayed contour lines.

Finally, Eq. (4.41) defines two surfaces in the $(\delta, \eta, h)$-space on which the cusps emerge. The two surfaces stem from the two solutions when solving the quadratic

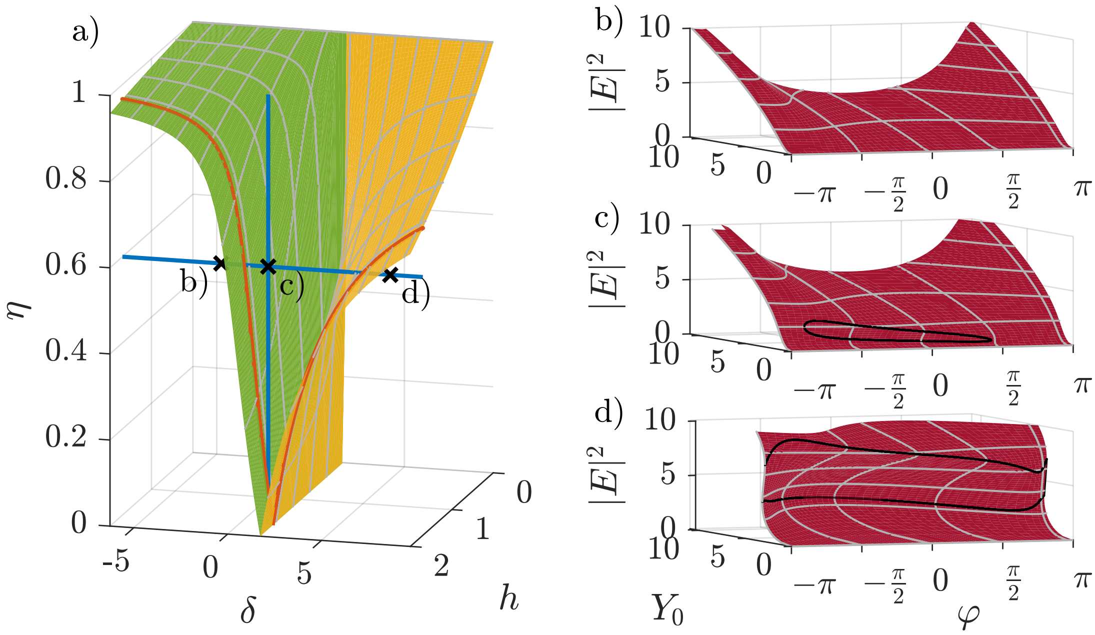


**Figure 4.13:** The surfaces represent the onset of the cusp in the three-parameter space $(h, \delta, \eta)$ according to Eq. (4.41). The blue horizontal and vertical line mark the positions for which Fig. 4.11 (a) and (b) are shown, respectively. The red line is the same as in Fig. 4.12. Each point in this space corresponds to a $(\varphi, Y_0)$-bifurcation diagram. Three exemplary points are marked along the horizontal blue line and the corresponding $(\varphi, Y_0)$-diagrams are shown in panels (b)–(d) for $\delta = (-1, 1.5, 8)$.

equation 4.40 for $\eta$. They are shown in Fig. 4.13 (a). The blue lines are cuts along $\delta$ and $\eta$, respectively, and hence, mark the positions for which the cusp lines in Fig. 4.11 (a) and (b) are shown. Further, the red line along the surfaces corresponds to the red dashed line in Fig. 4.12. The two surfaces meet at $\delta = \sqrt{3}$, where we find $\eta_c = 0 \; \forall h, \varphi$.

Each point in this space of Fig. 4.13 (a) corresponds to a two-parameter bifurcation diagram in the $(Y_0, \varphi)$-plane. Three exemplary points are marked along the horizontal blue line and the corresponding steady state planes are shown in panels (b)–(d). There, the black lines mark the folds of the steady states derived from Eq. (4.38). Note, that Fig. 4.13 (c) is for the same parameters as Fig. 4.10 (c). Further, we note, that the projection of Fig. 4.13 (b) onto the $(Y_0, \varphi)$-plane is empty as no folds of the steady state are present. On the other hand, in Fig. 4.13 (d), there are folds in $Y_0$ for any $\varphi$. This allows us to separate the $(\delta, \eta, h)$-space in Fig. 4.13 (a) in three different sections:

- To the left of the green surface, no folds are present on the CW branch in the $(Y_0, |E|^2)$-diagram for any $\varphi$, cf. Fig. 4.13 (b).
- Between the surfaces, there are folds in $Y_0$ for some $\varphi$, cf. Fig. 4.13 (c).
- To the right of the yellow surface, there are folds in $Y_0$ for any $\varphi$, cf. Fig. 4.13 (d).

### 4.2.4. Instabilities of Steady State Solutions

The branches of the pseudo-continuous spectrum of eigenvalues defined in Section 2.2.1 reveal the fundamental dynamics of emerging patterns as they indicate which frequencies are stable and unstable, respectively. This shows a fundamental similarity between delayed systems in the long-delay limit and spatially extended systems, where the stability is governed by the dispersion relation. Before explicitly calculating the pseudo-continuous spectrum of eigenvalues for the KGTI in Section 4.2.5, here, we focus on different fundamental scenarios that can occur.

In time-delayed systems, TLSs are periodic solutions which can emerge from Andronov-Hopf bifurcations along the steady state branch. The imaginary part of the eigenvalue responsible for the Andronov-Hopf bifurcation defines the frequency and therefore the period of the emerging periodic orbit. For long delays, many eigenvalues cross the imaginary axis (basically) simultaneously as the distance of the eigenvalues on the pseudo-continous spectrum scales with $\frac{1}{\tau}$. Mostly, one is interested in the primary bifurcation. Hence, one needs to classify the type of instability depending on the shape of the pseudo-continuous spectrum as depending on its shape the primary instability occurs via high or low frequency [110]. First, for the uniform instability the spectrum has a tip on the real axis which crosses the imaginary axis first leading to the instability of low frequencies, see Fig. 4.14 (a). Next, for the Turing instability the spectrum is stable around low frequencies but a band of higher frequencies crosses the imaginary axis, see Fig. 4.14 (b). Last, for the modulational instability, the zero frequency is meta stable, i.e., it touches the imaginary axis without crossing it, while higher frequency bands become unstable, see Fig. 4.14 (c).

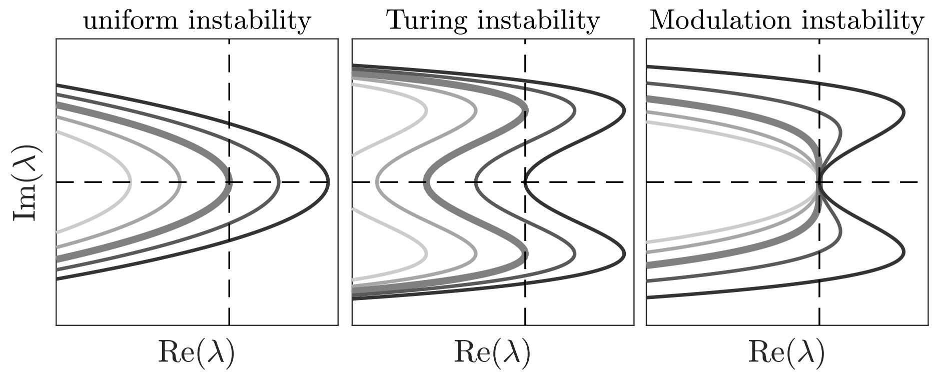


**Figure 4.14:** Shape of the pseudo-continuous spectrum of eigenvalues for different types of instabilities of steady state solutions in time-delayed systems. In each panel, the thick line corresponds to the critical value which is the onset of the respective instability.

### 4.2.5. Linear Stability of CW Solutions in the KGTI System

We calculate analytically the pseudo-continuous spectrum of eigenvalues following Section 2.2.1 for the CW solutions $(E_s, Y_s)$ of the KGTI system (3.83),(3.84). For this, we separate $E_s$ and $Y_s$ into real and imaginary parts ($E_{s,x}, E_{s,y}, Y_{s,x}$ and $Y_{s,y}$). Then, the matrices $A = \frac{\partial f(x,x_\tau)}{\partial x}\Big|_{x=\tilde{x}}$ and $B = \frac{\partial f(x,x_\tau)}{\partial x_\tau}\Big|_{x=\tilde{x}}$ (cf. Eq. (2.7)) read

$$A = \begin{pmatrix} -2E_{s,x}E_{s,y} - 1 & \delta - 3E_{s,y}^2 - E_{s,x}^2 & h & 0 \\ -\delta + E_{s,y}^2 + 3E_{s,x}^2 & 2E_{s,y}E_{s,x} - 1 & 0 & h \\ 0 & 0 & -1 & 0 \\ 0 & 0 & 0 & -1 \end{pmatrix}, \tag{4.42}$$

$$B = \eta \begin{pmatrix} 0 & 0 & 0 & 0 \\ 0 & 0 & 0 & 0 \\ \cos(\varphi) & -\sin(\varphi) & -\cos(\varphi) & \sin(\varphi) \\ \sin(\varphi) & \cos(\varphi) & -\sin(\varphi) & -\cos(\varphi) \end{pmatrix}. \tag{4.43}$$

The characteristic equation (2.12) has the following two solutions for $g$,

$$g_\pm = \frac{n_1 \pm n_2}{d}, \tag{4.44}$$

which defines the real part of the eigenvalues as $\gamma_\pm = -\frac{\ln|g_\pm(\mu)|}{\tau}$. Here, we define

$$n_1 = h(\delta - 2I)\sin(\varphi) + \cos(\varphi)\left(-\delta^2 + ih\mu + h - 3I^2 + 4\delta I + (\mu - i)^2\right), \tag{4.45}$$

$$\begin{aligned} n_2^2 = &\left(h(2I - \delta)\sin(\varphi) + \cos(\varphi)\left(\delta^2 - i(h-2)\mu - h + 3I^2 - 4\delta I - \mu^2 + 1\right)\right)^2 \\ &- \left(\delta^2 + 3I^2 - 4\delta I - (\mu - i)^2\right)\left(\delta^2 + (h - i\mu - 1)^2 + 3I^2 - 4\delta I\right), \end{aligned} \tag{4.46}$$

$$d = \eta\left(\delta^2 + (h - i\mu - 1)^2 + 3I^2 - 4\delta I\right), \tag{4.47}$$

where $I = |E_s|^2$. Next, we calculate the instantaneous eigenvalues which are the solutions of the characteristic equation (2.16):

$$\lambda_\pm = -1 \pm \sqrt{-3I^2 + 4I\delta - \delta^2}. \tag{4.48}$$

From this, we can even compute the bifurcation points, i.e., the values of $I$ where $\lambda_+$ crosses the imaginary axis:

$$\lambda_+ = 0 = -1 \pm \sqrt{-3I^2 + 4I\delta - \delta^2} \tag{4.49}$$

$$\Leftrightarrow I_\pm = \frac{2\delta}{3} \pm \frac{\sqrt{\delta^2 - 3}}{3}. \tag{4.50}$$

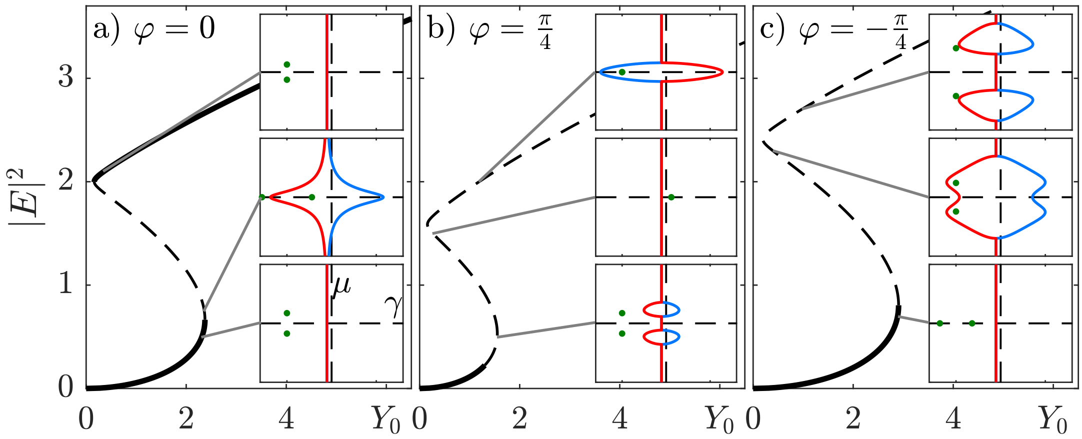


**Figure 4.15:** Steady state branches for different values of $\varphi$ in the long-delay limit, other parameters: $(\delta, h, \eta) = (2, 2, 0.9)$. The insets show the pseudo-continuous spectrum of eigenvalues $\lambda = \frac{\gamma}{\tau} + i\mu$ at the positions on the branch connected by the gray line. Here, the blue and red lines correspond to the two solutions branches $g_\pm$ as defined in Eq. (4.44). The green dots are the instantaneous eigenvalues as defined in Eq. (4.48).

This shows that an instability due to the instantaneous eigenvalues can only occur for $\delta > \sqrt{3}$.

In Fig. 4.15, we show three CW branches and eigenvalue spectra for exemplary points along the branches. We can categorize the instabilities following Section 4.2.4. Panel (a), shows a uniform instability of the CW branch, that occurs at the lower fold. At the upper fold the spectrum crosses the imaginary axis again resulting in another uniform instability. Next, in panel (b), the situation is different as the primary instability on the lower part of the CW branch is of the Turing type. Finally, in panel (c), the primary bifurcation on the lower part of the CW branch is of the uniform type. However, in between, the folds the pseudo-continuous spectrum changes is shape such that the upper CW is not stable as in panel (a), but Turing unstable (even though no Turing bifurcation occurred). As a side-note, the middle spectrum in panel (b) shows a peculiar situation in which the spectrum of eigenvalues is stable but an instantaneous eigenvalue destabilizes the CW state.

Next, we calculate the discrete eigenvalues explicitly using Eq. (2.15). However, the pseudo-continuous spectrum is only an exact solution in the limit of an infinite delay. Yet, in the long-delay limit, it still gives an excellent approximation as shown in Fig. 4.16. In panel (a), a steady state branch is shown and for four marked points on the branch, analytical eigenvalues (black circles) are compared to numerically calculated eigenvalues (red dots) in panels (b)–(e) for $\tau = 100$ and $\tau = 300$, respectively. Note that for the analytical values, one still has to numerically solve the implicit equation defining the position of the eigenvalues on the spectrum, cf. Eq. (2.15). For both delay

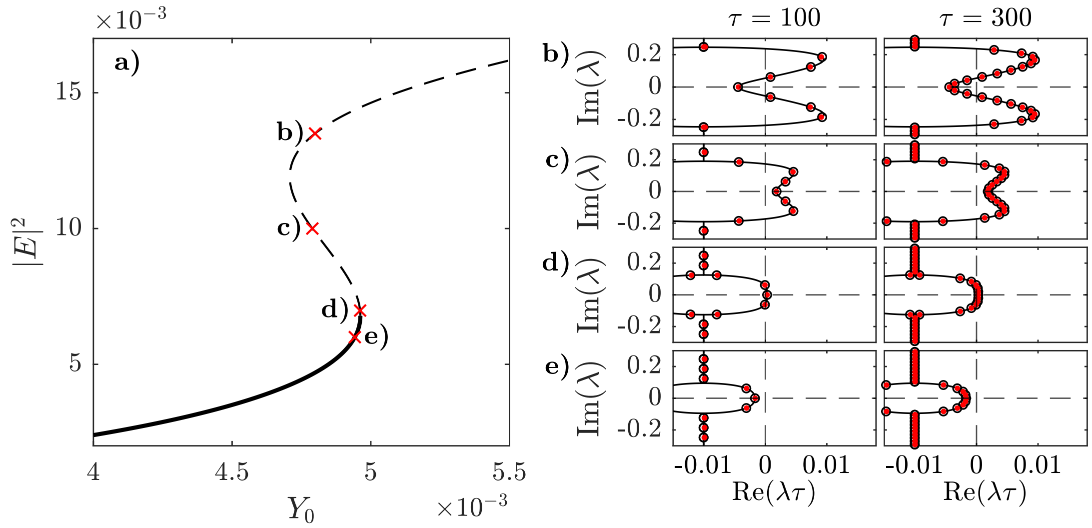


**Figure 4.16:** (a) Steady state branch for $(\delta, \varphi, h, \eta) = (-1/\sqrt{3}, -0.34\pi, 2, 0.99)$ and $\tau = 100, 300$. Red crosses indicate the values for which panels (b)–(e) are shown. (b)–(e) Comparison between eigenvalues computed analytically (black circles) defined by Eq. (2.15) which lie on the pseudo-continuous spectrum of eigenvalues (black line) given by Eq. (4.44) and numerically computed eigenvalues (red dots) from `DDE-BIFTOOL`.

values, the agreement is excellent. Further, we see that, with increasing $\tau$, the shape of the pseudo-continuous spectrum does not change, while the density of the eigenvalues on it increases. In particular, both the real and imaginary parts of the eigenvalues scale with $1/\tau$.

From the shape of the pseudo-continuous spectrum of eigenvalues and the location of the eigenvalues on it, one can conclude what kind of periodic solutions emerge. In particular, it is important whether the zero frequency is present as it determines for the uniform instability whether the primary bifurcation is a fold or an Andronov-Hopf. This lets us differentiate two regimes. For a leading zero eigenvalue, the first Andronov-Hopf is of frequency $\omega_1^{(r)} \approx \frac{2\pi}{\tau}$, i.e., the periodic solution that emerges there has a period of approximately $T_1^{(r)} \approx \tau$. Then the next Andronov-Hopf bifurcation has a frequency of $\omega_2^{(r)} \approx \frac{4\pi}{\tau}$ such that the period is approximately $T_2^{(r)} \approx \frac{\tau}{2}$. In general, the frequency of the $n$-th Andronov-Hopf bifurcation is $\omega_n^{(r)} \approx \frac{2n\pi}{\tau}$ such that the corresponding period is $T_n^{(r)} \approx \frac{\tau}{n}$.

On the other hand, if there is no leading zero eigenvalue, the first Andronov-Hopf bifurcation must have a frequency of $\omega_1^{(c)} \approx \frac{\pi}{\tau}$ because the distance of the eigenvalues on the spectrum still scales with $\frac{2\pi}{\tau}$ and the spectrum is symmetric with respect to the real axes. Hence, the corresponding period is approximately $T_1^{(c)} \approx 2\tau$. The following Andronov-Hopf bifurcation have frequencies of $\omega_n^{(c)} \approx \frac{(2n+1)\pi}{\tau}$ and periods of $T_n^{(c)} \approx \frac{2}{2n+1}\tau$.

### 4.2.6. Stability Map of the KGTI System

To get an overview over the dynamical regimes, it has proven to be extremely useful to generate a map of the steady states together with their stability, see Fig. 4.17. For that, we combine the results of many previous subsections. In particular, we use the CW branch defined by Eq. (4.32) in Section 4.2.1 and the input-output relation (4.37) from Section 4.2.2 together with the analytical fold branches defined in Eq. (4.39) from Section 4.2.3 to calculate the two-parameter plane $(\varphi, Y_0)$. Further, we compute the pseudo-continuous spectrum of eigenvalues defined by Eq. (4.44) in Section 4.2.5 and classify it according to Section 4.2.4. All of this leads to Fig. 4.17. Each point on the surface corresponds to a steady state solution. Hence, the cuts in $Y_0$- and $\varphi$-direction (cf. gray lines in (a) and panels (b),(c)) correspond to the CW branches (cf. Figs. 4.6 and 4.7). The color encodes the shape of the pseudo-continuous spectrum (cf. legend in Fig. 4.17): blue regions are stable, orange regions are uniformly unstable, yellow regions are Turing unstable and purple regions correspond to a mix of uniform and Turing instability. Here, the most unstable frequency is nonzero, however, the zero frequency is also unstable. The boundaries between these colored patches are bifurcation. For instance, the boundary between a blue (stable) and a yellow (Turing unstable) region is a Turing bifurcation. The final result gives an overview of which primary instability the CW state experiences and thus, a first indication on what kind of periodic solutions one can expect. One can identify regions where multiple CW states exist for a single injection value and quickly check whether more than one of them is stable (and thus creates bistability). Further, we can identify the regimes discussed in Section 4.2.5 such that we know where to expect $\tau$- and $2\tau$-periodic solutions, respectively. In particular, $\tau$-periodic solutions can only occur when also a fold bifurcation is present. On the other hand, if there is a regime destabilized by an Andronov-Hopf without encountering a fold, the solution must be $2\tau$-periodic.

Next, it can also be helpful to consider the projection of the bifurcation lines onto the $(\varphi, Y_0)$-plane (cf. Fig. 4.17 (d). For instance, we can see that $\tau$ and $2\tau$-periodic solutions can coexist where the red Andronov-Hopf line and the black fold lines overlap.[12]

Further, the projection of the stability map onto the $(\varphi, |E|^2)$-plane shown in Fig. 4.17 (e) reveals an interesting property: the projection is $\pi$-periodic in $\varphi$. This means, that the form of the pseudo-continuous spectrum is invariant under a $\pi$ shift in $\varphi$. However, from Fig. 4.17 (a), we can see that shifting $\varphi$ by $\pi$ leads to a different injection value $Y_0$ to reach the same steady state intensity. The symmetry can be explained when considering the explicit form of the spectra. From the definition of the spectra, cf. Eqs. (4.45)–(4.47), we can see that $n_1(\varphi) = -n_1(\varphi + \pi)$ and $n_2(\varphi) = n_2(\varphi + \pi)$ and

[12] As a spoiler, we note, that this regime gives rise to peculiar solutions, cf. Fig. 4.45.

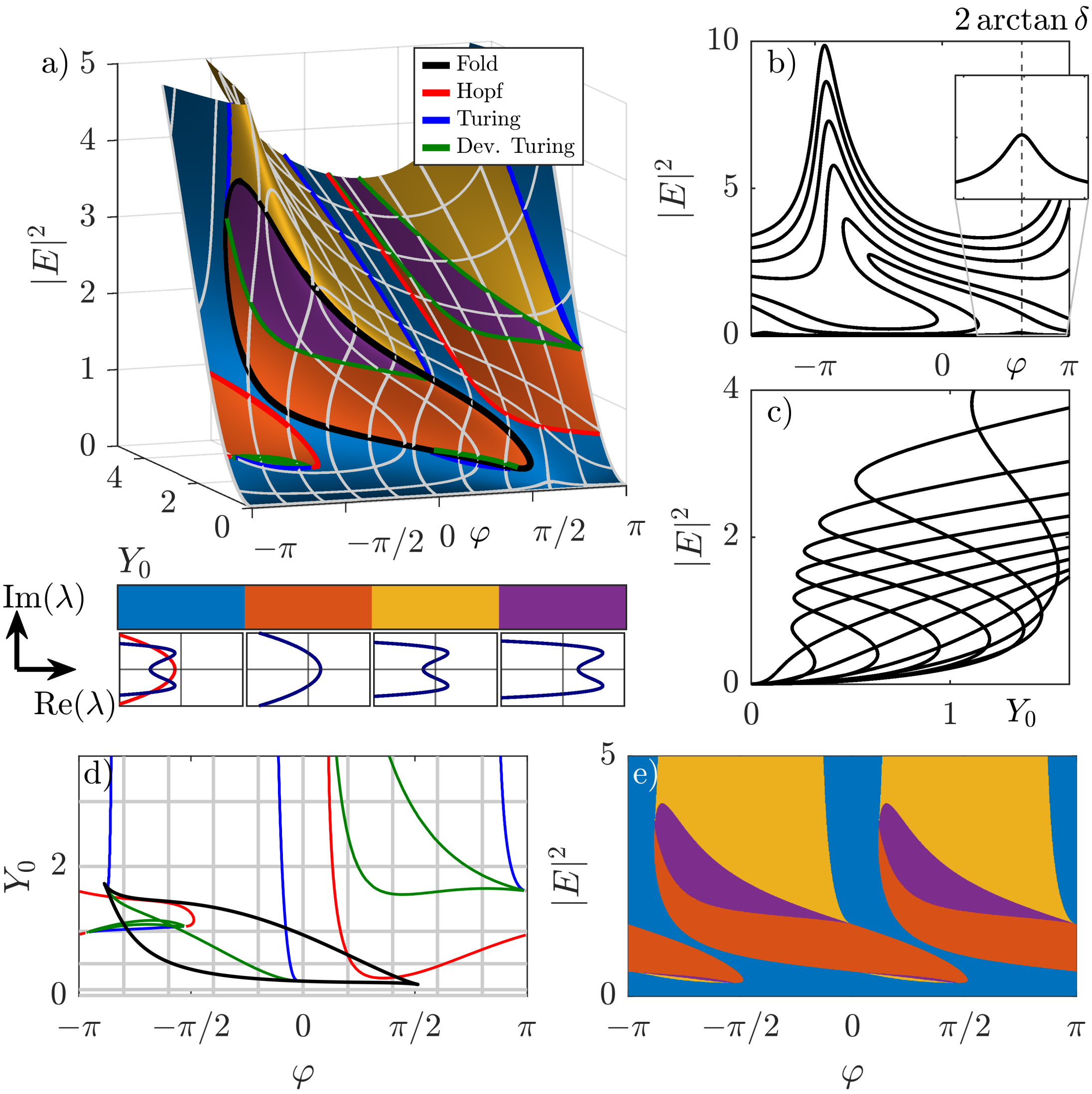


**Figure 4.17:** (a) The surface corresponds to CW solutions (cf. Eq. (4.32) for $(\delta, \eta, h) = (1.5, 0.75, 2)$. The color encodes the stability information in the long-delay limit as indicated in the legend at the bottom where the respective shapes of the pseudo-continuous spectra are shown: blue, orange, yellow and purple correspond to stable, uniformly unstable, Turing unstable as well as developed Turing unstable, respectively. The boundaries between the color-patches are bifurcations of the CW solution as indicated by the legend at the top. The light gray lines are cuts in the one-parameter planes $(\varphi, |E|^2)$ and $(Y_0, |E|^2)$ and are shown in panels (b) and (c), respectively. Panels (d), (e) show the projections of (a) onto the $(\varphi, Y_0)$- and $(\varphi, |E|^2)$-plane, respectively.

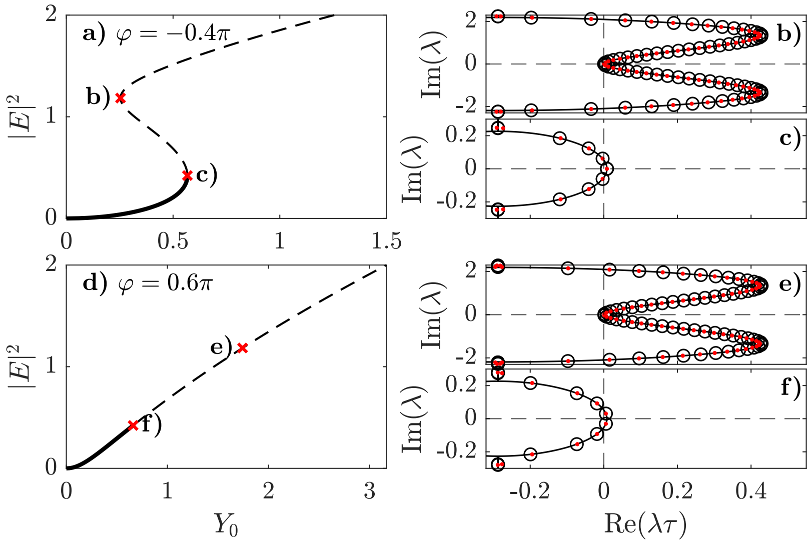


**Figure 4.18:** (a),(d) Steady state branches for different values of $\varphi$ and $(\delta, h, \tau, \eta) = (0.5, 2, 100, 0.75)$. Red crosses indicate the values for which panels (b),(c),(e),(f) are shown. (b),(c),(e),(f) Pseudo-continuous spectrum of eigenvalues $\lambda$ (black line), analytically computed eigenvalues (black circles) and numerically computed eigenvalues (red dots). A shift of $\pi$ in $\varphi$ leads to the same pseudo-continuous spectrum. However, the eigenvalues are shifted by $\frac{\pi}{\tau}$ in the imaginary part.

therefore

$$g_{\pm}(\varphi) = -g_{\mp}(\varphi + \pi). \tag{4.51}$$

Because the real part of the eigenvalue is $\gamma_{\pm} = -\frac{\ln|g_{\pm}(\mu)|}{\tau}$, the minus sign in Eq. (4.51) does not play a role such that the branches are simply exchanged.

However, even though the the spectra are invariant under a shift of $\pi$ in $\varphi$, this does not necessarily needs to be the case for the position of the eigenvalues on the spectra. In particular, considering Eq. (2.15), we find

$$\mu_{\pm}(\varphi + \pi) = -\frac{\arg\left(g_{\pm}(\varphi + \pi)\right) + 2\pi k}{\tau} = \mu_{\mp}(\varphi) + \frac{\pi}{\tau}. \tag{4.52}$$

This demonstrates, that by adding $\pi$ to $\varphi$, the occurring frequencies are changed. In particular, when operating in a bistable regime, shifting $\varphi$ by $\pi$ can lead to a regime without bistability because the are no folds as the leading zero eigenvalue does not exist anymore. Consequently, the fundamental emerging periodic solutions are $2\tau$-periodic instead of $\tau$-periodic. This is shown in Fig. 4.18 where steady state branches are plotted for two values of $\varphi$ which are $\pi$ apart. While the steady state branches are vastly different (panels (a), (d)), the pseudo-continuous spectra are identical. However, the location of the eigenvalues on it is shifted by $\frac{\pi}{\tau}$ in the imaginary part. While in Fig. 4.18 (b),(c) we observe fold bifurcations, in Fig. 4.18 (e),(f) we see Andronov-Hopf bifurcations giving rise to $2\tau$-periodic solutions.

## 4.3. Formation of Locked Domain Walls in the Normal Dispersion Regime

The current Section 4.3 (in particular Section 4.3.1 including the figures) is based on the publication:

[99] T. G. Seidel, J. Javaloyes, and S. V. Gurevich. "A normal form for frequency combs and localized states in Kerr–Gires–Tournois interferometers". In: *Opt. Lett.* 47.12 (2022), pp. 2979–2982. DOI: 10.1364/OL.457777

TGS carried out the analytical and numerical work under the supervision of SVG and JJ. All figures were created by TGS. A first draft of the text was created by TGS and gradually refined by all authors.

In this section, we consider the KGTI system in Eqs. (3.83) and (3.84) in the case of normal dispersion, i.e., $\delta > 0$, for parameter values, where optical bistability is present (see e.g. Fig. 4.6 (c)). In this regime, we find *domain walls*, which are profiles that connect the two bistable CW states. In the limit of an infinite delay, they can be understood as heteroclinic orbits. For finite delay values, these fronts can interlock at discrete distances (if they have oscillating tails) forming bright and dark TLSs, which are peaks on the lower CW value and dips in the upper CW value, respectively. In Fig. 4.19 we show typical traces in this regime. Panel (a) shows a bright TLS, panel (b) a dark TLS and panel (c) a state that resides for half the round-trip on the lower and for the other half on the upper CW state. We can observe that each TLS is followed by an decaying oscillating tail that is induced by TOD. As a result, the envelope of the corresponding frequency spectra shown in Fig. 4.19 (d)–(f) are asymmetrical.

For details on the bifurcation structure[13] of these solutions, we consider Fig. 4.20. Panel (a) shows a bifurcation diagram in the injection $Y_0$ where black lines corresponds to the CW state and blue lines to the TLS branch. On the $y$-axis, we show the normalized integrated intensity defined as

$$\langle |E|^2 \rangle = \frac{1}{T} \int_0^T |E(t)|^2 \, dt. \tag{4.53}$$

The TLS branch emerges and ends in a Andronov-Hopf bifurcations close to the fold points of the CW branch. Note that there exists multiple TLS branches corresponding to the multiple eigenvalues that cross the imaginary axis (for more details, see e.g. Fig. 4.47). Here, we focus on the fundamental TLS branch belonging to the orbits of period $\approx \tau$. This branch forms a *collapsed snaking* structure [113]. Here, the snaking branch accumulates in a vertical line (black dashed), which is typically denoted the

[13] The bifurcation analysis was conducted using the `MATLAB` package `DDE-BIFTOOL` [105, 111]. Recently, the support for DAEs was added by members of our group [112].

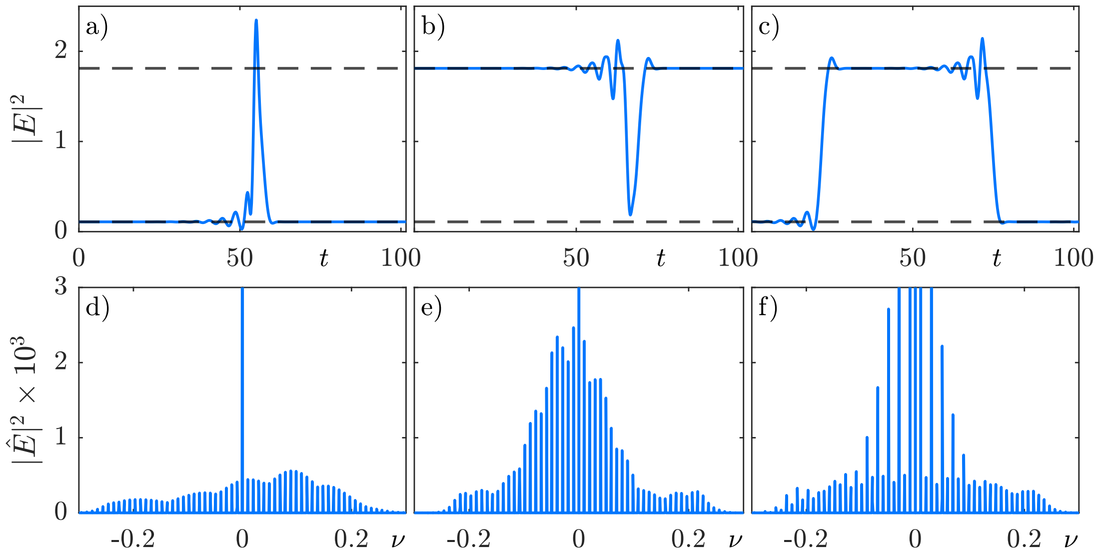


**Figure 4.19:** (a)–(c) Typical time trace obtained from DNSs of Eqs. (3.83) and (3.84) showing bright and dark TLS as well as a state in between. Black dashed lines show the two stable CW states. (d)–(f) Corresponding frequency spectra. Parameters are $(Y_0, \delta, h, \eta, \varphi, \tau) = (0.61, 1.5, 2, 0.75, 0, 100)$.

Maxwell line [114]. The profiles along this line correspond to the domain walls locking at different distances. The corresponding temporal profiles are shown in Fig. 4.20 (d) in different shades of blue. Solid lines show stable solutions, while dashed lines are unstable solutions. Light blue corresponds to bright TLSs, while darker hues of blue are dark TLSs. The profiles can also be understood as trajectories in the (infinite-dimensional) phase space. In order to visualize this, we need to project the phase space onto a lower-dimensional subset. In this case, we use the $(|E|^2, |Y|^2)$-plane (cf. Fig. 4.20 (b)). Here, we can see that the trajectories connect the two stable CW states indicated by the filled black dots. While the trajectories of the bright and dark TLSs are unique, the trajectories of the other solutions are hardly distinguishable as they all follow the trajectory describe by the heteroclinics shown in red and green.

Another important quantity that describes TLSs is their drift velocity. The drift velocity for delayed systems is defined as the difference between the period $T$ and the time delay $\tau$. Figure (4.20) (c) shows the TLS branch from panel (a) with the drift velocity as the norm. Here, the branch forms a spiral that intersects at a central point on the Maxwell line. This central point marked by a red cross converges for an infinite delay towards a *Bykov T-point* [115–118]. In this codimension-two bifurcation, two homoclinic orbits exchange their saddles by transitioning through a heteroclinic orbit. At this point both domain walls travel with the same velocity enabling them to lock at arbitrary distances. This fact also gives an explanation for the shape of the bifurcation diagram in Fig. 4.20 (a). For the first bright TLSs in the snaking structure,

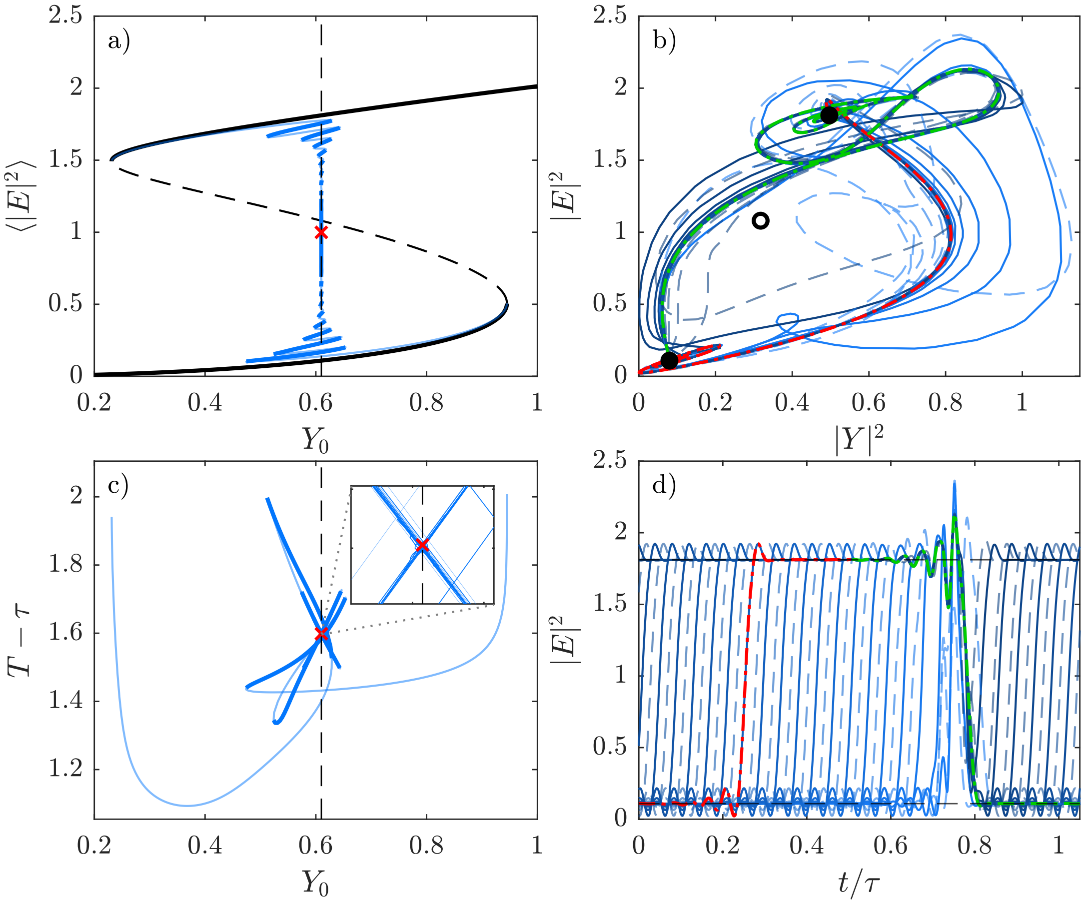


**Figure 4.20:** (a) Bifurcation diagram in injection against integrated intensity showing the CW branch (black) as well as the TLS branch (blue). Thin lines are stable and thick lines unstable solutions. The red cross marks the Bykov T-point which lays on the Maxwell line (black dashed). (c) Same TLS branch as in (a) but using the drift velocity as a norm. The solution profiles along the Maxwell line are shown in the temporal domain in (d) and a projection od the phase space in (b). Here, the red and green dashed-dotted lines are the profiles at the Bykov T-point. Same parameters as in Fig. 4.19.

the fronts are close together enabling them to lock and thus exist in a wider injection range (the so-called *pinning region*) around the Maxwell line. The further we ascend in the snaking structure, the further apart the domain walls are and the weaker the interaction becomes. The interaction via the oscillating tails causes the domain walls to only lock at discrete distances (corresponding to wavelength of the oscillations), while the pinning region becomes smaller due to the exponential decay of the tails. Thus, when the fronts are far apart, a solution can only exist at the Maxwell line where the fronts naturally have the same drift. Ascending further in the snaking structure, one arrives at the dark TLSs where the fronts are closer again and therefore can form a non-vanishing pinning region. The profiles at the Bykov T-point are highlighted in Fig. 4.20 (b),(d) in red and green which form the two domain walls.

### 4.3.1. Normal Form at the Onset of Bistability

In the next steps, we want to give additional insight on the formation process of the bright and dark TLSs presented in Fig. 4.20. The dynamical equations (3.83),(3.84) of the KGTI system naturally capture dispersive effects including GDD and TOD [55, 57]. Further, we demonstrated in Section 4.1, that in the mean-field limit, the KGTI system is described by the LLE (cf. Eq. (4.30)), which predicts the existence of bright and dark TLSs [108]. A detailed comparison between the KGTI and the LLE in the mean-field limit is provided in Section 4.5. Here, we want to reduce the complexity further by providing a minimal pattern formation scenario. For that, we consider a normal form derived at the onset of bistability which results in a PDE for a single real field.

We begin by characterizing the onset of bistability caused by the Kerr nonlinearity (cf. Fig. 4.6). For simplicity, we consider the situation in which the injection was set to be resonant with an external cavity mode, i.e., $\varphi = 0$ in this subsection. Hence, we can reuse and simplify the results from the detailed multi-parameter study of the steady state (cf. Section 4.2.3). For $\varphi = 0$, the expression in Eq. (4.32) becomes

$$Y_0^2 = \frac{k^2 + (I_s - \delta)^2}{h^2 \frac{1-\eta}{1+\eta}} I_s \,, \qquad \text{where } k = \frac{1 + (1-h)\,\eta}{1+\eta}. \tag{4.54}$$

Further, the critical detuning defining the onset of optical bistability (cf. Eq. (4.40)) simplifies considerably and reads $\delta_c = \sqrt{3}k$. For $\delta < \delta_c$ the system is monostable whereas for $\delta > \delta_c$ it shows a bistable response, see Fig. 4.6.

We use the onset of bistability $(Y_0^c, I_s^c)$ at $\delta = \delta_c$ as the expansion point for a rigorous multiple time scale analysis. For that, we define deviations from the critical values $\theta = \delta - \delta_c$, $z_0 = Y_0 - Y_0^c$ and $u + iv = E - E_s^c$. It needs to be stressed that accurate predictions can be obtained from the resulting PDE only in the vicinity of the onset of optical bistability. We denote $\epsilon = 1/\tau \ll 1$ as a smallness parameter in which the deviations are expanded, and define multiple time scales in powers of $\epsilon$, as the dynamics of the TLSs can be separated into a slow time scale $\xi$ governing the evolution between round-trips and a fast time scale $z$ describing the dynamics within one round-trip. After inserting all expansions in the original model (3.83),(3.84), one can solve the resulting equations order by order, see Appendix B.1 for the full derivation. The resulting equation governing the dynamics of the real part of the deviation of the electric field $u = u(\xi, z)$ is

$$\partial_\xi u = d_2 \partial_z^2 u + d_3 \partial_z^3 u + \varrho u^2 \partial_z u + f(u) \,. \tag{4.55}$$

The diffusion and TOD coefficients $d_j = d_j(\eta, h)$, as well as the coefficient $\varrho$ of the nonlinear drift term read

$$d_2 = \frac{\omega_1^2}{2}\frac{1-\eta}{1+\eta}, \qquad d_3 = -\frac{|\omega_1|^3}{3}\frac{1-\eta\,(1-\eta)}{(1+\eta)^2}\,,$$
$$\varrho = \frac{4|\omega_1|}{\sqrt{3}}\frac{(1+\eta)\,(1-\eta)}{h\eta}, \qquad \omega_1 = -\frac{(1+\eta)^2}{h\eta}\,.$$

Equation (4.55) is a *real Ginzburg–Landau equation* with TOD, nonlinear drift and a cubic nonlinearity $f(u) = c_0 + c_1 u + c_2 u^2 + c_3 u^3$. Its ingredients are particularly instructive and tell us how each of the physical effects is influenced by the system parameters. In particular, the diffusion and TOD coefficients $d_j$ are functions of the reflectivity $\eta$ and of the light coupling efficiency $h$. The coefficients of the inhomogeneity are

$$c_0 = \frac{1+\eta}{\eta}\sqrt{1-\eta^2}\,[Y_0 - Y_0^c] + \omega_1\,[\delta - \delta_c]\left(\sqrt{\frac{k}{2\sqrt{3}}} + \frac{1}{8}\sqrt{\frac{\sqrt{3}}{2k}}\,[\delta - \delta_c]\right)\,,$$
$$c_1 = |\omega_1|\,\frac{\delta - \delta_c}{\sqrt{3}}, \quad c_2 = |\omega_1|\,\frac{\delta - \delta_c}{\sqrt{6\sqrt{3}k}}, \quad c_3 = -\frac{4|\omega_1|}{3\sqrt{3}}\,.$$

In the good cavity limit $\eta \to 1$, $d_2$ vanishes and the dynamics is entirely controlled by TOD, which explains the strongly oscillating tails observed for large values of $\eta$. In this regime, the nonlinear drift becomes negligible as $\varrho$ vanishes. In contrast, the coefficients $c_i$ are controlled by detuning, injection, and the distance from the onset of bistability. Hereby, they define the values of the CW solutions and the width of the bistability region. The tails of appearing fronts connecting these CW states are,

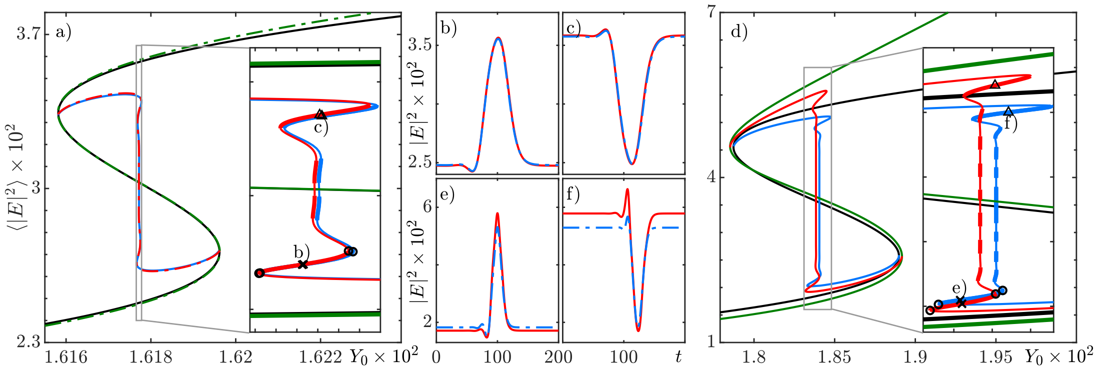


**Figure 4.21:** (a),(d): Integrated intensity of the $E$-field of the full DAE (3.83),(3.84) as a function of the injection $Y_0$ superposed with the solutions of the normal form PDE (4.55) obtained for $\delta - \delta_c =$ (a) $10^{-3}$, (d) $9 \times 10^{-3}$. The CW and TLSs branches of the DAE (PDE) are depicted in black and blue (green and red), respectively. For clarity, stability information is only shown in the insets which give a zoomed view on the snaking region. Here, thick (thin) lines denote stable (unstable) solutions. (b),(c),(e),(f): Solution profiles of the DAE (blue dashed) and the normal form PDE (red solid) at the locations marked in the insets in (a),(d) by crosses (bright TLSs, cf. (b),(e)) and triangles (dark TLSs, cf. (c),(f)). The black circles denote the folds limiting the stability of the bright TLS (cf. Fig. 4.22). The parameters are $(h, \eta, \varphi) = (2, 0.95, 0)$, $\delta_c = 0.044$, and $\tau = 200$.

however, controlled by the spatial operator and ultimately the values of $(\eta, h)$. This, in turn, affects the front interaction and the possible amount of TLSs that may appear within the snaking region. Note that in [119], an amplitude equation for a photonic crystal fiber resonator was derived close to the onset of bistability. There, starting form a generalized LLE in the anomalous dispersion regime, a Swift-Hohenberg model with TOD was obtained. In our case, however, as we operate with normal dispersion ($\delta > 0$), $d_2 > 0$ making further expansion of the spatial operator to fourth order unnecessary.

We compare the solutions of the normal form (4.55) with those obtained from the full DAE model (3.83),(3.84); our results are presented in Fig. 4.21. Since (4.55) governs the real part of $E$, we reconstructed the full electric field as $E = E_s^c + u + iv$, where $v$ is obtained from the multiscale analysis (cf. Appendix B.1) and $E_s^c$ is obtained from Eqs. (4.33), (4.35) and (4.54). Figure 4.21 (a),(d) show branches of the CW solution and TLSs, obtained from the full DAE model (black, blue) and the PDE normal form (green, red), respectively, for different deviations from the critical detuning $\delta_c$. For the small deviation (cf. Fig 4.21 (a)), one observes an excellent agreement between the branches (see the inset). In Fig. 4.21 (b), [(c)], we compare the profiles of a bright [dark] TLS marked on the branch by a cross [triangle], respectively. Again, the agreement is excellent. Moving further away from the onset (cf. Fig. 4.21 (d)), the agreement between the DAE and PDE models is still qualitatively good but the branches deviate from each other at high intensities or when looking at the profiles in Fig. 4.21 (e) and (f), respectively.

The agreement between the PDE (4.55) and the DAE (3.83-3.84) close to the bistability onset can be best observed when looking at the two-parameter-plane ($Y_0$, $\delta$) in Fig. 4.22, where the evolution of the folds limiting the stability of the bright TLS are shown (cf. the black circles in the insets of Fig. 4.21). Naturally, the agreement is best close to the onset of bistability where the two folds merge (see inset) as this point was used as the expansion point. Note that here, the injection values are shifted by a value $Y_{0,MP}$, which we define as the mean between the two CW folds, such that $Y_0 - Y_{0,MP}$ is centered around zero which provides a much better clarity for the comparison. To calculate it, we consider the derivative of the CW curve with respect to the intensity which for $\varphi = 0$ reads

$$\frac{dY_0^2}{dI} = \frac{3I^2 - 4\delta I + k^2 + \delta^2}{h^2 \frac{1-\eta}{1+\eta}}. \tag{4.56}$$

We find the folds at the intensities $I_\pm$ where this derivative vanishes:

$$I_\pm = \frac{1}{3}\left(2\delta \pm \sqrt{\delta^2 - 3k^2}\right). \tag{4.57}$$

Next, we can find the critical injections $Y_{0,\pm} = Y_0\left(I_\pm\right)$ which read

$$Y_{0,\pm}^2 = \frac{2}{27}\frac{\delta(\delta^2 + 9k^2) \pm (3k^2 - \delta^2)^{\frac{3}{2}}}{h^2 \frac{1-\eta}{1+\eta}} \tag{4.58}$$

such that we can find the mean:

$$Y_{0,MP} = \frac{Y_{0,+} + Y_{0,-}}{2} = \frac{1}{\sqrt{27}}\frac{\left(\delta + \sqrt{3}k\right)^{\frac{3}{2}}}{h\sqrt{\frac{1-\eta}{1+\eta}}}. \tag{4.59}$$

Finally, the excellent quantitative prediction of the normal form (Eq. (4.55)) lets us believe that it is widely applicable to other systems close to the onset of bistability and where high-order effects are responsible for domain wall dynamics.

### 4.3.2. Spatial Eigenvalues

In the next step, we want to analytically describe the (oscillating) tails of the domain walls. The tails emerge from an instability of the CW background. However, the lower and upper CW states are both linearly stable, cf. Fig. 4.20. That is, the spectrum of eigenvalues is not responsible for the instability leading to the tail. In order to find this instability, we calculate the linear stability of the CW background with the premise of

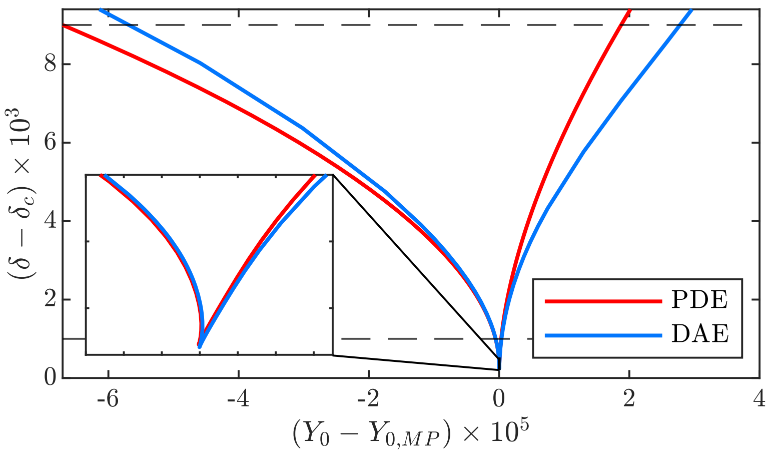


**Figure 4.22:** Evolution of the folds limiting the stability of the bright TLS (cf. circles in Fig. 4.21 (a),(d)) for the full system described by the DAE in Eqs. (3.83-3.84) (blue) and the developed normal form PDE (4.55) (red) in the two-parameter plane $(Y_0, \delta)$. The horizontal dashed lines correspond to the detuning values for which Fig. 4.21 (a) and (d) are shown. For clarity, the injection values are shifted by $Y_{0,MP}$ which is a function of the other parameters (in particular, of $\delta$) giving an approximate analytical solution for the Maxwell point. Parameters as in Fig. 4.21.

a periodic solution, which are the TLSs fulfilling $E(t) = E(t+T)$. This allows us to transform Eqs. (3.83) and (3.84) into a *time-advanced equation* by replacing $E(t-\tau)$ with $E(t+\rho)$, where $\rho = T - \tau$ is the drift velocity of the TLS. Linearizing around a steady state yields the following characteristic equation (cf. Eq. (2.9))

$$\det\left(A + Be^{\lambda\rho} - M\lambda\right) = 0, \tag{4.60}$$

where $A$ and $B$ are the derivatives of Eqs. (3.83) and (3.84) with respect to the instant and the delayed variable, respectively, and the solutions $\lambda$ are the *spatial eigenvalues*. The name stems from the similarity to spatially extended systems where spatial eigenvalues determine the spatial instability of a steady state. That is, one can use an ansatz $\sim e^{ikz}$ in a PDE and solve for the spatial eigenvalues $k$ under the premise of a drift velocity $v$ that corresponds to a certain spatially localized state. For the case of time-delayed systems, one has to solve the (in general) transcendental equation (4.60). In particular, as the spatial eigenvalues do not follow a particular scaling (in contrast to the pseudo-continuous spectrum of eigenvalues, cf. Section 2.2.1), this has to be done numerically. One approach is to consider the residuum of the LHS of Eq. (4.60). In Fig. 4.23 we show the nullclines of the real and imaginary part of this residuum as contour lines. The intersections of these lines are the spatial eigenvalues. Here, a positive/negative real part describes the ascending/decaying tail. The dominant eigenvalues are the ones with the smallest absolute value of the real part. We denote

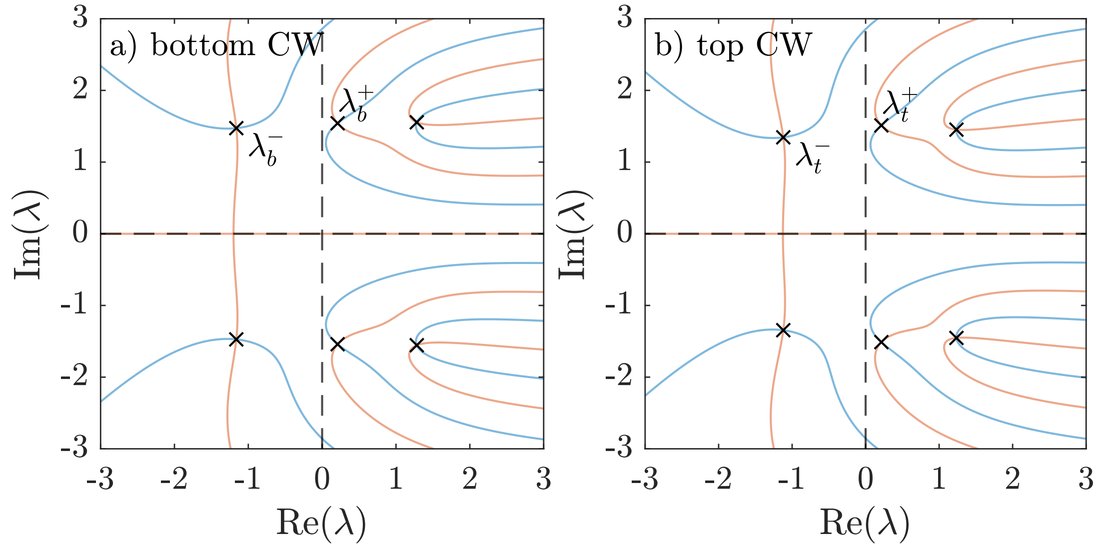


**Figure 4.23:** Spatial eigenvalues of the solution in Fig. 4.19 (c) of the bottom (a) and top (b) CW states. The contour lines correspond to the nullclines of the real (blue) and imaginary (red) parts of Eq. (4.60), respectively.

these eigenvalues $\lambda_b^+$, $\lambda_t^+$, $\lambda_b^-$ and $\lambda_t^-$ where the lower index stands for bottom/top (the respective CW state) and the upper index for ascending (+)/descending (−) tails. Next, one has to compute the corresponding eigenvectors $v_b^+$, $v_t^+$, $v_b^-$ and $v_t^-$. Each component of the perturbations $(\delta x)_{t,b}^{\pm}$ to the state vector $(E_{s,x}, E_{s,y}, Y_{s,x}, Y_{s,y})$ follows

$$\left[(\delta x)_k^l\right]_i = a \ \mathrm{Re}\left(\left[v_k^l\right]_i e^{\lambda_k^l (t-t_0)}\right), \tag{4.61}$$

where $a$ is a constant and $t_0$ leads to a phase. These parameters need to be found by fitting Eq. (4.61) to the actual tails. This is shown in Fig. 4.24 where we used the profile of Fig. 4.19 (c) as an example as it exhibits both a lower and an upper plateau. In Fig. 4.24 (d), we show exemplarily the real part of the profile at the lower CW state. The same has to be done for the imaginary part at the lower CW as well as the real and imaginary parts at the upper CW state. Combining these results leads to Fig. 4.24 (a)–(d) where we can see excellent agreement between the fitted tails and the actual profile even on logarithmic scales.

For the explicit case in Fig. 4.24, the eigenvalues of the lower and upper CW states are complex leading to oscillatory tails. This explains that both bright and dark TLS can be observed in the corresponding bifurcation diagram (cf. Fig. 4.19) as the oscillations allow the fronts to lock. On the other hand, if some spatial eigenvalues are real, locking of fronts cannot occurs leading to a vanishing pinning region [120].

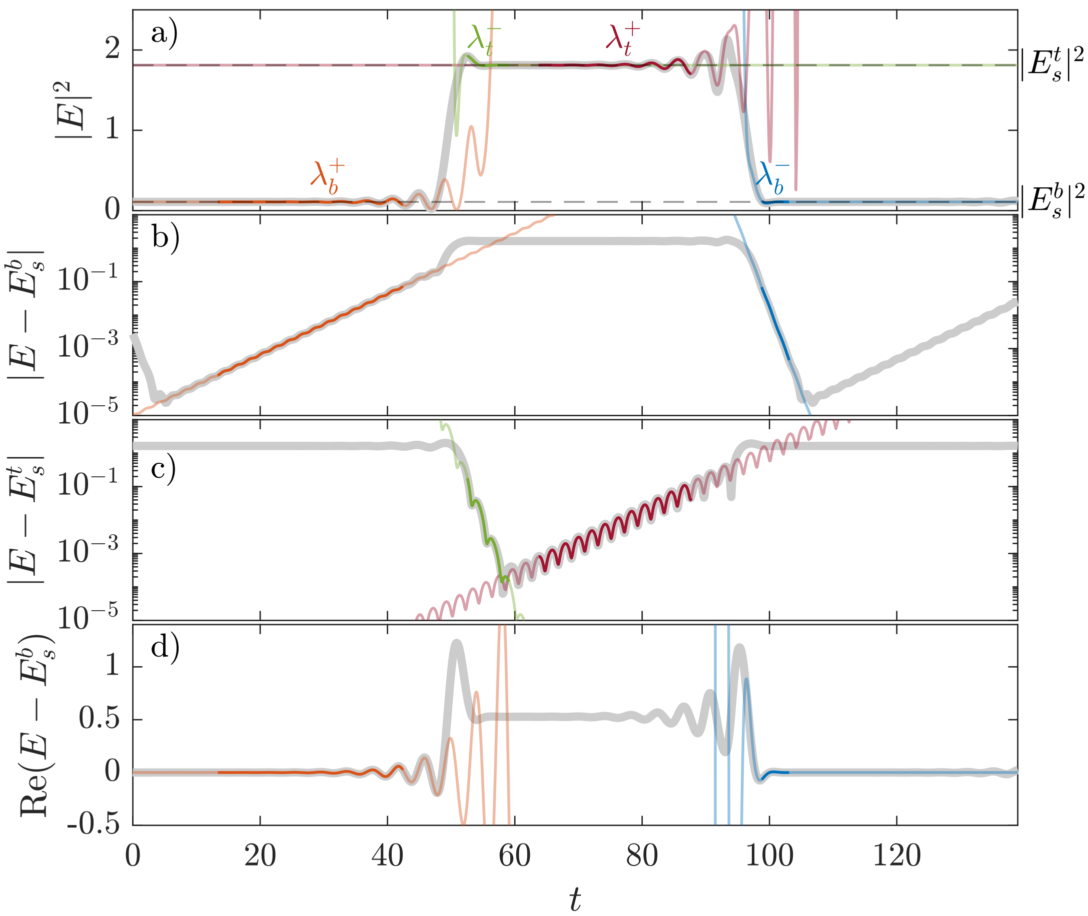


**Figure 4.24:** The profile of Fig. 4.19 (c) in light gray compared to the fitted tails. We show the intensity, the field normalized to the bottom and top CW states, respectively, and the fitted profiles of the real part of bottom CW (exemplary for all the fits one has to conduct). The solid lines of the fits are the parts, which were actually fitted, while the opaque parts are simply their prolongations.

## 4.4. Existence-Range of Locked Domain Walls

After presenting the mechanism of locked domain walls in Section 4.3, we study the range in different system parameters for which these solutions exist. We begin with the study with the feedback rate $\eta$ (cf. Section 4.4.1), next the detuning $\delta$ (cf. Section 4.4.2), and finally the cavity coupling $h$ (cf. Section 4.4.3). In the process, we explore many interesting dynamical regimes of locked domain walls.

### 4.4.1. Influence of the Feedback Rate

The feedback rate $\eta$ describes how much of the output $O = E - Y$ of the setup is fed back into the external cavity field $Y$. To get an overview, we create bifurcation diagrams in the injection for various values of $\eta$ as shown in Fig. 4.25. Starting with $\eta = 0.5$ in Fig. 4.25 (a), the TLS branch only exist in a small range around the Maxwell line. The pinning region widens as $\eta$ is increased (cf. Fig. 4.25 (b),(c)). This makes sense intuitively as $\eta$ controls the strength of the oscillatory tail as it defines how fast the series in Eq. (3.87), describing the multiple external cavity reflections, can be truncated. The increased amplitude of the oscillations enables for a larger range in which the domain walls can lock at each other. Starting from Fig. 4.25 (d) where $\eta = 0.8$ the bifurcation diagram has no visible vertical part anymore, i.e., also the TLSs in the middle of the branch have a none-vanishing locking range. Going further to $\eta = 0.85$

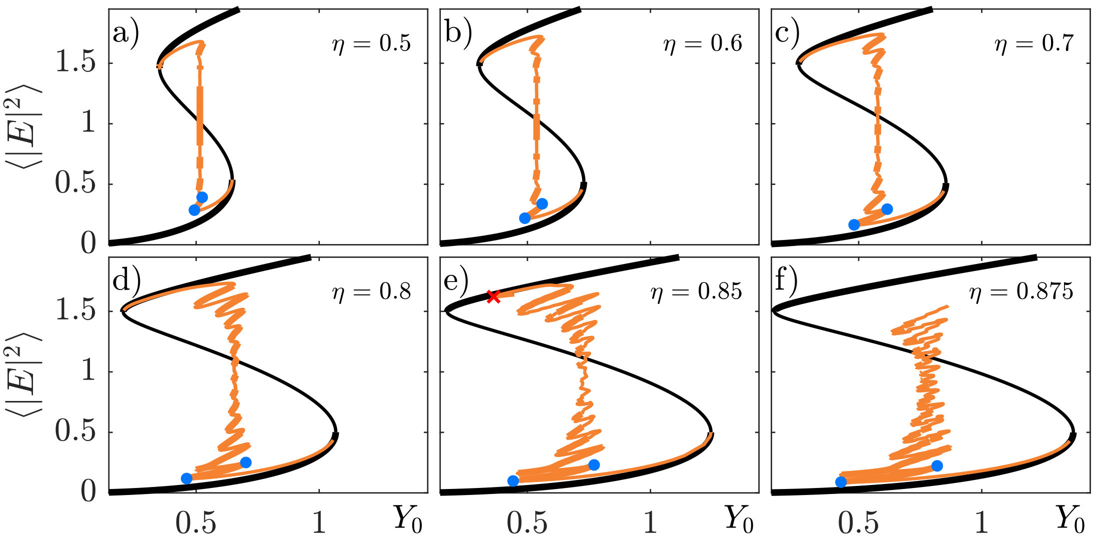


**Figure 4.25:** Bifurcation diagrams of a TLS (orange) and a CW branch (black) for different values of $\eta$. The blue dots marking the folds of the bright TLS refer to the two-parameter bifurcation diagram in Fig. 4.27. The red cross in panel (e) marks a fold detailed in Fig. 4.28. Profiles along the branch in panel (f) are shown in Fig. 4.26. Other parameters are $(\delta, h, \varphi, s, \tau) = (1.5, 2, 0, 1, 50)$.

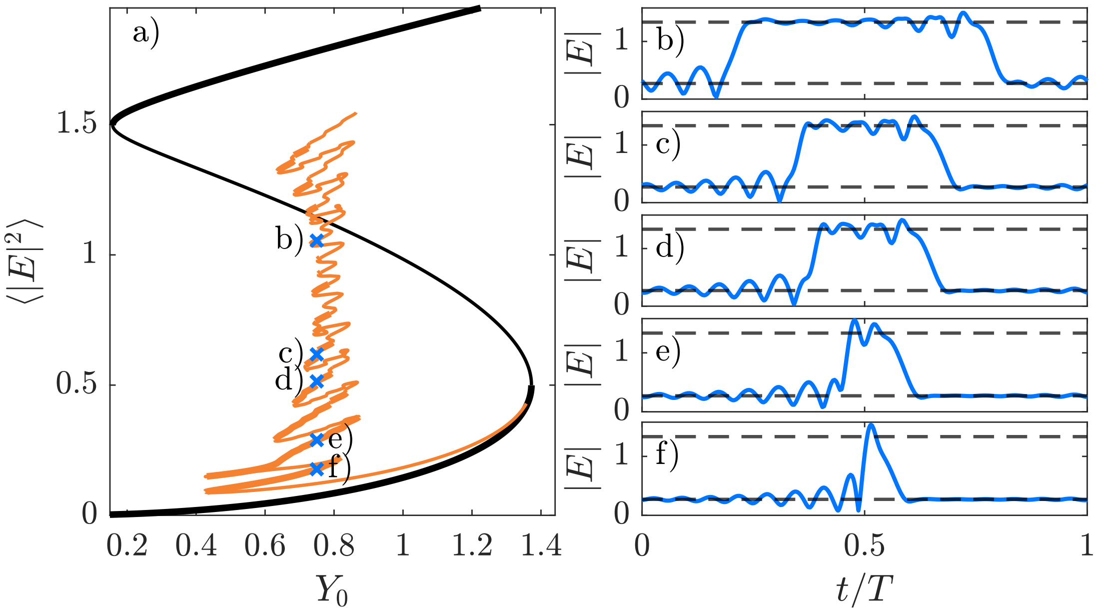


**Figure 4.26:** (a) Detailed view on the branch from Fig. 4.25 (f). (b)–(f) Profiles along the branch in (a) at locations marked by blue crosses. The black dashed lines correspond to the upper and lower CW states, respectively.

in Fig. 4.25 (e), the TLS branch becomes deformed due to "steps" appearing on it. Further, torus bifurcations emerge along the branch which explains the unstable parts found on previously stable sections. Lastly, the upper part of the branch disconnects from the CW branch. The fold involved in this separation is marked with a red cross and is detailed further down below. Finally, for $\eta = 0.875$ the steps along the branch become more prominent. Only a part of the branch is shown here, as it was not possible to perform the continuation of the full branch due to numerical problems.

In order to explain the deformations emerging along the branch, we consider its profiles which are shown in Fig. 4.26. Starting at the bottom of the TLS branch, the branch of the bright TLS is not deformed. Its profile exhibits a strongly oscillating tail shown in Fig. 4.26 (f) which, however, decays fully when reaching the TLS from the other side. Going up the the ladder in the snaking branch, the TLSs become wider as they spend more time on the upper CW and thus, the separation of the strongly oscillating tail on the left and the domain wall on the right becomes smaller. Consequently, the oscillations have decayed less and less the higher we go on the ladder. These non-vanishing oscillations lead to a self interaction of the TLSs, which, in turn, create the deformation on the higher stairs of the TLS branch.

In order to quantify the range in which the TLS exist, we consider the two-parameter plane $(Y_0, \eta)$ and follow the folds limiting the range of the bright TLS (cf. blue dots in Fig. 4.25) as well as the folds of the CW branch. The result is shown in Fig. 4.27.

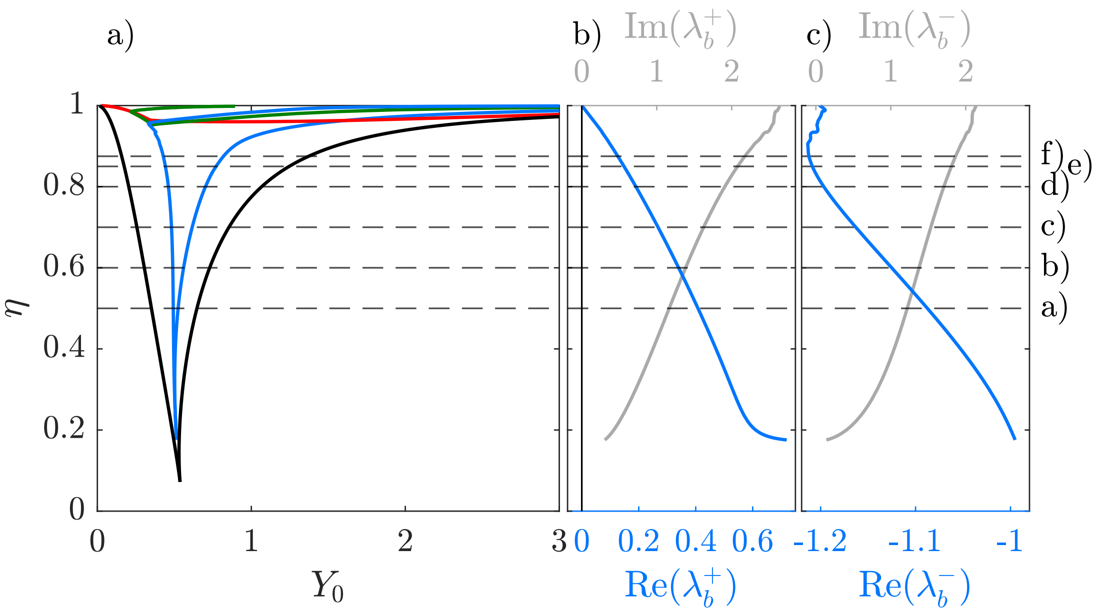


**Figure 4.27:** (a) Two-parameter bifurcation diagram in the $(Y_0, \eta)$-plane. In black are the folds of the CW branch and in colors are the folds of the bright TLS branch (cf. blue dots in Fig. 4.25). (b),(c) Evolution of the spatial eigenvalues $\lambda_b^\pm$ along the left part of the TLS-fold branch. The horizontal black dashed lines mark the locations at which the branches in Fig. 4.25 (a)–(f) are shown.

In panel (a), one can see that the CW-folds emerge in a cusp marking the onset of bistability. Close to this cusp, another cusp occurs at which the bright TLS are born (cf. blue line in Fig. 4.27 (a)). As demonstrated before, increasing $\eta$ leads to a larger separation of the left and right TLS-fold as the width of the pinning region increases. This can even be further quantified by considering the spatial eigenvalues $\lambda_b^\pm$ of the lower CW state. In Fig. 4.27 (b),(c), we show the real and imaginary parts of $\lambda_b^\pm$ (top and bottom $x$-axes, respectively) along the left TLS-fold branch. We can observe, that as $\eta$ reaches unity, the real part of $\lambda_b^+$ goes towards zero while the real part of $\lambda_b^-$ remains approximately constant, i.e., the tail ascends slowly for larger $\eta$ but descends at a constant rate. This enables an increased locking strength and, hence, a wider pinning region. Further, the imaginary parts of $\lambda_b^\pm$ increases as $\eta \to 1$, which explains the strong oscillations that can be observed in, e.g., Fig. 4.25 (b)–(f). It shall be noted, that for the right TLS-fold branch, the same qualitative behavior can be observed. Finally, considering again the limit $\eta \to 1$, we can observe in Fig. 4.27 (a) that the mechanism becomes very involved as now also the bright TLS experiences the influence of self-interaction explained above. Hence, more fold bifurcations occur and the role of the leading leftmost fold is exchanged. Two of these fold branches are shown in red and green (more are present that are not shown for clarity). However, generally in the

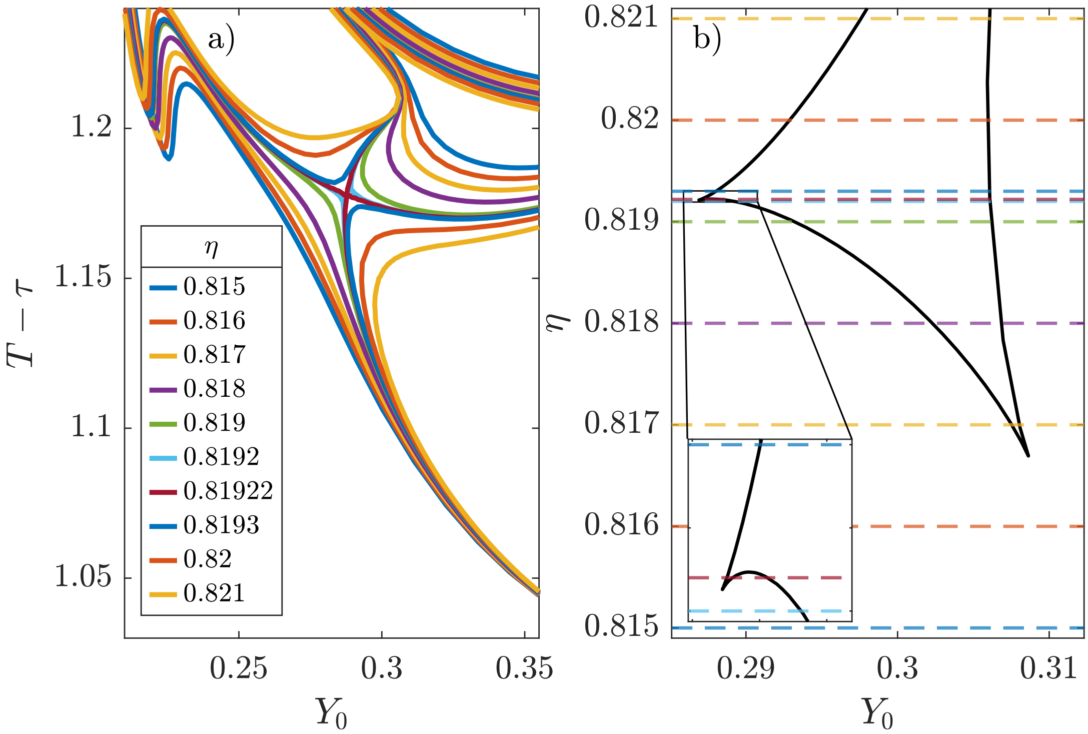


**Figure 4.28:** (a) Bifurcation diagram in $Y_0$ with the divergence of the period $T$ of the delay time $\tau$ as a norm. The fold detailed here is marked by a red cross in Fig. 4.25 (e). (b) Two-parameter bifurcation diagram in the $(Y_0, \eta)$-plane showing the folds visible in (a). The horizontal colored dashed lines refer to the same parameter values as in (a).

limit of large feedback rates the rightmost TLS-fold diverges towards large injection value while the leftmost fold converges to $Y_0 \to 0$.

Finally, we detail the mechanism of the disconnection of the TLS branch from the upper CW state (cf. red cross in Fig. 4.25 (e)), which occurs around $\eta \approx 0.8192$. In Fig. 4.28 (a) we show multiple branches around this value of $\eta$. To present the unfolding more clearly, we use the divergence of the period from the time-delay, i.e., $T - \tau$, as the norm. Further, in Fig. 4.28 (b) we provide a two-parameter bifurcation diagram of the folds involved. Around the feedback value at which the reconnection occurs, we find a cusp, which appears to lay almost horizontally in the bifurcation diagram (which would correspond to a pitchfork bifurcation). However, the zoomed view provided in the inset in Fig. 4.28 (b) reveals that there are in fact a cusp and a transcritical bifurcation in close succession (the transcritical bifurcation occurs at the tip of a parabula in the two-parameter plane). This reordering of branches demonstrates the complex dynamics inflicted by large feedback values.

### 4.4.2. Influence of the Detuning

The multi-parameter analysis of the steady state (cf. Fig. 4.10 (a)) revealed that increasing the detuning beyond the onset of bistability at $\delta_c$ leads to a more nonlinear regime where higher injections are required to achieve bistability. Hence, the difference in intensity between the lower and upper CW states increases. This is shown in Fig. 4.29, where bifurcation diagrams of the CW and TLS branch for $\delta = (1, 1.5, 1.6, 2)$ are displayed (note the different scalings of the $y$-axis). While the general relative shape of the branches remain the same between the different panels, starting from $\delta = 1.6$, we can observe the appearance of period-doubling (PD) bifurcations on the TLS branch which are marked by red triangles in Fig. 4.29 (c),(d). This type of bifurcation is characterized by a Floquet multiplier leaving the unit circle at $-1$. This can be detected by the numerically calculating the Floquet multipliers using `DDE-BIFTOOL`. For $\delta = 1.6$ the PD bifurcations appear on many levels of the snaking structure (however, not on the fist one), while for $\delta = 2$ they only remain on the first and last level.

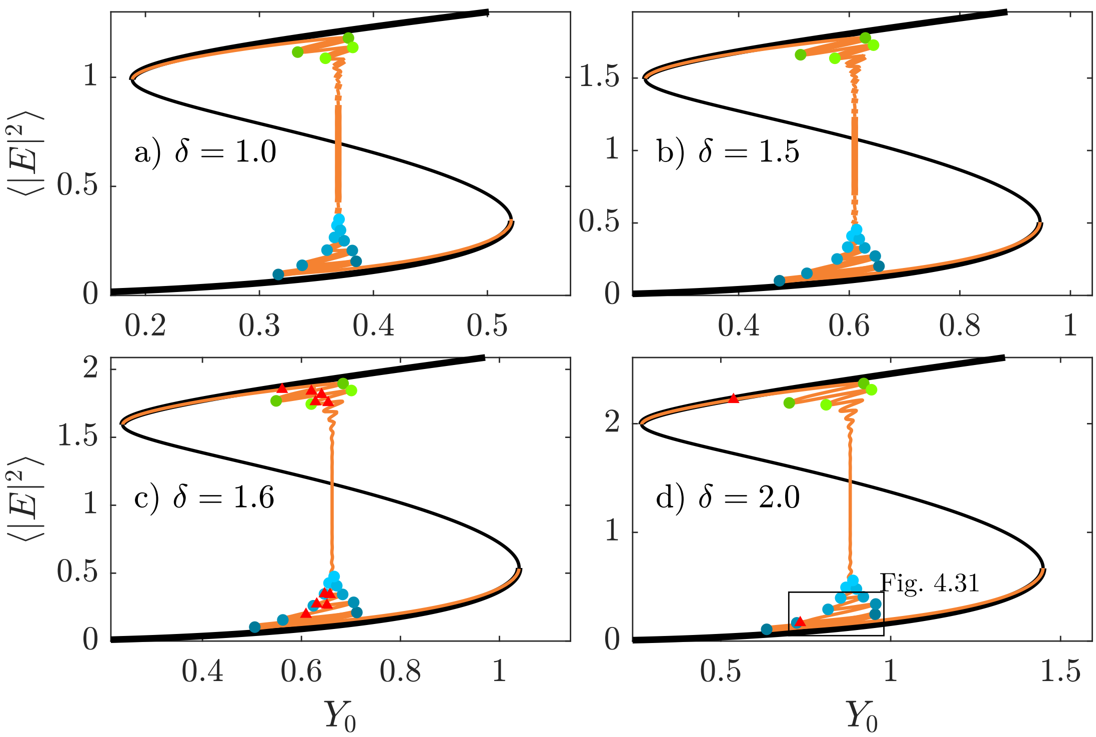


**Figure 4.29:** Bifurcation diagrams in the injection $Y_0$ for increasing values of $\delta$. The colored markers correspond to the bifurcations shown in Fig. 4.30, i.e., hues of blue and green are the SN bifurcations limiting the stairs of the snaking branch while red triangles stand for period-doubling bifurcations. The area marked by the rectangle in panel (d) is visualized in more detail in Fig. 4.31. Other parameters are $(\eta, h, \varphi, \tau) = (0.75, 2, 0, 100)$.

To further study the emergence of the PD bifurcations, we consider the two-parameter bifurcation diagram presented in Fig. 4.30. There, the colors match to Fig. 4.29, i.e., the red line describes the PD bifurcation, the black line the fold of the CW state and lines in hues of blue and green stand for folds of the TLS branch. Note that for better readability, the injection values are shifted by $Y_{0,MP}$, which is defined as the median of the left and right fold of the CW value (cf. Eq. (4.59)). In Fig. 4.30 (a) the two-parameter bifurcation diagram is presented as a three-dimensional plot with the integrated intensity on the $z$-axis as this allows to observe much better how the branches are organized. Interestingly, the PD branch forms a snaking structure which is emphasized in Fig. 4.30 (c) where the PD branch is shown in the $(Y_0 - Y_{0,MP}, \langle |E|^2 \rangle)$-plane. In the two-parameter-plane $(\delta, Y_0 - Y_{0,MP})$ this corresponds to a spiral (cf. Fig. 4.30 (b)). Further, one observes that each time the PD branch folds, it touches a fold branch, i.e., it goes around the fold and thus appears on all levels of the snaking branch. The two ends of the spiral shape are the PD bifurcations on the dark and 2nd bright TLSs, respectively. These PD bifurcations are the only ones which exist for $\delta \gtrsim 1.7$, i.e., above the small range of $\delta$-values where the the spiral exists (cf. Fig. 4.29 (d)).

Next, we want to study the emerging period-doubled solution. For that, we consider again Fig. 4.29 (d) and zoom into the region around the PD bifurcation, cf the black rectangle. This closeup is provided in Fig. 4.31 (a). Here, the green line is the period-doubled branch of period $T_2 \approx 2\tau$. The two parts of the green branch correspond to the integration of the intensity over $t \in [0, T_2/2], [T_2/2, T_2]$, respectively. However, the two parts of the green lines form a single solution branch.

The period-doubled solution emerges on an unstable part of the TLS branch and thus, only stabilizes after undergoing a fold (cf. zoom in Fig. 4.31 (a)). However, then the period-doubled branch destabilizes in another PD bifurcation. In fact, with increasing injection, there is a cascade of PD bifurcations leading to the well-known *Feigenbaum diagram* in Fig. 4.31 (a). It was obtained by conducting DNSs over many round-trips and then integrating the profile over intervals of length $T$ (the period of the corresponding fundamental TLS on the orange branch). Each integral corresponds to a blue dot in the diagram. Further, one also finds a large window of period-3 and period-6 solutions. Figure 4.31 (b) shows an extract of a time trace over 50 round-trips (cf. black dashed line in 4.31 (a)). One can see that the intensity of the pulses strongly fluctuates over time such that the integrated intensity changes from round-trip to round-trip.

The occurrence of the Feigenbaum diagram is an indicator for chaotic behavior. To show this explicitly, we perform the simulation of Fig. 4.31 (b) again but slightly perturb the initial condition by adding noise with an amplitude of $10^{-15}$. This way, we want to demonstrate the sensitive dependence of the dynamics on the initial conditions,

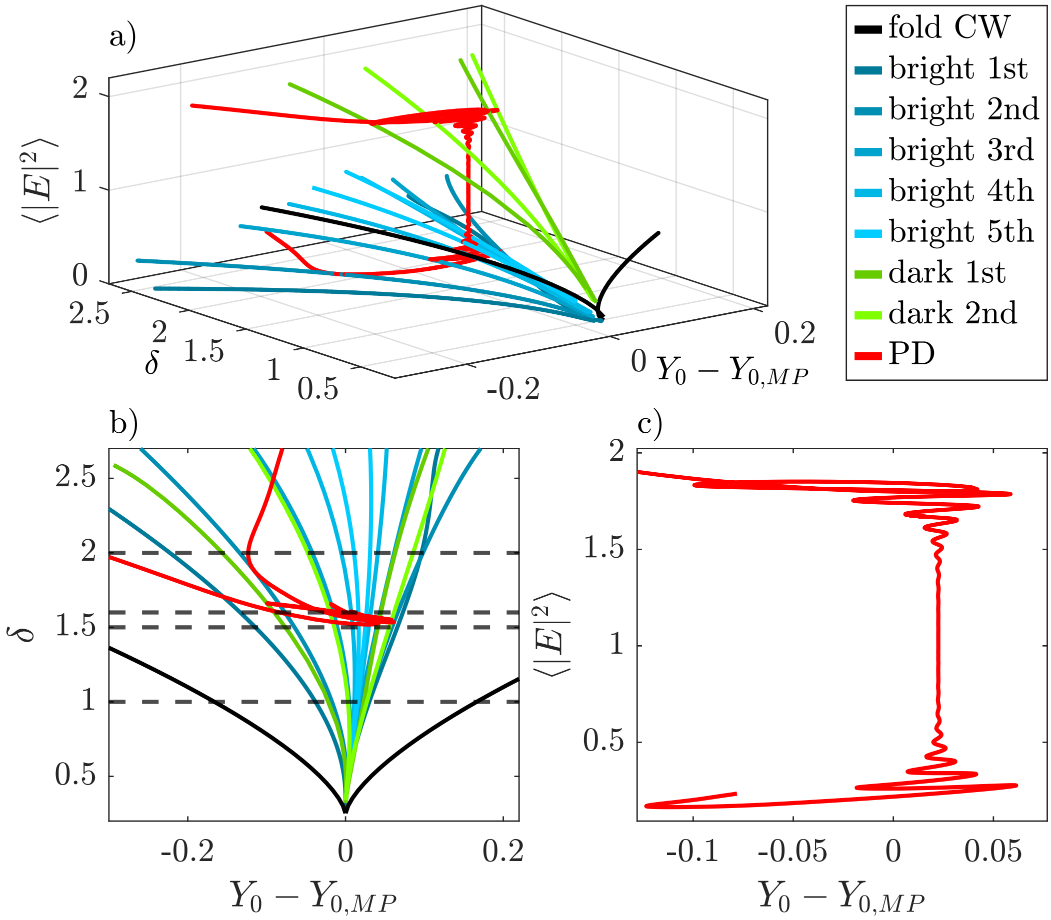


**Figure 4.30:** (a) Two parameter bifurcation diagram showing the folds limiting the stairs of the snaking branch (shadings of blue and green, respectively), the folds of the CW branch (black) and PD bifurcations (red). The colors correspond to the markers in Fig. 4.29. For better readability, the injection values are shifted by $Y_{0,MP}$ defined in Eq. (4.59). (b) Projection in the $(\delta, Y_0 - Y_{0,MP})$-plane. The black dashed lines mark the bifurcation diagrams shown in Fig. 4.29. (c) Projection of the PD branch in the $(Y_0 - Y_{0,MP}, \langle|E|^2\rangle)$-plane.

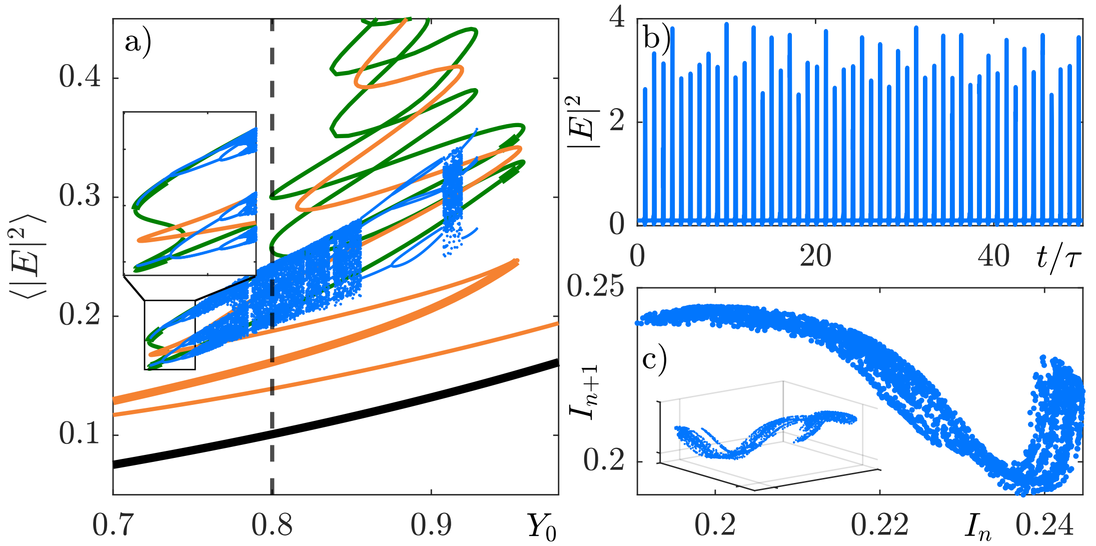


**Figure 4.31:** (a) Bifurcation diagram in $Y_0$. The extract shown here is marked by a black rectangle in Fig. 4.29 (d). The black line is the CW state, orange the TLS branch, green is the period-doubled branch and blue are results from DNSs. Each blue dot corresponds to the integrated intensity of an interval of length $T$. (b) Extract of a DNS at the injection value marked by the black dashed line in (a). (c) First return map of the blue dots at the black dashed line in (a). The inset shows the second return map.

which is characteristic for chaos. The evolution of the integrated intensity for the two simulations is shown in Fig. 4.32 (a). While at the beginning, the two simulations are almost indistinguishable, they differ notably for later round-trips. Plotting the integrated absolute value of the difference between the two simulations (cf. Fig. 4.32 (b)), shows that the this distance grows exponentially, i.e., the maximal *Lyapunov exponent* [69] of the system is positive and, thus, the system is indeed chaotic. Lastly, we can further study the chaotic regime by visualizing the first return map, see 4.31 (c), of the simulation shown in 4.31 (b). We can observe that all points lie on a certain manifold, which forms the chaotic attractor. The inset shows the second return map, and thus, a three dimensional view on the chaotic attractor.

Finally, we emphasize that further analyses showed, that a cascade of PD bifurcations can be found on all the other stairs of the snaking branch as well such that there is a multistability between different chaotic attractors. Further, in the KGTI, the emergence of a chaotic pulse amplitude is not unique to the regime of domain walls. It was found and studied in the regime of square waves in [121].

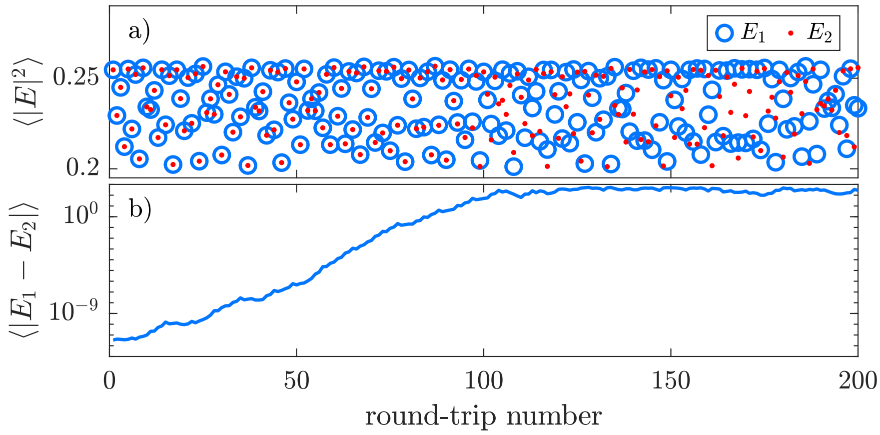


**Figure 4.32:** (a) Integrated intensity for two simulations (as in Fig. 4.31), where the second simulation $E_2$ starts with a slightly perturbed initial condition of the first simulation $E_1$. (b) Integrated absolute value of the difference between the two simulations on a logarithmic scale.

### 4.4.3. Influence of the Cavity Coupling Factor

The parameter $h$ controls the coupling of the external cavity field $Y$ to the micro-cavity field $E$. It is defined by the transmission and reflection coefficients of the micro-cavity (cf. Eq. (3.75)). In order to analyze its influence, we consider bifurcation diagrams in the injection for different values of $h = (0.5, 1, 1.5, 2)$ in Fig. 4.33 (a)–(d). First, we notice that for lower couplings the bistable region becomes narrower and a stronger injection is required to obtain optical bistability. The larger injection values for smaller coupling balance such that the micro-cavity field is in the same order of magnitude throughout Fig. 4.33 (a)–(d). Note however, that naturally, the external cavity field increases with larger injection and hence, also the cavity output $O$.

Next, we focus on the folds along the TLS branches. For that we consider the two-parameter plane $(Y_0, h)$ shown in Fig. 4.33 (e), where the injection values are shifted by $Y_{0,MP}$ (cf. Eq. (4.59)) for better readability. The value of $Y_{0,MP}$ is shown in Fig. 4.33 (g). The colored lines in Fig. 4.33 (e) correspond to the markers in Fig. 4.33 (a)–(d) in same colors. Further, in Fig. 4.33 (f) the fold lines of Fig. 4.33 (e) are shown in the $(\langle|E|^2\rangle, h)$-plane in order to visualize their unfolding. Here, we can observe something peculiar as the organization of the folds in the two-parameter plane is different compared to the previous sections. In the $(Y_0, \delta)$- and $(Y_0, \eta)$-planes (cf. Figs. 4.27 and 4.30), folds of the same level in the snaking branch are connected in cusps. However, in the $(Y_0, h)$-plane, folds from the lower levels are connected to folds on the upper levels. For instance, the folds denoted with $F_1$ and $F_2$ belong to the same two-parameter branch while being the folds limiting the bright TLS to the left and the dark TLS to the right, respectively. The same holds for $F_{3,4}$, $F_{7,8}$, $F_{9,10}$ and

$F_{11,12}$. The only exception are folds $F_5$ and $F_6$ which belong to the same level in the snaking branch. Hence, in the regular patter that is visible in the $(\langle|E|^2\rangle, h)$-plane in Fig. 4.33 (f) the $F_{5,6}$-branch forms a defect.

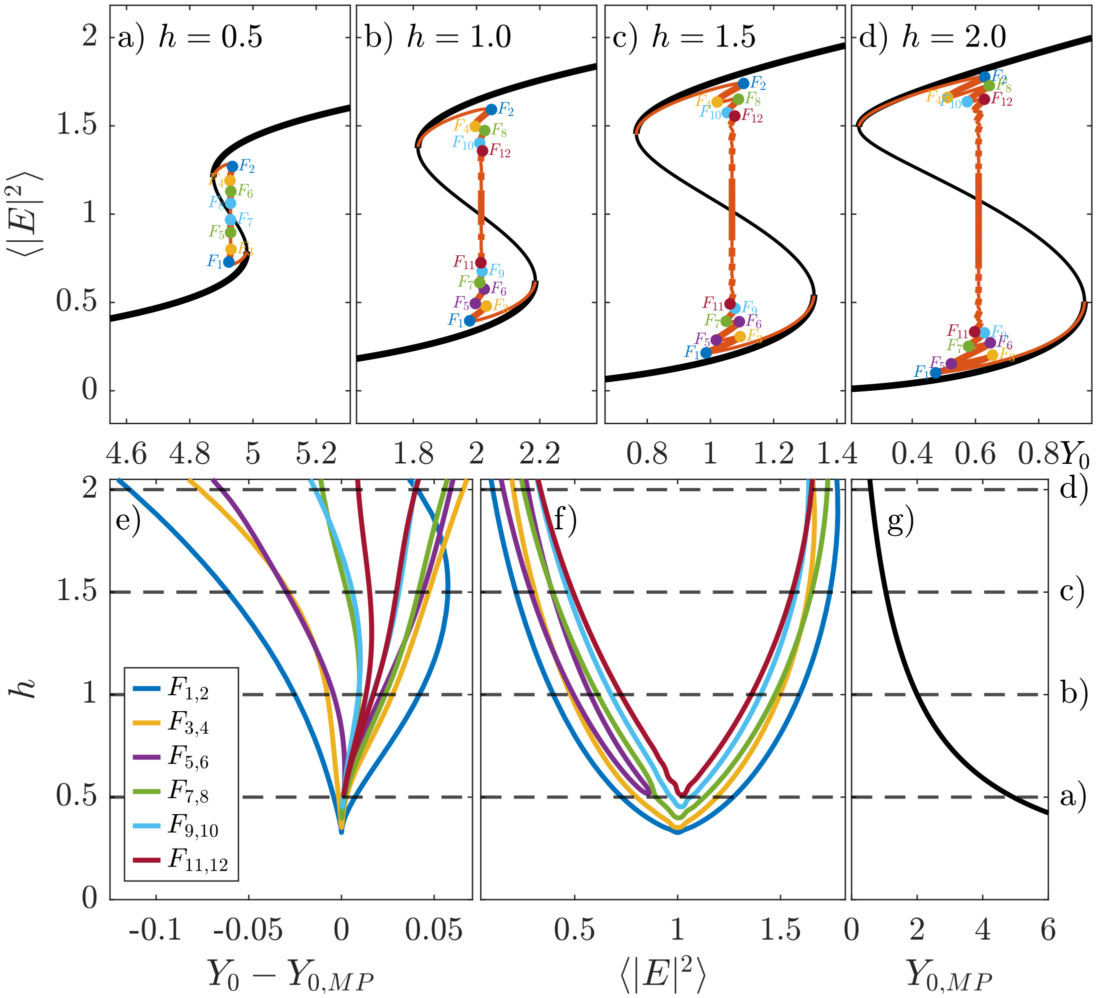


**Figure 4.33:** (a)–(d) Bifurcation diagrams in the injection $Y_0$ for increasing values of $h$. The colored markers correspond to the bifurcations shown in the two-parameter plane $(Y_0 - Y_{0,MP}, h)$ in panel (e) and the $(\langle|E|^2\rangle, h)$-plane in (f). The diagram in (e) is shifted by $Y_{0,MP}$ for better readability. The value of $Y_{0,MP}$ is shown in (g). The dashed lines correspond to the values of $h$ in panels (a)–(d). Other parameters are $(\delta, \eta, \tau, \varphi) = (1.5, 0.75, 100, 0)$.

## 4.5. Domain Walls in the Weakly Dissipative Limit

In the limit $\eta \to 1$, the KGTI system exhibits small losses, which in general, complexifies the dynamics because with increasing $\eta$, oscillatory tails become stronger (cf. Section 4.4.1). In particular, the chain in Eq. (3.87) can not be truncated quickly as all multiple reflections are of order 1. Hence, in order to find stable TLSs, we consider the regime close to the nonlinear cavity response. That is, according to the input-output relation in Eq. (4.37), the CW intensity is low and the effective phase $\tilde{\varphi} = \varphi - 2\arctan\delta$ is small. Performing a multiple time scale analysis of the KGTI system in Eqs. (3.83) and (3.84) with these requirements yields the Lugiato–Lefever equation (LLE) with third-order dispersion (cf. Section 4.1.1):

$$\frac{\partial E}{\partial \xi} = -i\frac{\beta_2}{2}\partial_z^2 E + \frac{\beta_3}{6}\partial_z^3 E + \left[\eta - 1 + i\tilde{\varphi}\right] E + i\gamma \left|E\right|^2 E + F, \tag{4.62}$$

$$\text{where } \beta_2 = \frac{4\delta}{\left(1+\delta^2\right)^2}, \quad \beta_3 = \frac{4\left(3\delta^2 - 1\right)}{\left(1+\delta^2\right)^3},$$

$$\gamma = \frac{2}{1+\delta^2}, \quad F = \frac{2}{1+i\delta}\sqrt{1-\eta^2}Y_0.$$

For details on the derivation of Eq. (4.62) see Appendix B.2. Note that Eq. (4.62) is truncated such that TOD is the highest order effect, however generally, also other higher order effects can play a role.

The linear operator can also be understood by considering the DAEs (3.83),(3.84) as a map. For that, we combine Eq. (3.83) with itself at a delayed state such that we obtain in the GTI limit ($h = 2$)

$$E\left(t\right) = e^{i\left(\varphi - 2\arctan\delta\right)} E\left(t-\tau\right) + \mathcal{O}\left(\epsilon\right), \tag{4.63}$$

where we used the long-delay limit ($\epsilon = \tau^{-1} \ll 1$) such the temporal derivative is $\mathcal{O}\left(\epsilon\right)$. That is, we find an frequency dependent phase shift

$$\beta\left(\omega\right) = \varphi - 2\arctan\left(\omega_c - \omega\right), \tag{4.64}$$

which is simply the phase in Eq. (4.63) with $\delta$ written out explicitly. Our profile is a wave packet centered around the carrier frequency $\omega_0$. That is, each plane wave of frequency $\omega$ experiences the phase shift $\beta\left(\omega\right)$. As all $\omega$ are close to $\omega_0$, we expand $\beta\left(\omega\right)$ around $\omega_0$ and obtain

$$\beta_n = \left.\frac{\partial^n \beta}{\partial \omega^n}\right|_{\omega_0}, \tag{4.65}$$

where we explicitly note that $\beta_0 = \beta\left(\omega_0\right) = \tilde{\varphi} = \varphi - 2\arctan\delta$. For more details on this,

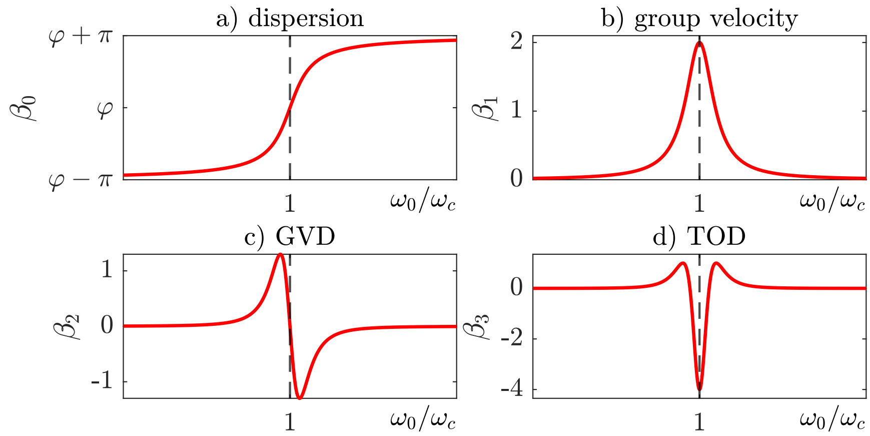


**Figure 4.34:** Dispersive effects in the KGTI system in Eqs. (3.83) and (3.84). The curves correspond to the $\beta_i$ defined in Eq. (4.65).

see Appendix B.2.3, where we also demonstrate that even the nonlinear terms can be calculated with this approach. Finally, we visualize the corresponding dispersion curves in Fig. 4.34 which characterize the dispersive effects in the KGTI. We can observe, that GVD changes its sign at $\omega_0 = \omega_c$ and TOD vanishes for $\delta_c = \pm\frac{1}{\sqrt{3}}$.

The LLE is a well-established framework for modeling Kerr resonators in the mean-field limit [66, 108]. In particular, it can be derived in the mean-field limit from the nonlinear Schrödinger eqaution (NLS) with boundary condition defined by the Ikeda map. As we demonstrated that in the conservative limit, the dynamics in the KGTI is governed by the NLS (cf. Section 4.1), it is not surprising that we find the LLE in the weakly dissipative limit as the time-delayed description can be understood as a realization of the Ikeda map. The LLE was studied in great detail in, e.g. [108] for both the normal and anomalous dispersion regime. In this section, we focus on the comparison of the KGTI with the LLE in the normal dispersion regime, where the LLE describes TLSs as locked domain walls. For a comparison in the anomalous dispersion regime, see [107].

First, we perform an analysis of the steady states in the weakly dissipative limit and consider the stability map introduced in Section 4.2.6, which is shown in Fig. 4.35. We operate close to the onset of the nonlinear response where the effective phase $\tilde{\varphi}$ is small as the cavity response curve is centered around $\tilde{\varphi} = 0$, i.e., $\varphi = 2\arctan\delta$. The onset of the nonlinear response is characterized by a cusp bifurcation as there, two folds emerge. In particular, the deviation between the onset of bistability and the linear cavity response is in the same order of magnitude ($\approx 0.01$ in this case) as the deviation of $\eta$ from unity. This assumption is part of the derivation of Eq. (4.62) (both $1-\eta$ and $\tilde{\varphi}$ scale as $\epsilon^2$). Next, we notice that only for small $\tilde{\varphi}$ the first bifurcation along

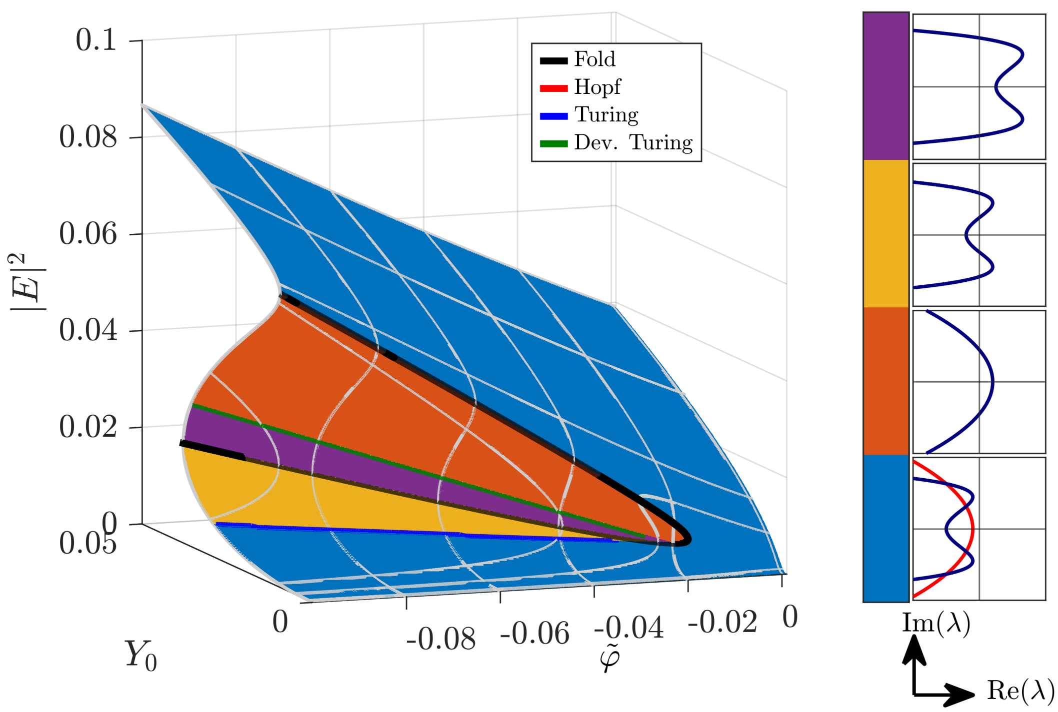


**Figure 4.35:** Stability map (cf. Section 4.2.6) in the mean-field limit. The parameters are $(\eta, \delta, h) = (0.99, 0.5, 2)$.

the CW branch is a fold and for most of the range the primary bifurcation is a Turing (cf. yellow region in Fig. 4.35). The upper CW is stable in the weakly dissipative limit which allows the formation of stable locked domain walls.

In order to test the validity of the derived normal form, we compare it quantitatively with the full system in Eqs. (3.83) and (3.84). This is shown in Fig. 4.36 where bifurcation diagrams for the full system and the normal form are overlayed for two different values of $\eta$. Here, we choose the specific value of $\delta = \frac{1}{\sqrt{3}}$ for which $\beta_3 = 0$, i.e., we expect to see perfectly symmetric solution profiles as the effect of TOD vanishes. Figure (4.36) (a), where $\eta = 0.99$, show a good, yet not perfect agreement. While the profiles of the PDE normal form are perfectly symmetric, the profiles of the delayed system exhibit an asymmetry (panels (b),(c)), which shows that higher order effects are present. The agreement is improved when going closer to the expansion point as seen in Fig. 4.36 (d)–(f) where $\eta = 0.998$.

Next, we want to study the regime, where TOD becomes dominant in the KGTI. The impact of TOD on the LLE was studied in detail in [108]. In our work, the dispersion coefficients are not directly accessible but are functions of the original system parameter. When changing the detuning $\delta$, not only the TOD coefficient changes but also other components in Eq. (4.62). To circumvent this problem, we nondimensionalize Eq. (4.62)

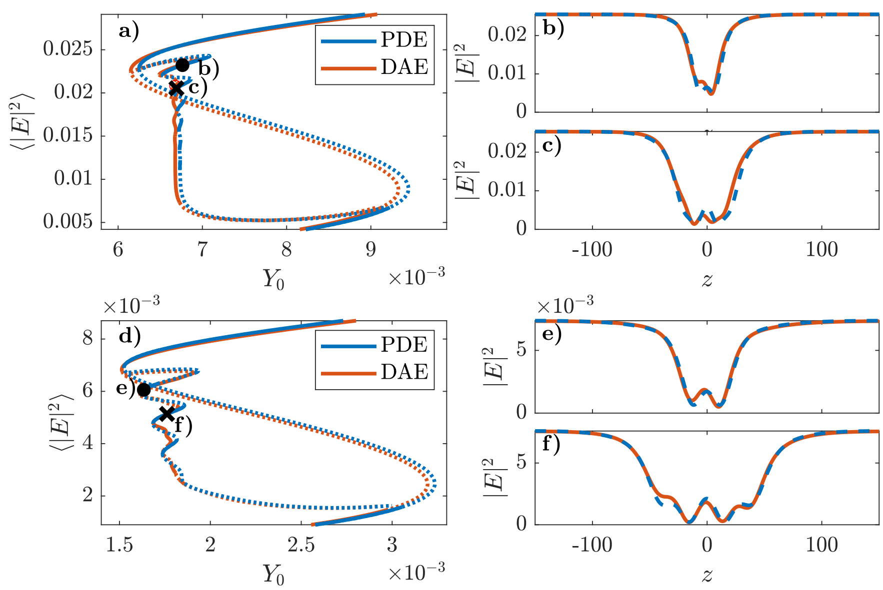


**Figure 4.36:** Comparision between full KGTI system in Eqs. (3.83) and (3.84) and normal form in Eq. (4.62) for $(\delta, \tau) = (\frac{1}{\sqrt{3}}, 300)$ and (a)–(c) $\eta = 0.99, \varphi = 0.322\pi \Rightarrow \tilde{\varphi} \approx -0.036$ and (d)–(f) $\eta = 0.998, \varphi = 0.33\pi \Rightarrow \tilde{\varphi} \approx -0.0105$.

following the approach in [108]. We introduce the following scalings:

$$A = E\sqrt{\frac{\gamma}{1-\eta}}e^{i\arctan(\delta)}, \tag{4.66}$$

$$\tilde{\xi} = (1-\eta)\,\xi, \tag{4.67}$$

$$\tilde{z} = \sqrt{\frac{2\,(1-\eta)}{|\beta_2|}}z, \tag{4.68}$$

$$\alpha = -\frac{\tilde{\varphi}}{1-\eta}. \tag{4.69}$$

With that, Eq. (4.62) reads

$$\frac{\partial A}{\partial \tilde{\xi}} = i\nu\partial_{\tilde{z}}^2 A + d_3\partial_{\tilde{z}}^3 A - (1+i\alpha)\,A + i\,|A|^2\,A + \tilde{Y}_0, \tag{4.70}$$

$$\text{where } d_3 = \sqrt{\frac{1-\eta}{18}}\frac{3\delta^2-1}{|\delta|^{\frac{3}{2}}}, \tag{4.71}$$

$$\tilde{Y}_0 = \frac{4}{1+\delta^2}\frac{1}{1-\eta}Y_0, \tag{4.72}$$

$$\nu = -\mathrm{sgn}\,(\beta_2) = -\mathrm{sgn}\,(\delta) = \begin{cases} +1 & \delta < 0 \text{ anomalous} \\ -1 & \delta > 0 \text{ normal} \end{cases} \tag{4.73}$$

In this version of the LLE all effects are decoupled as now, $\delta$ only changes the effective

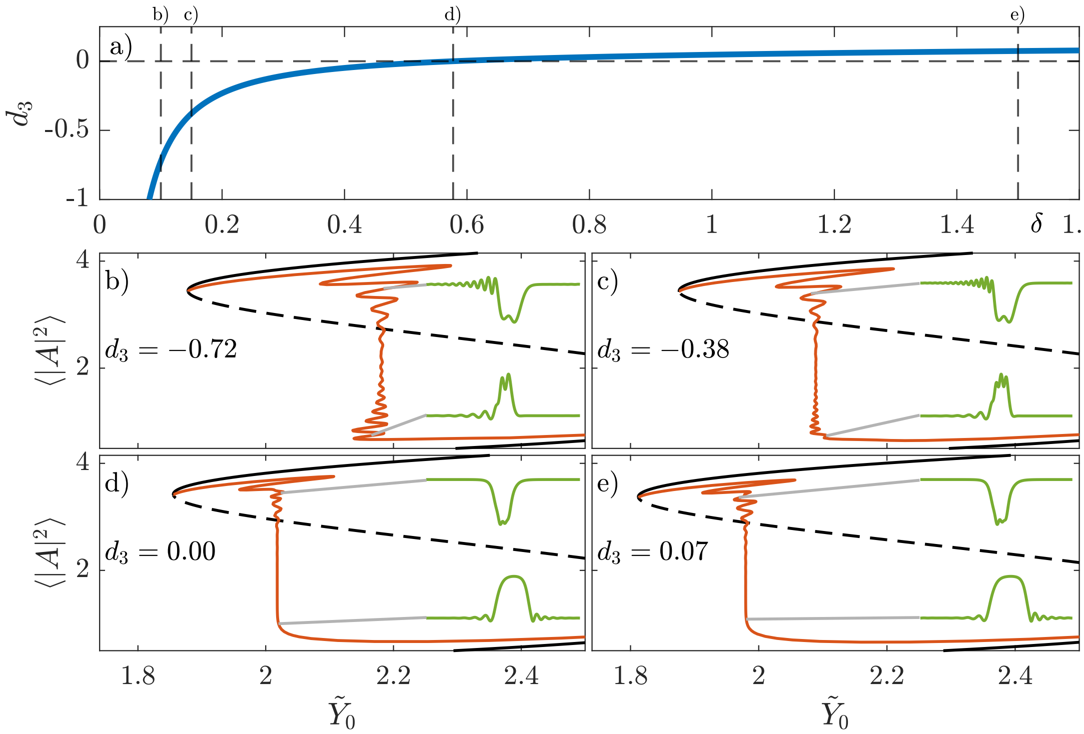


**Figure 4.37:** (a) Third-order-dispersion coefficient $d_3$ as a function of $\delta$ (cf. Eq. (4.71)) where $\eta = 0.99$. (b)–(d) Bifurcation diagrams for $\delta = 0.1, 0.15, \frac{1}{\sqrt{3}}, 1.5$. $\tilde{\varphi}$ is fixed at $-0.036$ for all panels, i.e., $\varphi$ is defined as $\varphi = \tilde{\varphi} + 2\arctan(\delta)$. This corresponds to $\alpha = 3.6$ (cf. Eq. (4.69)). The delay $\tau$ is adapted such that the scaled length (cf. Eq. (4.68)) is $\tilde{\tau} = 60$ for all panels, i.e., $\tau \approx 265.7, 321.4, 483.6, 319.8$. Note that the norms on the axes are the scaled quantities $\tilde{Y}_0$ and $\langle|A|^2\rangle$ (cf. Eqs. (4.67) and (4.72)). Stability is omitted for clarity.

TOD coefficient $d_3$, which we show as a function of $\delta$ in Fig. 4.37 (a). We notice that $d_3$ vanishes for $\delta_c = \frac{1}{\sqrt{3}}$. For $\delta < \delta_c$ the coefficient is negative, while for $\delta > \delta_c$ it is positive. However, the sign of $d_3$ can be flipped by defining $z \to -z$ in Eq. (4.70), i.e., only the magnitude $d_3$ is important for the bifurcation structure.

Next, we consider bifurcation diagrams for different values of $\delta$, which is shown in Fig. 4.37 (b)–(e) for $\delta = (0.1, 0.15, \frac{1}{\sqrt{3}}, 1.5)$. Note that in order to obtain compatible results, we fix the value of $\tilde{\varphi} = \varphi - 2\arctan\delta = -0.036$. That is, in all panels $\varphi$ is adapted as $\varphi = \tilde{\varphi} + 2\arctan\delta$. This leads to an effective phase of $\alpha = 3.6$ as $\eta = 0.99$ (cf. Eq. (4.69)). The same is done for the cavity length $\tau$ as it scales according to Eq. (4.68). That is, we set a fixed length of $\tilde{\tau} = 60$ and adapt $\tau$ accordingly. Finally, we use the scaled injection $\tilde{Y}_0$ (cf. Eq. (4.72)) and scaled integrated intensity $\langle|A|^2\rangle$ as the norms on the axes. As a result, the different panels in Fig. 4.37 (b)–(e) are all in the same order of magnitude, while the actual quantities (e.g. $Y_0$ and $\langle|E|^2\rangle$) in the delayed system are vastly different.

For small $\delta$ the dynamics is influenced by TOD as can be seen from the oscillating tails of the profiles in Fig. 4.37 (b),(c). As a consequence, the bright TLSs have a non-vanishing pinning region. In contrast, for $\delta = \delta_c$ in Fig. 4.37 (c) we find $d_3 = 0$ and consequently (approximately) symmetric profiles. Hence, the pinning region for bright TLSs is infinitesimally narrow [120]. The fact, that the profiles are not perfectly symmetric shows that higher order effects are still present. Lastly, for $\delta = 1.5$, the value of $d_3$ is small and thus the profiles exhibit a small asymmetry. However, the oscillations are on the other side of the TLS as $d_3$ changed its sign. The pinning region is still very narrow as GVD is the dominating effect. In summary, Fig. 4.37 unveils that in order to see significant effects of TOD in the mean-field limit of the KGTI, one has to operate using small detunings as for large detunings the increase in $d_3$ is slow as it scales with $\mathcal{O}\left(\sqrt{\delta}\right)$.

Next, we note that the TLS branch emerges from the CW branch in different ways depending on the detuning. In order to visualize this, we consider the projection of the stability map in Fig. 4.35 onto the $(\tilde{\varphi}, Y_0)$-plane, see Fig. 4.38 (a). We show the folds of the CW branch in black and the Turing bifurcation in blue. For $\tilde{\varphi} = -0.02 \Leftrightarrow \alpha = 2$ the Turing branch meets the fold branch. This particular point can be derived analytically for the LLE [108]. Considering cuts into the $Y_0$-direction, we observe that while in panel (c) the TLS branch (orange) emerges directly from the CW branch (black), in (b) the primary bifurcation is of the Turing type (marked by a blue dot). There, a pattern branch emerges from which the TLS branch eventually bifurcates.

Finally, the nondimensionalized form of the LLE allow us to easily identify parameters of the full system for which the normal form is valid. This becomes important as performing simulations and continuations in these parameter regimes is difficult due to the feedback values $\eta$ being close to unity leading to a stiff system. For instance, it is difficult to estimate which value of $\tau$ is necessary to be in the long-delay limit as it depends on the other system parameters (cf. Eq. (4.68)). This simplifies when using Eqs. (4.68), (4.69) and (4.72) to find proper values for $\varphi, \tau$ and $Y_0$, respectively. For instance, we can improve Fig. 4.36 by going even closer to the expansion point and set $\eta = 0.9999$. Further, we set $\alpha = 3$ and $\tilde{\tau} = 100$, which leads to $\varphi \approx \pi/3$ and $\tau \approx 8059.3$. The corresponding bifurcation diagram is shown in Fig. 4.39 (a). As the parameters are very close to the expansion point, we expect good agreement with the normal form. Looking at the profiles in Fig. 4.39 (b)–(g), this is verified as they are perfectly symmetric due to the value of the detuning that cancels TOD. In contrast, in Fig. 4.36 the same detuning was chosen, however, higher order effects lead to unsymmetrical profiles. This demonstrates that the quantitative agreement between the normal form and the full system should only be expected very close to the expansion point.

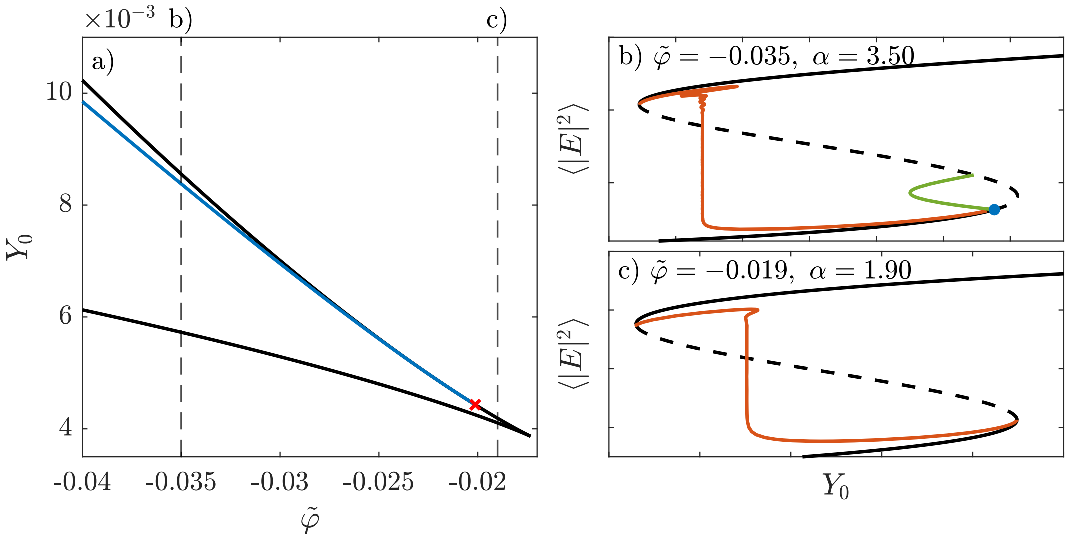


**Figure 4.38:** (a) Two-parameter bifurcation diagram in $(\tilde{\varphi}, Y_0)$ (corresponds to the projection of Fig. 4.35). The folds of the CW state are shown in black and the the Turing bifurcation in blue. At the red cross at $\tilde{\varphi} = -0.02 \Leftrightarrow \alpha = 2$ the Turing bifurcation meets the fold. (b),(c) Cuts indicated in (a) in $Y_0$-direction bellow and above the modulational instability showing the CW branch (black), TLS branch (orange) and pattern branch (green) as well as the Turing bifurcation (blue dot). While (a) is a general result in the long-delay limit, (b),(c) are obtained for $\tau = 800$.

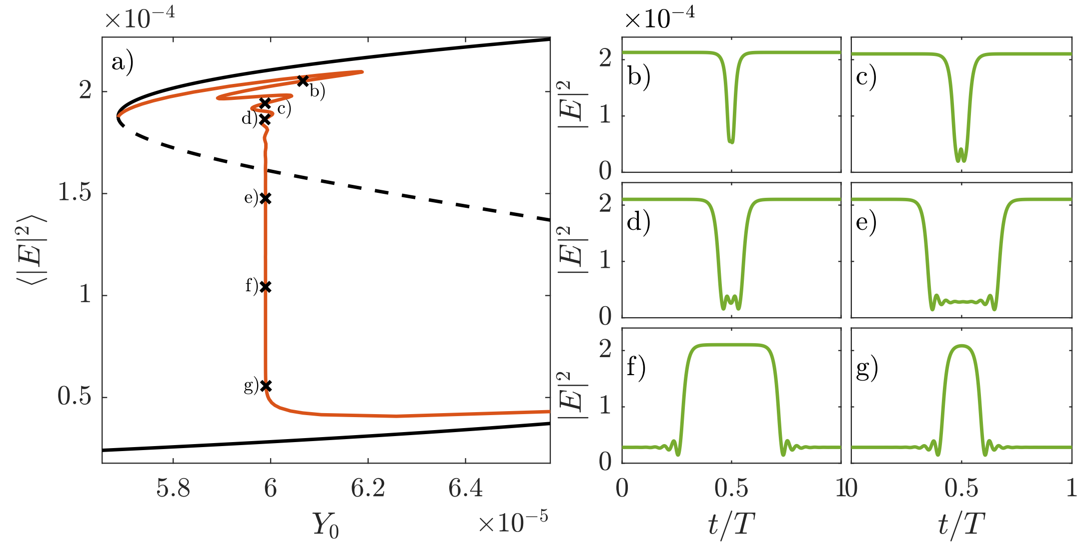


**Figure 4.39:** (a) Bifurcation diagram of Eqs. (3.83) and (3.84) for $\eta = 0.9999$, $\delta = \frac{1}{\sqrt{3}}$, $\alpha = 3$ and $\tilde{\tau} = 100$ leading to $\varphi \approx \pi/3$ and $\tau \approx 8059.3$. The value of $\delta$ is chosen such that it cancels $\beta_3$. As we are operating very close to the expansion point of the normal form, the agreement is excellent which can be seen from the perfectly symmetric profiles in (b)–(g).

## 4.6. Square Waves

When studying the possible frequencies, we found that the KGTI system can give rise to not only $\tau$ but also $2\tau$ periodic solutions (cf. Section 4.2.5). These come in form of so-called square waves, i.e., states that switch between two different plateaus. A simple time trace is shown in Fig. 4.40 (a) where one can see that the intensity remains on each of the two plateau values over intervals of length $\approx \tau$. The corresponding branch in the injection is shown in Fig. 4.40 (b), where the Andronov-Hopf bifurcation on the CW branch from which the square wave branch emerges, is marked by a purple dot. The eigenvalues of CW solution at this point are shown in the inset. The ones in red cross the imaginary axis with a frequency of $\omega = 0.01039 \approx \frac{\pi}{\tau}$.

It is possible to compute the plateau values analytically by assuming $E$ and $Y$ remain constant over an interval of length $\tau$. Denoting the plateau values as $(E_1, Y_1)$ and $(E_2, Y_2)$ over the intervals $[0, \tau]$ and $[\tau, 2\tau]$, respectively, and plugging this into Eqs. (3.83) and (3.84) leads to a set of four algebraic equations which can then be solved. For details on the plateau analysis and a bifurcation analysis of the square waves regime, see [118, 121–123]. Here, we want to build upon this work and present some further interesting dynamics that were found in the course of studying the KGTI system.

In addition to the square wave solutions of length $2\tau$ we also find $\frac{2}{2n+1}\tau$-periodic states, where $n \in \mathbb{N}$, which are called subharmonic square waves. The branches of the first five subharmonic square waves emerging from the CW are shown in Fig. 4.41 (a).

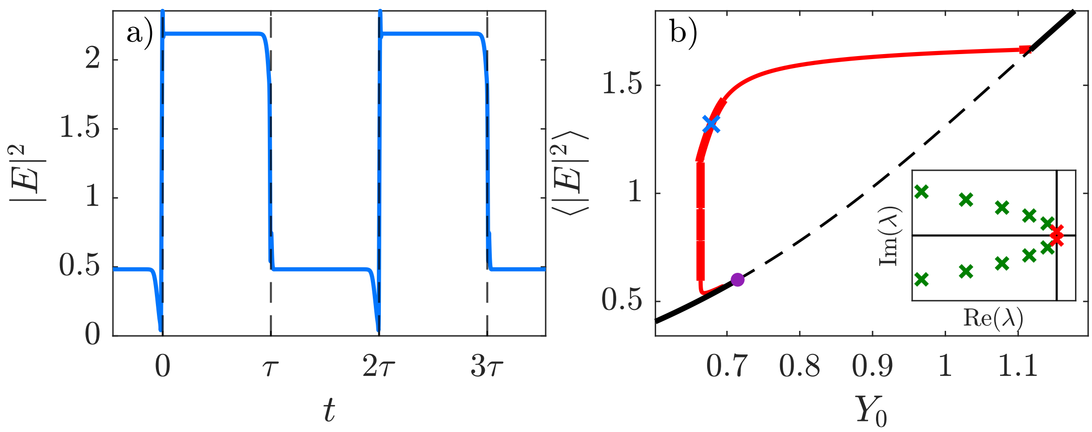


**Figure 4.40:** (a) Time trace of a square wave over four round-trips. The period is $T \approx 603.7$ while $\tau = 300$. (b) Bifurcation diagram of a square wave branch. The state from panel (a) is marked by a blue cross. The Andronov-Hopf bifurcation on the CW branch from which the square wave branch emerges is marked by a purple dot and the corresponding eigenvalues are shown in the inset. Other parameters are $(\delta, \eta, \varphi, h) = (1.7, 0.5, \pi, 2)$.

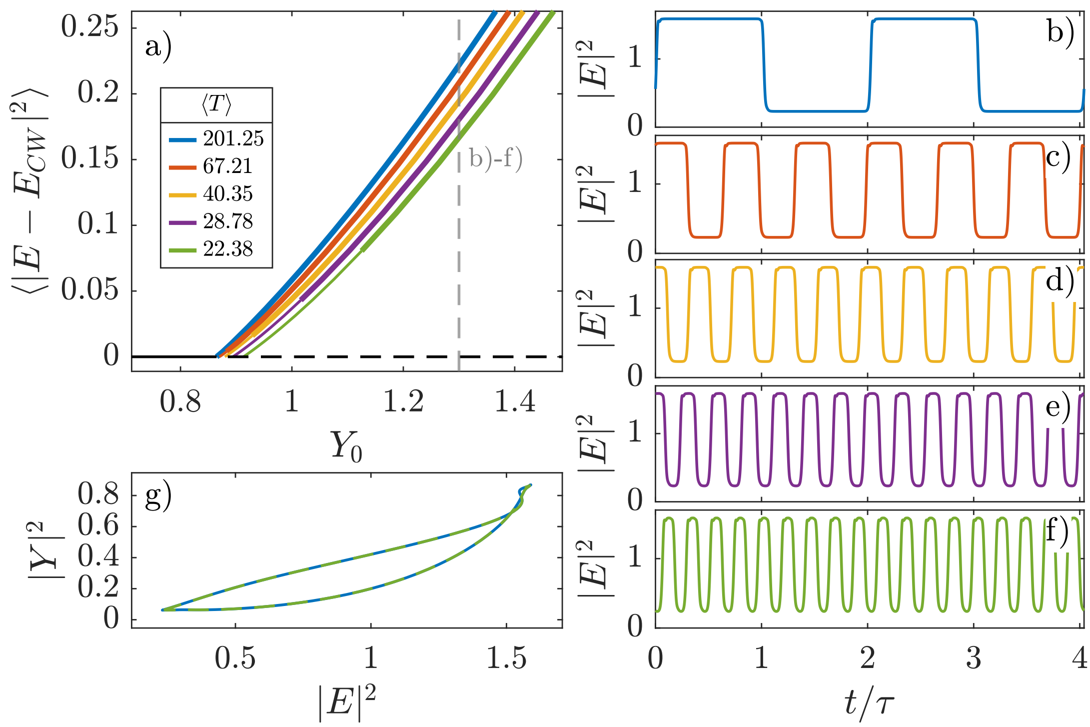


**Figure 4.41:** (a) Bifurcation diagram in $Y_0$ of the first five subharmonic square wave branches. The branches are labeled in the legend according to the average period along the branch. (b)–(f) Profiles in same colors along the vertical dashed gray line in (a) located at $Y_0 = 1.3$. (g) Projection of phase space onto the $(|E|^2, |Y|^2)$-plane with the profiles from (b) (solid blue) and (f) (dashed green). Other parameters are $(\delta, \eta, \varphi, h, \tau) = (0.5, 0.75, \pi/3, 2, 100)$.

Profiles of the different branches for the same injection value are shown in Fig. 4.41 (b)–(f). Over an interval of length $\tau$, the profile in (b) remains on one plateau value, in (c) we find three plateaus, in (d) five and so on. However, when plotting the profiles in the projection of phase space onto the $(|E|^2, |Y|^2)$-plane shown in Fig. 4.41 (g), they are almost indistinguishable. This is due to the defining part of the profile (the orbit connecting the two plateaus) being the same for all subharmonic square wave states. These orbits, which connect the two plateaus, can be understood as heteroclinic orbits in a system with infinite delay [118].

A further interesting scenario emerges when for the parameters in Fig. 4.41 a higher injection values are considered. There, the plateaus become unstable and a high frequency Turing pattern emerges on them. In Fig. 4.42 (a),(b) an exemplary trace is shown in the two-time representation folded using two different periods $T_1$ and $T_2$. The inset in panel (a) shows that $T_1$ is chosen according to the frequency of the pattern on the plateaus while $T_2$ is the period of the underlying square wave itself. A zoomed view of the pattern is shown in the inset of Fig. 4.42 (c). The existence of two periods of the

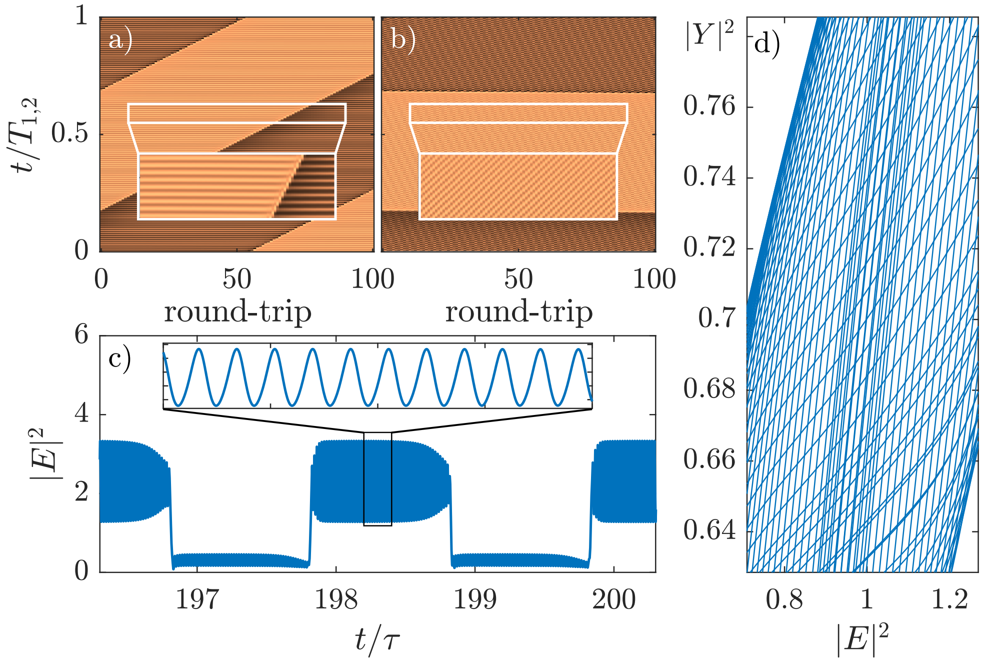


**Figure 4.42:** Result of a DNS of Eqs. (3.83) and (3.84) with parameters as in Fig. 4.41 and $Y_0 = 2$. (a),(b) Two-time representation of the same trace folded with $T_1 = 200.308$ and $T_2 = 201.5$, respectively. (c) Extract of the trace over the last four round-trips. The inset shows the pattern on the upper plateau. (d) Extract of the projection of the phase space onto the $(|E|^2, |Y|^2)$-plane diagram showing the projection of a torus.

profile suggests that the attractor is a torus. The projection of the phase space onto the $(|E|^2, |Y|^2)$-plane (panel (d)) confirms this assumptions. Note, that the frequency of the Turing pattern can not be obtain from a linear stability analysis of the CW solution. Instead, one would need to follow [118] and find the plateaus as steady states of an advanced equation and compute their stability.

Finally, increasing the injection further, leads to the profiles depicted in Fig. 4.43. There, the amplitude of the oscillation on the plateaus is not constant over many round-trips. Hence, one can assume that the system underwent another Andronov-Hopf bifurcation, which leads to a chaotic attractor via the Ruelle–Takens–Newhouse route. To further support the hypothesis of a chaotic attractor, we can measure the largest Lyapunov exponent of the system. We perform the simulation from Fig. 4.43 (b) again with a slightly perturbed initial condition, which is defined over an interval of length $\tau$. Here, we added noise with an small amplitude to the initial condition array. Next, we take the absolute value of the difference between the two simulations, i.e., the evolution of the perturbation. This is shown in Fig. 4.44 (a) on a logarithmic scale. One can observe that the perturbation indeed grows exponentially, i.e., the largest Lyapunov exponent is positive and hence, the attractor is chaotic. In contrast, in Fig. 4.44 (b)

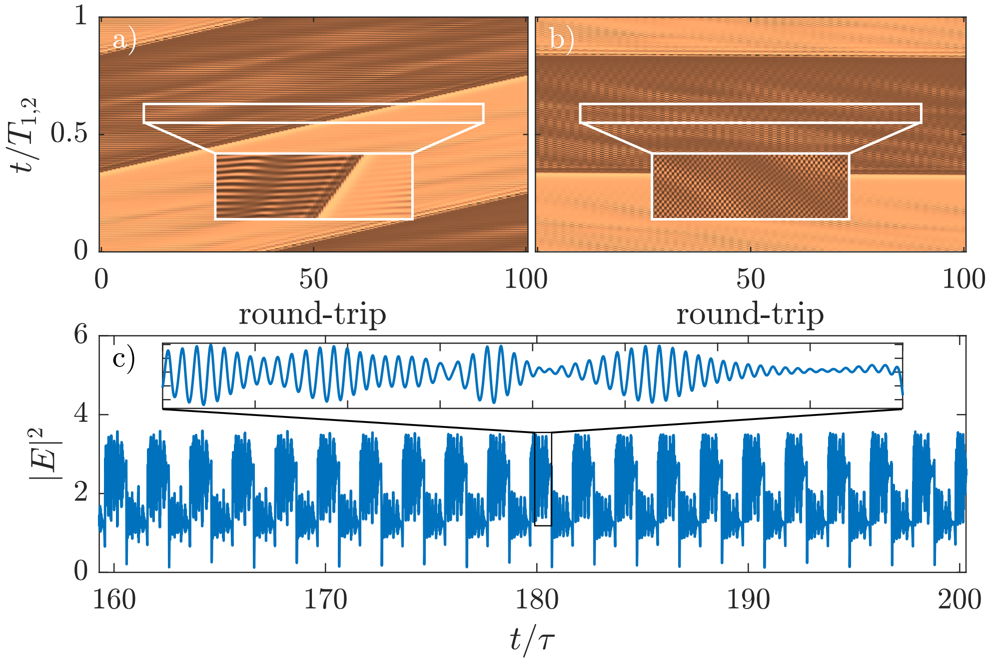


**Figure 4.43:** Same as Fig. 4.42 for $Y_0 = 2.5$. The folding factors of panels (a) and (b) are $T_1 = 200.308$ and $T_2 = 201.16$, respectively.

the perturbation decays and thus, the largest Lyapunov exponent is negative. This result is expected as it was shown in Fig. 4.42 (d) that the attractor is a torus. As the aforementioned mechanism stem from instabilities of the plateaus, they can be found for the subharmonic square waves shown in Fig. 4.41 as well.

Lastly, other peculiar solutions exist in the regime of square waves. When looking at the stability map in Fig. 4.17, in particular the projection on the $(\varphi, Y_0)$-plane in panel (d), we observed that the square wave regime can coexist with locked domain walls. This situation is shown in Fig. 4.45 (a). Here, the square wave branch (yellow) bifurcates from the upper CW state such that it becomes unstable. Hence, the dark TLSs here become unstable here as they reside on that unstable upper CW. Interestingly, a stable dark TLS still exists in a slightly other form: instead of reaching the upper CW state, it settles on the stable plateaus of the SW solution. This is shown in Fig. 4.45 (b),(c). This mixed solution originates in a period-doubling bifurcation of the TLS branch.

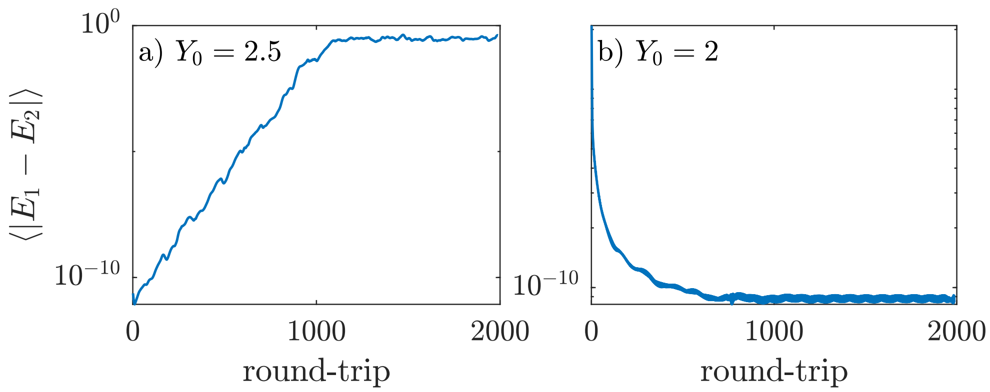


**Figure 4.44:** Evolution of the perturbation $\langle|E_1 - E_2|\rangle$ for injection values from Figs. 4.42 and 4.43. The integral is defined over intervals of length $T_2$. Noise of the amplitude $10^{-10}$ (a) and $10^{-8}$ (b) was added to the initial condition of the simulation of $E_2$.

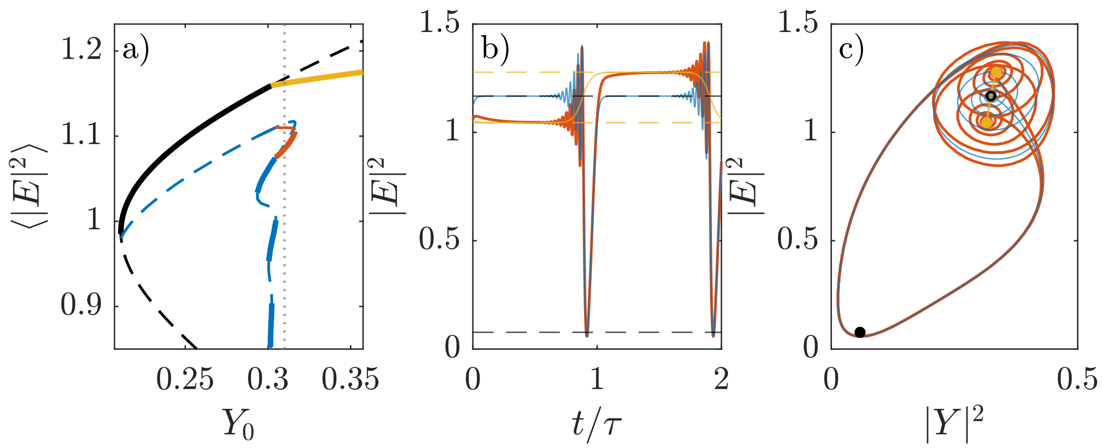


**Figure 4.45:** (a) Bifurcation diagram for $(\delta, \eta, h, \varphi, \tau) = (1.5, 0.75, 2, 0.3\pi, 100)$ with the TLS branch in blue, the square wave branch in yellow and a mixed solution in orange. (b),(c) Profiles for the injection value indicated by the gray dotted line in (a) in the temporal domain and a lower dimensional projection of the phase space, respectively.

## 4.7. Temporal Localized States Beyond the Mean-Field Limit

The current Section 4.7, including the figures, is based on the publication:

[100] T. G. Seidel, J. Javaloyes, and S. V. Gurevich. "Normal dispersion Kerr cavity solitons: beyond the mean-field limit". In: *Opt. Lett.* 49.24 (2024), pp. 7008–7011. DOI: 10.1364/OL.538135

TGS carried out the analytical and numerical work under the supervision of SVG and JJ. All figures were created by TGS. A first draft of the text was created by TGS and gradually refined by all authors.

Mean-field models such as the LLE (4.62) are not always able to account for the complete range of complex dynamics observed and alternative approaches based on, e.g., extended LLE equations [124] or Ikeda map [65] models are used. The latter allows the accurate theoretical and experimental description of several nonlinear resonances and high-power "super cavity solitons" associated with the multistable states [67, 68]. Here, on the other hand, the LLE appears only as a limit case of the model derived from first principles described by Eqs. (3.83) and (3.84) such that we can study regimes beyond the mean-field limit by simply dropping the restrictions of small losses, weak fields and small phases. In this section, we want to systematically study the transition from the mean-field limit towards highly nonlinear regimes.

To get an overview over the occuring dynamics, we once again consider a stability map as described in Section 4.2.6. The results for the normal dispersion regime, i.e., for $\delta > 0$ are summarized in Fig. 4.46(a) together with the corresponding cuts in $\varphi$- and $Y_0$-directions in panels (b) and (c), respectively. Here, the cuts in $\varphi$ in Fig. 4.46(b) correspond to the resonances of the nonlinear cavity. For low injection values, the intensity $|E|^2$ is small such that the effective detuning $\theta = \delta - |E|^2$ fulfills $\theta \sim \delta$. In this case the input-output relation in Eq. (4.37) describes the linear cavity response that has its maximum at $2 \arctan \delta$ where the effective phase $\tilde{\varphi} = \varphi - 2 \arctan \delta$ vanishes; cf. the inset.

Close to the onset of bistability located at $\varphi \approx 0.15\pi$ ($\Leftrightarrow \tilde{\varphi} \approx 0$) yielding the linear cavity response, the dynamics is governed by the LLE with third-order dispersion, cf. Eq. (4.62). This regime persists qualitatively up to a phase of $\varphi \approx -0.05\pi$ from where on the upper CW state becomes Turing unstable as indicated by the emerging yellow region in Fig. 4.46(a). The transition between the two regimes is illustrated in Fig. 4.47 (a),(b), where bifurcation diagrams in $Y_0$ for $\varphi = 0$ and $\varphi = -0.1\pi$, respectively, are presented. Here, not only the TLSs with a periodicity of $\tau$ are shown but also the higher harmonic solutions with shorter periods such that the TLS repeats multiple times per round-trip. These solutions originate in the various Andronov-Hopf bifurcations that occur when the pseudo-continuous spectrum of eigenvalues crosses

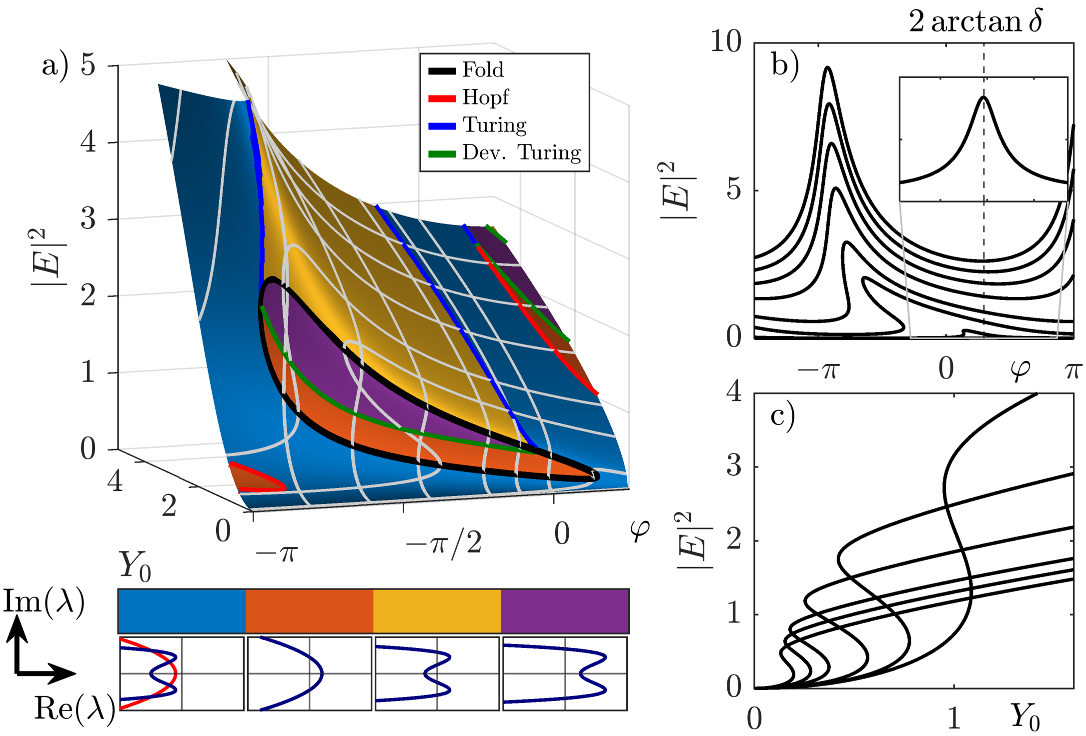


**Figure 4.46:** (a) CW state defined in Eqs. (4.32) and (4.37) in the $(\varphi, Y_0)$-plane for $(\delta,\, h,\, \eta) = (0.5,\, 2,\, 0.75)$. The colors encode the stability information as indicated in the legend at the bottom: blue, orange, yellow, and purple correspond to stable, uniformly unstable, Turing unstable, and developed Turing unstable, respectively. The boundaries between the color patches are bifurcations of the HSSs as indicated by the legend at the top. The white lines are cuts in the one-parameter planes $(\varphi, |E|^2)$ and $(Y_0, |E|^2)$ and are shown in panels (b) and (c), respectively.

the imaginary axis. Due to the scaling of the eigenvalues on the spectrum of $2\pi/\tau$, the emerging periodic solutions possess a periodicity of $T_n \approx \frac{\tau}{n}, n \in \mathbb{N}$, cf. Section 4.2.5.

For $\tau = 50$ and $\varphi = 0$, we find TLSs up to $T_8$ while for $\varphi = -0.1\pi$ we find solutions up to $T_{17}$ while only $T_{1-5}, T_9, T_{13}$ and $T_{15-17}$ are depicted in Fig. 4.47 (b) for clarity. The right insets show exemplary solution profiles of bright TLSs over the length of $\tau$ for $Y_0 = 0.1655$ ($\varphi = 0$) and $Y_0 = 0.22$ ($\varphi = -0.1\pi$), respectively. The occurrence of higher frequencies for $\varphi = -0.1\pi$ can be explained by the change of shape of the pseudo-continuous spectrum, which is depicted in the left insets in Figs. 4.47(a) and 4.47 (b), where it is shown close to the upper fold. Here, one can see the transition from a uniform spectrum with a leading zero eigenvalue to a Turing unstable, i.e., a double well-like-shaped spectrum centered around a finite frequency. One can also observe a reordering of the Andronov-Hopf bifurcation points: While for $\varphi = 0$, the appearing branches are ordered as $T_1$ to $T_8$ and they disappear as $T_8$ to $T_1$ when following the CW branch, for $\varphi = -0.1\pi$ this is not the case. The fact that in Fig. 4.47 (b) the $T_1$

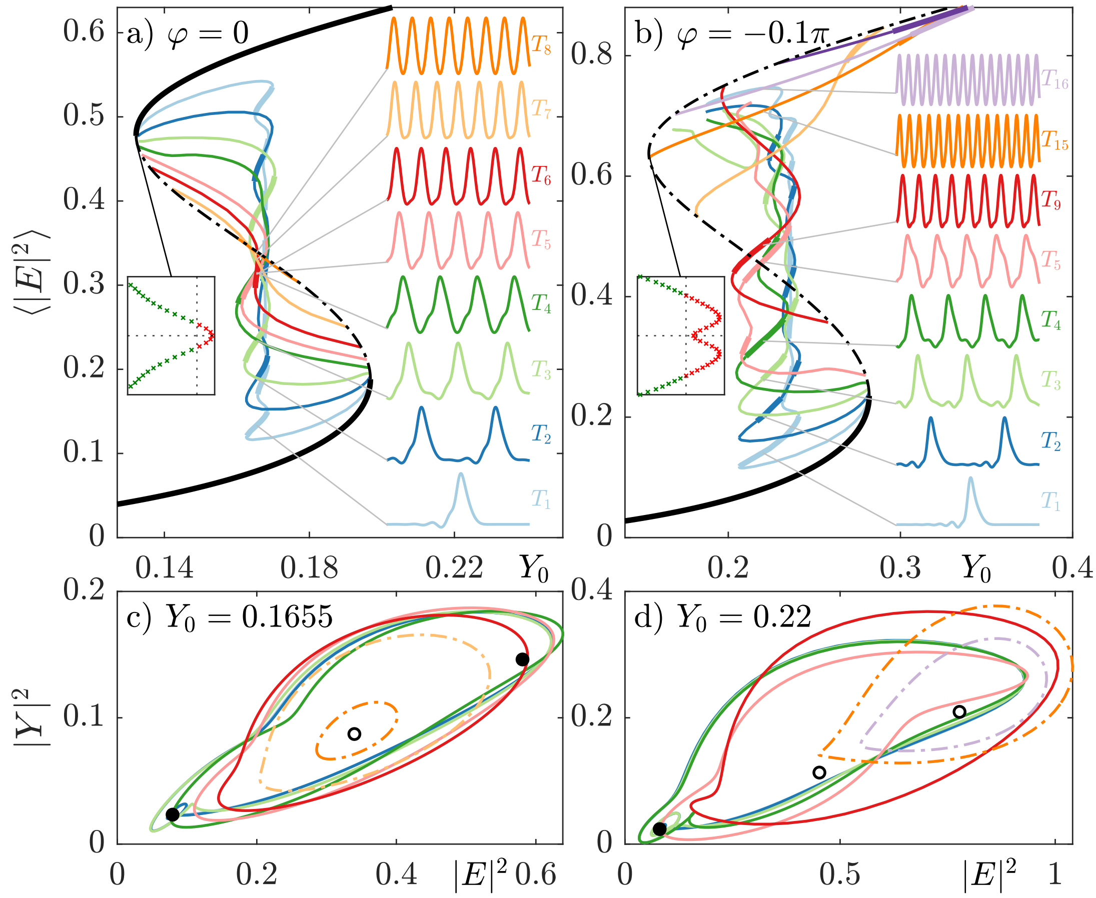


**Figure 4.47:** (a) and (b) Bifurcation diagram of Eqs. (3.83) and (3.84) obtained for $\tau = 50$ for $\varphi = 0$ and $\varphi = -0.1\pi$, respectively. The CW and the TLS branches are depicted in black and colored lines. On the right, solution profiles along the branch indicated by the gray lines are plotted. The insets show the eigenvalue spectrum close to the left fold of the CW branch. (c) and (d): Projection of the phase space onto the $(|E|^2, |Y|^2)$ plane in which the trajectories from the profiles in (a) and (b) are plotted in the same colors. Solid thick (dashed-dotted thin) lines are stable (unstable) solutions, respectively. Other parameters as in Fig. 4.46.

solution does not connect back to the CW is because many more branches exist for the given parameters but are left out because they are unstable (cf. the reconnection of branches shown in Fig. 4.28). The reordering of the Andronov-Hopf bifurcations is also detailed in Fig. 4.48, where the left panel shows the Andronov-Hopf bifurcations in the $(Y_0, \varphi)$-plane and in a three-dimensional representation. One can observe that the Andronov-Hopf branches intersect and thus, the order of the Andronov-Hopf bifurcations is exchanged. This is further clarified in the right panels, where cuts in the $Y_0$-direction are shown, in which the Andronov-Hopf bifurcations are numbered in the order of emergence.

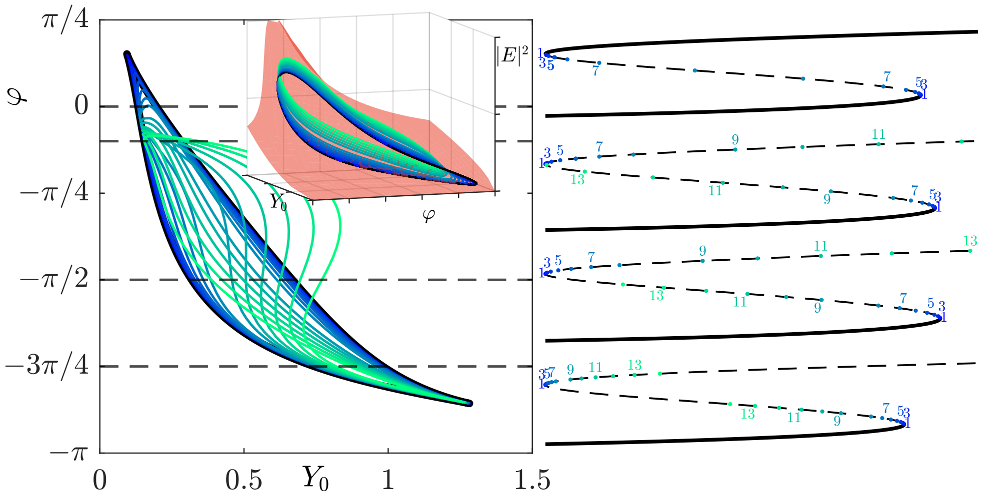


**Figure 4.48:** Reordering of Andronov-Hopf bifurcations. left: two parameter diagram showing the fold of the CW branch (black) as well as Andronov-Hopf bifurcations (colored). The inset shows the steady state plane in red and the Andronov-Hopf and fold branches. Right: Bifurcation diagrams in the injection corresponding to the dashed lines in the left panel. The Andronov-Hopf bifurcations are marked in same colors as in the left panel. The numbers correspond to the order in which the Andronov-Hopf bifurcations emerge close to the lower branch, i.e., the emerging orbit has a period of $\tau/n$ where $n$ is the shown index. For clarity, only every second number is shown. The upper two panels correspond to the cuts shown in Fig. 4.47.

Turning our attention back to Fig. 4.47, we show in panels (c) and (d) a projection of the infinite-dimensional phase space onto the $(|E|^2, |Y|^2)$-plane in which the trajectories of the exemplary bright TLSs in panels (a) and (b) are plotted. Here, solid and dashed-dotted lines correspond to stable and unstable orbits, respectively. Further, the filled and open circles mark the position of the stable and unstable CWs. Notably, the trajectories of the $T_{1-3}$ solutions are almost indistinguishable since the size of the domain is much bigger than the size of the individual structures. These trajectories consist in an excursion close to the upper CW that connects to the lower CW. These are periodic orbits that converge towards a homoclinic connection in the limit of infinite delay $\tau$ [82]. However, for higher harmonic solutions, the TLSs start to interact with each other which leads to a deformation of their temporal shapes as well as their phase space trajectories. These deformations can affect the stability: For $\varphi = 0$, we find stable solutions up to $T_6$ while for $\varphi = -0.1\pi$ solutions remain stable up to $T_9$. The high-frequency solutions $T_{13-17}$ are all unstable in the bistable regime but can be stabilized for higher injection.

To further explore the regime where the upper CW is Turing-unstable, we perform a two-parameter continuation in the $(Y_0, \varphi)$-plane, cf. Fig. 4.49(a). Here, black lines stand for the folds of the CW branch, whereas green and purple lines mark the position

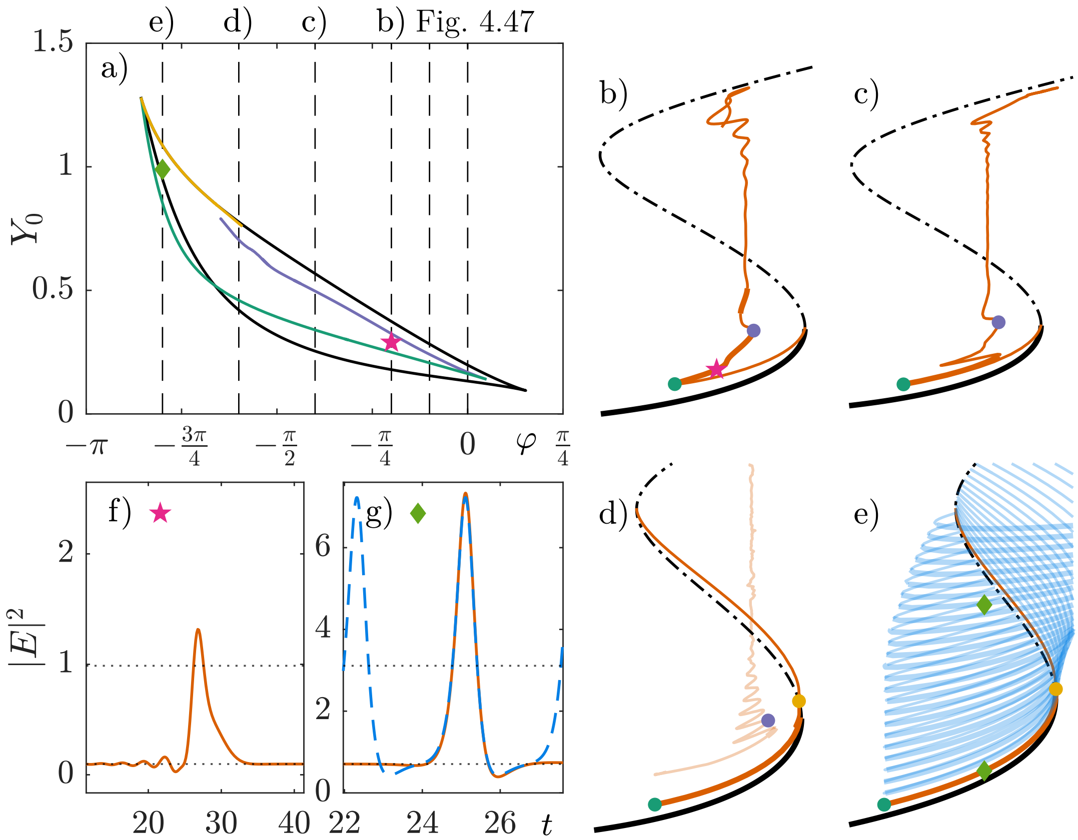


**Figure 4.49:** (a) Two-parameter bifurcation diagram in the ($\varphi$, $Y_0$)-plane. The black and colored lines correspond to the folds of the CW and TLS solutions, respectively. (b)–(e) Cuts in the $Y_0$-direction for $\varphi = \{-0.2\pi, -0.4\pi, -0.6\pi, -0.8\pi\}$ (marked by dashed lines in (a)) with the CW solution in black and the TLS branch in orange. For (e) the harmonic branches are shown in blue up to $T_{25}$. Thick (thin) lines correspond to stable (unstable) solutions. The green, yellow, and purple dots mark the fold bifurcations from panel (a) in the same colors. At the positions marked with a pink star in (b) and light green diamond in (e), the profiles are plotted in panels (f) and (g), respectively. Here, the dotted lines stand for the lower and upper CW values. Other parameters as in Fig. 4.46.

of the folds of the leading bright TLS. Further, dashed vertical lines mark cuts at different $\varphi$ values. The first two cuts correspond to the bifurcation diagrams presented in Fig. 4.47, whereas other cuts are shown in Figs. 4.49 (b)–(e). Here, the corresponding folds of the leading bright TLS shown in (a) are marked by dots in the same color. In panel (e), we also show the harmonic solution branches up to $T_{25}$.

First, we notice that due to the unstable upper CW, the stability on the TLS branch changes as well; see Fig. 4.49(b). In particular, dark TLSs become unstable as they reside for a majority of their trajectory close to the unstable upper CW value and hence experience the same instability. Here, only the TLSs on the first two levels of the snaking structure remain stable. Next, one can see that the shape of the TLS branch changes drastically if $\varphi$ is changed further, cf. panels (c) and (d). This can be explained as the TLS branch reconnects transcritically to another branch with the same period which is shown as a transparent orange line in Fig. 4.49(d). In the course of the transition, the purple marked TLS fold moves to this branch, and a new fold, marked in yellow, appears on the TLS branch, cf. panel (a).

We notice in Fig. 4.49 (e) that the left TLS fold marked by the green dot moves out of the region of bistability. There, the corresponding bright TLS approaches a homoclinic solution in contrast to the double heteroclinic connection of two domain walls for the other TLSs in the bistable region. Additionally, the peak intensity of the resulting TLS is much higher here compared to the bistable case in panel (b). This is shown in panels (f) and (g) where profiles marked by a pink star and light green diamond in panels (a), (b), and (e) are presented. Here, the dotted horizontal lines correspond to the lower and upper CW values, respectively. The dashed blue line in panel (g) is the $T_{18}$ solution which is also marked by a green diamond in panel (e). We observe that profiles around the pulse are indistinguishable, and thus, the fundamental TLS can be interpreted to be an element of this higher frequency solution. The branches of the harmonic states shown in Fig. 4.49 (e) undergo a similar transformation as the fundamental solution from locked domain walls (cf. Fig. 4.47) toward homoclinic orbits. The resulting diagram resembles that of cavity solitons in the anomalous dispersion regime of the LLE [107]. However, there, the branches are organized in a homoclinic snaking diagram whereas here, the branches are independent. Note that also higher frequencies are present, however the shape of these densely packed pulses is altered. A further decrease in $\varphi$ results in a cusp for the folds of both the CW and TLS around the same value of $\varphi = -0.86\pi$, showing that the region of existence of TLSs is still restricted by the folds along the CW branch.

To further analyze the transition of the bright TLS, we investigate the left fold of the TLS branch (green in Fig. 4.49) in more detail. Figure 4.50 shows this branch in green in the $(\varphi, \max(|O|^2))$-plane. Note that the CW background on which this TLS resides changes with $\varphi$. Hence, we also plot the output intensity $|O_s|^2$ of the upper and lower CW values corresponding to the injection value of the TLS-fold branch (cf. black lines in Fig. 4.50(a)). Here, the point where the upper CW line ends, marks the value of $\varphi$ where the TLS branch leaves the bistable regime (cf. Fig. 4.49). Further, the dashed vertical lines are the cuts for Figs. 4.47(a),(b) and Figs. 4.49 (b)–(e). In the right inset in Fig. 4.50(a), one can see that close to $\varphi = 0$, the maximal output intensity $|O|^2$ is close to the upper CW value at the point of emergence since here the TLSs are composed of heteroclinic-like connections. Then, the maximal intensity grows steadily with decreasing $\varphi$ without encountering any discontinuity. It reaches a

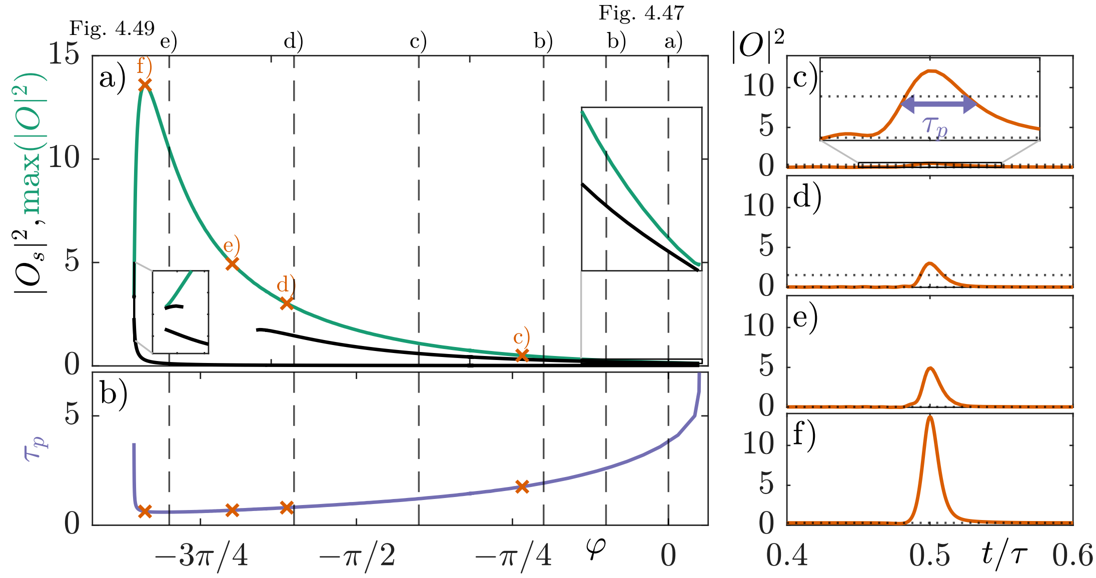


**Figure 4.50:** (a) Evolution of the shape of the TLS as a function of $\varphi$. The maximal intensity of the output field $O$ at the fold of the TLS branch (same data as in Fig. 4.49(a)) is shown in green, whereas black lines are the corresponding upper and lower CW values at the TLS fold. The inset shows a zoom onto the region where the TLS branch emerges. (b) Pulse width $\tau_p$. Orange crosses mark position for which exemplary TLS profiles are shown in (c)–(f). Here, dotted lines are the lower and upper CWs. The dashed lines in (a) and (b) mark the $Y_0$-cuts shown in Figs. 4.47(a) and 4.47(b) and 4.49 (b)–(e).

maximum around $\varphi \approx -0.83\pi$ before rapidly decreasing in intensity toward the lower CW value. This happens around $\varphi \approx -0.86\pi$ where the TLS-fold branch undergoes a cusp bifurcation. Note, that close to the cusp, the TLS-fold branch reenters the bistable region (see left inset). As the pulse amplitude increases, its width $\tau_p$ defined as the full width at half maximum (FWHM) of $|O|^2 - |O_s|^2$ decreases as depicted in Fig. 4.50(b). Both characteristics of the profiles from panels (a) and (b) can be seen in Figs. 4.50 (c)–4.50 (f) where profiles at different points along the fold TLS branch are shown.

In short, we have demonstrated that the KGTI system (3.83),(3.84), operated with normal dispersion and in the highly nonlinear regime where the mean-field approximation does not hold, exhibits a TLS that approaches a homoclinic orbit in the long-delay limit. The latter are stable outside of the bistability region and are devoid of the shortcomings of double heteroclinic solitons induced by domain wall locking which are usually observed in the normal dispersion regime.

## 4.8. Influence of Two-Photon Absorption

Finally, we study the influence of two-photon absorption (TPA). For that, we introduce the parameter $a$ which is the imaginary part of the Kerr parameter $s$ in Eq. (3.83): $s = s_r + ia$. That is, positive $a$ describe losses in the system. This can be understood when considering the effective (nonlinear) phase per round-trip (cf. Eq. (B.94)):

$$\beta = \varphi - 2\arctan\left(\delta - (s_r + ia)\,|E|^2\right). \tag{4.74}$$

The TPA-term results in an attenuation (for $a > 0$) of $|\exp(i\beta)|$ which reads

$$|\exp(i\beta)| = \sqrt{\frac{\left(1 - a\,|E|^2\right)^2 + \left(\delta - s_r\,|E|^2\right)^2}{\left(1 + a\,|E|^2\right)^2 + \left(\delta - s_r\,|E|^2\right)^2}} \leq 1. \tag{4.75}$$

These losses lead to a decreased bistability range until for some critical $a_c$ the bistabilty vanishes. On the other hand, it was demonstrated in the mean-field limit (cf. Section 4.5), that the width of the bistability range can be increased by increasing $\tilde{\varphi}$. Hence, the two effects are counteracting. This is summarized in Fig. 4.51, where we show the two-parameter plane $(Y_0, a)$ for different $\tilde{\varphi}$. We show the evolution of the CW folds (black) and the folds limiting the dark-TLS branch (orange). The smaller $\tilde{\varphi}$ is, the larger is the value of $a_c$, where the cusp of the TLS-folds occurs. In particular, for $\tilde{\varphi} = -0.025$, we find $a_c \approx 0.13$ and for $\tilde{\varphi} = -0.2$, we have $a_c \approx 0.51$, cf. Fig. 4.51 (a) and (c), respectively. Therefore, for an arbitrary value of $a$, one can tune $\tilde{\varphi}$ to reach a bistable regime.

Further, we can observe a stabilizing effect due to TPA. Figure 4.51 (c) was obtained far away from the mean-field limit because $\tilde{\varphi}$ is not small. Hence, due to the large value of $\eta = 0.99$, one could expect strongly oscillating tails, see e.g. Fig. 4.26. However, close to the cusp in Fig. 4.51 (c), the profile exhibits no oscillation on its tails and only if the value of $a$ is decreased, and thus the stabilizing effect of TPA becomes weaker, oscillation are present.

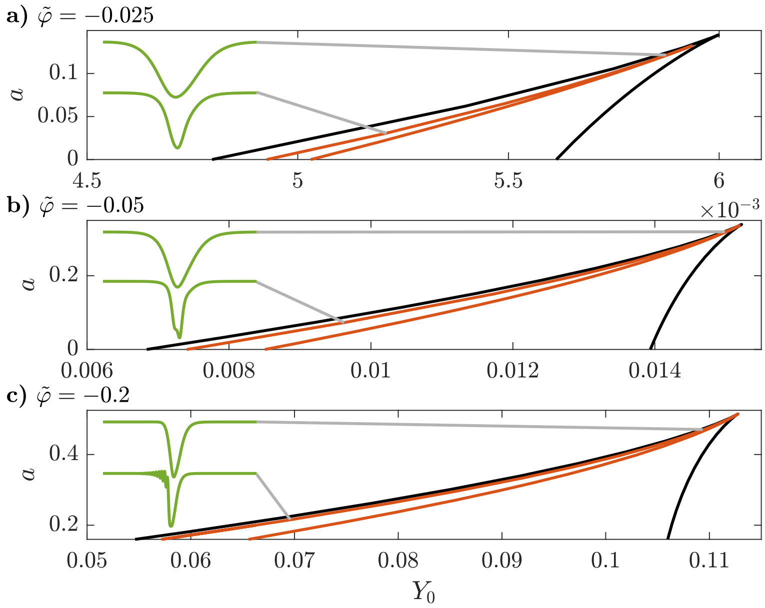


**Figure 4.51:** Two-parameter diagrams in the $(Y_0, a)$-plane for different values of $\tilde{\varphi}$. The CW-folds are shown in black and the folds of the dark-TLS branch in orange. The insets show exemplary profiles. Note the different scalings of the $y$-axis. The parameters are $(\eta, \delta, h, \tau, s_r) = (0.99, 0.5, 2, 300, 1)$ and $\varphi = \tilde{\varphi} + 2 \arctan \delta$.

## 4.9. Conclusion

In this chapter, we analyzed the dynamics found in the KGTI system that is defined by the DAEs (3.83),(3.84). In the process, we studied many different aspects and dynamical regimes of this newly proposed setup. Our findings lay a solid foundation for an experimental realization of the system but can also be regarded as a testbed for the study of dynamical systems with time delay.

First, we demonstrated, that the DAEs describing the KGTI system can be written as a NDDE , which – in the conservative case – is reversible. Hence, it preserves the solution smoothness upon forward and backward propagation and generates a unitary spectrum. Further, we demonstrated the existence of a conserved quantity. Finally, we linked the dynamics to the nonlinear Schrödinger equation with third-order dispersion via a multiple time scale analysis. Thereby, we were able to demonstrate bright solitons at small energies. For higher energies, we observe a lack of integrability. These results provide a novel view on conservative dynamics in time-delayed systems.

Transitioning towards the weakly dissipative regime, we find that the dynamics in the KGTI is captured by the Lugiato–Lefever equation [58] with third-order dispersion. The link to this well-established model allowed us to unveil how the system parameters influence the dispersive properties of the micro-cavity. In particular, we demonstrated that the ratio of TOD and GVD depends on the detuning between the micro-cavity resonance and the injection frequency. For a critical value of the detuning, the contributions of TOD vanish such that the GVD is the dominant effect. Here, the sign of the detuning controls the sign of the GVD, which decides whether the setup operates in the normal or anomalous dispersion regime.

In the following, we focused mainly on the normal dispersion regime, where temporal localized states are created as domain walls that can interlock at discrete distances [55, 120]. In the limit of an infinite delay, the domain walls are heteroclinic orbits that connect the bistable CW states. This enables the formation of both bright and dark TLSs depending on whether the trace resides longer on the lower or upper CW state. We highlighted that, close to the onset of optical bistability, the formation of locked domain walls can successfully be reproduced in a real order parameter equation which corresponds to a real Ginzburg–Landau equation with third-order dispersion and further nonlinear contributions. This normal form predicted a minimal pattern formation scenario for the bright and dark TLS.

Both normal forms allowed for valuable insights into the formation of TLSs which are hidden in the DDE formalism [57]. However, the validity of the DAE model for the KGTI is not limited to restrictions in which the normal forms were derived. Therefore, we were able to perform an analysis beyond the mean-field limit. In a first step, we identified many dynamical regimes from an analytical expression for the pseudo-continuous spectrum of eigenvalues. These findings were summarized in two-parameter bifurcation diagrams termed stability maps. We disclosed many interesting dynamics in the regime of locked domain walls that go beyond the mean-field descriptions. These include the chaotic behavior of the pulse amplitude in a cascade of period-doubling bifurcations, and the self-interaction of TLSs for high feedback values leading to TLS branches that are disconnected from the CW states. Going even further away from the uniform field limit, we found that the dark TLSs become unstable due to a Turing instability of the upper CW state. At the same time, we showed that the bright TLSs exist outside of the bistable regime, thus proving their transition from heteroclinic-like towards homoclinic-like orbits [100]. This was further underlined by the fact that these TLSs exhibit peak intensities that are much higher than the upper CW state. The TLS exist for a large parameter range which highlights their potential for optical frequency comb generation.

# 5. Dynamics of Pulses in Mode-Locked Lasers

Parts of this chapter are based on the publications [125, 126], as indicated at the beginning of the corresponding sections.

## 5.1. Introduction

In the second part of the thesis, we study the dynamics of multi-pulse states in the output of a passively mode-locked (PML) laser. For the theoretical description, many detailed parameter studies have been performed, that reveal how these structures emerges from the continuous-wave state; see e.g. [21, 25, 41, 44, 45, 127, 128]. In particular, pulses in a PML laser can be described as temporal localized states (TLSs) in long-delay limit and therefore, multiple pulses can be used to generate arbitrary patterns [21]. This reveals that TLSs exhibit translational symmetry, i.e., they can be moved freely in the cavity. At the same time the carrier interaction in PML lasers are phase-invariant (cf. Eqs. (3.156) and (3.157) which only depend on the intensity) such that the TLSs are rotational invariant as well. These two symmetries are undamped neutral modes of the TLSs, which means that they sensitive to small interactions between pulses. Studying the dynamics induced by the interactions is the topic of the chapter.

The mentioned symmetries influence the structure of the resulting frequency combs. For a single pulse in a cavity of size $\tau$ it is quite clear that the resulting spectrum consists in modes that are spaced by the free spectral range $\nu_{\mathrm{FSR}} = \frac{2\pi}{\tau}$; see e.g., the schematic of the frequency comb in the introduction in Fig. 1.1. However when we consider, for instance, two equidistant pulses the repetition rate effectively halves, such that one expects a comb with a spacing of $2\nu_{\mathrm{FSR}}$ meaning that every second mode must have canceled out. But is this always the case? How exactly do the symmetries discussed above influence the frequency spectrum? These are the main questions we want to answer in the part of the thesis. Note that our approach provides a novel viewpoint on the emergence of coherent states in mode-locked lasers as we consider the phases of the pulses, instead of, those of the cavity modes as in, e.g. [129–131].

For the theoretical modeling, we derived a model based upon DDEs in Section 3.3, cf. Eqs. (3.152)–(3.154). From that, a normal form PDE, the Haus master equation, can be derived in the mean-field limit, see Eqs. (3.155)–(3.157). While one could theoretically simply consider one of the two models and perform a parameter study, this is not a feasible approach as the phase and position dynamics occur on slow time scales. Consequently, simulations would be very computational costly and tedious as they need to be performed over many $\sim 10^5$ round-trips. Hence, we want to use a more refined approach by projecting the high-dimensional dynamics of the full models onto the low-dimensional subspace spanned by the pulses' phases and positions. This gives further insights on the dynamics of multi-pulse configurations as the resulting effective *equations of motion* (EOM) reveal the underlying interaction mechanisms. In this context, using the PDE model (3.155)–(3.157) is a more convenient choice because TLSs are steady states of the PDE model but periodic orbits in the DDE model. In particular, this makes it much easier to linearize the system equations as well as the corresponding adjoint system, which is more involved for a DDE model; see e.g. [132]. For these reason, we employ the PDE model (3.155)–(3.157) in the following derivation. However, key results are cross-checked using the DDE model (3.152)–(3.154).

The full derivation of the EOM is presented in Appendix C. Here, we want to present briefly the main steps and concepts. The dynamical system in Eqs. (3.155)–(3.157) is a system of PDEs, which can be broken down in its fundamental components such that the dynamics of the vector function[14] $\psi = (\mathrm{Re}(E),\, \mathrm{Im}(E),\, g - g_0,\, q - q_0)$ is described by

$$M\partial_\xi \psi = \mathcal{L}\left(\partial_z\right)\psi + \mathcal{N}(\psi) + \eta e^{i\Omega} M\psi(z - \tau_f)\,, \tag{5.1}$$

where $E$ is the optical field, $g$ and $q$ are the gain and absorber populations, $g_0$ is the pumping rate, $q_0$ is the value of the unsaturated losses, $\mathcal{L}$ and $\mathcal{N}$ are linear and nonlinear operators, $\xi$ and $z$ are the slow and fast time scales, and $M = \mathrm{diag}(1, 1, 0, 0)$ is a mass matrix, which needs to be included because Eqs. (3.156) and (3.157) do not contain derivatives with respect to the slow time $\xi$. The last term is a non-local term describing the effect of a time-delayed feedback (TDF) loop with a time-delay $\tau_f$ (cf. Section 3.3.6). We define a stationary solution of Eq. (5.1) (i.e., a single pulse) as

$$\psi_s = \psi_{s,f} + \psi_{s,c} = \left(\mathrm{Re}(E_s),\, \mathrm{Im}(E_s),\, g_s - g_0,\, q_s - q_0\right)^T, \tag{5.2}$$

which is composed of the stationary solution for the

$$\begin{aligned} \text{field components } \psi_{s,f} &= (\mathrm{Re}(E_s),\, \mathrm{Im}(E_s),\, 0,\, 0) \\ \text{and the carrier components } \psi_{s,c} &= (0,\, 0,\, g_s - g_0,\, q_s - q_0). \end{aligned}$$

Next, we employ the ansatz that a multi-pulse state $\Psi$ is the sum of multiple stationary TLSs $\psi_j$ which are shifted and rotated with respect to each other. We denote the shifts (resp. positions) $z_j$ and rotations (resp. phases) $\varphi_j$, respectively (cf. blue and orange

[14] The superposition ansatz below makes it necessary to consider $g_s - g_0$ as the carrier component and not just $g_s$. Same for $q_s$.

arrows in the schematic in Fig. 1.3):

$$\Psi = \sum_{j=1}^{N} \psi_j + \delta\psi\,, \tag{5.3}$$

where $\delta\psi$ accounts for small deviations from the simple summation and

$$\psi_j = R\left(\varphi_j\right)\psi_s\left(z - z_j\left(\xi\right)\right)\,, \tag{5.4}$$

where $R\left(\varphi\right)$ is a matrix that rotates the field components of $\psi_s$ by a phase $\varphi$. In the next step, we use the ansatz (5.3) and plug it into Eq. (5.1). Linearizing around the stationary solution $\psi_s$ leads to the linear eigenvalue problem $\mathcal{J}_s v = M\,\lambda v$, where $\mathcal{J}_s$ is the Jacobian of the stationary solution $\psi_s$. The latter possesses two zero eigenvalues corresponding to the neutral modes $v_t = \partial_z\psi_s$ and $v_p = \partial_\varphi\psi_s$ which describe the translational and phase invariance, respectively. Consequently, the adjoint system possesses two neutral modes as well because the eigenvalues of the adjoint Jacobian are the complex conjugated eigenvalues found in the direct system. We denote these eigenmodes as $w_t$ and $w_p$ which are defined as $\mathcal{J}_s^\dagger w = M\,\bar{\lambda} w$.

The core of the EOM derivation consists in noticing that the perturbation $\delta\psi$ in Eq. (5.3) must remain small and bounded. As such, all the terms in the EOM must be orthogonal to the kernel of $\mathcal{J}_s$ since, otherwise, $\delta\psi$ would grow without bound (cf. Eq. (C.33)). This condition is achieved by projecting onto the adjoint eigenmodes $w_t$ and $w_p$ and to use that $(v_i, w_i)$ form a biorthogonal set. We further assume that the pulses are well-separated so that the interactions are weak and that we can neglect shape deformation modes. Finally, notice that we consider the solution basis $\psi_s$ for the case of zero feedback (i.e., $\eta = 0$). This approach allows us to add weak feedback as a source of motion and phase dynamics. In other words, the TDF induced satellites are treated as a first order perturbation. In practice, it means that the feedback induced satellites are small enough that they do not induce any interaction with the carriers. This leads to the following EOM (see Appendix C for the complete derivation):

$$\begin{aligned}\dot{z}_m = \sum_{k\neq m} \big[ & A_t\left(\Delta_{km}\right)\sin\left[\theta_{km} + r_t\left(\Delta_{km}\right)\right] + B_t\left(\Delta_{km}\right) + \\ & \eta L_t\left(\tau_f + \Delta_{km}\right)\sin\left[\Omega + \theta_{km} + u_t\left(\tau_f + \Delta_{km}\right)\right]\big],\end{aligned} \tag{5.5}$$

$$\begin{aligned}\dot{\varphi}_m = \sum_{k\neq m} \big[ & A_p\left(\Delta_{km}\right)\sin\left[\theta_{km} + r_p\left(\Delta_{km}\right)\right] + B_p\left(\Delta_{km}\right) + \\ & \eta L_p\left(\tau_f + \Delta_{km}\right)\sin\left[\Omega + \theta_{km} + u_p\left(\tau_f + \Delta_{km}\right)\right]\big]\,,\end{aligned} \tag{5.6}$$

Here, we define the phase and position difference

$$\theta_{km} := \varphi_k - \varphi_m \text{ and } \Delta_{km} := z_k - z_m.$$

It is important to remember that periodic boundary conditions apply, i.e., $\varphi_0 = \varphi_N$, $\varphi_{N+1} = \varphi_N$, $z_0 = z_N - \tau$ and $z_{N+1} = z_1 + \tau$. While the phase interaction is encoded in the sine-terms, the position-dependent interaction strength is governed by the nonlinear functions $A_{t,p}(\Delta_{km}), B_{t,p}(\Delta_{km}), L_{t,p}(\Delta_{km}), r_{t,p}(\Delta_{km})$ and $u_{t,p}(\Delta_{km})$. These forces result from overlap integrals between the adjoint eigenvectors and the solution profile (see App. C, Eqs. (C.51), (C.52), (C.56), (C.60) and (C.61)) for the formal definitions). Note that the indices $p, t$ stand for the phase- and translation-invariance, respectively. The nonlinear functions represent the different possibilities in which the pulses can interact, namely

$A_{p,t}(\Delta)$ : Amplitude of phase-dependent term describing the exchange of phase information via overlap of the pulses' decaying tails

$r_{p,t}(\Delta)$ : The phase corresponding to $A_{p,t}(\Delta)$

$B_{p,t}(\Delta)$ : Phase-independent interaction describing interaction via carrier depletion

$L_{p,t}(\Delta)$ : Amplitude of phase-dependent term describing the exchange of phase information via overlap of a pulse and satellite induced by TDF

$u_{p,t}(\Delta)$ : The phase corresponding to $L_{p,t}(\Delta)$

Note that Eqs. (5.5) and (5.6) consider the couplings between all pulses. However, for the interaction via tails, the interaction with the nearest neighbors is dominant as the tails decay exponentially. The same reasoning applies to the carrier interaction. The interaction via time-delayed feedback depends on the value of the secondary time delay $\tau_f$. When $\tau_f$ is close to $p\frac{\tau}{N}, p \in \mathbb{N}$, the satellite of the $k$-th pulse influences the $(k-p)$-th pulse (cf. Fig. 1.3 where, e.g., the satellite of pulse two interacts with pulse one because $\tau_f \approx \tau/N$). Further, the time scales of the individual terms in Eqs. (5.5) and (5.6) are not necessarily in the same order of magnitude. For instance, in shorter cavities, interactions via carriers is dominant such that the pulses evolve rapidly towards an equidistant configuration. This property effectively decouples Eqs. (5.5) and (5.6) from each other, which leads to two distinct cases that will be considered in the following. In the decoupled case, we can observe a pure phase dynamics. This situation is detailed in Section 5.2. In the general case, phases and positions interact with each other, which is the subject of Section 5.3.

## 5.2. Phase Dynamics

The current Section 5.2, including the figures, is based on the following publication and the corresponding Supplemental Material:

[125] T. G. Seidel, A. Bartolo, A. Garnache, M. Giudici, M. Marconi, S. V. Gurevich, and J. Javaloyes. "Multistable Kuramoto Splay States in a Crystal of Mode-Locked Laser Pulses". In: *Phys. Rev. Lett.* 134 (2025), p. 033801. DOI: 10.1103/PhysRevLett.134.033801

TGS carried out the analytical and numerical work under the supervision of SVG and JJ. AB carried out the experimental work under the supervision of MM, MG and AG. The figures used in this section were created by TGS with the exception of Fig. 5.17 that was created by AB. A first draft of the text of the theoretical part was created by TGS and gradually refined by all authors.

We start with the case of equidistant pulses. That is, we consider solutions where the translational mode is strongly damped, i.e., $\dot{z}_m = 0$ and $z_m - z_{m-1} = \frac{\tau}{N}$. This applies to configurations where the pulses are densely packed and the resulting pulse configuration is called a *harmonic mode-locked* ($\mathrm{HML}_N$) state, which have been widely observed in mode-locked lasers [133–135]. Note that this situation does not correspond to the long-delay limit anymore, as the pulses are fixed in their position. However, the derived EOM are still valid, as we will demonstrate in this section. A sketch of the described situation is shown in Fig. 5.1 (a). There, we show in green the phases of the individual pulses (cf. panel (b)), and in purple the respective phase differences (cf. panel (c)). First, we can simplify the EOM in Eqs. (5.5) and (5.6) with these restrictions, which is shown in Appendix C.2.2. We obtain the Kuramoto model [136] with nearest neighbor interactions

$$\dot{\varphi}_m = A_+ \sin\left(\varphi_{m-1} - \varphi_m + \psi_+\right) + A_- \sin\left(\varphi_{m+1} - \varphi_m + \psi_-\right) + \zeta_j \,, \tag{5.7}$$

where $\zeta_j$ is the is the projection of the white Gaussian noise in Eq. (3.155) onto the phase- and position-modes. Here, we consider a cavity without an additional feedback loop, i.e., $\eta = 0$ for this whole subsection. However, we note that even in the presence of time-delayed feedback, the resulting equations are structurally the same, cf. Appendix C.2.2, such that the results presented here apply for this case as well.

The interactions described by Eq. (5.7) has important implications as PML lasers are often considered to be coherent by default, yet Eq. (5.7) implies that the phases evolve as individual oscillators. Whether and how much synchronization occurs, depends on the interplay between the coherent forces $A_\pm$ and the noise level $\zeta$. As such, we analyze Eq. (5.7) using statistical approaches. Further, we want to test the validity of Eq. (5.7) by comparing it to the full Haus master equation (3.155)–(3.157). First, we

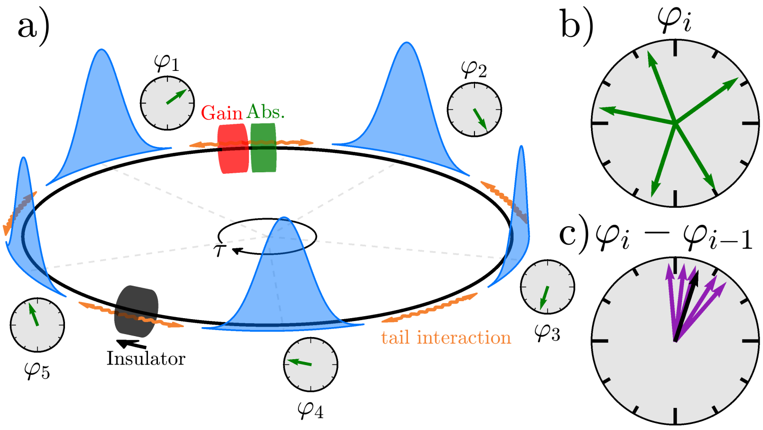


**Figure 5.1:** (a) Schematic of a unidirectional ring cavity mode-locked by a saturable absorber and operated in the $\mathrm{HML}_5$ regime. Each pulse possesses a phase $\varphi_i$, as indicated by the small clocks. The phases and their differences are shown in (b) and (c) while the black arrow in (c) denotes to value of the order parameter $b$ (cf. Eq. (5.12)) representing the average coherence.

introduce formally the concept of coherence in Section 5.2.1. Next, we considered the special case of reciprocal interaction (i.e., $A_+ = A_-$ and $\psi_+ = \psi_- = 0$ in Eq. (5.7)) in Section 5.2.2. The resulting symmetries allow for an analytical approach to compute statistical quantities. Finally, in Section 5.2.3, we consider the general, non-reciprocal case in detail, and describe in Section 5.2.4 how to measure the effects in an experiment.

### 5.2.1. Measuring Coherence

In order to measure the degree of coherence in a train of pulses, it is instructive to introduce an order parameter. We consider for a configuration of $N$ pulses the first order correlation function

$$g^{(1)}(s) = \frac{\langle E^*(t)\, E(t+s)\rangle}{\left\langle |E(t)|^2 \right\rangle}, \tag{5.8}$$

where we define the temporal average as

$$\langle E(t)\rangle := \frac{1}{\tau} \int\limits_0^\tau E(t)\, dt. \tag{5.9}$$

The first order correlation function needs to be evaluated at the position of the neighboring pulse, i.e., when $N$ pulses are present in the cavity of size $\tau$, we consider $g^{(1)}\left(\frac{\tau}{N}\right)$. Experimentally, this makes sense as the first order correlation function can be obtained by interfering the optical field with itself after a retarded time $\tau/N$. As described in the introduction of this chapter, we employ a superposition ansatz, i.e., we assume the pulses to be identical in shape. Hence, the full electrical field $E$ of an $N$-pulse state can be written as

$$E\left(t\right)=\sum_{k=1}^{N}E_s\left(t-\left(k-1\right)\frac{\tau}{N}\right)e^{-i\varphi_k}\,, \tag{5.10}$$

where $E_s\left(t\right)$ is the optical field for a single pulse. Further, we define $\bar{I}:=\left\langle\left|E_s\left(t\right)\right|^2\right\rangle$ as the average intensity of a single pulse. The first order correlation function then reads

$$\begin{aligned}
g^{(1)}\left(\frac{\tau}{N}\right) &= \frac{\left\langle\left[\sum_{k=1}^{N}E_s^*\left(t-\left(k-1\right)\frac{\tau}{N}\right)e^{i\varphi_k}\right]\left[\sum_{k=1}^{N}E_s\left(t-k\frac{\tau}{N}\right)e^{-i\varphi_k}\right]\right\rangle}{\left\langle\left|\sum_{k=1}^{N}E_s\left(t-k\frac{\tau}{N}\right)e^{i\varphi_k}\right|^2\right\rangle}\\
&= \frac{\left\langle\sum_{k=1}^{N}\left|E_s\left(t-k\frac{\tau}{N}\right)\right|^2e^{i\left(\varphi_{k+1}-\varphi_k\right)}\right\rangle}{N\bar{I}}\\
&= \frac{\left\langle\left|E_s\left(t\right)\right|^2\right\rangle}{N\bar{I}}\sum_{k=1}^{N}e^{i\left(\varphi_{k+1}-\varphi_k\right)}\\
&= \frac{1}{N}\sum_{k=1}^{N}e^{i\left(\varphi_{k+1}-\varphi_k\right)},
\end{aligned} \tag{5.11}$$

where we used the periodic boundaries, i.e., $E_s\left(t\right)=E_s\left(t-\tau\right)$ and considered the overlap of the pulses to be small such that we neglect all cross terms, i.e.,

$$\left\langle\left|\sum_{k=1}^{N}E_s\left(t-k\frac{\tau}{N}\right)e^{i\varphi_k}\right|^2\right\rangle=N\bar{I}.$$

Hence, we can define an order parameter $b$:

$$b:=g^{(1)}\left(\frac{\tau}{N}\right)=\frac{1}{N}\sum_{j=1}^{N}e^{i\left(\varphi_{j+1}-\varphi_j\right)}. \tag{5.12}$$

In the schematic setup in Fig. 5.1, the order parameter is visualized as a black arrow in panel (c). The value of $b$ contains two quantities. The modulus encodes the level of synchronization while the argument is the average phase. It makes sense to consider the limit cases of $b$. First, the modulus of $b$ is 1, if all pulses have the same phase difference with respect to their neighbor, i.e., if $\varphi_{j+1}-\varphi_j=\beta=const.\;\forall j$, then

$$b=\frac{1}{N}\sum_{j=1}^{N}e^{i\left(\varphi_{j+1}-\varphi_j\right)}=e^{i\beta}. \tag{5.13}$$

In contrast, the modulus of $b$ is 0 when the phase differences are equally spread, i.e., $\varphi_{j+1} - \varphi_j = \frac{2\pi p}{N} j$ where $p \in \mathbb{Z}$. Then we find

$$b = \frac{1}{N} \sum_{j=1}^{N} e^{i\frac{2\pi p}{N} j} = 0. \tag{5.14}$$

### 5.2.2. Reciprocal Interaction

As a first step, we consider the special case of reciprocal interaction where $A_+ = A_-$ and $\psi_+ = \psi_- = 0$ in Eq. (5.7). This introduces a symmetry in the EOM (5.7), which enables us to perform analytical calculations to obtain statistical quantities. The basis for that is laid by calculating the *probability density function* (PDF) for the distribution of the pulses' phases. Using the simplifications due to reciprocal interaction, we can write the Kuramoto model in Eq. (5.7) as

$$\dot{\varphi}_j = \sin\left(\varphi_{j-1} - \varphi_j\right) + \sin\left(\varphi_{j+1} - \varphi_j\right) + \zeta_j\left(t\right) \tag{5.15}$$
$$= F_j\left(\varphi_1, \ldots, \varphi_N\right) + \zeta_j\left(t\right). \tag{5.16}$$

Here, the amplitude of the force $A_\pm$ is scaled into the time. This symmetric form enables us to define a potential that satisfies $F_j = -\frac{\partial U}{\partial \varphi_j}$

$$U\left(\varphi_1, \ldots, \varphi_N\right) = -\int F_j\left(\varphi_1, \ldots, \varphi_N\right) d\varphi_j \tag{5.17}$$
$$= -\int \left[\sin\left(\varphi_{j-1} - \varphi_j\right) + \sin\left(\varphi_{j+1} - \varphi_j\right)\right] d\varphi_j \tag{5.18}$$
$$= -\sum_{k=1}^{N} \cos\left(\varphi_{k-1} - \varphi_k\right). \tag{5.19}$$

Note that this is the crucial step which cannot be accomplished in the general, non-reciprocal case. Using Eq. (5.19), we can establish the corresponding Fokker-Planck equation for the PDF $P\left(\varphi_1, \ldots, \varphi_N\right)$. It reads

$$\frac{\partial P}{\partial t} + \sum_j \frac{\partial}{\partial \varphi_j}\left[F_j P\right] = \frac{\sigma^2}{2} \sum_j \frac{\partial^2 P}{\partial \varphi_j^2}, \tag{5.20}$$

where we denote with $\sigma$ the amplitude of the noise $\zeta_j$ in Eq. (5.15)[15]. We solve for the steady state of the PDF, i.e., $\partial_t P = 0$. Introducing $\beta = \dfrac{2}{\sigma^2}$ and integrating a first time

[15] Note that this $\sigma$ is not the same as in Eq. (3.155). They are related by projecting the noise in Eq. (3.155) onto the phase- and translation-modes.

leads to

$$\sum_j F_j P = -\sum_j \frac{\partial U}{\partial \varphi_j} P = \frac{1}{\beta} \sum_j \frac{\partial P}{\partial \varphi_j} \tag{5.21}$$

This equation has the solution

$$P = \mathcal{N} \exp\left(-\beta U\right), \tag{5.22}$$

where $\mathcal{N}$ is a normalization constant. Its value is defined via the integral condition

$$1 = \int P\left(\varphi_1, \ldots, \varphi_N\right) d\varphi_1 \ldots d\varphi_N \tag{5.23}$$

and therefore

$$\frac{1}{\mathcal{N}} = \int \exp\left(\beta \sum_k \cos\left(\varphi_{k-1} - \varphi_k\right)\right) d\varphi_1 \ldots d\varphi_N. \tag{5.24}$$

To evaluate this integral, we define the phase difference $\theta_k = \varphi_{k-1} - \varphi_k$. However, in this notation, one variable is dependent of the other ones, i.e., we can write

$$\theta_j = -\sum_{k \neq j} \theta_k. \tag{5.25}$$

As a choice, we express $\theta_N$ in terms of the other phase differences without loss of generality. Then we obtain

$$\begin{aligned} \frac{1}{\mathcal{N}} &= 2\pi \int \exp\left(\beta \sum_{k=1}^{N-1} \cos\theta_k + \beta \cos\left(\sum_{k=1}^{N-1} \theta_k\right)\right) d\theta_1 \ldots d\theta_{N-1} && (5.26) \\ &= 2\pi \int \prod_{k=1}^{N-1} \exp\left(\beta \cos\theta_k\right) \exp\left(\beta \cos\left(\sum_{k=1}^{N-1} \theta_k\right)\right) d\theta_1 \ldots d\theta_{N-1}, && (5.27) \end{aligned}$$

where we have an additional factor of $2\pi$ because the integral is now over $N-1$ phases. Next, we introduce the *modified Bessel function of first kind* $I_n\left(x\right)$ which are defined as

$$I_n\left(x\right) = \frac{1}{\pi} \int_0^\pi \cos\left(n\theta\right) e^{x \cos\theta} d\theta. \tag{5.28}$$

In particular, we use the following expansion in terms of the Bessel functions

$$\exp\left(\beta \cos\theta\right) = \sum_{k=-\infty}^{\infty} I_k\left(\beta\right) e^{ik\theta}. \tag{5.29}$$

With that, we can simplify the expression in Eq. (5.27):

$$\begin{aligned}\frac{1}{\mathcal{N}} =& 2\pi \int \left( \sum_{n=-\infty}^{\infty} I_n(\beta) \exp(in\theta_1) \right) \dots \left( \sum_{n=-\infty}^{\infty} I_n(\beta) \exp(in\theta_{N-1}) \right) \\ & \left( \sum_{n=-\infty}^{\infty} I_n(\beta) \exp\left( in \sum_{k=1}^{N-1} \theta_k \right) \right) d\theta_1 \dots d\theta_{N-1}\end{aligned} \tag{5.30}$$

$$\begin{aligned}=& 2\pi \int \sum_{k_1,k_2,\dots,k_N=-\infty}^{\infty} I_{k_1}(\beta) I_{k_2}(\beta) \dots I_{k_N}(\beta) \exp(ik_1\theta_1) \exp(ik_2\theta_2) \dots \\ & \exp(ik_{N-1}\theta_{N-1}) \exp\left( ik_N \sum_{l=1}^{N-1} \theta_l \right) d\theta_1 \dots d\theta_{N-1}\end{aligned} \tag{5.31}$$

$$\begin{aligned}=& 2\pi \int \sum_{k_1,k_2,\dots,k_N=-\infty}^{\infty} I_{k_1}(\beta) I_{k_2}(\beta) \dots I_{k_N}(\beta) \\ & \exp\left[i\left((k_1+k_N)\theta_1 + \dots + (k_{N-1}+k_N)\theta_{N-1}\right)\right] d\theta_1 \dots d\theta_{N-1}.\end{aligned} \tag{5.32}$$

This can also be expressed as the product of $N-1$ integrals, each of which has the form

$$\int_0^{2\pi} e^{i(k+l)\theta} d\theta = 2\pi\delta_{k,-l}. \tag{5.33}$$

Using this, we can simplify Eq. (5.32) to obtain

$$\frac{1}{\mathcal{N}} = (2\pi)^N \sum_{k_1,k_2,\dots,k_N=-\infty}^{\infty} I_{k_1}(\beta) I_{k_2}(\beta) \dots I_{k_N}(\beta) \delta_{k_1,-k_N} \delta_{k_2,-k_N} \dots \delta_{k_{N-1},-k_N} \tag{5.34}$$

$$= (2\pi)^N \sum_{k_N=-\infty}^{\infty} \left(I_{-k_N}(\beta)\right)^{N-1} I_{k_N}(\beta) \tag{5.35}$$

$$= (2\pi)^N \sum_{k=-\infty}^{\infty} \left(I_k(\beta)\right)^N, \tag{5.36}$$

where we used that $I_{-k}(\beta) = I_k(\beta)$ in the last step. Finally, we obtain from Eq. (5.22) the PDF

$$P(\varphi_1, \dots, \varphi_N) = \frac{1}{(2\pi)^N} \frac{\exp\left(\beta \sum_{j=1}^N \cos(\varphi_{j-1} - \varphi_j)\right)}{\sum_{k=-\infty}^{\infty} \left(I_k(\beta)\right)^N}. \tag{5.37}$$

To make this expression more accessible, we want to calculate the projection on a single phase $\varphi_m$ as well as two phases $\varphi_m, \varphi_n$. After some algebra, we find

$$P(\varphi_m) = \frac{1}{2\pi}, \tag{5.38}$$

$$P(\varphi_m, \varphi_n) = \frac{1}{4\pi^2} \frac{\sum_{k,l=-\infty}^{\infty} \left(I_k(\beta)\right)^{N+m-n} \left(I_l(\beta)\right)^{n-m} \cos\left((k-l)(\varphi_m - \varphi_n)\right)}{\sum_{k=-\infty}^{\infty} \left(I_k(\beta)\right)^N}, \tag{5.39}$$

where $m > n$ without loss of generality. The result from Eq. (5.38) is highly intuitive as the EOM in the beginning has a rotational symmetry, such that all phases have the same probability. Equation (5.39) simplifies for neighboring phases, e.g., $\varphi_1$ and $\varphi_2$:

$$P(\varphi_1, \varphi_2) = \frac{\exp(\beta \cos(\varphi_1 - \varphi_2))}{4\pi^2} \frac{\sum_{k=-\infty}^{\infty} \cos(k(\varphi_1 - \varphi_2)) (I_k(\beta))^{N-1}}{\sum_{k=-\infty}^{\infty} (I_k(\beta))^N}. \tag{5.40}$$

In order to test the derived PDF (5.37) and the corresponding projections, we perform extended simulations of the EOM (5.15) to get a sufficient statistical average. As Eq. (5.15) is an ODE, the simulations are not computationally expensive and can be carried out using an Euler (or Runge–Kutta) scheme. An extract of a long simulation is shown in Fig. 5.2 in the top left panel. We can numerically obtain the corresponding PDF $P(\varphi_m)$ by considering an histogram (cf. Fig. 5.2 bottom left), which exhibits excellent agreement to the analytical PDF from Eq. (5.38) shown in red. The same can be done for the PDF $P(\varphi_1, \varphi_2)$ from Eq. (5.40) which is shown in Fig. 5.2 in the right panel. Again, we find excellent agreement between analytical and numerical results.

Next, the result from Eq. (5.39) can also be interpreted as the PDF for the phase difference, i.e., $P(\varphi_m - \varphi_n)$ which makes it a useful tool to measure the coherence between two phases $\varphi_m$ and $\varphi_n$. The projection on a single argument results in an additional factor of $2\pi$ such that

$$P(\varphi_m - \varphi_n) = 2\pi P(\varphi_m, \varphi_n). \tag{5.41}$$

This PDF is shown in Fig. 5.3, where one can observe that the level of correlation between pulses $\varphi_1$ and $\varphi_n$ is the highest for the directly neighboring pulses ($n = 2, 7$) and decreases when considering neighbors which are further away. For large distances, the distribution approaches $1/(2\pi)$ which corresponds the uncorrelated (i.e., random) case. The analytical results (red line) are in excellent agreement with the results from the numerical simulation (histogram).

There are further interesting projections one can consider, such as the projection onto the absolute value and argument of the order parameter $P(|b|, \arg(b))$. However, it is not possible to compute analytical expressions for arbitrary projections. For that reasons we just consider the numerical results which are shown in Fig. 5.4 in the right panel. We can observe, that the projection onto the argument of $b$ (bottom left) exhibits three distinct peaks located at $0, \pm\frac{2\pi}{7}$. These configurations correspond to the stable steady states of Eq. (5.15), see Section 5.2.3 for more details on the steady states and their stability. On the other hand, the projection onto the absolute value (top left) has a maximum around $|b| = 0.35$, while the average value $|\langle v \rangle| \approx 0.24$ is slightly lower.

As the order parameter corresponds to the first order correlation function (cf. Sec-

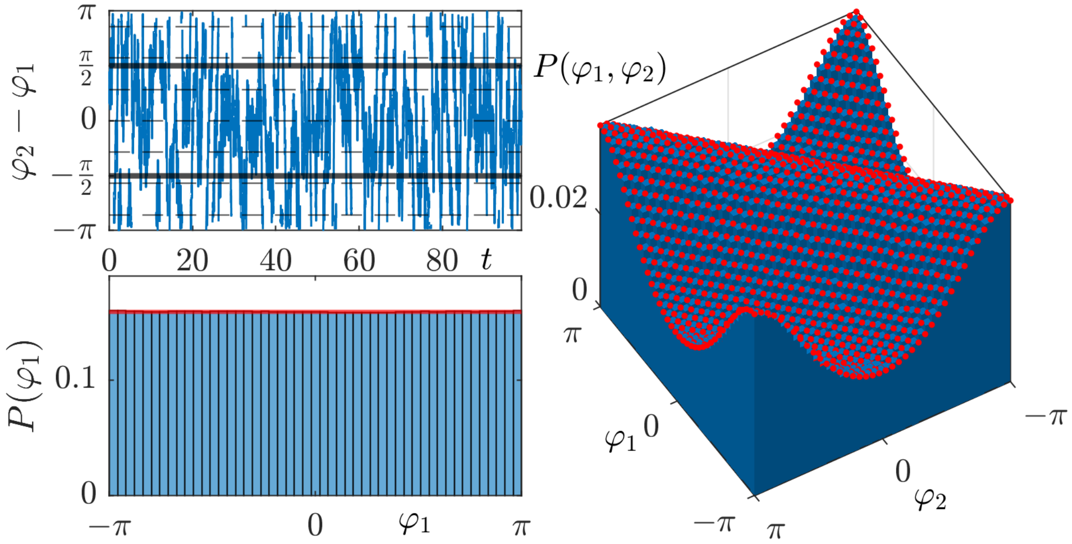


**Figure 5.2:** The top left panel shows an extract of a time trace of the EOM (5.15) with $N = 7$ phases, the full time trace has a length of $5 \times 10^5$. The histograms correspond to the numerical PDF projected on a single phase (left) and two phases (right), respectively. The red line and dots are the analytical results from Eqs. (5.38) and (5.40).

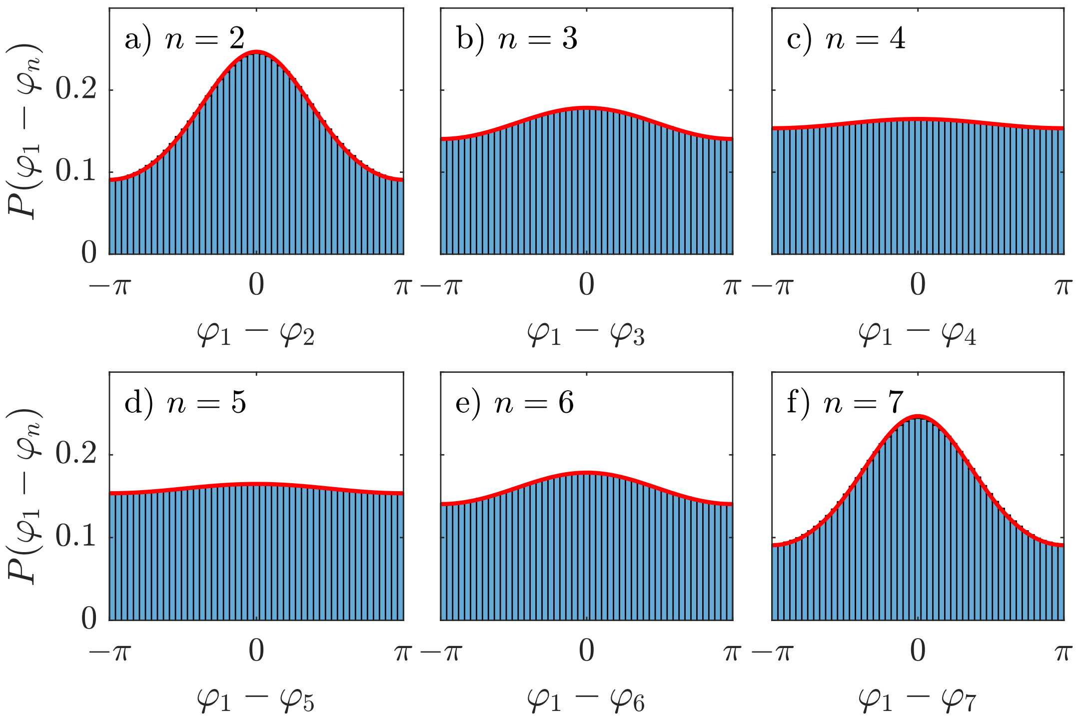


**Figure 5.3:** Same data as in Fig. 5.2. The PDF is projected on the phase difference: $P(\varphi_1 - \varphi_n)$ for $n = 2, \ldots, N$. The red lines are from the analytical solution Eq. (5.41).

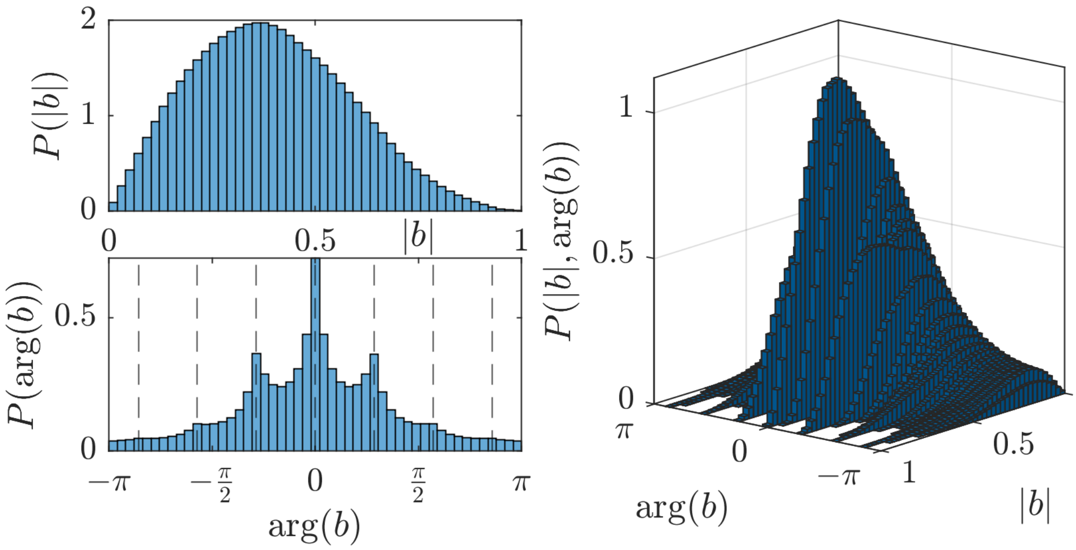


**Figure 5.4:** Same data as in Fig. 5.2. Here, the PDF is projected on the order parameter, in particular the absolute value of $b$ and the argument of $b$.

tion 5.2.1), it is of great importance for experimental realizations. Hence, we aim to calculate analytically its expectation value in the next step. For a quantity $q$, the expectation value is defined as $\langle q \rangle = \int qP(\varphi)d\varphi$. Applying this to the order parameter $b$, we obtain

$$
\begin{aligned}
\langle b \rangle &= \int_{-\pi}^{\pi} b\left(\varphi_1, \ldots, \varphi_N\right) P\left(\varphi_1, \ldots, \varphi_N\right) d\varphi_1 \ldots d\varphi_N && (5.42)\\
&= \int_{-\pi}^{\pi} \left(\frac{1}{N} \sum_k e^{i(\varphi_{k-1}-\varphi_k)}\right) P\left(\varphi_1, \ldots, \varphi_N\right) d\varphi_1 \ldots d\varphi_N && (5.43)\\
&= \frac{\mathcal{N}}{N} \int_{-\pi}^{\pi} \left(\sum_k \cos\left(\varphi_{k-1}-\varphi_k\right)\right) \exp\left(\beta \sum_k \cos\left(\varphi_{k-1}-\varphi_k\right)\right) d\varphi_1 \ldots d\varphi_N && (5.44)\\
&= \frac{\mathcal{N}}{N} \int_{-\pi}^{\pi} \partial_\beta \exp\left(\beta \sum_k \cos\left(\varphi_{k-1}-\varphi_k\right)\right) d\varphi_1 \ldots d\varphi_N && (5.45)\\
&= \frac{\mathcal{N}}{N} \partial_\beta \int_{-\pi}^{\pi} \exp\left(\beta \sum_k \cos\left(\varphi_{k-1}-\varphi_k\right)\right) d\varphi_1 \ldots d\varphi_N && (5.46)\\
&= \frac{\mathcal{N}}{N} \partial_\beta \frac{1}{\mathcal{N}}, && (5.47)
\end{aligned}
$$

where we used the definition of the normalization constant from Eq. (5.24) in the last step. As we need to compute the derivative of $\mathcal{N}$ with respect to $\beta$, we need to establish the derivative of the Bessel function:

$$\partial_\beta I_k(\beta) = I_{k-1}(\beta) - \frac{k}{\beta} I_k(\beta) \tag{5.48}$$

$$= \frac{k}{\beta} I_k(\beta) + I_{k+1}(\beta) . \tag{5.49}$$

With that and the normalization constant from Eq. (5.36), we can further simplify Eq. (5.47):

$$\langle b \rangle = (2\pi)^N \frac{\mathcal{N}}{N} \partial_\beta \left[ \sum_{k=-\infty}^{\infty} (I_k(\beta))^N \right] \tag{5.50}$$

$$= (2\pi)^N \mathcal{N} \sum_{k=-\infty}^{\infty} (I_k(\beta))^{N-1} \partial_\beta I_k(\beta) \tag{5.51}$$

$$= (2\pi)^N \mathcal{N} \sum_{k=-\infty}^{\infty} (I_k(\beta))^{N-1} \left( I_{k-1}(\beta) - \frac{k}{\beta} I_k(\beta) \right) \tag{5.52}$$

$$= \frac{\sum_{k=-\infty}^{\infty} (I_k(\beta))^{N-1} \left( I_{k-1}(\beta) - \frac{k}{\beta} I_k(\beta) \right)}{\sum_{k=-\infty}^{\infty} (I_k(\beta))^N} . \tag{5.53}$$

The last part of the sum vanishes because the sum is symmetric (from $k = -\infty$ to $k = \infty$). So we remain with

$$\langle b \rangle = \frac{\sum_{k=-\infty}^{\infty} (I_k(\beta))^{N-1} I_{k-1}(\beta)}{\sum_{k=-\infty}^{\infty} (I_k(\beta))^N} . \tag{5.54}$$

We want to consider the two limit cases, namely the thermodynamic limit ($N \to \infty$) and the limit of two pulses ($N = 2$). First, in the limit of $N \to \infty$, we find that Eq. (5.54) converges to

$$\lim_{N\to\infty} \langle b \rangle = \frac{I_1(\beta)}{I_0(\beta)} . \tag{5.55}$$

Next, the case of two pulses is special because left and right interaction go to the same neighbor. Therefore, the complete system is described by a single phase difference $\theta = \varphi_2 - \varphi_1$ and the calculations simplify a lot. First, the order parameter is $b = \frac{1}{2}\left(e^{i\theta} + e^{-i\theta}\right) = \cos\theta$. Next, the potential is $U_{N=2} = 2\cos(\theta)$ and therefore the PDF reads

$$P_{N=2}(\theta) = \mathcal{N} \exp[2\beta \cos\theta] . \tag{5.56}$$

The normalization constant is

$$\frac{1}{\mathcal{N}} = \int_{-\pi}^{\pi} \exp\left(-2\beta\cos\theta\right) d\theta = 2\pi I_0\left(2\beta\right) \tag{5.57}$$

and the expectation value for the order parameter reads

$$\begin{aligned}
\langle b_{N=2}\rangle &= \int_{-\pi}^{\pi} \cos\left(\theta\right) P_{N=2}\left(\theta\right) d\theta && (5.58)\\
&= \frac{1}{2\pi I_0\left(2\beta\right)} \int_{-\pi}^{\pi} \cos\left(\theta\right) \exp\left[2\beta\cos\theta\right] d\theta && (5.59)\\
&\overset{(5.28)}{=} \frac{I_1\left(2\beta\right)}{I_0\left(2\beta\right)}. && (5.60)
\end{aligned}$$

The two limit cases in Eqs. (5.55) and (5.60) will become important in Section 5.2.3 (in particular, see Fig. 5.13).

Finally, we consider the limit of low noise levels, i.e., low temperature, for the expectation value $\langle b\rangle$. As the noise level vanishes ($\sigma \to 0$), we find that $\beta \to \infty$. For large arguments the modified Bessel functions of first kind can be expanded as

$$I_k\left(\beta\right) = \frac{e^{\beta}}{\sqrt{2\pi\beta}} \left[1 - \frac{4k^2 - 1^2}{1\left(8\beta\right)} \left(1 - \frac{4k^2 - 3^2}{2\left(8\beta\right)} \left(1 - \frac{4k^2 - 5^2}{3\left(8\beta\right)} \left(1 - \dots\right)\right)\right)\right]. \tag{5.61}$$

We consider terms up to $\sigma^2$, i.e., up to $\beta^{-1}$. Then we remain with

$$\begin{aligned}
I_{k-1}\left(\beta\right) &= \frac{e^{\beta}}{\sqrt{2\pi\beta}} \left[1 - \frac{4\left(k-1\right)^2 - 1}{8\beta} + \mathcal{O}\left(\beta^{-2}\right)\right] && (5.62)\\
&= \frac{e^{\beta}}{\sqrt{2\pi\beta}} \left[1 - \frac{4k^2 - 1}{8\beta} - \frac{1-2k}{2\beta} + \mathcal{O}\left(\beta^{-2}\right)\right] && (5.63)\\
&= I_k\left(\beta\right) - \frac{e^{\beta}}{\sqrt{2\pi\beta}} \frac{1-2k}{2\beta} + \mathcal{O}\left(\beta^{-\frac{5}{2}}\right). && (5.64)
\end{aligned}$$

As we truncate all terms $\mathcal{O}\left(\beta^{-2}\right)$, we can rewrite the second term in Eq. (5.64) in terms of a Bessel function

$$\frac{1-2k}{2\beta} \frac{e^{\beta}}{\sqrt{2\pi\beta}} = \frac{1-2k}{2\beta} I_k\left(\beta\right) + \mathcal{O}\left(\beta^{-\frac{5}{2}}\right) \tag{5.65}$$

such that we can simplify Eq. (5.64) to

$$I_{k-1}\left(\beta\right) = \left(1 - \frac{1-2k}{2\beta}\right) I_k\left(\beta\right) + \mathcal{O}\left(\beta^{-\frac{5}{2}}\right). \tag{5.66}$$

Plugging this into Eq. (5.54), we obtain

$$\langle b\rangle = \frac{\sum_{k=-\infty}^{\infty}\left(I_k\left(\beta\right)\right)^{N-1}\left(1-\frac{1-2k}{2\beta}\right)I_k\left(\beta\right)}{\sum_{k=-\infty}^{\infty}\left(I_k\left(\beta\right)\right)^{N}} \tag{5.67}$$

$$= 1-\frac{\sum_{k=-\infty}^{\infty}\left(I_k\left(\beta\right)\right)^{N}\frac{1-2k}{2\beta}}{\sum_{k=-\infty}^{\infty}\left(I_k\left(\beta\right)\right)^{N}}. \tag{5.68}$$

Here, the term linear in $k$ vanishes as the sum is symmetric and we remain with

$$\langle b\rangle = 1-\frac{1}{2\beta} \tag{5.69}$$

$$= 1-\frac{\sigma^2}{4}. \tag{5.70}$$

This shows that for low noise values the order parameter is described by an inverted parabola.

### 5.2.3. Coherence and Phase Configurations in Harmonic Solutions

Finally, we consider the general, non-reciprocal case of the Kuramoto model in Eq. (5.7) (i.e., $A_+ \neq A_-$; $\psi_+, \psi_- \neq 0$). First, we want to study which pulse configurations can exist in an HML regime. Assuming that all pulses are identical, it is sufficient to consider the ring boundary conditions in Fig. 5.1(a). For a configuration to be a steady state, the phase difference $\Delta\varphi$ between neighboring pulses must be constant for all pulses. This condition is only fulfilled if $N$-times this phase difference sums up to a multiple of $2\pi$, i.e., $N\Delta\varphi = 2\pi p$ with $p \in [1, N]$. We characterize the steady states by the integer index $p$ or equivalently a phase difference

$$\Delta\varphi_p = \frac{2\pi}{N}p. \tag{5.71}$$

This is the definition of *a splay state* [137]. Note that while the splay state $\Delta\varphi_p$ is a steady state for $\dot{\Delta\varphi}$, the corresponding phases themselves are given by

$$\varphi_j^{(p)} = \Delta\varphi_p j + \omega_p t, \tag{5.72}$$

where $\omega_p$ is a common phase rotation that reads

$$\omega_p = A_+\sin\left(\psi_+ - \frac{2\pi p}{N}\right) + A_-\sin\left(\psi_- + \frac{2\pi p}{N}\right). \tag{5.73}$$

However, this common phase rotation is small as it scales with the amplitudes $A_\pm$.

Further analyzing the Kuramoto model in Eq. (5.7), we are interested in which of the splay states are stable. Hence, we perform a linear stability analysis of Eq. (5.7). We consider a perturbed state $\varphi_j = \varphi_j^{(p)} + \delta_j$ and obtain

$$\begin{aligned}\dot{\delta}_j =& A_+ \sin\left(-\Delta\varphi_p + \delta_{j-1} - \delta_j + \psi_+\right) + \\ & A_- \sin\left(\Delta\varphi_p + \delta_{j+1} - \delta_j + \psi_-\right)\end{aligned} \tag{5.74}$$

$$= \omega_p + k_+\left(\delta_{j-1} - \delta_j\right) + k_-\left(\delta_{j+1} - \delta_j\right) + \mathcal{O}\left(\delta^2\right), \tag{5.75}$$

$$\begin{aligned}\text{where } k_- =& A_- \cos\left(\psi_- + \Delta\varphi_p\right), \\ k_+ =& A_+ \cos\left(\psi_+ - \Delta\varphi_p\right).\end{aligned} \tag{5.76}$$

Next, we expand the perturbation in Fourier modes

$$\delta_j = \omega_p t + A_q\left(t\right) \exp\left[ijq\right], \tag{5.77}$$

where $t$ is the slow time and $A_q(t)$ is the amplitude of mode $q = \frac{2\pi p}{N}$. The amplitude evolves as

$$\dot{A}_q\left(t\right) = \left(\dot{\delta}_j - \omega_p\right) \exp\left(-ijq\right) \tag{5.78}$$

$$= \left[\left(k_+ + k_-\right)\left(\cos\left(q\right) - 1\right) + i \sin\left(q\right)\left(k_- - k_+\right)\right] A_q\left(t\right). \tag{5.79}$$

The stability is governed by the real part of $\dot{A}_q$, in particular by the sign of $k_+ + k_-$. Solving $0 = k_+ + k_-$ defines the borders of stability, which is given by

$$\alpha_k = k\pi + \arctan\left(\frac{A_- \cos\psi_- + A_+ \cos\psi_+}{A_- \sin\psi_- - A_+ \sin\psi_+}\right) \tag{5.80}$$

That is, $\Delta\varphi_p$ is stable if $\alpha_0 < \Delta\varphi_p < \alpha_1$ and unstable otherwise. We observe that the range of stability is always $\pi$ and that the corresponding half-circle of stability is simply rotated as a function of $(A_\pm, \psi_\pm)$. The most important consequence of Eq. (5.80) is that the splay states that are solutions of Eq. (5.7) can be *multistable*. In fact, for $N \geq 5$, there must be at least two states that fall within the range of stability and 50% of states are stable in the thermodynamic limit $N \to \infty$.

In order to test our predictions, we simulated numerically the full PDE model in Eqs. (3.155)–(3.157). To extract phase information from a time trace, one could simply take the phase at the maximum peak intensity. However, this approach results in discontinuities when the maximum intensity changes its index along the discrete numerical spatial grid. A better approach is to take the information of the full pulse into account. For that, we cut each round-trip into $N$ pieces such that in every piece of size $\tau/N$ a single pulse resides (approximately) in its center. Then we integrate the phase weighted by the intensity over this interval which reads $I_j = \left[\frac{(j-1)\tau}{N}, \frac{j\tau}{N}\right]$. That is, we

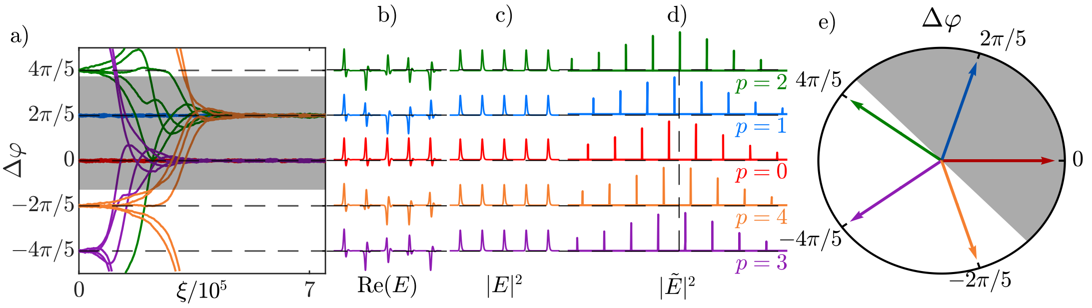


**Figure 5.5:** (a) Evolution over the slow time $\xi$ of various splay states associated to the $\text{HML}_5$ solutions obtained from solving Eqs. (3.155)–(3.157)) numerically. The initial phase differences are given by $\Delta\varphi_p = \frac{2\pi}{N}p$, and are shown in panels (b) and (c) where one can see that the intensity profiles are identical while the real parts of the electric fields differ. (d) Frequency spectrum of the initial conditions. For each phase difference the corresponding comb is shifted by $\frac{p}{\tau}$. (e) Phase plane visualization of the initial conditions used in (a)–(d). The shaded gray areas in panels (a) and (e) correspond to the region of stability which is of size $\pi$, cf. Eq. (5.80). The trajectories in (a) converge to steady states within the region of stability. Parameters are $(\gamma, k, \alpha_g, \alpha_q, \tau, g_0, \Gamma_g, q_0, \Gamma_q, s, \sigma) = (40, 0.1056, 1.5, 0.5, 12.5, 4g_{\text{th}}, 0.08, 0.27, 1, 10, 10^{-5})$. For the corresponding parameters $A_\pm, \psi_\pm$ of the phase model, see Fig. C.1.

compute

$$\varphi_j = \frac{\int_{I_j} |E|^2 \arg(E)\, dz}{\int_{I_j} |E|^2\, dz}. \tag{5.81}$$

This approach is motivated by calculating the center-of-mass of a profile, which can be done in a similar way and which we use to define the position $z_j$:

$$z_j = \frac{(j-1)\tau}{N} + \frac{\int_{I_j} |E|^2\, z dz}{\int_{I_j} |E|^2\, dz}. \tag{5.82}$$

While the positions are constant here, this quantity will be of use in Section 5.3. Note that the choice of weighting the integrals with $|E|^2$ is arbitrary, one could also choose higher (or lower powers) depending on how much one wants to weigh the center of the pulse.

Going back to testing our predictions, we initialize a configuration with five pulses for each of the five different splay states, see Fig. 5.5 (a),(b). All these solutions correspond to the same intensity profile as demonstrated in Fig. 5.5 (c). However, we note that a phase shift $\Delta\varphi_p$ between pulses separated by a distance $\Delta z = \tau/N$ corresponds to an offset of the carrier frequency $\nu_p = \Delta\varphi_p/(2\pi\Delta z) = p/\tau$. Consequently, these $N$ splay states correspond to frequency combs that are shifted of $p$ times the fundamental

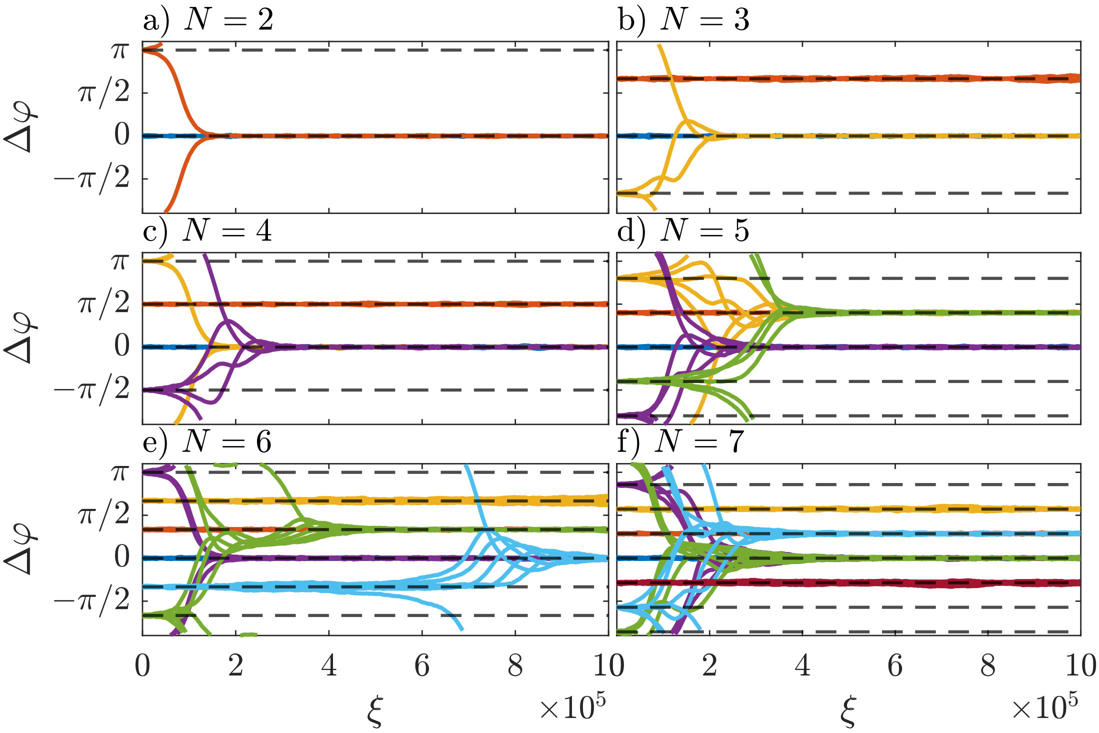


**Figure 5.6:** Same simulation as in Fig. 5.5 for different number pulses. The cavity length is adapted as $\tau = 2.5N$ such that the amount of interaction remains the same.

free spectral range (FSR) of the cavity, see Fig. 5.5 (d). We observe that two initial conditions remain stable upon their time evolution as they lie within the stable region defined by Eq. (5.80) and marked by the gray areas in Fig. 5.5 (a),(e). The other three trajectories correspond to unstable states and converge to one of the two stable configurations, cf. Fig. 5.5(a). The parameters $(A_\pm, \psi_\pm)$ in Eq. (5.7), that are necessary for predicting the stability of the steady states, were extracted from Eqs. (3.155)–(3.157) by using a perturbation analysis (cf. Appendix C.6). The phase model with extracted parameters exhibits very good agreement with the full PDE model (cf. Fig. C.2). We note that, the interaction with the left neighbor ($A_+ \sim 10^{-5}$) is three orders of magnitudes larger than the interaction with the right neighbor ($A_- \sim 10^{-8}$). This is because the pulses in the chosen parameter set have asymmetrical tails (cf. Fig. 5.7 (a)). Hence, the interaction is effectively unidirectional.

Finally, we repeat the simulation in Fig. 5.5 for different harmonic numbers, see Fig. 5.6 for $N = 2, \ldots, 7$. In all cases, the trajectories converges towards a central region of stability. Further, we observe that trajectories that start far away from stable states (such as the orange line for $N = 2$) exhibit a faster transient than configurations that are initialized close to the stable regime (such as the blue line for $N = 6$). This is because the evolution of the perturbation defined in Eq. (5.79) is proportional to

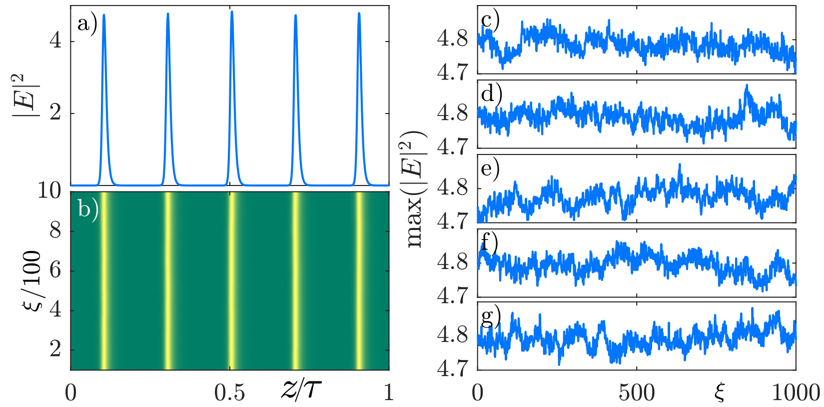


**Figure 5.7:** Short extract of a time trace from as in Fig. 5.5 (a) but with noise of amplitude $\sigma = 10^{-3}$. (a) Profile at the last step of the simulation. (b) Evolution of $|E|^2$ over $10^3$ round-trips. (c)–(g) Evolution of the maxima of the five pulses in (a),(b).

$\exp\left[(k_+ + k_-)(\cos(q) - 1)\, t\right]$. Because $(k_+ + k_-)$ is depends on the splay states $\Delta\varphi_p$, it can be close to zero for some $p$, rendering the transient very slow.

At this point, we want to stress the generality of the presented results. They apply for a wide range of system parameters, in particular, also under the influence of large fluctuations as the added noise in the simulation for Figs. 5.5 and 5.6 does not significantly change the pulse shape. This is underlined in Fig. 5.7, where a short extract of a simulation with an even larger noise amplitude is shown.

Finally, we can also observe the splay states in the model defined in Eqs. (3.152)–(3.154) based upon delay differential equations. To demonstrate this, we perform a direct numerical simulation of Eqs. (3.152)–(3.154) in analogy to Fig. 5.6. The result is presented in Fig. 5.8. In this case, the stable phase configurations are different from Fig. 5.6 due to different system parameters. However, in all panels of Fig. 5.8, the stable phase configurations lay within the same region defined by Eq. (5.80). We choose to perform the major part of the analysis with the PDE model as the DDE model is more difficult to handle numerically. For instance, for the PDE model a large timestep for the (slow) time can be chosen, however, for the DDE model, there is only one time component such that a large time step would lead to numerical problems. As a further confirmation of the validity, we perform a numerical continuation of the DDE model using `DDE-BIFTOOL`. In Fig. 5.9, we show three separate branches for pulses in the three splay states, where stability is omitted[16]. While the intensity profiles are identical (cf. panels (e)–(g)), the real part exhibit the characteristic phase profiles of the splay states (cf. panels (b)–(d)).

[16] In fact, `DDE-BIFTOOL` gave inconclusive results for the stability, which is why we do not make a statement about it here. A more detailed analysis would be necessary to draw credible conclusions.

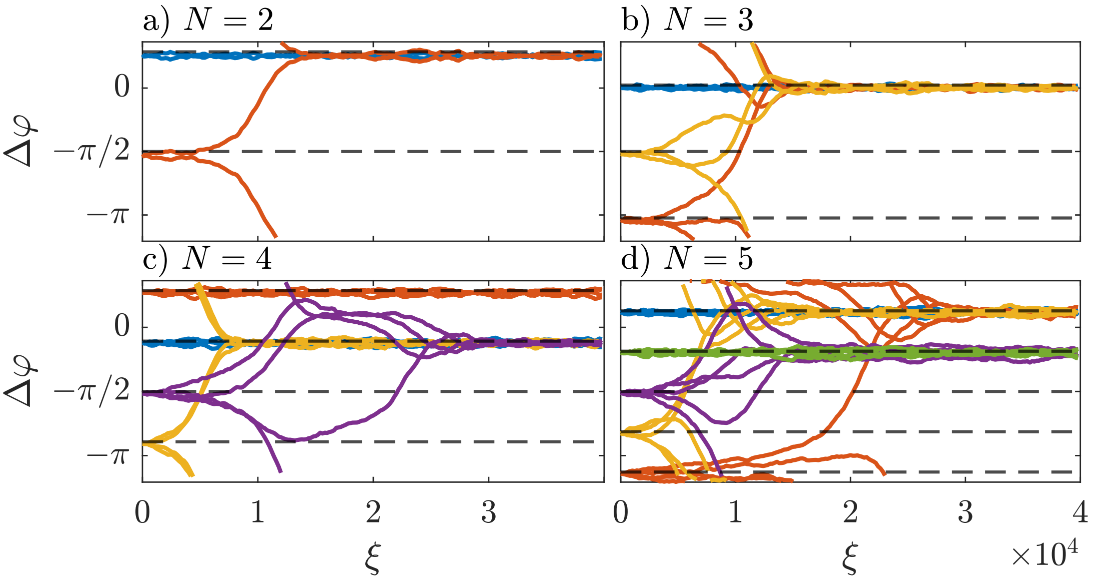


**Figure 5.8:** Results from a numerical simulations of the DDE model (3.152)–(3.154) with parameters $(\gamma, \kappa, \alpha_g, \alpha_q, G_0, \Gamma_g, Q_0, \Gamma_q, s) = (40, 0.8, 1.5, 0.5, 4G_{\text{th}}, 0.08, 0.3, 1, 10)$ for $N = (2,\ 3,\ 4,\ 5)$ pulses per round-trip, respectively, and white noise of the amplitude $\sigma = 5 \times 10^{-3}$ without feedback ($\eta = 0$). Note, that the cavity size is increased in accordance with the number of pulses such that the individual pulse shapes remain the same: $\tau = 1.5N$.

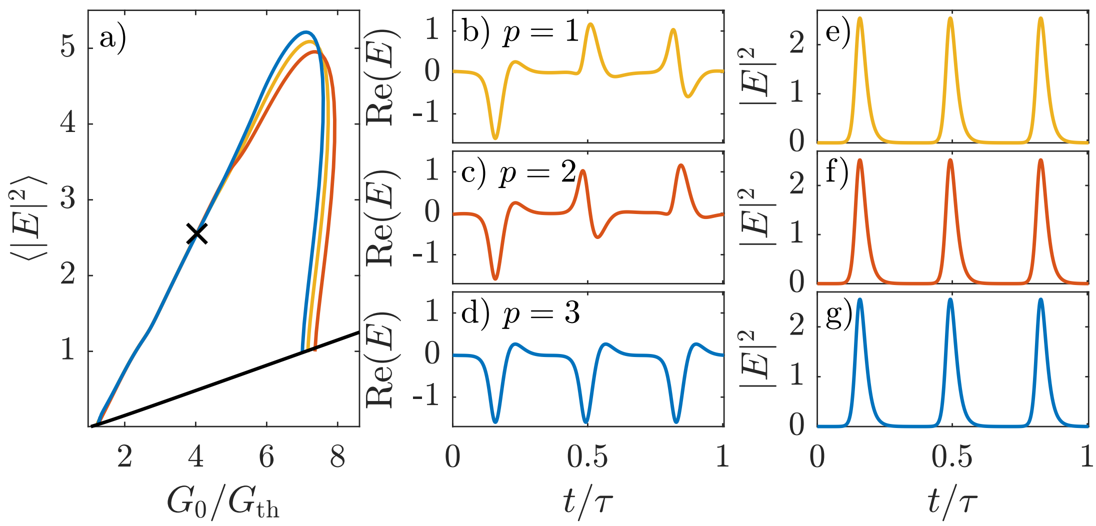


**Figure 5.9:** (a) Continuation of the DDE model (3.152)–(3.154) for the same parameters as in Fig. 5.8 (b). We find separate branches for the different splay states in accordance to Eq. (5.71). Stability is omitted. (b)–(g) Real part and intensity of the optical field at the position marked by the black cross in (a).

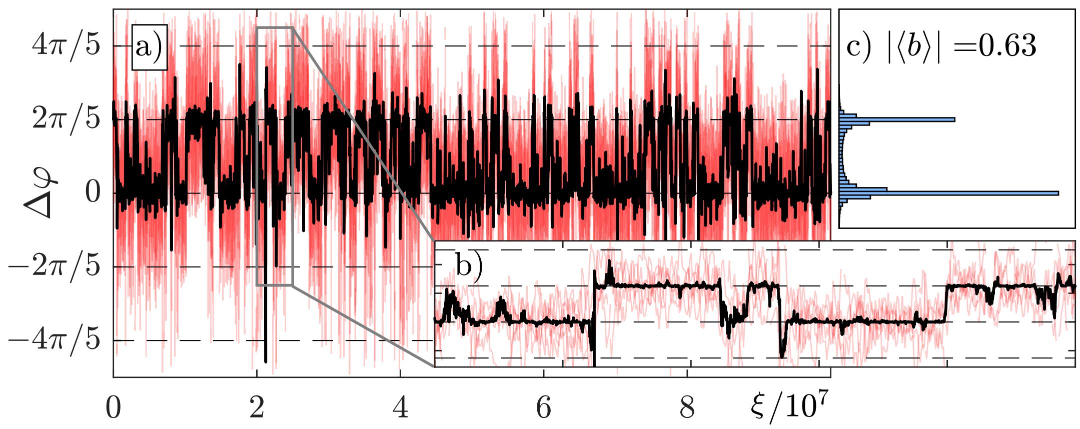


**Figure 5.10:** (a) Time evolution over slow time $\xi$ of phase differences for five pulses (light red) for the same parameters as in Fig. 5.5 obtained from a direct numerical simulation of Eqs. (3.155,3.156) with added noise of amplitude $\sigma = 4 \times 10^{-4}$. The black line denotes the phase of the order parameter $b$. As the system is bistable for $N = 5$, the order parameter jumps between the two stable steady states $\Delta\varphi_{0,1} = 0, \frac{2\pi}{5}$. (b) Zoomed view around a region with multiple jumps. (c) Statistical distribution of the phases visited by $\arg b$. The two peaks correspond to the two aforementioned steady states.

Turning our attention back to the prediction of multistability for $N \geq 5$, we find that it has a profound consequence on the measurement of the coherence as it must be interpreted by comparing the Kramers' escape time of each splay state [138] with the measurement time. The latter typically occurs experimentally over several tens of milliseconds, which corresponds to millions of round-trips. We show in Fig. 5.10 (a) the result of a long simulation of Eqs. (3.155)–(3.157) over $10^8$ round-trips. Due to noise, the system is able to visit many times all the stable states. This is best observed in Fig. 5.10 (b), which provides a zoom around a small part of the original time trace. We detail in Fig. 5.10 (c) a histogram of the value of $\arg b$.[17] Due to the low noise value, the distribution is narrowly peaked around each stable splay state and the theoretical value of the order parameter should be $\langle b_p \rangle = \exp(i\Delta\varphi_p)$. Indeed, if the value of the coherence is calculated over a time smaller than the average residence time, we obtain $|\langle b\rangle| \sim 0.9$. If instead the coherence is measured over the entire time trace, $|\langle b\rangle| = 0.63$; this is the result of the partial cancellation between $\langle b_0\rangle$ and $\langle b_1\rangle$. Hence, in this system, the ergodic hypothesis that consists in replacing statistical (ensemble) average by a single realization of a stochastic process, is valid only for extremely long measurement times. This result is underlined by Fig. 5.11 where we show an extract

[17] Note that this histogram defines the probability density function in the non-reciprocal case for which we cannot find an analytical expression, cf. Section 5.2.2. However, we can compare the histogram in Fig. 5.10(c) with the one shown for the reciprocal case, cf. Fig. 5.4.

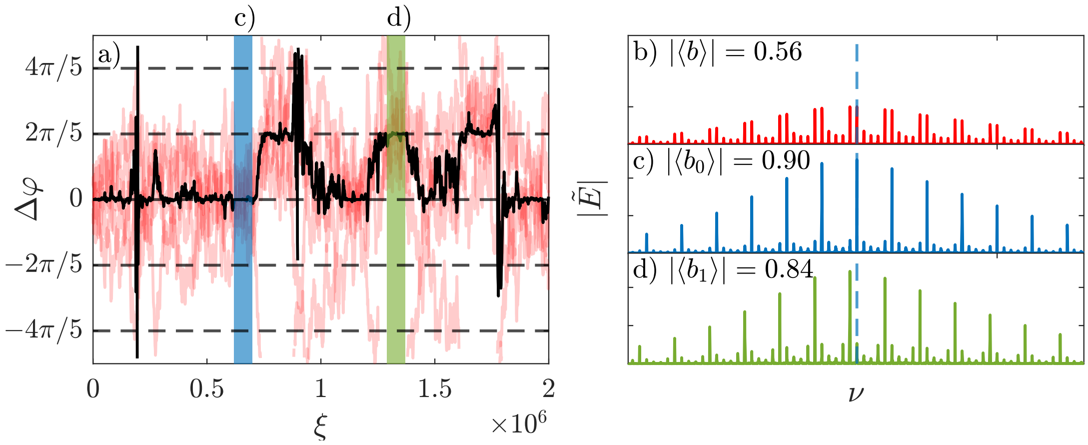


**Figure 5.11:** (a) Extract of the trace in Fig. 5.10. (b)–(d) Frequency spectra from (b) the whole trace, (c) the blue region and (d) the green region.

of the trace in Fig. 5.10 and show in panels (b)–(d) frequency spectra corresponding to different parts of the time trace. The spectrum in panel (b) is taken over the whole length of the trace in (a). Yet, the spectra in (c) and (d) are taken over shorter times marked by the blue and green regions in (a). The partial spectra have prominent peaks every $N\nu_{FSR}$ and are shifted with respect to each other by $\nu_{FSR}$[18]. Yet, the spectrum over the whole length exhibits two (prominent) peaks every $N\nu_{FSR}$, which stem from the average of the two aforementioned combs. We envision this effect to become even more prominent for higher number of pulses leading to a larger number of attractors in which the system may remain frozen.

Further, we note that visiting the unstable states is also possible for higher noise amplitudes. This is demonstrated in Fig. 5.12 where we show a similar simulation as before but with a larger noise amplitude. Here, the distribution broadens and also other states are visited. The histogram in Fig. 5.12 (c) exhibits five peaks corresponding to the five splay states. While it might be unintuitive at first sight that an unstable steady state results in a peak in the distribution, we have to remember that also at an unstable fixed point, the flux vanishes. Hence, the trajectories are repelled but diverge slowly leading to peaks in the histogram. Finally, we notice that the average residence time of $\arg b$ on one of the splay states becomes shorter for higher noise levels, which can be seen when comparing the insets of Figs. 5.10 and 5.12.

Having demonstrated the good agreement between the Haus master equation (3.155)–(3.157) and the Kuramoto model (5.7), in the next step, we study the influence of the number of pulses $N$ and the noise level on the coherence level. Our results are summarized in Fig. 5.13, where we compute for long time traces the average order parameter

[18]Actually, one also has to take into account the different common phase velocity $\omega_p$, cf. Eq. (5.73). However, this effect is negligible as $\omega_p$ scales with $A_\pm \sim 10^{-5}$.

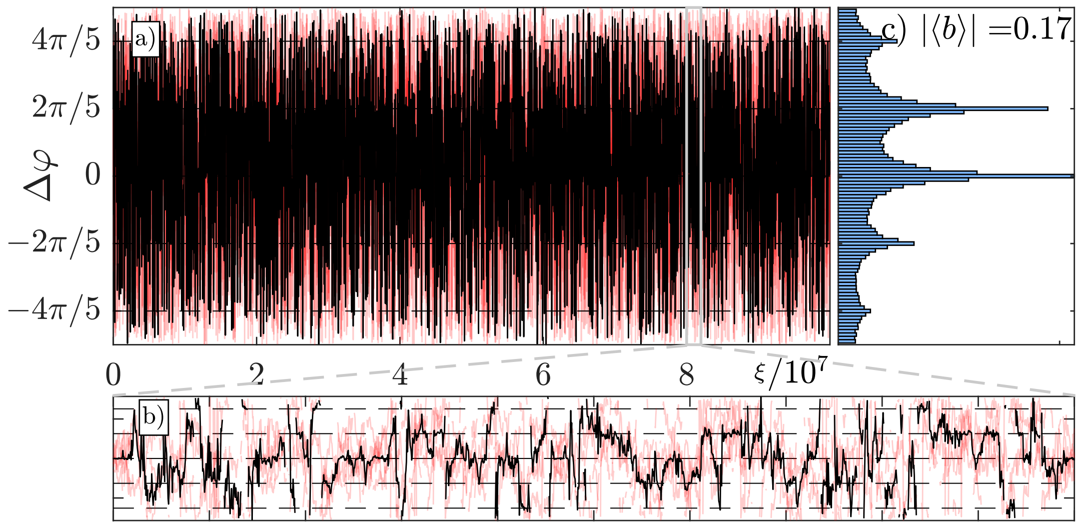


**Figure 5.12:** Same as Fig. 5.10 but with a larger noise of the amplitude $\sigma = 10^{-3}$ leading to much stronger fluctuations in the evolution of the phases and the order parameter. As a result, the distribution in panel (c) becomes wider as the system can explore more phase configurations.

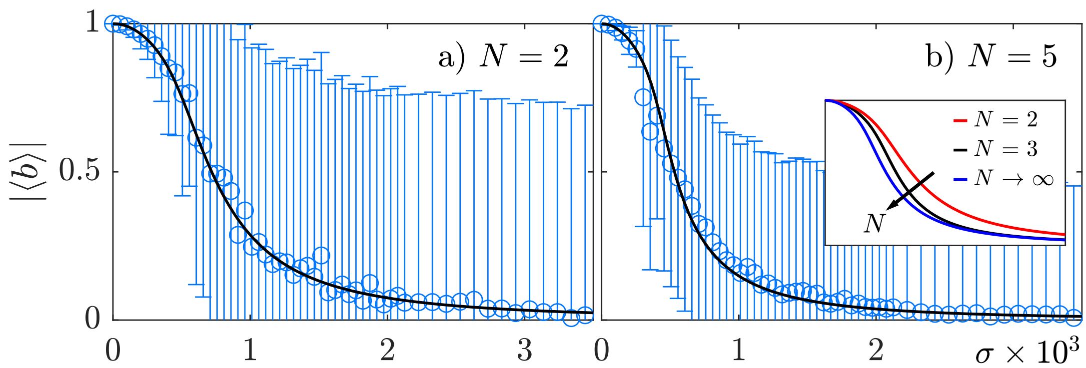


**Figure 5.13:** The order parameter $|\langle b\rangle|$ as a function of noise for different numbers of pulses in the cavity (blue: PDE model in Eqs. (3.155)–(3.157), black: phase model in Eq. (5.7)). The cavity round-trip is increased according to the HML number as $\tau = N \times 2.5$. Same parameters as in Figs. 5.5 and Fig. 5.10. Inset in (b): analytical result for the reciprocal phase model, see Eq. (5.54).

as a function of the noise amplitude for different numbers of pulses. If the amplitude of the noise is too low, the system will not be able to jump from one steady state to the other leading to a coherence close to unity. If it is too high, i.e., $\sigma \gg A_{\pm}$, coherence is entirely lost as $|\langle b \rangle| \to 0$. Yet, in this case the system continues to generate a very regular intensity pulse train (cf. Fig. 5.7) and it can therefore be interpreted as an *incoherent crystal*. The transition between these two extreme cases is continuous, i.e., the system does not exhibit a phase transition. Finally, the coherence decays faster for larger values of $N$. This can be understood intuitively from the distribution of the order parameter (e.g. in Fig. 5.12 (c)). The larger $N$ is, the more peaks are in the distribution. Therefore, the level of coherence is averaged over more states which cancel each other in the statistical average. We compare the numerical curves in Fig. 5.13 (in blue) with the analytical formula for the order parameter (in black) of the reciprocal case, see Eq. (5.54). While the interactions here are non-reciprocal (see e.g. the asymmetric pulse shape in Fig. 5.7 (a)), the black curve still describes the order parameter qualitatively and gives a good approximation. In particular, the dependence on $N$ is captured. The inset in 5.13 (b) also shows the two limit cases for $N = 2$ and $N \to \infty$, defined in Eqs. (5.55) and (5.60), respectively.

### 5.2.4. Measuring Splay States Experimentally

While we study the theoretical background of a PML laser in this thesis, we also want to present here the steps that are necessary for an experimental confirmation as carried out in [125]. In particular, we show how the splay states can be measured experimentally. As the carrier frequency of the pulses is very high (order of THz), the optical spectrum cannot be measured directly with high accuracy. Hence, we need to shift the spectrum down to the *radio frequencies* (RF) range, which can be measured with high precision. This can be achieved by a heterodyne measurement, which is schematically presented in Fig. 5.14. Here, we consider the signal $h_s = a_s e^{i\nu_s t}$ with an unknown frequency $\nu_s$ (blue) and the beat signal $h_b = a_b e^{i\nu_b t}$ of the known frequency $\nu_b$ (yellow), where $a_{s,b} \in \mathbb{R}$ are the corresponding amplitudes. Building the sum of the two signals gives the orange signal in Fig. 5.14, which contains both frequencies. Taking the modulus square (green) removes the high carrier frequencies $\nu_{s,b}$:

$$|h_s + h_b|^2 = a_s^2 + a_b^2 + 2a_s a_b \cos(\delta\nu t), \tag{5.83}$$

where $\delta\nu = \nu_b - \nu_s$. Hence, the RF spectrum exhibits beat notes at $\pm\delta\nu$. Applying this to the problem at hand, we beat the output of the laser in a multi-pulse state with a reference CW laser with known frequency $\nu_{CW}$. However, the situation becomes a bit more complicated because the signal is a frequency comb and therefore exhibits

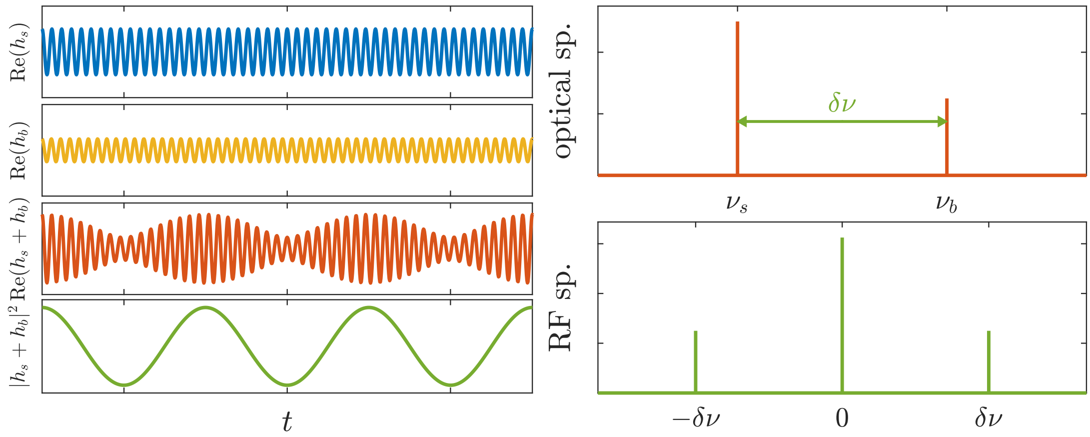


**Figure 5.14:** The signal $h_s$ (blue) has a frequency $\nu_s$ and is beaten by $h_b$ (yellow) with $\nu_b = \nu_s + \delta\nu$. The sum of the two (orange) has both frequencies in its spectrum. The spectrum of the intensity (green) has beat notes at $\pm\delta\nu$.

many frequencies. Hence, there will be many beat notes which all need to be taken into account.

For an $\mathrm{HML}_N$ state in one of the splay phase configurations the spacing between neighboring teeth in the spectrum is $N$ times the fundamental frequency $\nu_{FSR} = \frac{2\pi}{\tau}$: $\Delta\nu = N\nu_{FSR}$. Therefore, the spectrum consists of peaks located at

$$\nu_k = \nu_0 + k\Delta\nu,\ k \in \mathbb{Z}, \tag{5.84}$$

where $\nu_0$ is some offset around which the comb is centered. In the RF spectrum the main peaks are also separated by $\Delta\nu$. Hence, the beat notes in the RF spectrum for a given comb are found at

$$\Delta\nu_k = \pm\left(\nu_{CW} - \nu_k\right). \tag{5.85}$$

While all of this is quite straight forward, the tricky part is to realize which beat note belongs to which tooth in the comb. For that, we consider Fig. 5.15. The CW frequency falls between two teeth of the comb, which we denote $\nu_m$ and $\nu_{m+1}$. Hence, we obtain the two lowest beat notes $\Delta\nu_m$ and $\Delta\nu_{m+1}$ in the RF spectrum in the interval $[0, \Delta\nu]$ corresponding to the interaction with the left (index $m$) and to the right (index $m+1$) peak. It is important to note that in an experiment, just from looking at the RF spectrum, we cannot know which beat note belong the $\nu_m$ and $\nu_{m+1}$. Expressing this more accurately, the two beat notes with the lowest frequency in the RF spectrum are

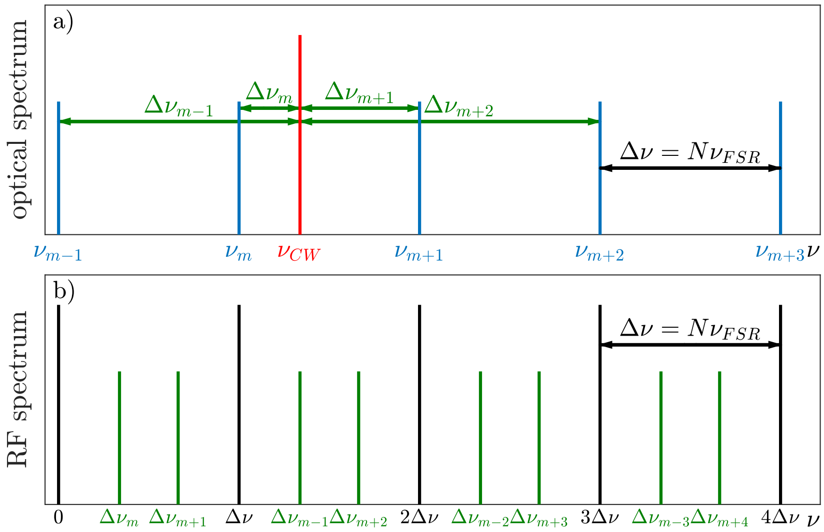


**Figure 5.15:** (a) The optical spectrum of an HML$_N$ state in a splay phase configuration, where the peaks of the comb are separated by $N\nu_{FSR}$. We use a CW beam (red) to create beat notes (green). (b) The RF spectrum with the beat notes shown in (a).

found for the value of $m$ such that $\nu_m < \nu_{CW} < \nu_{m+1}$ and hence,

$$\Delta\nu_m = \nu_{CW} - \nu_m = \nu_{CW} - \nu_0 - m\Delta\nu, \tag{5.86}$$

$$\text{and } \Delta\nu_{m+1} = \nu_{m+1} - \nu_{CW} = \nu_0 - \nu_{CW} + (m+1)\,\Delta\nu. \tag{5.87}$$

For simplicity, we define $\Delta\nu_0 = \Delta\nu_m + m\Delta\nu = \nu_{CW} - \nu_0$. Combining these results, we obtain the position of all beat notes:

$$\Delta\nu_k = \begin{cases} +\Delta\nu_0 - k\Delta\nu & k \leq m, \\ -\Delta\nu_0 + k\Delta\nu & k > m. \end{cases} \tag{5.88}$$

So what can we actually measure? In Section 5.2.3, we predict that an HML$_N$ state can be multistable. That is, each HML$_N$ solution has $N$ steady states corresponding to the splay states $\Delta\varphi_p = \frac{2\pi p}{N}$, where $p = 1, \ldots, N$, which correspond to a shift of the frequency comb by $p\nu_{FSR} = p\frac{2\pi}{\tau}$. Therefore, the beat notes in the RF spectrum also simply move by $p\nu_{FSR}$. So, we can compare the RF spectrum before and after the jump and we should see the offset of $p\nu_{FSR}$ in the beat notes. But we need to remember that we do not know which beat note belongs to which tooth in the comb, which makes the analysis a bit more involved.

We consider a comb in splay state $p$. Then, $\nu_0$ is shifted by $p\nu_{FSR}$. Therefore, we introduce the index $p$ in the previous notation such that the position of the $k$-th beat

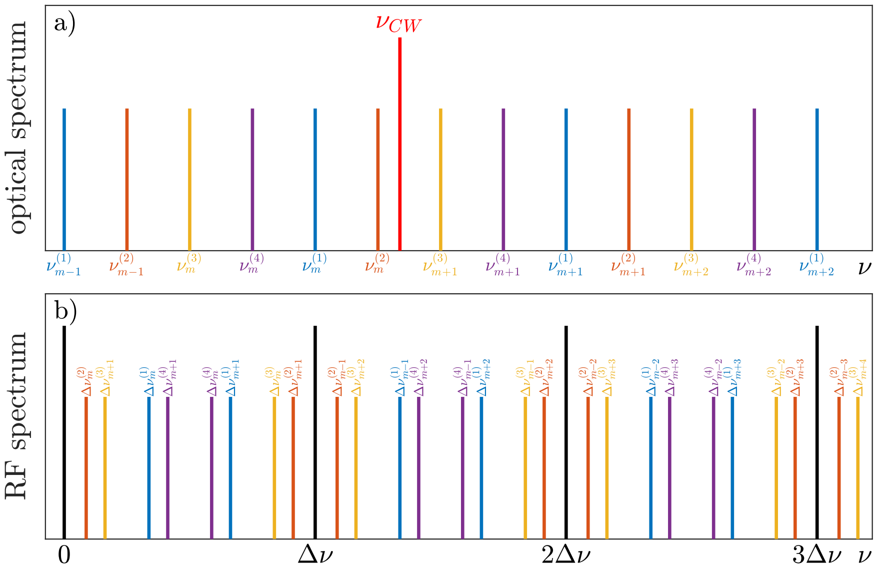


**Figure 5.16:** (a) The optical spectrum of an $HML_4$ state in a non-splay phase configuration. Here, the comb is a superposition of the four sub-combs shown in blue, orange, yellow and purple. The separation of two, e.g., blue peaks is $\Delta\nu = 4\nu_{FSR}$ while neighboring peaks (e.g., blue and orange) are separated by $\nu_{FSR}$. We use a CW beam (red) to create beat notes. (b) The RF spectrum with the beat notes. In each interval of size $\Delta\nu$, we find 8 beat notes.

note of pulses in the $p$-th splay state reads

$$\Delta\nu_k^{(p)} = \left|\nu_{CW} - \nu_k^{(p)}\right|, \tag{5.89}$$

where $\nu_k^{(p)} = \nu_0 - p\nu_{FSR} + k\Delta\nu$ (it is the position of the $k$-th tooth of the comb in state $p$). Hence, even when we do not know in which state $p$ the system is and which beat note belongs to which tooth, there are only $2N$ possible positions ($N$ for the left neighbor $m$ and $N$ for the right neighbor $m+1$) for the beat notes in each interval of size $\Delta\nu$ in the RF spectrum (cf. Fig. 5.16).

Finally, we want to draw conclusions on the phase relation of the pulses in two different RF spectra $p$ and $q$ based on the respective locations of the beat notes. We consider the beat notes $\Delta\nu_m^{(p)}$ and $\Delta\nu_m^{(q)}$. As expected, the distance between these quantities gives a multiple of $\nu_{FSR}$

$$\begin{aligned}\Delta\nu_m^{(p)} - \Delta\nu_m^{(q)} &= \Delta\nu_0^{(p)} - m\Delta\nu - \Delta\nu_0^{(q)} + m\Delta\nu \\ &= (p-q)\,\nu_{FSR}\end{aligned} \tag{5.90}$$

In the same way, we can also relate the left and the right beat notes of two different spectra $p$ and $q$

$$\begin{aligned}\Delta\nu_m^{(p)} + \Delta\nu_{m+1}^{(q)} &= \Delta\nu_0^{(p)} - m\Delta\nu - \Delta\nu_0^{(q)} + (m+1)\Delta\nu \\ &= (p-q)\,\nu_{FSR} + \Delta\nu. \end{aligned} \tag{5.91}$$

Hence, if the measured beat notes fulfill Eqs. (5.90) and (5.91), we know that comb experienced a shift of a multiple of $\nu_{FSR}$ and therefore the pulses are in fact in another splay state. We briefly summarize the consideration in the following list, which can be understood as a simple recipe for the experimental realization:

1. Measure a RF spectrum with the two beat notes $\Delta\nu_m^{(p)}$ and $\Delta\nu_{m+1}^{(p)}$ (say we are in the blue state in Fig. 5.16 without loss of generality).
2. Predict all other possible beat note positions by adding multiples of $\Delta\nu$ to the measured beat notes (i.e., the other colored lines in Fig. 5.16). Keep track of which of these predictions stem from which of the two beat notes (i.e., $m$ vs $m+1$).
3. The comb jumps in another state $q$ and we measure again the RF spectrum.
4. The new beat notes lie on the predictions. Therefore we know which beat notes in the new RF spectrum are related to the ones in the previous one.
5. We can confirm that the pulses changed their splay state by applying Eqs. (5.90) and (5.91).

To confirm our theoretical predictions, we compare them with an experimental setup consisting of a VECSEL [125]. Figure 5.17(a) shows a two-time diagram of the intensity for the $\mathrm{HML}_4$ state, where the horizontal axis represents the round-trip time and the vertical axis is the number of round-trips. We can observe that the pulses are equidistant, have the same amplitude, and are stable over more than $10^4$ round-trips. In panel (c), the RF spectrum shows the same features as panel (b) but the lines in the optical spectrum are shifted with respect to the previous case. In accordance with the theory, the shift $|\delta_1 - \delta_2|$ experienced by the optical lines corresponds to one FSR of the laser optical spectrum. In panel (d) the pulse train is in an incoherent state as here, the maximum number of 8 beat notes (cf. Fig. 5.16) is obtained which indicates that within the acquisition time of the RF spectrum analyzer (20 ms), the phase differences between pulses have explored all the four stable and unstable possible configurations (from 0 to $3\pi/4$) (cf. the noisy simulation in Fig. 5.12).

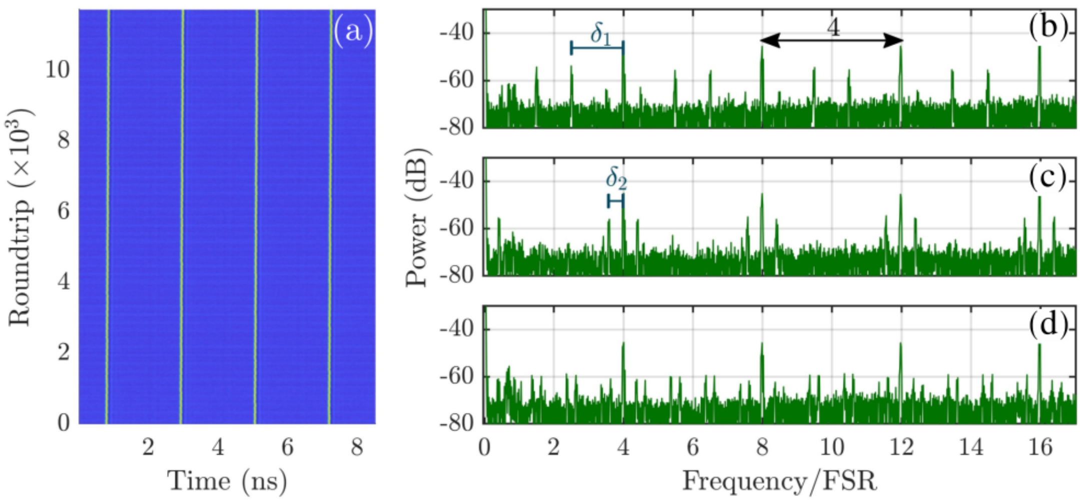


**Figure 5.17:** (a) Space-time diagram of the laser output showing four equidistant pulses. (b),(c) represent two heterodyne RF spectra showing a jump between two splay states spectrally separated by one FSR since $\delta_2 = \delta_1 - 1/\tau$. (d) RF spectrum of an incoherent state consisting of the average of all the splay states. The figure is adapted from [125].

## 5.3. Interplay of Positions and Phases under the Influence of Time-Delayed Feedback

The current Section 5.3, including the figures, is based on the publication:

[126] T. G. Seidel, J. Javaloyes, and S. V. Gurevich. “Coherent pulse interactions in mode-locked semiconductor lasers”. In: *Chaos, Solitons and Fractals* 195 (2025), p. 116244. DOI: 10.1016/j.chaos.2025.116244

TGS carried out the analytical and numerical work under the supervision of SVG and JJ. All figures were created by TGS. A first draft of the text was created by TGS and gradually refined by all authors.

After studying the simplified case of a damped translational mode in Section 5.2.3, we want to turn our attention to the most general case where each pulse in a PML laser has two degrees of freedom: phase and position, cf. blue and orange arrows in the schematic in Fig. 1.3. In Section 5.1, we derived that the underlying phase and position dynamics is governed by a set of $2N$ ODEs, cf. Eqs. (5.5) and (5.6). These nonlinear ODEs are characterized by the coherent interactions of the phases (cf. sine-terns), and the nonlinear amplitude functions $A_{t,b}$, $B_{t,b}$ and $L_{t,b}$. These quantities cannot be calculated analytically as they depend on the pulse shape which is not known analytically from the Haus master equation (HME) (3.155)–(3.157). According to their definitions (cf. Eqs. (C.51), (C.56) and (C.60)), they correspond to overlap integrals between the modes $w_{t,p}$ of the adjoint system and the pulse shape $\psi_s$ of a single pulse. In the TLS regime, numerically obtaining a single-pulse solution can be achieved by simply performing direct numerical simulation, as here the superposition ansatz in Eq. (5.3) is fulfilled. However, for shorter cavities, a single pulse solution does not exists as here the carriers do not recover in between pulses. Hence, a single pulse in a short cavity exhibits a higher intensity as, e.g., four pulses in the same cavity, such that the corresponding $\text{HML}_4$ state cannot be described as the sum of four individual pulses. This is why we had to settle with the perturbation ansatz described in Appendix C.6 to extract the parameters $A_\pm$ and $\psi_\pm$ in the previous Section 5.2. At the same time, the translational mode in shorter cavities is strongly damped such that an interplay of phase- and position-dynamics cannot be observed because their dynamics is decoupled. Consequently, to observe the interplay of the two symmetries, we perform the following simulations in the TLS regime. That is, we choose a gain value $g_0 < g_{\text{th}}$ such that the off-state $(E, g, q) = (0, g_0, q_0)$ is stable, see Section 3.3.5. Here, the interaction via overlapping tails can be neglected as the tails decay exponentially (i.e., $A_{t,p} = 0$). We remain with the interaction via carriers and via time-delayed feedback such that the

EOM in Eqs. (5.5) and (5.6) simplify to

$$\dot{\varphi}_m = \sum_{k \neq m} \left[ B_p \left( \Delta_{km} \right) + \eta L_p \left( \tau_f + \Delta_{km} \right) \sin \left( \Omega + \theta_{km} + u_p \left( \tau_f + \Delta_{km} \right) \right) \right], \tag{5.92}$$

$$\dot{z}_m = \sum_{k \neq m} \left[ B_t \left( \Delta_{km} \right) + \eta L_t \left( \tau_f + \Delta_{km} \right) \sin \left( \Omega + \theta_{km} + u_t \left( \tau_f + \Delta_{km} \right) \right) \right]. \tag{5.93}$$

In particular, we perform a parameter study of the feedback parameters $\eta$, $\Omega$ and $\tau_f$, which directly control the size, phase and position of the emerging satellites and which therefore control the amount of coherent interaction in Eqs. (5.92) and (5.93). As the feedback parameters are not part of the nonlinear forces $L_{t,b}, B_{t,b}$ and $u_{t,b}$ themselves, these quantities can be calculated numerically once and can be reused for arbitrary feedback parameters. Further, they do not depend on the number of pulses $N$ either, such that they can be used for arbitrary $N$. These two properties demonstrate a large benefit of the EOM because the nonlinear forces only need to be computed once, but can be used to study a large variety of regimes.

To gain intuition on the dynamics and the influence of TDF, we begin the study with the most simple case in which we consider $N = 2$ pulses leading to a two-dimensional phase space spanned with one position and one phase difference $\Delta_{21} = \Delta = z_2 - z_1$ and $\theta_{21} = \theta = \varphi_2 - \varphi_1$, respectively. Hence, the flow is described by the two ODEs $\dot{\Delta}\left(\Delta, \theta\right)$ and $\dot{\theta}\left(\Delta, \theta\right)$, which follow directly from Eqs. (5.5) and (5.6), see Appendix C.2.3, Eqs. (C.76), (C.77) for the formal definition. The gained insights for the two-pulse case can be used to identify dynamical regimes for higher pulse numbers where the phase space is higher dimensional which makes the analysis more involved.

As it might be difficult to keep track of the steps necessary to arrive at the results presented in this section, we want to briefly summarize them in the following list, which also outlines the rest of this section:

1. Remember that the phase and position dynamics of pulses in the HME (3.155)–(3.157) is described by effective equations of motion defined in Eqs. (5.92) and (5.93). While Eqs. (5.92) and (5.93) consider interactions between all pulses, generally nearest neighbor interactions provide the leading order term.

2. Obtain in the TLS regime via a simulation of the HME (3.155)–(3.157) a single-pulse solution $\psi_s$ for $\eta = 0$ as well as the direct and adjoint eigenmodes $v_{t,p}$ and $w_{t,p}$ (cf. Fig. 5.18).

3. From that, compute numerically the nonlinear forces $L_{t,b}, B_{t,b}$ and $u_{t,b}$ defined in Eqs. (C.51), (C.52) and (C.56) (cf. Fig. 5.19).

4. Study the two-pulse-case by calculating the flux defined by the EOM in the phase

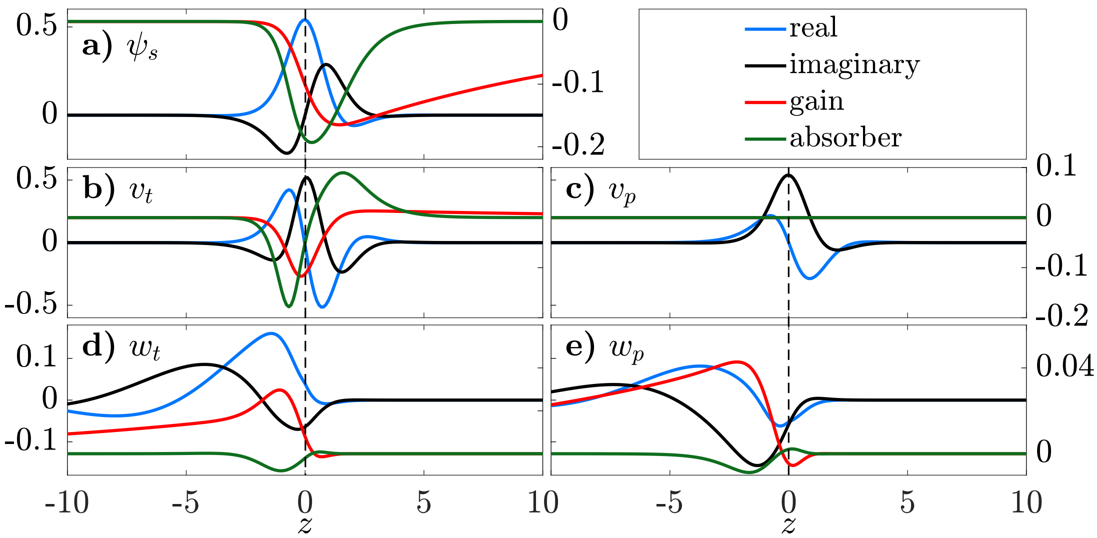


**Figure 5.18:** Exemplary stationary profiles of the (a) field and carrier components $\psi_s$, (b) translation and (c) phase neutral eigenfunctions, and (d) translational and (e) phase neutral eigenfunctions of the adjoint eigenvalue problem. For all panels, the left and right axis stands for the field and the carrier components, respectively. Obtained from a simulation of the HME (3.155)–(3.157) using the parameters $(\gamma, k, \alpha_g, \alpha_q, g_0, \Gamma, q_0, s, \eta) = (5, 0.1056, 1.5, 0.5, 0.99g_{\text{th}}, 0.08, 0.268, 10, 0)$ in a domain of length $\tau = 200$.

space spanned by $(\Delta, \theta)$. From that, calculate numerically the steady states and their stability (cf. Fig. 5.20 and Appendix C.5). To test the validity of the EOM, compare the result with dynamics from the HME (3.155)-(3.156).

5. Repeat the last step for different feedback parameters $\eta$, $\Omega$ and $\tau_f$, respectively, to obtain bifurcation diagrams for the respective parameter (cf. Fig. 5.22).

6. Use the same nonlinear forces $L_{t,b}, B_{t,b}$ and $u_{t,b}$ and the obtained intuition to infer to the general case where $N > 2$ (cf. Fig. 5.28).

### 5.3.1. Deriving the Amplitude-Functions

We show in Fig. 5.18 (a) the solution profile of a single pulse obtained from a DNS of the HME (3.155)–(3.157). Observing the shape of the profiles, we can infer that the interaction is not symmetrical as can be seen from the asymmetrical pulse shape (blue, black) and, in particular, the asymmetric carrier dynamics (red, green). The asymmetry is even more pronounced in the adjoint modes $w_{t,p}$ in Fig. 5.18 (d),(e)[19]. From the profiles, we can compute the forces $L_{t,b}, B_{t,b}$ and $u_{t,b}$, which are shown in Fig. 5.19. The asymmetrical pulse shape results in an asymmetrical force $L_{t,p}$ (cf.

[19]The adjoint eigenmodes $w_{t,p}$ can be obtained using the approach presented in Appendix C.4.

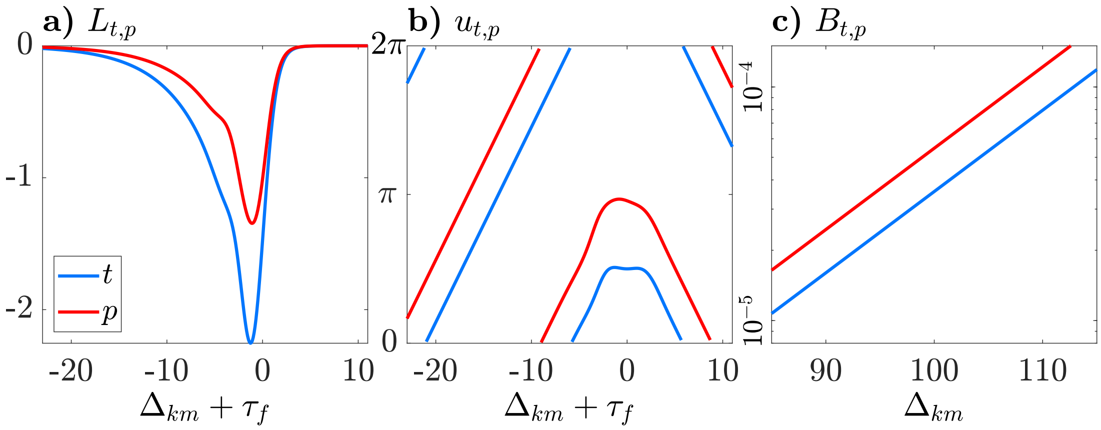


**Figure 5.19:** Numerically computed nonlinear force contributions $L_{t,p}$, $u_{t,p}$ and $B_{t,p}$ of EOM (5.92), (5.93) as a function of $\Delta_{km}$. All the forces are periodic functions with a periodicity of $\tau$. Note, that panel (c) is given on a logarithmic scale. Parameters are as in Fig. 5.18. Formal definitions given in Eqs. (C.51), (C.52) and (C.56), respectively.

Fig. 5.19 (a)) because a satellite exhibits a stronger overlap on the trailing compared to the leading edge of the tail. Further, it is shown in Appendix C.3 that the carrier interaction results in an exponential force $B_{t,p}(\Delta) \sim \exp(\Gamma\Delta)$ (cf. Fig. 5.19 (c)) because the gain itself recovers exponentially (cf. Eq. (3.156) for $E = 0$). While this result can be understood intuitively for the dynamics of the pulses' positions $z_j$, it can be surprising that the phases $\varphi_j$ are also influenced by this phase-independent force. The answer to this lies in the line-width enhancement factors $\alpha_{g,q}$ which couple the real and imaginary parts of the electric field, i.e., for $\alpha_{g,q} = 0$ we find $B_p(\Delta) = 0$.

### 5.3.2. Phase Space Analysis for a Configuration of two Pulses

In order to visualize the EOM (5.92), (5.93), we start with a simple configuration of two pulses. Here, the flow is described by the two ODEs $\dot{\Delta}(\Delta, \theta)$ and $\dot{\theta}(\Delta, \theta)$ which follow directly from the EOM (5.92), (5.93) (cf. Eqs. (C.76) and (C.77)). First, it is instructive to look at symmetries in the resulting equations. From Eqs. (5.92), (5.93) we can directly see, that

$$\dot{\Delta}(\Delta, \theta) = -\dot{\Delta}(-\Delta, -\theta). \tag{5.94}$$

The same property holds for $\dot{\theta}$ and can be concluded from the exchanging the numbering of the two pulses. Further, $\dot{\Delta}$ and $\dot{\theta}$ are $\tau$- and $2\pi$-periodic in the first and second variable, respectively. Therefore, one obtains

$$\dot{\Delta}(\Delta, \theta) = -\dot{\Delta}(\tau - \Delta, 2\pi - \theta). \tag{5.95}$$

Having that in mind, we can deduce two steady states: $(\Delta^*, \theta^*) = \left(\frac{\tau}{2}, \pi\right)$ and $(\Delta^*, \theta^*) = \left(\frac{\tau}{2}, 0\right)$. These states correspond to the splay states of the $\mathrm{HML}_2$ regime, which were discussed in detail in Section 5.2.3. Expressing the symmetries with respect to to these steady state, we obtain

$$\dot{\Delta}\left(\frac{\tau}{2} + \delta, \pi + \alpha\right) = -\dot{\Delta}\left(\frac{\tau}{2} - \delta, \pi - \alpha\right). \tag{5.96}$$

Next, for the sake of simplicity, we start with the case of resonant feedback, i.e., the situation when the satellite of a pulse induced by the feedback loop coincides with another pulse, i.e., $\tau_f = \tau/2$. The other parameters are set to $\Omega = 0.25\pi$ and $\eta = 10^{-4}$ such that the interactions via TDF and carriers are in the same order of magnitude (cf. $y$-scales in Fig. 5.19). For each point in the phase space ($\Delta$, $\theta$), one can evaluate the flux of the EOM (5.92),(5.93) and reconstruct the corresponding vector field, see Fig. 5.20 (a). Following the process described in Appendix C.5, we can extract the steady-states and their stability from the flux. Due to the aforementioned symmetries, we find one stable ($\Delta^*$, $\theta^*$) = ($\tau/2$, 0) (filled circle) and one unstable ($\Delta^*$, $\theta^*$) = ($\tau/2$, $\pi$) (open circle) fixed point. Furthermore, we find two other steady states corresponding to non-equidistant configurations. In Fig. 5.20 (a) they are placed at around $\Delta \approx 95$ and $\Delta \approx 105$, however, they are both unstable.

At this point, we want to emphasize the excellent quantitative predictions by the EOM. For that, we performed four DNSs (cf. black labels (d)–(g) in Fig. 5.20 (a) for the corresponding initial conditions) of the HME (3.155)–(3.157) with two pulses, see also Fig.5.20 (d)–(g) for the two-time representation of the corresponding time traces. Here, vertical red lines visualize the equilibrium positions at $z_1 = 50$ and $z_2 = 150$ for $\tau = 200$ and $\tau_f = 100$. Note that in panels (d), (f) the effect of the satellites due to TDF is especially visible: at the steady state, the one pulse is sitting on the satellite of the second one and vise versa. From the resulting time trace, the positions and phases of the pulses are extracted[20] and plotted as trajectories in the phase space (cf. green lines in Fig. 5.20 (a)). One can see that not only stable steady states are predicted correctly, but in the whole phase space the trajectories are tangent to the predicted vector field. Note that as the present interaction forces are small, the simulations of the HME (3.155)–(3.157) need to performed over several $10^5$ round-trips. This reveals a strong advantage of the EOM (5.92), (5.93) as the vector field for the complete phase space can be reconstructed in seconds versus hours it would take to achieve a similar result with the full PDE model.

In this case, the feedback delay $\tau_f = 100$ was chosen such that it mainly acts around the equidistant position at $\Delta = 100$. The width of the area where the feedback has a

[20] How this is done, is described in Eqs. (5.81) and (5.82).

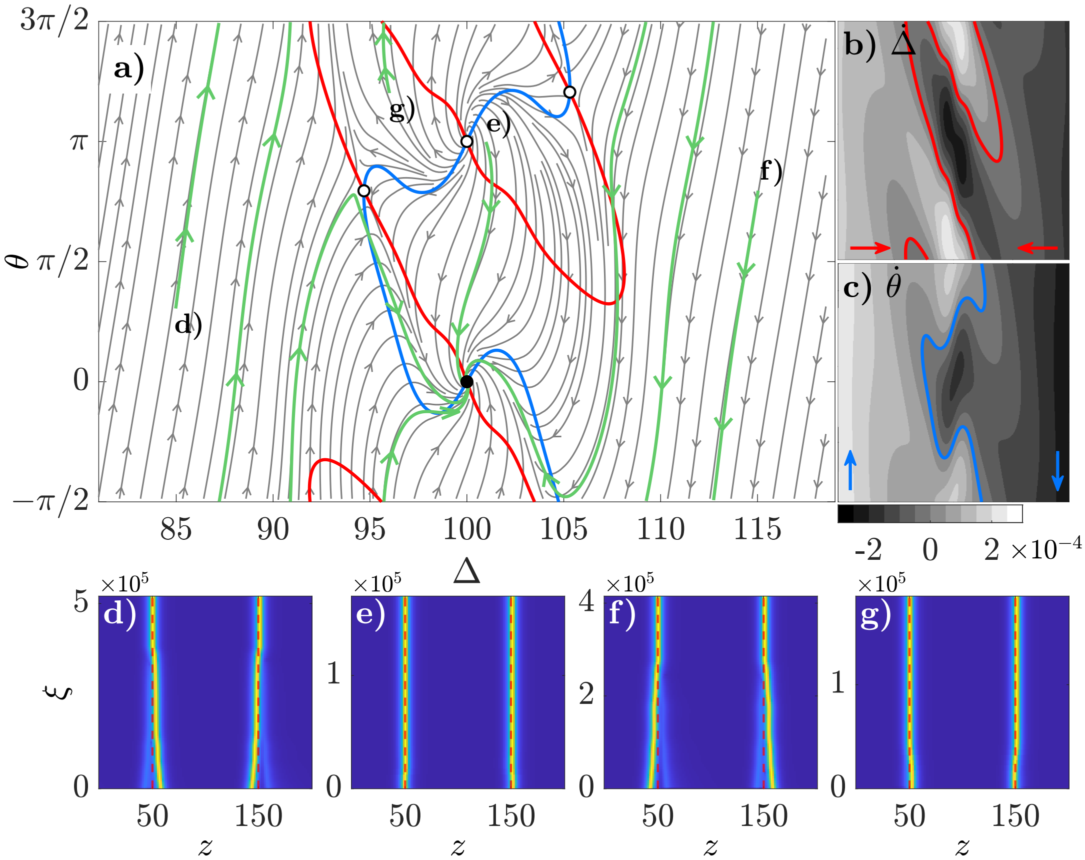


**Figure 5.20:** (a) Vector field diagram of the phase space ($\Delta$, $\theta$) governed by the EOM (5.92),(5.93) for two pulses. Red and blue contour lines correspond to the $\Delta$- and $\theta$-nullclines, respectively. Black (white) circles at the intersections of the nullclines correspond to stable (unstable) fixed points. Light green lines correspond to four exemplary trajectories obtained from time simulations of the full HME (3.155)–(3.157). The respective two-time representations of the intensities are shown in (d)–(g). There, vertical red dashes lines indicate the equidistant position, i.e., $z_1 = 50$, $z_2 = 150$. (b),(c) The magnitude of $\dot{\Delta}$ and $\dot{\theta}$, respectively. (d)–(g): Four exemplary time traces corresponding to the four initial states in (a). To emphasize the presence of the satellite, the colormap corresponds to $|E|^{1/4}$. Parameters are: $\tau_f = 100$, $\eta = 10^{-4}$, $\Omega = \pi/4$, other parameters as in Fig. 5.18.

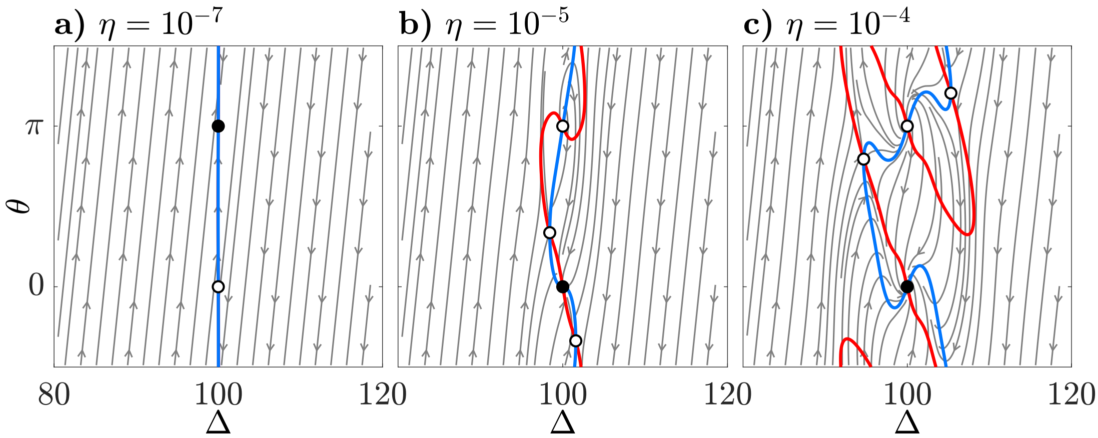


**Figure 5.21:** Vector field diagrams of the phase space $(\Delta, \theta)$ governed by the EOM (5.92), (5.93) for two pulses for three different values of $\eta$. Red and blue contour lines correspond to the $\Delta$- and $\theta$-nullclines, respectively. Black (white) circles at the intersections of the nullclines correspond to stable (unstable) fixed points. Other parameters as in Fig. 5.20.

strong influence is given by the width of the amplitude of the phase dependent force $L_{t,p}$ (cf. Fig. 5.19 (a)). In regions, where the influence of the feedback is small ($\Delta \lesssim 90$ and $\Delta \gtrsim 110$), the system is driven by gain repulsion. This force pushes the pulses to equidistance, hence, it points towards the center (cf. red arrows in Fig. 5.20 (b)), where the magnitude of $\dot{\Delta}$ is shown together with its nullcline (red contour line). At the same time, due to the carrier frequency, the phase changes at a similar rate (cf. blue arrows and $\dot{\theta}$ nullcline in Fig. 5.20 (c)), resulting in the effective diagonal motion in the phase space (cf. Fig. 5.20 (a)).

For the results presented in Fig. 5.20, the value of $\eta$ was chosen in a way that the phase dependent force is in the same order of magnitude as the phase independent force. A situation, when this is not the case can be seen in Fig. 5.21, where the phase space $(\Delta, \theta)$ together with the corresponding nullclines is presented for three values of $\eta$. One can see in Fig. 5.21 (a), that for smaller values of $\eta$, the phase space is solely dominated by the force due to gain repulsion, which results in diagonal vector field lines towards the equidistant positions as discussed above. For larger values of $\eta$, more complex dynamics can appear as seen in Fig. 5.21 (b), (c). Note that there is an upper bound for what values of $\eta$ provide good predictions as in the derivation of the EOM (5.92), (5.93), it is assumed, that the satellite stemming from the time-delayed feedback loop is not sufficiently intense to create a carrier depletion. While this is valid for small values of $\eta$, this is not the case for large $\eta$.

### 5.3.3. Influence of the Feedback Delay

In order to gain a full overview of the phase and position dynamics in dependence of the feedback parameters $\tau_f$ and $\Omega$, we perform a detailed bifurcation analysis of the EOM (5.92),(5.93). It is conducted by calculating the vector field as was presented in Fig. 5.20, extracting the steady states ($\Delta^*$, $\theta^*$) from it and analyzing its behavior by changing the control parameters. The results of a scan in the feedback delay time $\tau_f$ are presented in Fig. 5.22 (a), (b), where the equilibrium phase $\theta^*$ and position $\Delta^*$ differences are shown, respectively. Note that the stable (solid line) and unstable (dashed line) steady states at $\theta^* = (0, \pi)$ in the panel (a) lie on top of each other in the panel (b) as they both correspond to the equidistant case $\Delta^* = 100$. Further, different phase space configurations, corresponding to different $\tau_f$ values labeled with the vertical black dashed lines in Fig. 5.22 (a),(b), are shown in Fig. 5.22 (c)–(h). Lastly, the gray dashed line indicates the $\tau_f = 100$-cut previously presented in Fig. 5.20 (a).

One can see that the bifurcation diagrams in Fig. 5.22 (a),(b) reveal a complex dynamic with many interesting regimes. First, at low values of $\tau_f$, there are only the two fixed points corresponding to the in-phase and anti-phase equidistant configurations (cf. filled and open circles in Fig. 5.22 (c), where both $\dot{\Delta}$ (red) and $\dot{\theta}$ (blue) nullclines cross). This means that the satellites are too far away from the pulses for them to interact. This is emphasized by the green trajectory corresponding to the result of a time simulation of the HME (3.155)–(3.157), where the pulses settle on an equidistant configuration (cf. also Fig. 5.22 (i)). However, in the final state, pulses and satellites exhibit small overlap which is in contrast to the situation shown in Fig. 5.20 (d)–(g). This results in a de facto decoupling of phase and position dynamics as the pulses quickly settle on an equidistant state, yet the phases take much longer to reach the steady state.

Next, by increasing $\tau_f$, two non-equidistant configurations emerge from the in-phase solution $\theta^* = 0$ (cf. Fig. 5.22 (d)) in a pitchfork bifurcation (cf. blue square in Fig. 5.22 (a)). Further, on these branches, two Andronov-Hopf bifurcations denoted $H_1$ and $H_2$ occur leading to the emergence of time-periodic solutions. In fact, in the range of $\tau_f \approx [82, 86]$, all fixed points are unstable such that the limit cycle is the only stable manyfold. This can be seen in the phase space in Fig. 5.22 (e). Here, the green line is a trajectory obtained from a time simulation of the HME (3.155)–(3.157), which confirms the presence of a stable periodic orbit. The two-time representation of the trace is shown in Fig. 5.22 (j). Again, the quantitative agreement between the HME and the EOM is excellent.

To clarify the question, why only one stable limit circle emerges in time-simulations (while two Andronov-Hopf bifurcations occur), we consider the three-dimensional space

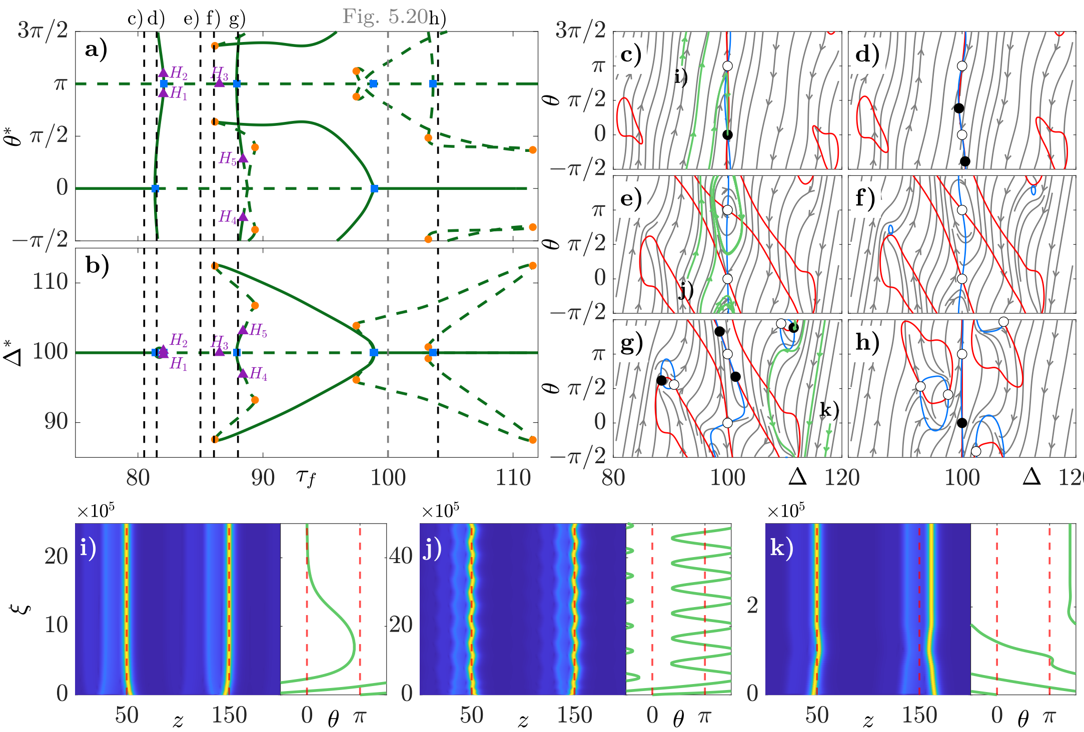

**Figure 5.22:** (a),(b) Bifurcation diagrams in $\tau_f$ of the EOM (5.92),(5.93) for $\eta = 10^{-4}$ and $\Omega = \pi/4$ showing steady states $(\theta^*, \Delta^*)$ in phase and position differences, respectively. Solid (dashed) green lines stand for stable (unstable) unstable solutions. Purple triangles, blue squares and orange dots correspond to Andronov-Hopf, pitchfork and saddle-node bifurcation points, respectively. (c)–(h) Vector field diagrams for values of $\tau_f$ indicated by black dashed lines in panels (a) and (b). Red and blue contour lines correspond to the $\dot{\Delta}$- and $\dot{\theta}$-nullclines, respectively. Black (white) circles at the intersections of the nullclines correspond to stable (unstable) fixed points. (i)–(k) Result of time simulations of the full PDE model (3.155)–(3.157), where equidistant positions and phases are indicated by red dashed lines. The corresponding trajectories are shown in panels (c), (e) and (g), respectively. Other parameters as in Fig. 5.20.

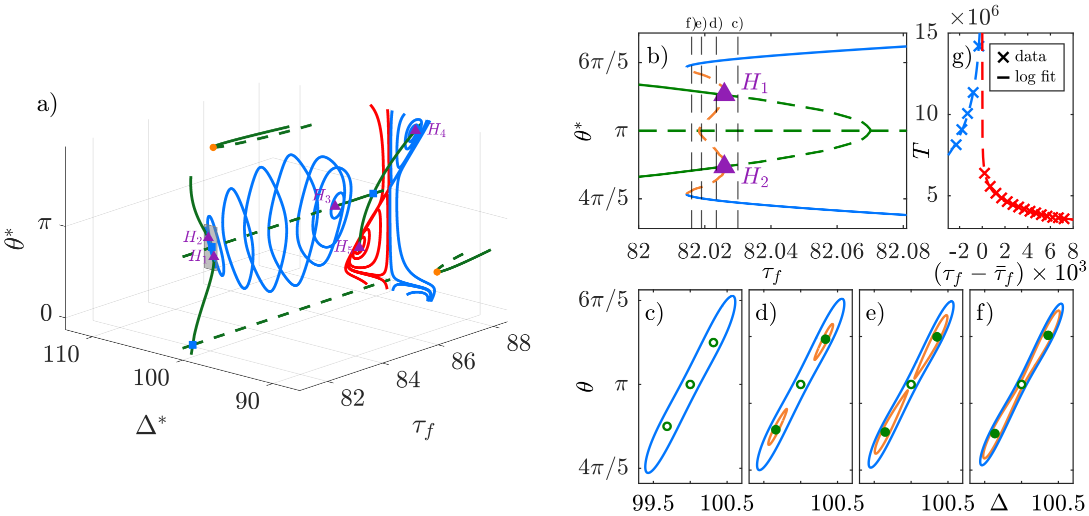


**Figure 5.23:** (a) Three-dimensional phase space spanned by ($\tau_f$, $\Delta^*$, $\theta^*$) of the EOM (5.92),(5.93). Steady states are depicted in green and emerging periodic solutions in blue and red. Purple triangles, blue squares and orange dots correspond to AH, pitchfork and saddle-node bifurcation points, respectively. (b) Close-up of the region marked in (a) by a gray rectangle (close to $H_{1,2}$). (c)–(f) Cuts showing the phases at dashed lines in (b). Blue and orange stand for stable and unstable cycles, respectively. (g) Scaling of the period of the limit cycle as a function of the distance to the critical value $\bar{\tau}_f$. The data (crosses) is fitted with a logarithmic fit.

($\Delta^*$, $\theta^*$, $\tau_f$) in an interval $\tau_f \approx [80, 88]$, see Fig. 5.23 (a). The bifurcation analysis detailed in the close-up in Fig. 5.23 (b) reveals that the Andronov-Hopf bifurcations $H_{1,2}$ are subcritical and the two unstable periodic orbits connect in a double-homoclinic bifurcation (cf. the scaling law in Fig. 5.23 (g)) leading to a single unstable limit cycle[21]. The latter undergoes a saddle-node bifurcation resulting in a single stable limit cycle. Note that the emerging periodic orbit oscillates around the equidistant steady state $(\Delta^*, \theta^*) = (100, \pi)$. Further, the branch of periodic solutions merges with the equidistant steady state branch in the subcritical Andronov-Hopf bifurcation $H_3$ around $\tau_f \approx 86$. Furthermore, around $\tau_f \approx 88.5$, we find another regime of periodic orbits. Here, they bifurcate at points $H_{4,5}$ from two branches emerging from a pitchfork bifurcation of the equidistant steady state (cf. Fig. 5.23 (a)). However, the Andronov-Hopf bifurcations $H_4$ and $H_5$ are supercritical, i.e., one finds stable periodic orbit oscillating around the non-equidistant steady states. However, with increasing $\tau_f$, these limit cycles from both sides recombine at the unstable equidistant steady states in homoclinic bifurcations such that the periodic orbits now perform full phase rotations of $2\pi$.

[21]The unstable limit cycles can be found by performing a DNS with inverted time because for 2D systems, stable attractors become unstable and vice versa.

Bringing our attention back to the bifurcation diagram in Fig. 5.22 after the regime of periodic solutions, we find a broad range of stable non-equidistant configurations. Figure 5.22 (f) indicates the presence of two saddle-node bifurcations (cf. orange circles in Fig. 5.22 (a),(b) and Fig. 5.23), leading to the emergence of fixed point pairs. These fixed points correspond to situations, where one pulse sits on the satellite of the other pulse acting as an anchor, while its satellite does not interact with the other pulse. That is, the coupling is unidirectional; cf. the time simulation in Fig. 5.22 (k). As the anchor satellite moves linearly with $\tau_f$, we can see an approximately linear response of the steady state position $\Delta^*$ in this regime. A particularly interesting situation can be seen in Fig. 5.22 (g), where four stable non-equidistant solutions coexist. The regime of stable non-equidistant states disappears in a pitchfork bifurcation (cf. blue square in Fig. 5.22 (a),(b) around $\tau_f \approx 100$) as the difference between the equidistant state and the time delay $\tau_f$ approaches the pulse width. Then the satellite is absorbed into the main pulse resulting in a pitchfork bifurcation.

Finally, considering time delays larger than $\tau/2$, we do not observe other stable steady states than the equidistant ones, see Fig. 5.22 (h). This is because the interaction of the pulses with satellites is much stronger on the leading than on the trailing edge. As a result, the pulses are almost decoupled in this regime and hence, the equidistant steady states are only weakly stable and unstable, respectively. The fact that the interaction via satellites is not symmetrical around the pulse can already be observed in the form of the amplitude of force $L_{t,p}$ in Fig. 5.19 (a) which has a much larger tail on the leading side than on the trailing edge. This property is inherited from the asymmetric pulse profile shown in Fig. 5.18 (a).

### 5.3.4. Influence of the Feedback Phase

Next, we consider the influence of the feedback phase $\Omega$ on possible pulse configurations. First, we notice a further symmetry in the EOM (5.92),(5.93):

$$\dot{\Delta}\left(\Delta,\theta,\Omega\right) = \dot{\Delta}\left(\Delta,\theta+\pi,\Omega+\pi\right). \tag{5.97}$$

The same relation holds for $\dot{\theta}$. The symmetry can be observed in Fig. 5.24, where bifurcation diagrams in $\Omega$ for various values of $\tau_f$ are shown. In all panels, the black vertical dashed lines correspond to the cuts at $\Omega = \pi/4$, where the phase spaces in Fig. 5.22 (c)–(h) are shown. In Fig. 5.24 (a), one can see that when pulse and satellite are far from each other, stable non-equidistant states resulting from the pitchfork bifurcations (cf. blue squares) can only occur for a very narrow range of the feedback phases as interactions are weak in this regime. Slightly increasing $\tau_f$ (cf. panel (b)) enables the emergence of Andronov-Hopf bifurcations (see the purple triangles) leading to periodic

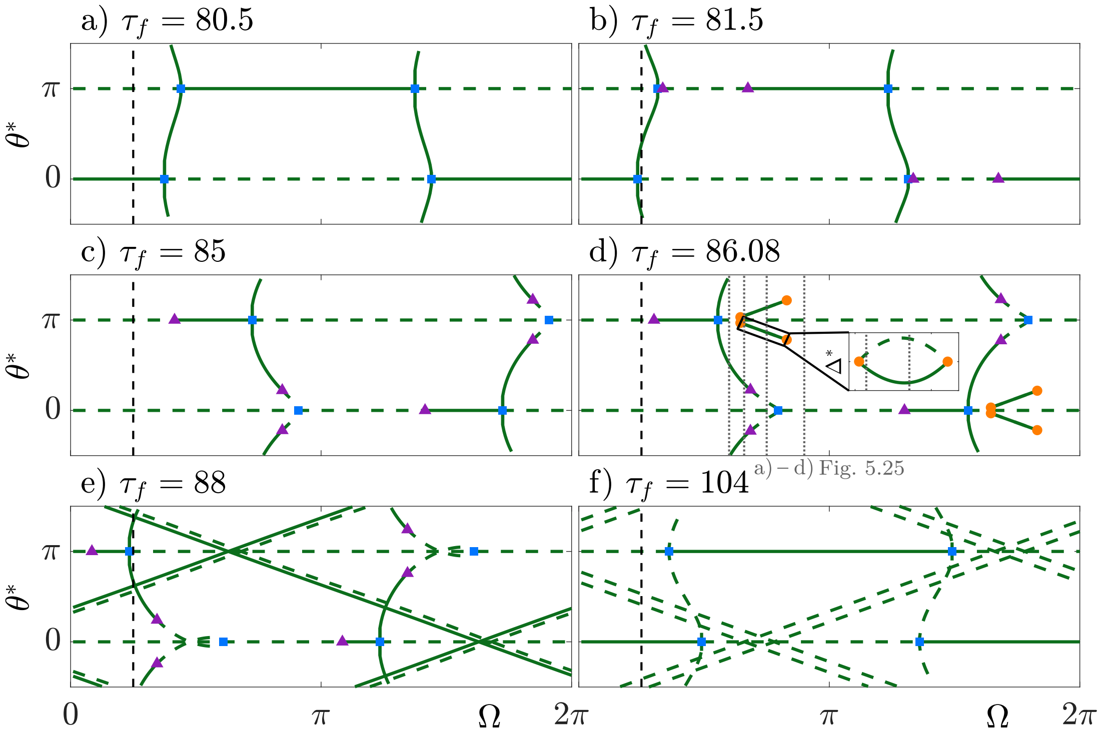


**Figure 5.24:** Bifurcation diagrams of the steady state $\theta^*$ as function of $\Omega$ for different values of $\tau_f$ (the same values as in Fig. 5.22 (c)–(h) are used). The black dashed line at $\Omega = \pi/4$ marks the cross-sections shown in Fig. 5.22 (c)–(h). In panel (d), the gray dashed lines correspond to the vector field diagrams presented in Fig. 5.25. The inset shows the appearance of the saddle-node bifurcation of steady states which lie inside the black rectangle on the position norm.

solutions whose range in $\Omega$ increases for larger values of $\tau_f$ (cf. panel (c)). Next, increasing $\Omega$, we find multistabilty of non-equidistant states as two pairs of saddle-node bifurcations (cf. orange circles panel (d)) emerge (cf. the inset).

To further understand this emergence, we consider the phase space $(\Delta, \theta)$ for four values of the feedback phase in Fig. 5.25. There, one can observe the nullclines of phase- and position-dynamics to be very close (cf. the inset in panel (a)). Next, in panels (b) and (c), they intersect which explains the emergent stable and unstable steady states (cf. the insets). This fixed points exists far away from equidistant states and corresponds to the situation where one pulse sits on satellite of the second pulse, while the satellite of the second pulse does not interact with the first pulse. Finally, the nullclines separate again (cf. panel (d)). Interestingly, in Fig. 5.24 (e) the aforementioned non-equidistant configuration exists for all $\Omega$ as becomes evident by the emerging cross-shaped structure of the branches. Further, this shape reveals that the phase relation in this case depends almost perfectly linearly on $\Omega$. At the same time, it was shown in Fig. 5.22 (b), that in this regime the position also depends linearly on $\tau_f$, i.e., in this case the TDF

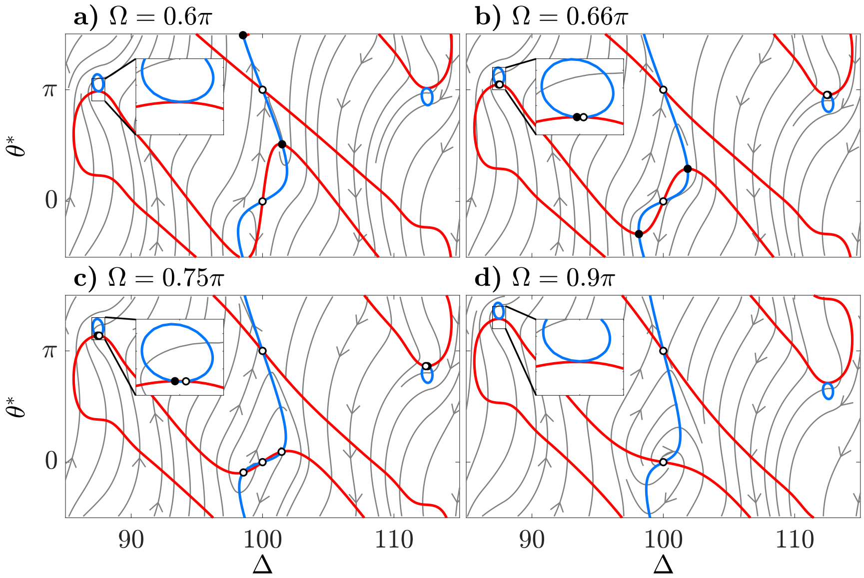


**Figure 5.25:** Vector field diagrams evaluated at positions marked in Fig. 5.24 (d) by gray dashed lines. Red and blue contour lines correspond to the $\dot{\Delta}$- and $\dot{\theta}$-nullclines, respectively. Black (white) circles at the intersections of the nullclines correspond to stable (unstable) fixed points. The insets show close-ups on the area at around $\Delta \approx 88$, where a pair of fixed points emerges (b),(c) and vanishes (a),(d) in a saddle-node bifurcation. Due to the symmetry around $\Delta = 100$, a pair of fixed points emerges simultaneously at around $\Delta \approx 112$.

parameters directly control the pulse configuration in phase and position. Finally, in Fig. 5.24 (f) for $\tau_f = 104$, all non-equidistant steady states became unstable and only – depending on $\Omega$ – the in-phase or anti-phase configurations remain stable, which, however, can be bistable for a small parameter range.

Finally, we summarize the findings in the two-parameter bifurcation diagram on the plane $(\tau_f, \Omega)$ in Fig. 5.26. Here, the positions of all the previously shown one-parameter diagrams and corresponding phase spaces are marked by dashed lines and red crosses, respectively. Blue, orange and purple lines correspond to the pitchfork, saddle-node and Andronov-Hopf lines. First, we notice the $\pi$-periodicity in $\Omega$ due to Eq. (5.97). Further, the colormap encodes the number of stable steady states. In white regions, where no steady state is stable, periodic solutions are the global attractors. While we detailed the region around $(\tau_f, \Omega) \approx (85, \pi/4)$ in Fig. 5.23, we find another region around $(\tau_f, \Omega) \approx (97, 0.8\pi)$. Next, non-equidistant states always appear in pairs due to symmetry reasons. Hence, in regions with an odd number of stable steady states, one of the equidistant configurations must be stable. On the other hand, in regions with an even number of steady states, either both equidistant states are stable or only non-equidistant states are stable. While the aforementioned case only applies in a

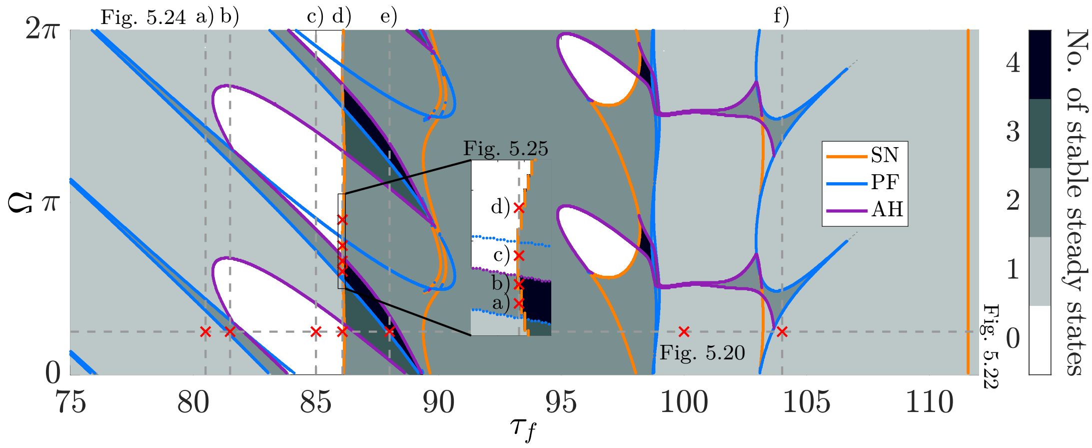


**Figure 5.26:** Two-parameter bifurcation diagram in the $(\tau_f, \Omega)$-plane. Orange, blue and purple lines stand for saddle-node (SN), pitchfork (PF) and Andronov-Hopf bifurcations, respectively. The colormap encodes the number of stable steady states of EOM (5.92),(5.93). Dashed lines correspond to the cross-sections where one-parameter bifurcation diagrams are shown in Fig. 5.22 (a),(b) and Fig. 5.24. At the positions marked with red crosses the phase spaces are presented in Figs. 5.20, 5.22 (c)–(h) and Fig. 5.25.

small range of parameter values where $\tau_f > 100$ (cf. Fig. 5.24 (f)), the latter regime dominates the range of $\tau_f \in [87, 97]$.

### 5.3.5. Dynamics of a General Multi-Pulse State

So far, we presented the results of a system consisting of two pulses, i.e., a two-dimensional phase space. However, the EOM (5.92),(5.93) are valid for an arbitrary number of pulses. In fact, we can reuse the calculated profiles and eigenfunctions (cf. Fig. 5.18) and define them over a cavity of length $\tau_N = \frac{\tau}{2}N$ as they all decay to zero. Then, as the profiles and eigenmodes remain unchanged, the forces $L_{t,p}, u_{t,p}, B_{t,p}$ (cf. Fig. 5.19) remain the same as well but just need to be defined on a larger domain. However, $L_{t,p}$ converges to zero when its argument is not in the vicinity of zero (such that it is not necessary to compute $u_{t,p}$ on a larger domain) and $B_{t,p}$ is known analytically. This enables us to predict the system's behavior even though the phase space of higher dimensional systems cannot be visualized easily.

It was demonstrated that in the range where gain repulsion is dominant the two pulses converge exponentially to the equidistant configuration (cf. Fig. 5.21 (a)). This property can be generalized to $N$ pulses neglecting the influence of feedback ($\eta = 0$). Here the gain repulsion is dominated by the first neighbor to the left, i.e., the EOM for

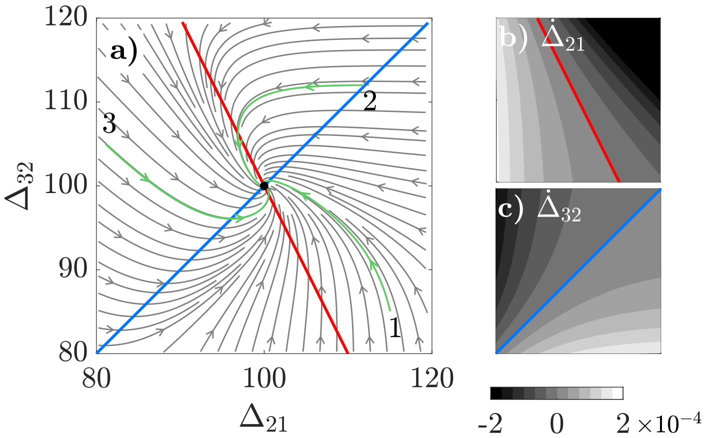


**Figure 5.27:** (a) Vector field diagrams of the $(\Delta_{21}, \Delta_{32})$-phase space for three pulses which dynamics is governed by the EOM (5.92), (5.93) for $\eta = 0$. Red and blue contour lines correspond to the $\Delta$- and $\theta$-nullclines, respectively. Black circle at the intersections of the nullclines correspond to the stable fixed point. The green lines are traces of three numerical simulations of the full HME (3.155)–(3.157) and show excellent quantitative agreement with the predictions of the EOM. The magnitude of $\dot{\Delta}_{21}$ and $\dot{\Delta}_{32}$ is plotted in panels (b) and (c), respectively.

the positions read

$$\dot{z}_n = B_t \left(z_{n-1} - z_n\right) \tag{5.98}$$

with the boundary conditions $z_0 = z_N - \tau$ and $z_{N+1} = z_1 + \tau$. Then the equidistant configuration is defined by $z_n^* = n\frac{\tau}{N} + v_0 t$ where $v_0$ is a constant drift. Using the ansatz $\delta_n = \sum_p a_p e^{\lambda_p \xi + i q_p n}$ for perturbations from these steady states (where $q_p = \frac{2\pi}{N}p, p = 0, \ldots, N-1$), one obtains (see App. C.2.4 for more details)

$$\lambda_p = B_t'\left(-\frac{\tau}{N}\right)\left[\left(\cos\left(q_p\right) - 1\right) - i \sin\left(q_p\right)\right] . \tag{5.99}$$

As $B_t'\left(-\frac{\tau}{N}\right) > 0$ (cf. Fig. 5.19 (c)) and $\left(\cos\left(q_p\right) - 1\right) < 0$, the steady state is stable as expected for all $N$. However, for $N \geq 3$ the imaginary part does not vanish such that these fixed points are stable spirals. To support this hypothesis we choose $N = 3$ as here, the $(\Delta_{21}, \Delta_{32})$-plane visualizes the complete position dynamics, see Fig. 5.27. Note that the complete phase space is four-dimensional. However, due to the absence of feedback the dynamics in the $(\theta_{21}, \theta_{32})$-plane is decoupled from the dynamics in the $(\Delta_{21}, \Delta_{32})$-plane. Here, the green lines are obtained from three time simulations of the HME (3.155)–(3.157) and show excellent quantitative agreement with the flow predicted by the EOM (5.92),(5.93). Although the dynamics between pulses is given by a first order system of exponential relaxation, the ensemble gives rise to oscillatory

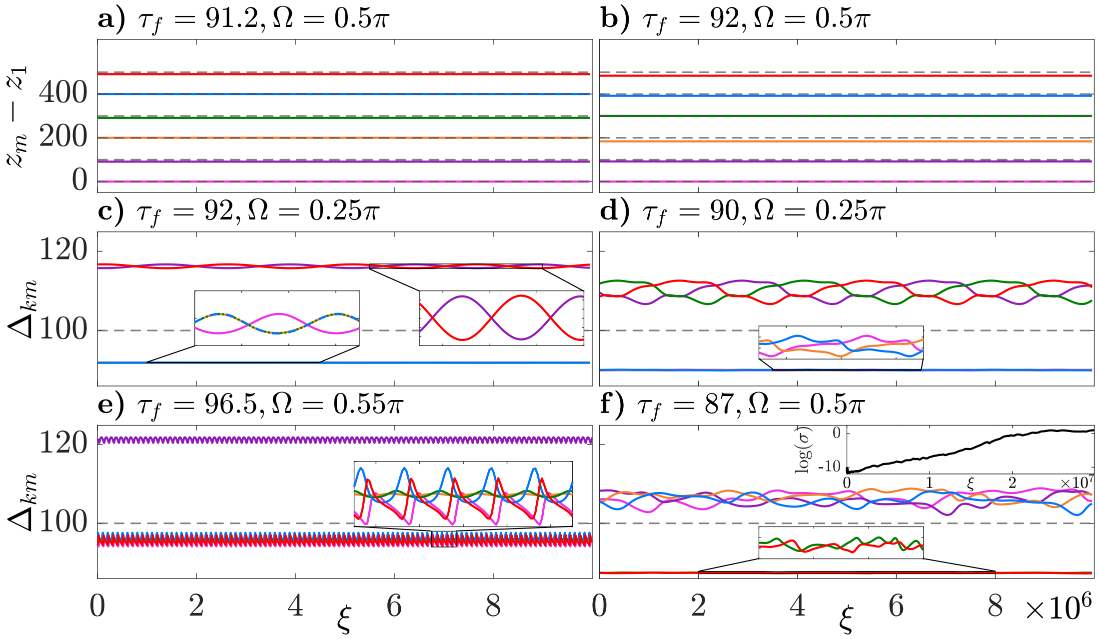


**Figure 5.28:** Time traces of numerical time simulations of EOM (5.92), (5.93) for six pulses for $\eta = 10^{-4}$ and for different values of $\tau_f$ and $\Omega$ yielding different configurations of phases and positions. (a) Two sets of three bound pulses. (b) Three sets of two bound pulses. (c)–(e) Different periodic states with shorter and longer periods. (f) Chaotic solution, inset: evolution of Euclidian norm $\sigma$ of perturbed and unperturbed trajectories.

behavior.

Finally, including the effects of TDF again, going to even higher harmonic numbers and taking the phase dynamics into account makes the resulting dynamics more and more complex due to the added degrees of freedom. Performing various time simulations of the EOM (5.92),(5.93) using different initial conditions and feedback parameters for $N = 6$ reveals a variety of possible configurations as presented in Fig. 5.28. Here, panels (a) and (b) show the resulting steady states difference $z_m - z_1$ for two different $(\tau_f, \Omega)$ values, where the corresponding equidistant configurations are marked by dashed lines.

In particular, panel (a) shows a stable configuration, where the distance between neighboring pulses alternates between a higher and a lower value, i.e., there are three chunks of two bound pulses. This is analogous to the stable non-equidistant configurations found for two pulses (as seen in Fig. 5.22 (d), (g), (k)). However, in panel (b), by a slight change in $\tau_f$, we find another solution, where two chunks of three bound pulses exist.

Further, panels (c)–(e) show various periodic states. In the panel (c), we see two position differences oscillating regularly, while the remaining exhibit a much smaller amplitude (cf. the insets). Figure 5.22 (d) presents a similar situation, however, the oscillations are not sine-like as before. Next, in panel (e), we find another periodic state which in this case has a much higher frequency, see the inset. Finally, also aperiodic oscillations can be found as shown in panel (f). Performing the simulations in panel (f) again with a small perturbation ( $10^{-10}$) and comparing the two results, reveals that the trajectories diverge exponentially. To show this, we define $\sigma$ as the Euclidian norm of the phase difference between the perturbed and unperturbed trajectories, i.e., their distance in phase space. The result is shown in the inset of Fig. 5.28 (f) where one can observe an exponential increase in $\sigma$. Hence, in this situation, the maximal Lyapunov exponent is positive and therefore, the system is chaotic.

## 5.4. Conclusion

In this chapter, we studied interactions of pulses in the output of a PML laser. We derived from the HME (3.155)–(3.157) effective equations of motion describing the dynamics of the pulses' phases and positions. The EOM enabled us to unveil the different mechanism in which the TLSs can interact.

We studied the EOM in two distinct cases. In short cavities, the interaction via gain depletion is the dominating effect. This effectively decouples the phase and position dynamics in the EOM, and forces the pulses in an equidistant configuration called the harmonic mode-locked state. We demonstrated that in this case, the EOM is equivalent to the Kuramoto model with nearest neighbor coupling and highlighted the important consequences this has on the notion of coherence in PML lasers. First, we predicted the existence of multiple different frequency combs for a single HML state, which correspond to the splay states of the Kuramoto model. For $N$ pulses, there are $N$ different combs and each of them is shifted by a multiple of the free spectral range $\nu_{\mathrm{FSR}} = 1/\tau$. A linear stability analysis revealed that half of the states are stable, which implies that multistability must occur for $N \geq 5$ pulses. These findings were confirmed in simulations of the HME and in an experimental setup consisting of a VECSEL [125].

Further, we predicted that the level of coherence in an HML state is a result of the interplay between the coherent forces in the Kuramoto model and noise stemming from, e.g., spontaneous emission. To quantify this property, we introduced an order parameter that corresponds to the first order correlation function. For the case of reciprocal interaction, we were able to express the order parameter analytically as function of the noise amplitude, which also captured the main properties of the general non-reciprocal case. In particular, we showed that the transition from high to low coherence is continuous, i.e., no phase transition occurs. Further, we demonstrated that the level of coherence decays faster the more pulses are in the HML state. This was explained by the higher number of attractors (i.e., the splay states) in the corresponding phase space. Next, we disclosed that the notion of coherence must be interpreted by comparing the duration of the measurement time with the Kramers' escape time of each splay state. We highlighted, that this implies that the intensity trace of a pulse train can be highly regular, while the phases are not in a coherent state. We denoted this situation as an incoherent crystals.

In the second case, we considered for the EOM, we studied the full $2N$ dimensional phase space spanned by the $N$ phases and $N$ positions. In particular, we analyzed the effects of time-delayed feedback on the possible configurations. We performed a detailed bifurcation analysis of the feedback parameters describing the size, phase and position of the satellites, respectively, for the case of two interacting pulses. We demonstrated that the EOM exhibits an excellent quantitative agreement with the HME over a wide range of the phase space. So far, comparisons in other approaches remained on the qualitative level [42, 43]. In the next step, we discussed many intricate scenarios, which can be controlled by the feedback parameters. In particular, we described the existence of non-equidistant states, where the feedback-induced satellite can be used as an anchor for a second pulse, thus directly controlling its position and phase. Further, we predicted time-periodic states, where the pulses oscillate around a splay state. Finally, we were able to infer the intuition obtained from the two-pulse-case to higher pulse numbers. In particular, the higher number of degrees of freedom enabled a more complex dynamics including chaotic states.

# 6. Summary and Outlook

In this thesis, we analyzed nonlinear optical systems that can generate frequency combs and temporal localized states. In particular, we considered both Kerr resonators and passively mode-locked lasers. The models derived from first principles rely on a time-delayed description in their dynamical equations, which we have studied using a combination of analytical and numerical methods. The latter consisted in time simulations and path continuation using the `MATLAB`-package `DDE-BIFTOOL` [105, 111].

In the first part of the thesis, we performed a detailed analysis of the dynamics of a Kerr–Gires–Tournois interferometer (KGTI) which consists in an injected micro-cavity containing a thin slice of a nonlinear Kerr medium (see Fig. 1.4). This newly proposed setup promises to combine the advantages of dispersive Kerr micro-resonators and mode-locked VECSELs, while mitigating their limitations. The dynamical model derived from first principles is given by the DAEs (3.83),(3.84), which captures all the multiple external cavity reflections and naturally includes higher-order dispersive effects [57]. Here, the sign of the detuning between the injection and the micro-cavity resonance, defines whether the KGTI system operates in the normal or anomalous dispersion regime, respectively.

An important tool in the analytical study was the derivation of multiple PDE normals forms that capture the dynamics of the full DAE model in certain limits. In particular, the normals forms revealed how the system parameters influence the dispersive properties of the micro-cavity [57]. We demonstrated that the dynamics in the mean-field limit, where losses and phase shifts are small, is captured by the well-established Lugiato–Lefever equation [58] with third-order dispersion. In the normal dispersion regime, we described bright and dark TLSs that are formed by domain walls that can interlock at discrete distances. This formation process was detailed by a normal form close to the onset of optical bistability, which corresponds to a real Ginzburg–Landau equation with third-order dispersion and further nonlinear contributions. Hence, this equation provided an explanation for the minimal pattern formation scenario. It was derived under the premise of a vanishing round-trip phase. However, a derivation for a general phase is possible, yet challenging, and could help to clarify a more general pattern formation scenario in the future. This would also help to understand the link between the normal forms in the mean-field limit and at the onset of bistability.

Next, we emphasize that the validity of the full DAE model is not limited by the restrictions of typical mean-field or coupled-mode models [24, 58–64], which underlines the importance of a time-delayed description of optical systems. Hence, we were able to perform a detailed analysis of dynamical regimes beyond the mean-field limit. For instance, we described a regime, where the amplitude of the TLSs becomes chaotic in a cascade of period doubling bifurcations. Further, we found a novel type of bright TLSs that form as homoclinic orbits instead of the usual double heteroclinic connection. These high-intensity solitons are stable over a wide parameter range, which makes them a promising candidate for future applications. To fully understand the corresponding pattern formation mechanism, it would be helpful to derive an additional normal form close to the onset of their emergence. This would also help to clarify the link to TLSs found in the anomalous dispersion regime, where the KGTI can support similar structures [107, 139].

In the conservative case, the link to the Nonlinear Schrödinger equation reveals important implications as we demonstrated that reversibility and conservative solitons exist in a time-delayed system. The property of reversibility became apparent when transforming the DAEs (3.83),(3.84) into a bilateral NDDE. We believe that bilateral NDDEs open an avenue for the potential realization of further conservative nonlinear dynamics in time-delayed systems, such as, e.g., the Fermi–Pasta–Ulam–Tsingou recurrence [140] or the observation of the Korteweg–de Vries solitons.

Finally, it is to mention that the model of the KGTI system can be extended to introduce additional effects. First, one can take thermal effects into account, which stem from heating of the micro-cavity due to two-photon absorption [89]. This effect results in a state dependent detuning. Next, the effects of two-photon absorption are only briefly studied here, such that more work is necessary to fully understand their impact on the stability of TLSs in the KGTI. First preliminary experimental results suggest, that both effects are present in the experiment, such that further studies in this direction are required. Further, one can consider a modulation of the feedback phase, which can be realized by shifting the external mirror. This creates a potential in which the TLSs evolve and enables a finer control over them [141, 142]. Finally, for a complete description, one has to include the dynamics in the transversal plane. The resulting model is a mix between an DAE and a PDE, which goes beyond the scope of currently available continuation tools. At least in the mean-field limit, one can use the equivalence between the KGTI model and the generalized LLE to obtain a pure PDE description [91]. However, a study of the full DAE-PDE model is still lacking.

In the second part of the thesis, we studied the interaction of TLSs in multi-pulse states in PML lasers. We demonstrated that the pulses exhibit two degrees of freedom: position and phase. These properties determine the exact form of the resulting frequency comb, which makes their study relevant. The positions and phases evolve on slow time scales, i.e., over many round-trips, whereas the pulses themselves are formed on a fast time scale. The dynamics of the pulses on these two timescales is modeled by the well-established Haus master equation [25] for the optical field and the carriers (gain and absorber population). This PDE model can be derived from the a time-delayed model [41] in the mean-field limit. In a next step, we were able to reduce the complexity of the problem by projecting the high-dimensional PDE onto a lower-dimensional subset. In particular, we derived effective equations of motion (EOM) in form of coupled ODEs for the phases and positions, thereby unveiling the key mechanisms in which the pulses can interact. First, the pulses create a depletion in the gain medium that influences consecutive pulses [43]. Second, the decaying tails can exhibit an overlap leading to a coherent interaction [42]. Finally, the introduction of time-delayed feedback (TDF) stemming from, e.g. small reflections of lenses, leads to the emergence of satellites, i.e., small copies of the pulses appearing throughout the cavity that can influence the laser output [44–48]. Here, this mechanism enables the interplay between pulses and their respective satellites, which was not considered in other approaches so far [42, 43]. We demonstrated that TDF plays an important role in the organization of the phases and positions, and leads to the emergence of many interesting dynamical regimes. This was underlined by a detailed parameter study of the EOM. Here, we want to stress the excellent predictive power of the EOM, which exhibit high quantitative agreement in several tests with the HME over a wide range of parameter sets. This makes the EOM a good candidate for further predictive studies for PML lasers. In particular, a more detailed bifurcation analysis of the general $N$ pulse state would help the understanding of their dynamics. For instance, one could unveil how the different periodic and chaotic states emerge, which were only briefly discussed in this thesis.

Further, we demonstrated that the EOM is also valid in the regime of shorter cavities, where pulses cannot be seen as TLSs as they are trapped in position by strong carrier interactions. This is interesting, as a fundamental step in the derivation of the EOM was a superposition ansatz for a multi-pulse state. That is, this ansatz relies on the existence of a single pulse. However, in a short cavity a single pulse exhibits a different shape as, e.g., two pulses creating an $HML_2$ state. This fact made our analysis more involved as the parameters of the EOM could not be simply calculated from the pulse shape (as we did for the long cavity case), but we had to rely on a perturbation analysis to determine them. Hence, further work is necessary to find the fundamental building blocks that make up an HML state and therefore, shed light on this ambiguity. One approach would be the inclusion of further effects in the EOM such as shape deformation modes.

Nevertheless, our work revealed important consequences on our understanding of coherence in ML lasers, as we demonstrated that the phase dynamics of the harmonic pulse trains emitted is governed by the Kuramoto model with short range interactions. This provides a novel view on how coherent states emerge, as we consider the phases of the pulses, instead of those of the cavity modes; see e.g. [129–131]. Consequently, the associated optical frequency comb actually corresponds to one of the splay states found in the Kuramoto model. Our prediction of multistability of the splay states for $N \geq 5$ pulses has profound implications. In particular, the notion of coherence should be interpreted by comparing the duration of the measurement time with the Kramers' escape time [138] of each splay state, since averaging over different splay states decreases the measured coherence. Our theoretical predictions are supported by experimental validation based upon a VECSEL [125]. While this setup relies on passive mode-locking, we believe that our results are general, and therefore, also apply to system using active mode-locking.

Further, we studied the transition between ordered and disordered states. In particular, we demonstrated that the transition between the two is continuous. This is supported by the Mermin–Wagner theorem [143], which prohibits any ordering phase transition in uni-dimensional systems (which is clearly the case of the ring laser we studied). The situation changes for a two-dimensional system, where the splay states do not exist. Here, phase transitions from disordered to ordered states are possible, allowing for a more stable high-coherent state. For the realization of a two-dimensional ML system, one can connect the two cases studied in this thesis. Therefore, one can use that the phase dynamics induced by TDF is structurally the same as in the case of overlapping tails. Further, one can create additional synthetic dimensions [144, 145] employing the effects of TDF. Here, one can utilize a feedback cavity that is $p$-times shorter than the main cavity, such that a state of $N$ pulses effectively corresponds to a grid with dimensions $p \times N/p$. Hence, this technique effectively creates a two-dimensional system that can give rise to vortices and promises the existence of phase transitions towards more coherent states, which, in turn, has direct applications in the field of frequency combs and metrology.

# A. Numerical Methods

In general, a complex dynamical system described by a set of nonlinear differential equations cannot be solved analytically. Hence, one has to rely on numerical methods to study the corresponding system. The most important numerical tools used in this thesis are *time simulations* and *arclength path continuation*.

## A.1. Time Simulations

The systems which are studied in this thesis are initial value problems. To study the evolution of the initial condition, we integrate the corresponding dynamical system, which can be done using a numerical scheme for a short time step. There are countless numerical schemes for the integration (see e.g. [146]); here, we present the employed schemes for time simulations of the DAEs (3.83),(3.84) describing the dynamics in the KGTI, and the Haus master equation (3.155)–(3.157) describing the dynamics of a PML laser.

### A.1.1. Semi-Implicit Euler Scheme for the KGTI

We use a semi-implicit Euler scheme to integrate the DAE (3.83),(3.84). That is, we make the step in the nonlinearity explicitly, but the linear part semi-implicitly (i.e., we average $E_n$ and $E_{n+1}$ where $E_n$ is the $n$-th point in time). This results in the following scheme:

$$\frac{E_{n+1}-E_n}{\Delta t} = \underbrace{\left[-1+i\left(s\left|E_n\right|^2-\delta\right)\right]}_{U_n}\frac{E_{n+1}+E_n}{2}+h\frac{Y_{n+1}+Y_n}{2}. \tag{A.1}$$

Rearranging gives an explicit expression for $E_{n+1}$

$$E_{n+1} = \frac{\left(1+\frac{\Delta t}{2}U_n\right)E_n+\frac{\Delta t}{2}h\left(Y_{n+1}+Y_n\right)}{1-\frac{\Delta t}{2}U_n}. \tag{A.2}$$

Here, $Y_{n+1}$ can simply be computed from the algebraic condition in Eq. (3.84), i.e.,

$$Y_{n+1} = \eta e^{i\varphi}\left(E_{n-M}-Y_{n-M}\right)+\sqrt{1-\eta^2}Y_0, \tag{A.3}$$

where $M=\left\lfloor\frac{\tau}{\Delta t}\right\rfloor$ is the (rounded) number of points corresponding to the time-delay. While this scheme is $\mathcal{O}\left(\Delta t\right)$, it is generally sufficient for the applications in this thesis. However, we also implemented a scheme in which we use the step in Eq. (A.2) to compute the midpoint $U_{n+\frac{1}{2}}$ of the the nonlinear part:

$$U_{n+\frac{1}{2}} = -1 + i\left(s\left|\frac{E_{n+1}+E_n}{2}\right|^2 - \delta\right). \tag{A.4}$$

With that, we find the following second order scheme

$$E'_{n+1} = \frac{\left(1+\frac{\Delta t}{2}U_{n+\frac{1}{2}}\right)E_n + \frac{\Delta t}{2}h\left(Y_{n+1}+Y_n\right)}{1-\frac{\Delta t}{2}U_{n+\frac{1}{2}}}. \tag{A.5}$$

### A.1.2. Split-Step Method for the Haus Master Equation

For the time simulation of the Haus master equation (3.155)–(3.157), we use a split-step semi-implicit pseudo-spectral method. That is, we compute nonlinearities in the space-domain, while the linear operators are computed using spectral methods in the Fourier space. Further, we need to integrate the carriers separately from the field because the carriers in Eqs. (3.156) and (3.157) do not contain a temporal derivative. We denote with $g_i^j$ the $i$-th point in slow time and the $j$-th point fast time (i.e. the space-like variable).

We begin to update the gain $g$. We employ a semi-implicit step in space and use a midpoint ansatz, which leads to:

$$\frac{g_{i+1}^{j+1}-g_{i+1}^{j}}{\Delta z} = \Gamma_g\left(g_0 - \frac{g_{i+1}^{j+1}+g_{i+1}^{j}}{2}\right) - \frac{g_{i+1}^{j+1}I_i^{j+1}+g_{i+1}^{j}I_i^{j}}{2} \tag{A.6}$$

$$\Leftrightarrow g_{i+1}^{j+1} = \frac{\Delta z\Gamma_g g_0 + \left[1-\frac{\Delta z}{2}\left(\Gamma_g+I_i^j\right)\right]g_{i+1}^{j}}{1+\frac{\Delta z}{2}\left(\Gamma_g+I_i^{j+1}\right)}. \tag{A.7}$$

That is, we can compute $g_{i+1}^{j+1}$ from $g_{i+1}^{j}$. However, this implies that the scheme does not provide us with the first point $g_{i+1}^{1}$. For that, we consider again the equation for the gain in Eq. (3.156) that is the following ODE

$$\partial_z g\left(z\right) = \Gamma_g g_0 - P'\left(z\right)g\left(z\right), \tag{A.8}$$

where we define

$$P\left(z\right) = \int_0^z\left(\Gamma_g + \left|E\left(z'\right)\right|^2\right)dz'. \tag{A.9}$$

Here, we first compute the cumulative intensity

$$I_c\left(z\right) = \int_0^z I\left(z'\right)dz' \tag{A.10}$$

such that $P(z) = \Gamma_g z + I_c(z)$. The integral for $I_c(z)$ can be obtained using, e.g., the trapezoid method. Equation (A.8) can be solved using the method of integrating factors. The general solution reads

$$g(z) = e^{-P(z)} \left( g(0) + \Gamma_g g_0 \int_0^\tau e^{P(z')} dz' \right). \tag{A.11}$$

Now, we apply the periodic boundary conditions, i.e., we evaluate for $z = 0 = \tau$ and solve for $g(0)$:

$$g(0) = g^1_{i+1} = \Gamma_g g_0 \frac{\int_0^\tau e^{P(z')} dz'}{e^{P(\tau)} - 1}. \tag{A.12}$$

With that, we can apply Eq. (A.7) iteratively to obtain all points for the next time step. On the other hand, one could also simply update the carrier using the analytical expression in Eq. (A.11). The steps to obtain the updated absorber $q$ are equivalent.

In the next step, we consider the updating scheme for the field $E$. We need to integrate

$$\partial_\xi E = (\mathcal{L} + M) E, \tag{A.13}$$

$$\text{where } \mathcal{L} = v\partial_z + \frac{1}{2\gamma^2}\partial_z^2 + \eta e^{i\Omega}\mathcal{S}_{-\tau_f}, \tag{A.14}$$

$$M = -k + \frac{1 - i\alpha_g}{2} g - \frac{1 - i\alpha_q}{2} q + i\omega, \tag{A.15}$$

where $\mathcal{S}_{-\tau_f} = e^{-\tau_f \partial_z}$ is the shift operator, $v$ is the drift velocity and $\omega$ is the carrier frequency. We first make an explicit half-step in time

$$E^j_{i+\frac{1}{2}} = \left(1 + \frac{\Delta t}{2} M\right) E^j_i. \tag{A.16}$$

Then, we refine the step by applying the linear operator (which is done in Fourier space to handle the spatial derivatives)

$$\tilde{E}^j_{i+\frac{1}{2}} = e^{\Delta t \mathcal{L}} E^j_{i+\frac{1}{2}} = \mathcal{F}^{-1}\left[e^{\Delta t \hat{\mathcal{L}}} \mathcal{F}\left[E^j_{i+\frac{1}{2}}\right]\right]. \tag{A.17}$$

And finally, we make an implicit half-step to obtain $E^j_{i+1}$:

$$E^j_{i+1} = \frac{\tilde{E}^j_{i+\frac{1}{2}}}{1 - \frac{\Delta t}{2} M}. \tag{A.18}$$

Finally, let us discuss how to find $v$ and $\omega$. While these quantities can be scaled out of the equation, we need to find them in order to arrive at a steady state. While at the beginning of a simulation, these are additional free parameters, they can be found in a simulation using a control loop. For the drift, we expand

$$I_i(z) = I_{i+1}(z + v\Delta t) = I_{i+1}(z) + \frac{dI_{i+1}}{dz} v\Delta t, \tag{A.19}$$

where $\frac{dI_{i+1}}{dz} = 2\mathrm{Re}\left(E^* \frac{dE}{dz}\right)$. Now we weight both sides of the equation additionally with $\frac{dI_{i+1}}{dz}$ to take the tilt of the intensity profile into account. We integrate over $z$ (e.g. by summing up) and solve for $v$:

$$v = \frac{1}{\Delta t} \frac{\int_0^\tau \left(I_i(z) - I_{i+1}(z)\right) \frac{dI_{i+1}}{dz} dz}{\int_0^\tau \left(\frac{dI_{i+1}}{dz}\right)^2 dz}. \tag{A.20}$$

For the carrier frequency $\omega$, we first find the phase difference as

$$\arg\left(E_{i+1}E_i^*\right) = \arg\left[|E_{i+1}|\,|E_i^*| \exp\left(i\phi_{i+1} - i\phi_i\right)\right] = \phi_{i+1} - \phi_i. \tag{A.21}$$

But we do not simply want to sum this up because we want to the pulse itself to have a higher influence. Therefore, we obtain

$$\omega = \frac{1}{\Delta t} \frac{\int_0^\tau \arg\left(E_{i+1}E_i^*\right) I_{i+1} dz}{\int_0^\tau I_{i+1} dz}. \tag{A.22}$$

Both equations for $v$ and $\omega$ can be understood as corrections to an already existing drift and carrier frequency, that is, they are rather $\Delta v$ and $\Delta\omega$ because $E_i$ was already computed with some $v_i$ and $\omega_i$ such that the updated quantities are $v_{i+1} = v_i + \Delta v$ and $\omega_{i+1} = \omega_i + \Delta\omega$.

## A.2. Path Continuation

While time simulation are useful to gain an overview over the dynamical regimes of a system, there is a fundamental drawback, which is that one can only explore stable manifolds while unstable ones are inaccessible. However, studying all solutions is often crucial to fully understand how certain states emerge. Further, one is often only interested in the final solution of a time simulation and not the transient towards it. This makes time simulations inefficient for large parameter scans.

These limitations are circumvented by path continuation techniques. Here, solutions to a system are obtained by finding their roots which does not differentiate between stable and unstable solutions. This also allows to follow solutions in parameter space. Furthermore, eigenvalues can be computed numerically allowing to detect bifurcations, which offers the possibility to find new solution branches. Finally, bifurcation points can be tracked in a second control parameter, thereby allowing to gain an overview of the dynamics in a two-parameter-diagram. Depending on what kind of dynamical system is analyzed, different software packages are available. For the time-delayed systems in this thesis, the `MATLAB` package `DDE-BIFTOOL` [105, 111] is used. In particular, we emphasize that Eqs. (3.83) and (3.84) describing the the KGTI system contain a DAE. The implementation of DAEs in `DDE-BIFTOOL` was only realized recently [112]. Further, we compare bifurcation diagrams of the DAE with the PDE normal forms. These continuations were obtained using `pde2path` [147] (cf. Fig. 4.36) and `BICE` [148] (cf. Fig. 4.21).

In the following, we present the main concepts of path continuation. We consider a system of $n$ differential equations with a control parameter $\mu$ that reads $\dot{\boldsymbol{x}} = \boldsymbol{f}(\boldsymbol{x}, \mu)$ where $\boldsymbol{x}_0^* = (x_{0,1}^*, x_{0,2}^*, ..., x_{0,n}^*)$ is a stationary solution for $\mu = \mu_0$. The goal is to find the solution $\boldsymbol{x}_1^*$ for the parameter $\mu_1 = \mu_0 + \Delta\mu$. First, we make a prediction step $\boldsymbol{x}_1^{*(0)}$ for $\mu_1$ by using the tangent of the curve $\boldsymbol{x}^*(\mu)$ at $(\boldsymbol{x}_0^*, \mu_0)$:

$$\boldsymbol{x}_1^{*(0)} = \boldsymbol{x}_0^* + \Delta\mu \left.\frac{\partial \boldsymbol{x}^*}{\partial \mu}\right|_{(\boldsymbol{x}_0^*, \mu_0)}. \tag{A.23}$$

The slope can be found by differentiating $\boldsymbol{f}(\boldsymbol{x}^*(\mu), \mu) = 0$:

$$\begin{aligned} \left[\underbrace{\frac{\partial \boldsymbol{f}}{\partial \boldsymbol{x}}}_{\text{Jacobian}} \frac{\partial \boldsymbol{x}}{\partial \mu} + \frac{\partial \boldsymbol{f}}{\partial \mu}\right]_{(\boldsymbol{x}_0^*, \mu_0)} &= 0 \\ \Leftrightarrow \left.\frac{\partial \boldsymbol{x}}{\partial \mu}\right|_{(\boldsymbol{x}_0^*, \mu_0)} &= -\left.\left[\left(\frac{\partial \boldsymbol{f}}{\partial \boldsymbol{x}}\right)^{-1} \cdot \frac{\partial \boldsymbol{f}}{\partial \mu}\right]\right|_{(\boldsymbol{x}_0^*, \mu_0)}. \end{aligned} \tag{A.24}$$

Next, we need to find the actual solution $\boldsymbol{x}_1^*$ that satisfies $\boldsymbol{f}(\boldsymbol{x}_1, \mu_1) = 0$ from the approximation $\boldsymbol{x}_1^{*(0)}$. Hence, the we need to "improve" the guess. This can be achieved with *Newton's method* for finding roots of functions up to an arbitrary accuracy. The scheme is defined by the following iteration rule

$$\boldsymbol{x}_1^{*(n+1)} = \boldsymbol{x}_1^{*(n)} - \left.\left(\frac{\partial \boldsymbol{f}}{\partial \boldsymbol{x}}\right)^{-1}\right|_{(\boldsymbol{x}_1^{*(n)}, \mu_0)} \cdot \boldsymbol{f}\left(\boldsymbol{x}_1^{*(n)}\right). \tag{A.25}$$

This process is repeated until $\left|\boldsymbol{f}(\boldsymbol{x}_1^{(n)}, \mu_1)\right| < \epsilon$, where $\epsilon$ defines the accuracy. Then we return to changing $\mu$ to the next value, find the root for the new parameter and continue like that to follow a solution branch.

This method works until the branch approaches a fold for some $\mu = \mu_\mathrm{f}$. The problem is, that while for $\mu < \mu_\mathrm{f}$ two solutions exist, there is none for $\mu > \mu_\mathrm{f}$. Therefore, in order to follow the branch around the fold, we need to define a parameter which is unique along the branch. This issue is addressed with *arclength continuation*. Here, the control parameter $\mu$ is interpreted as an additional element of the extended solution $\boldsymbol{y^*} = (\boldsymbol{x}^*, \mu)$. Instead of $\mu$, the new control parameter is the arclength $s$, which can be approximated locally with Pythagoras' theorem:

$$|\boldsymbol{x}^*|^2 + (\Delta\mu)^2 = (\Delta s)^2. \tag{A.26}$$

With this, we can define the condition $\boldsymbol{p}(\boldsymbol{x}^*, \mu, s)$ as

$$\boldsymbol{p}(\boldsymbol{x}^*, \mu, s) = |\boldsymbol{x}^*|^2 + (\Delta\mu)^2 - (\Delta s)^2, \tag{A.27}$$

that supplements $\boldsymbol{f}(\boldsymbol{x}^*, \mu)$, so that the extended system reads

$$\boldsymbol{E}(\boldsymbol{x}^*, s) = \begin{pmatrix} \boldsymbol{f}(\boldsymbol{x}^*, \mu) \\ \boldsymbol{p}(\boldsymbol{x}^*, \mu, s) \end{pmatrix}. \tag{A.28}$$

The following steps are equivalent to the method described above but instead of changing $\mu$, we change $s$, and instead of finding roots of $\boldsymbol{f}$, we search for the roots of $\boldsymbol{E}$. Finally, this technique can be extended to time-periodic solutions. In this case, one seeks time-periodic trajectories $\boldsymbol{x}^*(t)$ with period $T$ such that $\dot{\boldsymbol{x}}^*(t) = \boldsymbol{f}(\boldsymbol{x}^*(t), \mu)$ and $\boldsymbol{x}^*(t+T) = \boldsymbol{x}^*(t)$. This defines a boundary value problem, where $T$ is treated as an additional unknown parameter. To resolve the time-translation invariance of periodic solutions, a phase condition is imposed [111, 149]. The boundary value problem is then discretized, for instance using collocation methods, and the resulting algebraic system is solved using path continuation techniques applied to the extended system $(\boldsymbol{x}^*(t), T, \mu)$. Arclength continuation can similarly be employed by defining a suitable pseudo-arclength condition.

# B. Derivation of Normal Forms for the KGTI

In this chapter, we derive explicitly two normal forms for the KGTI system (3.83),(3.84). The first one is derived at the onset of optical bistability for vanishing phase ($\varphi = 0$) and is used in Section 4.3. The second one is derived in the mean-field limit where $\eta \to 1$ and $\tilde{\varphi} = \varphi - 2\arctan\delta \to 0$. It is used in Sections 4.1 and 4.5.

## B.1. Normal Form at the Onset of Bistability

This derivation follows the lines of the supplementary material of [99].

### The Onset of Bistability

The steady state CW solutions $I_s = |E_s|^2$ of Eqs. (3.83) and (3.84) for the case $\varphi = 0$ read (cf. Section 4.2.1)

$$Y_0^2 = \frac{k^2 + (I_s - \delta)^2}{h^2 \frac{1-\eta}{1+\eta}} I_s, \qquad \text{where } k = \frac{1 + (1-h)\,\eta}{1+\eta}. \tag{B.1}$$

For certain system parameters, the curve $I_s(Y_0)$ exhibits bistabile response. In fact, the onset of bistability can be calculated analytically (cf. Section 4.2.3). It is defined as the value of the critical detuning $\delta_c$ for which the steady state solutions $I_s$ possesses a saddle point, i.e., $\frac{\partial Y_0}{\partial I_s} = \frac{\partial^2 Y_0}{\partial I_s^2} = 0$. At this point, we find critical values for the detuning $\delta_c$ (cf. Eq. (4.40)), the injection $Y_0^c$ and the electric field $E_s^c$:

$$\delta_c = \sqrt{3}k, \quad Y_0^c = \frac{2k}{3}\sqrt{\frac{2\sqrt{3}}{h^2 \frac{1-\eta}{1+\eta}}}k, \quad E_s^c = \sqrt{\frac{3k}{2\sqrt{3}}}\left(1 - i\frac{1}{\sqrt{3}}\right). \tag{B.2}$$

### Expansions

Next, we apply a multiple time scale method to the periodic solution of Eqs. (3.83),(3.84). For this purpose, we normalize the long delay time $\tau$ and define an smallness parameter $\epsilon = \tau^{-1}$ which yields

$$\varepsilon \dot{E} = \left[-1 + i\left(|E|^2 - \delta\right)\right] E + hY\,, \tag{B.3}$$

$$Y = \eta\left[E(t-1) - Y(t-1)\right] + \sqrt{1 - |\eta|^2} Y_0\,. \tag{B.4}$$

We define new variables $e$ and $y$ as small deviations from the steady states at the critical point and separate into real and imaginary parts: $E = E_s^c + e = E_{sx}^c + iE_{sy}^c + e_x + ie_y$

and $Y = Y_s^c + y = Y_s^c + y_x + iy_y$. Further, we define $\theta$ and $z_0$ as the deviation from the critical parameter values for detuning and injection, respectively: $\delta = \delta_c + \theta$ and $Y_0 = Y_0^c + z_0$. Then the equations for the fields deviations read

$$\begin{aligned} \epsilon\frac{de_x}{dt} =& -\sqrt{\frac{k}{2\sqrt{3}}}\theta - (1-k)\,e_x + \theta e_y + hy_x - \sqrt{2\sqrt{3}k}e_x e_y \\ &+ \sqrt{\frac{k}{2\sqrt{3}}}e_x^2 + \sqrt{\frac{3\sqrt{3}k}{2}}e_y^2 - e_x^2 e_y - e_y^3\,, \end{aligned} \tag{B.5}$$

$$\begin{aligned} \epsilon\frac{de_y}{dt} =& -\sqrt{\frac{\sqrt{3}k}{2}}\theta + \left(\frac{2}{\sqrt{3}}k - \theta\right)e_x - (1+k)\,e_y + hy_y - \sqrt{\frac{2k}{\sqrt{3}}}e_x e_y \\ &+ 3\sqrt{\frac{\sqrt{3}k}{2}}e_x^2 + \sqrt{\frac{\sqrt{3}k}{2}}e_y^2 + e_x e_y^2 + e_x^3\,, \end{aligned} \tag{B.6}$$

$$y_x = \eta\left(e_x\,(t-1) - y_x\,(t-1)\right) + \sqrt{1-|\eta|^2}z_0\,, \tag{B.7}$$

$$y_y = \eta\left(e_y\,(t-1) - y_y\,(t-1)\right)\,. \tag{B.8}$$

We define new time scales $t_0 = \omega t$, $t_1 = 0$, $t_2 = \epsilon^2 t$ and $t_3 = \epsilon^3 t$, where small changes in $\omega$ account for the drift: $\omega = 1 + \epsilon\omega_1 + \epsilon^2\omega_2 + \epsilon^3\omega_3 + \ldots$. Therefore, the time derivative is $\dfrac{d}{dt} = \mathcal{T}_0 + \epsilon\mathcal{T}_1 + \epsilon^2\mathcal{T}_2 + \epsilon^3\mathcal{T}_3 + \ldots$, where $\mathcal{T}_0 = \partial_0$, $\mathcal{T}_1 = \omega_1\partial_0$, $\mathcal{T}_2 = \omega_2\partial_0 + \partial_2$ and $\mathcal{T}_3 = \omega_3\partial_0 + \partial_3$. Further, the delayed fields are now functions of the new time scales, i.e., $\Lambda\,(t-1) = \Lambda\left(t_0 - \omega, t_2 - \epsilon^2, t_3 - \epsilon^3\right)$ for $\Lambda = e_x, e_y, y_x, y_y$. This expression needs to be expanded in powers of $\epsilon$:

$$\Lambda\,(t-1) = \left(\mathcal{S}_0 + \epsilon\mathcal{S}_1 + \epsilon^2\mathcal{S}_2 + \epsilon^3\mathcal{S}_3 + \ldots\right)\Lambda\,(t_0 - 1, t_2, t_3)\,, \tag{B.9}$$

where $\mathcal{S}_0 = 1$, $\mathcal{S}_1 = -\omega_1\partial_0$, $\mathcal{S}_2 = -\omega_2\partial_0 + \frac{\omega_1^2}{2}\partial_0^2 - \partial_2$ and $\mathcal{S}_3 = -\omega_3\partial_0 - \frac{\omega_1^3}{6}\partial_0^3 + \omega_1\omega_2\partial_0^2 + \omega_1\partial_0\partial_2 - \partial_3$. Further, we need to define the expantions of the fields and parameters. First, all fields are expanded as

$$\Lambda\,(t) = \varepsilon\Lambda^{(1)}\,(t_0, t_2, t_3) + \varepsilon^2\Lambda^{(2)}\,(t_0, t_2, t_3) + \cdots\,. \tag{B.10}$$

Finally, we also expand the variations to the critical parameter values

$$\theta = \epsilon\theta_1 + \epsilon^2\theta_2 + \epsilon^3\theta_3 + \epsilon^4\theta_4 + \ldots\,, \tag{B.11}$$

$$z_0 = \epsilon z_0^{(1)} + \epsilon^2 z_0^{(2)} + \epsilon^3 z_0^{(3)} + \epsilon^4 z_0^{(4)} + \ldots\,. \tag{B.12}$$

We insert all expansions and scalings into Eqs. (B.5)–(B.8) and sort for orders in $\epsilon$. As we stretched the $t_0$-scale in such a way that the drift is cancelled, we can assume that $e$ and $y$ are 1-periodic, i.e., $\Lambda\,(t_0 - 1) = \Lambda\,(t_0)$ for $\Lambda = (e_x, e_y, y_x, y_y)$.

### Solving the Orders

Next, we need to solve each order separately.

### First Order

In the first order $\mathcal{O}(\epsilon)$, we obtain the following linear system:

$$0 = Pv^{(1)} + b\,, \tag{B.13}$$

$$\text{where } P = \begin{pmatrix} k-1 & 0 & h & 0 \\ \frac{2k}{\sqrt{3}} & -(k+1) & 0 & h \\ \eta & 0 & -(1+\eta) & 0 \\ 0 & \eta & 0 & -(1+\eta) \end{pmatrix}, \tag{B.14}$$

$$v^{(1)} = \begin{pmatrix} e_x^{(1)} \\ e_y^{(1)} \\ y_x^{(1)} \\ y_y^{(1)} \end{pmatrix}, \quad b = z_0^{(1)}\sqrt{1-\eta^2}\begin{pmatrix} 0 \\ 0 \\ 1 \\ 0 \end{pmatrix} - \sqrt{\frac{k}{2\sqrt{3}}}\theta_1 \begin{pmatrix} 1 \\ \sqrt{3} \\ 0 \\ 0 \end{pmatrix}. \tag{B.15}$$

The homogeneous system $0 = Pv^{(1)}$ has a kernel, i.e., the kernel eigenvector $\mu$ is the solution of the linear system:

$$\mu = \begin{pmatrix} 1 \\ \frac{1}{\sqrt{3}} \\ \frac{\eta}{1+\eta} \\ \frac{\eta}{\sqrt{3}(1+\eta)} \end{pmatrix}. \tag{B.16}$$

The adjoint linear operator $P^\dagger$ also has a kernel, which is spanned by the eigenvector

$$\nu = \begin{pmatrix} \frac{1+\eta}{h} \\ 0 \\ 1 \\ 0 \end{pmatrix}. \tag{B.17}$$

With this, one can use a technique from linear algebra to arrive directly at the solvability condition: the Fredholm alternative. For this we project eq. (B.13) onto $\nu^\dagger$.

$$0 = \nu^\dagger \left(Pv^{(1)} + b\right) = \underbrace{\left(\nu^\dagger P\right)}_{\left(P^\dagger \nu\right)^\dagger = 0} v^{(1)} + \nu^\dagger b \Rightarrow \nu^\dagger b = 0. \tag{B.18}$$

Applying this to the specific equations at hand yields the following solvability condition

$$z_0^{(1)}\sqrt{1-\eta^2} - \frac{1+\eta}{h}\sqrt{\frac{k}{2\sqrt{3}}}\theta_1 = 0. \tag{B.19}$$

Next, we need the solution of the inhomogeneous system, that we can obtain by finding any specific solution of Eq. (B.13), e.g., we can set $v_1^{(1)} = 0$ and solve for the other components. Taking this and the solvability condition into consideration the full solution of the first order reads

$$v^{(1)} = v_1^{(1)} \begin{pmatrix} 1 \\ \frac{1}{\sqrt{3}} \\ \frac{\eta}{1+\eta} \\ \frac{\eta}{\sqrt{3}(1+\eta)} \end{pmatrix} + \sqrt{\frac{\sqrt{3}}{2k}}\theta_1 \begin{pmatrix} 0 \\ -\frac{1}{2} \\ \frac{k}{h\sqrt{3}} \\ -\frac{1}{2}\frac{\eta}{1+\eta} \end{pmatrix}. \tag{B.20}$$

### Second Order

In the next second order $\mathcal{O}\left(\epsilon^2\right)$, one obtains

$$0 = Pv^{(2)} + z_0^{(2)}\sqrt{1-\eta^2}\begin{pmatrix} 0 \\ 0 \\ 1 \\ 0 \end{pmatrix} - \mathcal{T}_0 \begin{pmatrix} v_1^{(1)} \\ v_2^{(1)} \\ 0 \\ 0 \end{pmatrix} + \eta\mathcal{S}_1 \begin{pmatrix} 0 \\ 0 \\ v_1^{(1)} - v_3^{(1)} \\ v_2^{(1)} - v_4^{(1)} \end{pmatrix} + \Theta_2 + N_2\,, \tag{B.21}$$

where $\Theta_2$ and $N_2$ are the terms stemming from detuning $\theta e_{x,y}$ and the nonlinearities. The homogeneous system is the same as before such that we again apply the Fredholm alternative to obtain the following solvability condition:

$$0 = z_0^{(2)}\sqrt{1-\eta^2} - \sqrt{\frac{k}{2\sqrt{3}}}\frac{1+\eta}{h}\theta_2 + \frac{1+\eta}{\sqrt{3}h}\theta_1 v_1^{(1)} - \frac{1+\eta}{8h}\sqrt{\frac{\sqrt{3}}{2k}}\theta_1^2. \tag{B.22}$$

Here, the drift was cancelled by choosing $\omega_1 = -\frac{(1+\eta)^2}{\eta h}$. This can be done as no assumptions concerning the scaling factor $\omega$ of the $t_0$-time scale were made such that we can choose the $\omega_i$ in a way, which is convenient (i.e., to cancel the drift).

Equation (B.22) implies that $v_1^{(1)}$ is a constant which depends only on the deviations to the critical point and which are time independent. This is problematic as we later want to derive a differential equation. However, we remember that we can choose the scaling of the parameter deviations, and, at this point, we find, that we have to set

$\theta_1 = 0$ (i.e., $\theta = \mathcal{O}\left(\epsilon^2\right)$) in order to proceed. Then the solvability condition reads

$$z_0^{(2)} = \sqrt{\frac{1}{2\sqrt{3}}\frac{\eta\left(1-h\right)+1}{1-\eta}\frac{\theta_2}{h}}. \tag{B.23}$$

In order to solve the following orders, one has to compute the full solution including the inhomogeneous system for the second and third components:

$$v_2^{(2)} = \frac{1}{\sqrt{3}}v_1^{(2)} - \frac{1}{2\sqrt{k}}\left[\sqrt{\frac{\sqrt{3}}{2}}\theta_2 - 4\sqrt{\frac{2}{3\sqrt{3}}}\left(v_1^{(1)}\right)^2\right], \tag{B.24}$$

$$v_3^{(2)} = \frac{\eta}{1+\eta}v_1^{(2)} + \frac{1}{1+\eta}z_0^{(2)}\sqrt{1-\eta^2} + \frac{1}{h}\partial_0 v_1^{(1)}. \tag{B.25}$$

### Third Order

Following the same procedure, we find the following solvability condition at third order $\mathcal{O}\left(\epsilon^3\right)$:

$$\begin{aligned}\partial_2 v_1^{(1)} =& \frac{1+\eta}{\eta}\sqrt{1-\eta^2}z_0^{(3)} - \frac{1}{2}\frac{\left(1-\eta\right)\left(1+\eta\right)}{\eta h}\omega_1\partial_0^2 v_1^{(1)} + \frac{4}{3\sqrt{3}}\omega_1\left(v_1^{(1)}\right)^3 \\ &+ \omega_1\sqrt{\frac{k}{2\sqrt{3}}}\theta_3 - \frac{1}{\sqrt{3}}\omega_1\theta_2 v_1^{(1)},\end{aligned} \tag{B.26}$$

where the drift was canceled by choosing $\omega_2 = \frac{(1+\eta)^4}{\eta^2 h^2} = \omega_1^2$. We only need to compute the full solution for the third component:

$$v_3^{(3)} = \frac{\eta}{1+\eta}v_1^{(3)} - \frac{1}{h}\left[-\sqrt{\frac{k}{2\sqrt{3}}}\theta_3 + \frac{1}{\sqrt{3}}\theta_2 v_1^{(1)} - \partial_0 v_1^{(2)} - \omega_1\partial_0 v_1^{(1)} - \frac{4}{3\sqrt{3}}\left(v_1^{(1)}\right)^3\right]. \tag{B.27}$$

### Fourth Order

Finally, in the fourth order $\mathcal{O}\left(\epsilon^4\right)$ the solvability condition reads

$$
\begin{aligned}
\partial_3 v_1^{(1)}+\partial_2 v_1^{(2)}=&-\tfrac{3(1-\eta)(1+\eta)}{2\eta h}\omega_1^2\partial_0^2 v_1^{(1)}-\tfrac{1}{2}\tfrac{(1+\eta)(1-\eta)}{\eta h}\omega_1\partial_0^2 v_1^{(2)}\\
&+\tfrac{1}{3}\tfrac{1+\eta(\eta-1)}{(1+\eta)^2}\omega_1^3\partial_0^3 v_1^{(1)}-\tfrac{4}{3\sqrt{3}}\tfrac{(1+\eta)(1-\eta)}{h\eta}\omega_1\partial_0\left(v_1^{(1)}\right)^3\\
&-\omega_1\tfrac{1}{\sqrt{3}}v_1^{(1)}\theta_3-\tfrac{1}{\sqrt{3}}\omega_1^2\theta_2 v_1^{(1)}-\omega_1\tfrac{1}{\sqrt{3}}\theta_2 v_1^{(2)}-\tfrac{1}{\sqrt{6\sqrt{3}\sqrt{k}}}\theta_2\left(v_1^{(1)}\right)^2\\
&+\tfrac{4}{3\sqrt{3}}\omega_1^2\left(v_1^{(1)}\right)^3+\omega_1\tfrac{4}{\sqrt{3}}\left(v_1^{(1)}\right)^2 v_1^{(2)}+\omega_1\tfrac{1+\eta}{\eta}\sqrt{1-\eta^2}z_0^{(3)}\\
&+\tfrac{1+\eta}{\eta}\sqrt{1-\eta^2}z_0^{(4)}+\sqrt{\tfrac{k}{2\sqrt{3}}}\omega_1^2\theta_3+\tfrac{1}{8\sqrt{k}}\omega_1\sqrt{\tfrac{\sqrt{3}}{2}}\theta_2^2+\omega_1\sqrt{\tfrac{\sqrt{3}k}{6}}\theta_4\,,
\end{aligned}
\tag{B.28}
$$

where the drift was canceled by setting $\omega_3=\omega_1^3+\frac{1}{\sqrt{3}}\frac{(1+\eta)(1-\eta)}{h\eta}\omega_1\theta_2$.

### Building the Normal Form

Next, we define an effective slow time scale as $\partial_\xi=\varepsilon^2\partial_2+\varepsilon^3\partial_3$ and evaluate

$$
\begin{aligned}
\partial_\xi e_x &= \left(\varepsilon^2\partial_2+\varepsilon^3\partial_3\right)\left(\epsilon v_1^{(1)}+\epsilon^2 v_1^{(2)}\right)+\mathcal{O}\left(\epsilon^5\right) && \text{(B.29)}\\
&= \epsilon^3\partial_2 v_1^{(1)}+\epsilon^4\left(\partial_3 v_1^{(1)}+\partial_2 v_1^{(2)}\right)+\mathcal{O}\left(\epsilon^5\right)\,, && \text{(B.30)}
\end{aligned}
$$

where we can insert the solvabiliy conditions found before. Next, we rescale the space with $\epsilon$ such that $\partial_0=\frac{1}{\epsilon}\partial_z$. Then, we are in a good position to find all necessary terms to rebuild $e_x=\epsilon v_1^{(1)}+\epsilon^2 v_1^{(2)}+...$ and the parameters $\theta=\delta-\delta_c$ and $z_0=Y_0-Y_0^c$ up to $\mathcal{O}\left(\epsilon^5\right)$. Finally, we obtain the following amplitude equation:

$$
\begin{aligned}
\partial_\xi e_x =& \frac{\omega_1^2}{2}\frac{1-\eta}{1+\eta}\partial_z^2 e_x-\frac{|\omega_1|^3}{3}\frac{1-\eta\left(1-\eta\right)}{\left(1+\eta\right)^2}\partial_z^3 e_x+\frac{4\left|\omega_1\right|}{3\sqrt{3}}\frac{\left(1+\eta\right)\left(1-\eta\right)}{h\eta}\partial_z e_x^3\\
&+\frac{1+\eta}{\eta}\sqrt{1-\eta^2}\left[Y_0-Y_0^c\right]+\omega_1\left[\delta-\delta_c\right]\left(\sqrt{\frac{k}{2\sqrt{3}}}+\frac{1}{8}\sqrt{\frac{\sqrt{3}}{2k}}\left[\delta-\delta_c\right]\right)\\
&-\frac{\delta-\delta_c}{\sqrt{3}}\omega_1 e_x-\omega_1\frac{\delta-\delta_c}{\sqrt{6\sqrt{3}k}}e_x^2-\frac{4\left|\omega_1\right|}{3\sqrt{3}}e_x^3+\mathcal{O}\left(\epsilon\right).
\end{aligned}
\tag{B.31}
$$

### Rebuilding the Full Field

The full complex $E$ field can be reconstructed via $E=E_{sx}^c+iE_{sy}^c+e_x+ie_y$ ($=E_s^c+u+iv$ in the notation of [99]) where $e_y$ is given by $e_y=\epsilon v_2^{(1)}+\epsilon^2 v_2^{(2)}+\epsilon^3 v_2^{(3)}+\mathcal{O}\left(\epsilon^4\right)$. Inserting the solutions from each order yields

$$\begin{aligned} e_y = & \frac{1}{\sqrt{3}} e_x - \frac{2}{3k} \left(\delta - \delta_c\right) e_x + \frac{2}{3} \sqrt{\frac{2\sqrt{3}}{k}} e_x^2 + \frac{8}{9k} e_x^3 - \frac{1}{6} \sqrt{\frac{2\sqrt{3}}{k}} \left(\delta - \delta_c\right) \\ & - \frac{\sqrt{3}h}{6k} \sqrt{\frac{1-\eta}{1+\eta}} \left(Y_0 - Y_0^c\right) + \mathcal{O}\left(\epsilon^4\right). \end{aligned} \tag{B.32}$$

## B.2. Derivation of the Normal Form in the Mean-Field Limit

### B.2.1. Normal Form via a Multiple Time Scale Analysis

We begin with the DAE model of the KGTI system defined in Eqs. (3.83) and (3.84). We normalize the delay time $\tau$ and define a smallness parameter $\epsilon = \tau^{-1}$. Further, we scale the fields $E$ and $Y$ and the parameter $Y_0$ as

$$\tilde{E} = \varepsilon^{-\alpha} E, \tag{B.33}$$

$$\tilde{Y} = \varepsilon^{-\alpha} Y, \tag{B.34}$$

$$\tilde{Y_0} = \varepsilon^{-\alpha} Y_0, \tag{B.35}$$

such that Eqs. (3.83) and (3.84) read (we dropped the tilde again for better readability)

$$\epsilon \frac{dE}{dt} = -\left(1 + i\delta\right) E + hY + i\epsilon^{2\alpha} \left|E\right|^2 E, \tag{B.36}$$

$$Y = \eta e^{i\varphi} \left[E\left(t-1\right) - Y\left(t-1\right)\right] + \sqrt{1-\eta^2} Y_0. \tag{B.37}$$

The choice of $\alpha$ determines at which order the contributions from the cubic nonlinearity play a role. Specifically, for $\alpha = 1$ and $\alpha = \frac{3}{2}$, nonlinear terms emerge in the second and third order, respectively. In the following, we use the approach with $\alpha = 1$. For $\alpha = \frac{3}{2}$, see further below.

#### The KGTI Neutral Delay Differential Equation

Next, we derive a neutral delay differential equation (NDDE) for the KGTI. In NDDEs, the derivative of the delayed state appears in the system description. We obtain the NDDE by combining Eq. (B.36) with itself at a delayed state:

$$\begin{aligned} \varepsilon \frac{d}{dt}\Big[E\left(t\right) + \eta e^{i\varphi} E\left(t-1\right)\Big] = &-\left[1 + i\delta\right] E + \left[h - 1 - i\delta\right] \eta e^{i\varphi} E\left(t-1\right) \\ &+ h\sqrt{1-\eta^2} Y_0 \\ &+ \epsilon^2 i \left(\left|E\right|^2 E + \eta e^{i\varphi} \left|E\left(t-1\right)\right|^2 E\left(t-1\right)\right), \end{aligned} \tag{B.38}$$

where we used Eq. (B.37) to eliminate $Y$. Rewriting Eq. (B.38) yields

$$E = \frac{h - 1 - i\delta}{1 + i\delta} \eta e^{i\varphi} E\left(t-1\right) - \varepsilon \frac{d}{dt} \frac{E\left(t\right) + \eta e^{i\varphi} E\left(t-1\right)}{1 + i\delta} + K, \tag{B.39}$$

where we defined the terms with injection and nonlinearity as

$$K = h\frac{\sqrt{1-|\eta|^2}}{1+i\delta}Y_0 + \epsilon^2 i\frac{|E|^2 E + \eta e^{i\varphi}|E(t-1)|^2 E(t-1)}{1+i\delta}. \tag{B.40}$$

We consider the perfect GTI case where $h=2$ such that Eq. (B.39) simplifies:

$$E = \frac{1-i\delta}{1+i\delta}\eta e^{i\varphi}E(t-1) - \varepsilon\frac{d}{dt}\frac{E(t)+\eta e^{i\varphi}E(t-1)}{1+i\delta} + K. \tag{B.41}$$

Here, we can identify an effective phase per round-trip $\tilde{\varphi}$, which is defined as

$$e^{i\tilde{\varphi}} = \frac{1-i\delta}{1+i\delta}e^{i\varphi} = e^{i(\varphi-2\arctan(\delta))}. \tag{B.42}$$

Hence, we also write all terms containing $\varphi$ as

$$e^{i\varphi} = e^{i\tilde{\varphi}}e^{i2\arctan(\delta)} = \frac{1+i\delta}{1-i\delta}e^{i\tilde{\varphi}}. \tag{B.43}$$

## Expansions

The critical parameters around which we expand are $\eta_c = 1$ and $\tilde{\varphi}_c = 0$. We define the deviation from these parameters as

$$\eta = 1-\varepsilon^2\Delta\eta_2 - \varepsilon^3\Delta\eta_3, \tag{B.44}$$

$$\text{and } \tilde{\varphi} = \varepsilon^2\Delta\theta_2 + \varepsilon^3\Delta\theta_3. \tag{B.45}$$

Further, in order to obtain small amplitudes in $E$ the injection needs to be small such that its critical value is $Y_0^{(c)} = 0$ and it is expanded as

$$Y_0 = \varepsilon z_0^{(1)} + \varepsilon^2 z_0^{(2)} + \mathcal{O}\left(\epsilon^3\right). \tag{B.46}$$

With that, we can calculate certain combinations of expanded parameters which appear in the equations. In particular, we find

$$\sqrt{1-\eta^2} = \sqrt{1-\left(1-\varepsilon^2\Delta\eta_2-\varepsilon^3\Delta\eta_3\right)^2} = \epsilon\sqrt{2\Delta\eta_2} + \epsilon^2\frac{\Delta\eta_3}{\sqrt{2\Delta\eta_2}} + \mathcal{O}\left(\epsilon^3\right) \tag{B.47}$$

$$\eta e^{i\tilde{\varphi}} = \left(1-\varepsilon^2\Delta\eta_2-\varepsilon^3\Delta\eta_3\right)e^{i\left(\varepsilon^2\Delta\theta_2+\varepsilon^3\Delta\theta_3\right)} \tag{B.48}$$

$$= 1+\epsilon^2\left(i\Delta\theta_2-\Delta\eta_2\right)+\epsilon^3\left(i\Delta\theta_3-\Delta\eta_3\right)+\mathcal{O}\left(\epsilon^4\right). \tag{B.49}$$

Next, we define new time scales $t_0 = \omega t$, $t_1 = 0$, $t_2 = \epsilon^2 t$ and $t_3 = \epsilon^3 t$, where small changes in $\omega$ account for the drift: $\omega = 1+\epsilon\omega_1+\epsilon^2\omega_2+\epsilon^3\omega_3+\dots$. Therefore, the time derivative is $\frac{d}{dt} = \mathcal{T}_0+\epsilon\mathcal{T}_1+\epsilon^2\mathcal{T}_2+\epsilon^3\mathcal{T}_3+\dots$, where $\mathcal{T}_0 = \partial_0$, $\mathcal{T}_1 = \omega_1\partial_0$, $\mathcal{T}_2 = \omega_2\partial_0+\partial_2$

and $\mathcal{T}_3 = \omega_3\partial_0 + \partial_3$. Further, the delayed fields are now functions of the new time scales, i.e., $E(t-1) = E\left(t_0 - \omega, t_2 - \epsilon^2, t_3 - \epsilon^3\right)$. This expression needs to be expanded in powers of $\epsilon$:

$$E(t-1) = \left(\mathcal{S}_0 + \epsilon\mathcal{S}_1 + \epsilon^2\mathcal{S}_2 + \epsilon^3\mathcal{S}_3 + \dots\right) E\left(t_0 - 1, t_2, t_3\right), \tag{B.50}$$

where $\mathcal{S}_0 = 1$, $\mathcal{S}_1 = -\omega_1\partial_0$, $\mathcal{S}_2 = -\omega_2\partial_0 + \frac{\omega_1^2}{2}\partial_0^2 - \partial_2$ and $\mathcal{S}_3 = -\omega_3\partial_0 - \frac{\omega_1^3}{6}\partial_0^3 + \omega_1\omega_2\partial_0^2 + \omega_1\partial_0\partial_2 - \partial_3$.

Next, we can separate the nonlinearity into orders of $\epsilon$

$$\epsilon^2 i\frac{|E|^2 E + \eta e^{i\varphi}|E(t-1)|^2 E(t-1)}{1+i\delta} = \epsilon^2 i\frac{2}{1+\delta^2}|E|^2 E + \epsilon^3\frac{i}{1-i\delta}\mathcal{S}_1\left(|E|^2 E\right) \tag{B.51}$$

With this, we can separate $K$ into an injection part $I$ and a nonlinear part $N$

$$K = I + N = \epsilon^2\left(I_2 + N_2\right) + \epsilon^3\left(I_3 + N_3\right) \tag{B.52}$$

where $N_0 = N_1 = 0$ because of Eq. (B.51) and $I_0 = I_1 = 0$ because of Eqs. (B.46) and (B.47). Last, we expand the field $E$ in order of $\epsilon$, i.e., ,

$$E(t) = E_0 + \epsilon E_1 + \epsilon^2 E_2 + \epsilon^3 E_3 + \mathcal{O}\left(\epsilon^4\right). \tag{B.53}$$

Finally, we can plug all expansions into Eq. (B.41):

$$\begin{aligned} E_0+\epsilon E_1+\epsilon^2 E_2+\epsilon^3 E_3 =& \left[1+\epsilon^2(i\Delta\theta_2-\Delta\eta_2)+\epsilon^3(i\Delta\theta_3-\Delta\eta_3)\right]\left[1+\epsilon\mathcal{S}_1+\epsilon^2\mathcal{S}_2+\epsilon^3\mathcal{S}_3\right] \\ & \left[E_0(t_0-1)+\epsilon E_1(t_0-1)+\epsilon^2 E_2(t_0-1)+\epsilon^3 E_3(t_0-1)\right] \\ & -\epsilon\left[\mathcal{T}_0+\epsilon\mathcal{T}_1+\epsilon^2\mathcal{T}_2\right]\Bigg\{\frac{E_0+\epsilon E_1+\epsilon^2 E_2}{1+i\delta} \\ & +\left[1+\epsilon^2(i\Delta\theta_2-\Delta\eta_2)+\epsilon^3(i\Delta\theta_3-\Delta\eta_3)\right]\left[1+\epsilon\mathcal{S}_1+\epsilon^2\mathcal{S}_2\right] \\ & \frac{E_0(t_0-1)+\epsilon E_1(t_0-1)+\epsilon^2 E_2(t_0-1)}{1-i\delta}\Bigg\}+K+\mathcal{O}\left(\epsilon^4\right). \end{aligned} \tag{B.54}$$

### Solving the Orders

We separate Eq. (B.54) into orders of $\epsilon$ and solve each order separately.

### Zeroth Order

In the zeroth order of Eq. (B.54), we just find the condition for periodic solutions:

$$E_0 = E_0\left(t_0 - 1\right). \tag{B.55}$$

### First Order

In the first order we find

$$E_1 = E_1\left(t_0 - 1\right) - \left(\omega_1 + \frac{2}{1+\delta^2}\right)\partial_0 E_0. \tag{B.56}$$

In order to cancel the drift, we choose

$$\omega_1 = -\frac{2}{1+\delta^2}. \tag{B.57}$$

The remaining terms are the condition for periodic solutions for $E_1$.

### Second Order

In the second order of Eq. (B.54) we find

$$\begin{aligned} E_2 =& E_2\left(t_0 - 1\right) + \left(-\omega_1 - \frac{2}{1+\delta^2}\right)\partial_0 E_1 - \left(\omega_2 + \frac{2}{1+\delta^2}\omega_1\right)\partial_0 E_0 \\ &+ \left(\frac{\omega_1^2}{2} + \frac{\omega_1}{1-i\delta}\right)\partial_0^2 E_0 - \partial_2 E_0 + \left(i\Delta\theta_2 - \Delta\eta_2\right)E_0 + I_2 + N_2, \end{aligned} \tag{B.58}$$

where the term containing $\partial_0 E_1$ cancels due to the choice of $\omega_1$ from Eq. (B.57). We choose $\omega_2$ in a way that it cancels the drift of $E_0$

$$\omega_2 = -\frac{2}{1+\delta^2}\omega_1 = \omega_1^2. \tag{B.59}$$

The coefficient of $\partial_0^2$ is

$$\frac{\omega_1^2}{2} + \frac{\omega_1}{1-i\delta} = -i\delta\frac{\omega_1^2}{2}. \tag{B.60}$$

Further, we demand periodicity for $E_2$. Then we remain with

$$\partial_2 E_0 = -i\delta\frac{\omega_1^2}{2}\partial_0^2 E_0 + \left(i\Delta\theta_2 - \Delta\eta_2\right)E_0 + h\frac{\sqrt{2\Delta\eta_2}}{1+i\delta}z_0^{(1)} + \frac{2i}{1+\delta^2}\left|E_0\right|^2 E_0. \tag{B.61}$$

## Third Order

In the third order of Eq. (B.54), we find

$$\begin{aligned} E_3 =& E_3\left(t_0 - 1\right) + \left(-\omega_3 - \left(i\Delta\theta_2 - \Delta\eta_2\right)\omega_1 - \frac{i\Delta\theta_2 - \Delta\eta_2}{1-i\delta} - \frac{2}{1+\delta^2}\omega_2\right)\partial_0 E_0 \\ & - \left(\frac{\omega_1^3}{6} + \frac{1}{1-i\delta}\frac{\omega_1^2}{2}\right)\partial_0^3 E_0 + \left(\omega_1\omega_2 + \frac{1}{1-i\delta}\omega_2 + \frac{1}{1-i\delta}\omega_1^2\right)\partial_0^2 E_0 \\ & + \left(\omega_1 + \frac{1}{1-i\delta}\right)\partial_0\partial_2 E_0 - \frac{2}{1+\delta^2}\partial_2 E_0 - \partial_3 E_0 + \left(i\Delta\theta_3 - \Delta\eta_3\right)E_0 \\ & - \left(\omega_2 + \frac{2}{1+\delta^2}\omega_1\right)\partial_0 E_1 + \left(\frac{\omega_1^2}{2} + \frac{1}{1-i\delta}\omega_1\right)\partial_0^2 E_1 + \left(i\Delta\theta_2 - \Delta\eta_2\right)E_1 \\ & - \partial_2 E_1 - \left(\omega_1 + \frac{2}{1+\delta^2}\right)\partial_0 E_2 + I_3 + N_3, \end{aligned} \tag{B.62}$$

where the term containing $\partial_0 E_1$ and $\partial_0 E_2$ cancel due to the choice of $\omega_1$ and $\omega_2$ from Eqs. (B.57) and (B.59). Next, we use the solvability condition from the second order in Eq. (B.61) to replace the terms containing $\partial_2 E_0$. Then we get

$$\begin{aligned} \partial_3 E_0 + \partial_2 E_1 =& \left(-\omega_3 - \frac{2}{1+\delta^2}\omega_2\right)\partial_0 E_0 \\ & - \left(\frac{\omega_1^3}{6} + \frac{1}{1-i\delta}\frac{\omega_1^2}{2} + \left(\omega_1 + \frac{1}{1-i\delta}\right)i\delta\frac{\omega_1^2}{2}\right)\partial_0^3 E_0 \\ & + \left(\omega_1\omega_2 + \frac{1}{1-i\delta}\omega_2 + \frac{1}{1-i\delta}\omega_1^2\right)\partial_0^2 E_0 \\ & + \left(\omega_1 + \frac{1}{1-i\delta}\right)\partial_0 N_2 \\ & - \frac{2}{1+\delta^2}\left[-i\delta\frac{\omega_1^2}{2}\partial_0^2 E_0 + \left(i\Delta\theta_2 - \Delta\eta_2\right)E_0 + I_2 + N_2\right] \\ & + \left(i\Delta\theta_3 - \Delta\eta_3\right)E_0 - i\delta\frac{\omega_1^2}{2}\partial_0^2 E_1 + \left(i\Delta\theta_2 - \Delta\eta_2\right)E_1 + I_3 + N_3. \end{aligned} \tag{B.63}$$

We choose $\omega_3$ in a way that it cancels the drift of $E_0$

$$\omega_3 = -\frac{2}{1+\delta^2}\omega_2 = \omega_1^3. \tag{B.64}$$

Simplifying the coefficient of $\partial_0^2$ and $\partial_0^3$ gives

$$\partial_0^3: \quad -\left(\frac{\omega_1^3}{6}+\frac{1}{1-i\delta}\frac{\omega_1^2}{2}+\frac{1-i\delta}{1+\delta^2}i\delta\frac{\omega_1^2}{2}\right)=\frac{1-3\delta^2}{12}\omega_1^3; \tag{B.65}$$

$$\partial_0^2: \omega_1\omega_2+\frac{1}{1-i\delta}\omega_2+\frac{1}{1-i\delta}\omega_1^2-i\delta\frac{\omega_1^3}{2} \quad =-i\frac{3}{2}\delta\omega_1^3. \tag{B.66}$$

Further, we have a nonlinear drift $\partial_0\left(|E|^2 E\right)$, which has the coefficient

$$\left(\omega_1+\frac{1}{1-i\delta}\right)\partial_0 N_2+N_3=-\omega_1^2\delta\partial_0\left(|E|^2 E\right). \tag{B.67}$$

The remaining terms are the solvability condition for the third order

$$\begin{aligned}\partial_3 E_0+\partial_2 E_1=&\frac{1-3\delta^2}{12}\omega_1^3\partial_0^3 E_0-i\frac{3}{2}\delta\omega_1^3\partial_0^2 E_0-i\delta\frac{\omega_1^2}{2}\partial_0^2 E_1\\ &-\omega_1^2\delta\partial_0\left(|E|^2 E\right)+\left(i\Delta\theta_3-\Delta\eta_3\right)E_0\\ &+\omega_1\left(i\Delta\theta_2-\Delta\eta_2\right)E_0+\left(i\Delta\theta_2-\Delta\eta_2\right)E_1\\ &+\omega_1 I_2+I_3+\omega_1 N_2.\end{aligned} \tag{B.68}$$

### Building the Normal Form

We define an effective time scale $\partial_\xi=\epsilon^2\partial_2+\epsilon^3\partial_3$ and compute $\partial_\xi E$ up to third order

$$\frac{\partial E}{\partial\xi}=\left(\epsilon^2\partial_2+\epsilon^3\partial_3\right)\left(E_0+\epsilon E_1\right) \tag{B.69}$$

$$=\epsilon^2\partial_2 E_0+\epsilon^3\left(\partial_2 E_1+\partial_3 E_0\right)+\mathcal{O}\left(\epsilon^4\right). \tag{B.70}$$

Here, we can use the solvability conditions from second and third order (Eqs. (B.61) and (B.68)) to obtain

$$\begin{aligned}\frac{\partial E}{\partial\xi}=&-\epsilon^2 i\delta\frac{\omega_1^2}{2}\partial_0^2\left(E_0+\epsilon E_1\right)+\epsilon^3\frac{1-3\delta^2}{12}\omega_1^3\partial_0^3 E_0-\epsilon^3\omega_1^2\delta\partial_0\left(|E|^2 E\right)\\ &+\left[\epsilon^2\left(i\Delta\theta_2-\Delta\eta_2\right)+\epsilon^3\left(i\Delta\theta_3-\Delta\eta_3\right)\right]\left[E_0+\epsilon E_1\right]\\ &+\epsilon^2 I_2+\epsilon^3 I_3+\epsilon^2 N_2\\ &+\epsilon^3\left[-i\frac{3}{2}\delta\omega_1^3\partial_0^2 E_0+\omega_1\left(i\Delta\theta_2-\Delta\eta_2\right)E_0+\omega_1 I_2+\omega_1 N_2\right]+\mathcal{O}\left(\epsilon^4\right),\end{aligned} \tag{B.71}$$

where we can rebuild the field $E=E_0+\epsilon E_1$. Next, we define a space-like variable $z$ as $t_0=\epsilon z$ such that $\epsilon\partial_0=\partial_z$. Note that this scaling basically is the inverse of normalizing the time delay such that the new space-like variable $z$ is in the same order of magnitude as $\tau$. Further, we remember that at the beginning we introduced a scaling $\tilde{E}=\varepsilon^{-1}E$

(all $E$ in Eq. (B.71) are actually $\tilde{E}$, we dropped the tilde for better readability). We remain with

$$\begin{aligned}\frac{\partial E}{\partial \xi} =& - i\delta \frac{2}{\left(1+\delta^2\right)^2} \partial_z^2 E + \frac{2}{3} \frac{3\delta^2 - 1}{\left(1+\delta^2\right)^3} \partial_z^3 E - \frac{4\delta}{\left(1+\delta^2\right)^2} \partial_z \left( \left|E\right|^2 E \right) \\ &+ \left[\eta - 1 + i\tilde{\varphi}\right] E + \frac{2}{1+i\delta} \sqrt{1-\eta^2} Y_0 + i \frac{2}{1+\delta^2} \left|E\right|^2 E + \mathcal{O}\left(\epsilon\right),\end{aligned} \tag{B.72}$$

where $\tilde{\varphi} = \varphi - 2 \arctan \delta$. Notice that all terms in the last line of Eq. (B.71) do not cancel all $\epsilon$ and are therefore $\mathcal{O}\left(\epsilon\right)$ in Eq. (B.72).

In general, it is difficult to quantify the range of validity of Eq. (B.72), however, from the initial assumptions it is clear, that the deviation of $\eta$ and $\tilde{\varphi}$ from their critical values $\eta_c = 1$ and $\tilde{\varphi}_c = 0$ are both $\mathcal{O}\left(\epsilon^2\right)$, i.e., they need to be in the same order of magnitude.

## Period

For the frequency $\omega$, we found

$$\omega = 1 - \epsilon \frac{2}{1+\delta^2} + \epsilon^2 \frac{4}{\left(1+\delta^2\right)^2} - \epsilon^3 \frac{8}{\left(1+\delta^2\right)^3} = \frac{1}{1+\epsilon \frac{2}{1+\delta^2}} + \mathcal{O}\left(\epsilon^4\right). \tag{B.73}$$

Hence, the period in the reference frame, where the time delay is normalized, reads

$$T = \frac{1}{\omega} = 1 + \epsilon \frac{2}{1+\delta^2}. \tag{B.74}$$

Reversing the normalization of the time delay yields the period

$$T_\tau = \frac{T}{\epsilon} = \tau + \frac{2}{1+\delta^2} \tag{B.75}$$

where we used that $\tau = \epsilon^{-1}$. This validates the period found in, e.g., Fig. 4.2.

## Nonlinearity in the Third Order

We consider the case when the initial scaling is $\tilde{E} = \epsilon^{-3/2} E$. The nonlinear part in Eq. (B.51) has an additional factor of $\epsilon$ such that $N_2 = 0$ and $N_3 = i\frac{2}{1+\delta^2} \left|E\right|^2 E$ (what was $N_2$ in the case where $\tilde{E} = \epsilon^{-1} E$). Hence, the nonlinearity only appears in the third order, such that the nonlinear drift term does not appear in the third order. In particular, the solvability conditions for the second and third order read

$$\partial_2 E_0 = -i\delta\frac{\omega_1^2}{2}\partial_0^2 E_0 + (i\Delta\theta_2 - \Delta\eta_2)\,E_0 + h\frac{\sqrt{2\Delta\eta_2}}{1+i\delta}z_0^{(1)}, \tag{B.76}$$

$$\begin{aligned}\partial_3 E_0 + \partial_2 E_1 =&\frac{1-3\delta^2}{12}\omega_1^3\partial_0^3 E_0 - i\frac{3}{2}\delta\omega_1^3\partial_0^2 E_0 - i\delta\frac{\omega_1^2}{2}\partial_0^2 E_1\\ &+ (i\Delta\theta_3 - \Delta\eta_3)\,E_0\\ &+ \omega_1(i\Delta\theta_2 - \Delta\eta_2)\,E_0 + (i\Delta\theta_2 - \Delta\eta_2)\,E_1\\ &+ \omega_1 I_2 + I_3 + N_3.\end{aligned} \tag{B.77}$$

With that, we obtain the PDE normal form

$$\begin{aligned}\frac{\partial E}{\partial \xi} =& -i\delta\frac{2}{(1+\delta^2)^2}\partial_z^2 E + \frac{2}{3}\frac{3\delta^2-1}{(1+\delta^2)^3}\partial_z^3 E_0\\ &+ [\eta - 1 + i\tilde{\varphi}]\,E + \frac{2}{1+i\delta}\sqrt{1-\eta^2}Y_0 + i\frac{2}{1+\delta^2}|E|^2 E + \mathcal{O}(\epsilon),\end{aligned} \tag{B.78}$$

which is equivalent to Eq. (B.72) except for the nonlinear drift term. In the main text of the thesis, we use the version of the normal form without the nonlinear drift term because we found that it has a destabilizing effect. Whether these problems are intrinsic to the equation itself or stem from the employed numerical scheme, could not be determined ultimately. We concluded that the agreement between the full KGTI system and the LLE (without the nonlinear drift term) was already very good (cf. Section 4.5), such that we neglected the higher-order effects.

### Normal Form for the External Cavity Field $Y$

Note that equivalently, one can also derive a normal form for $Y$. For this, we derive a NDDE for $Y$ by eliminating $E$ from Eq. (B.38) instead of $Y$. For this we build $\epsilon\frac{d}{dt}\left(Y + \eta e^{i\varphi}Y(t-1)\right)$ and rewrite the expression analogously to Eq. (B.41)

$$\begin{aligned}Y =&\frac{1-i\delta}{1+i\delta}\eta e^{i\varphi}Y(t-1) - \epsilon\frac{d}{dt}\frac{Y + \eta e^{i\varphi}Y(t-1)}{1+i\delta} + \sqrt{1-\eta^2}Y_0\\ &+ i\epsilon^3\frac{1}{\eta^2}\frac{1}{1+i\delta}\left|\eta e^{i\varphi}Y(t-1) + Y - \sqrt{1-\eta^2}Y_0\right|^2\\ &\times\left(\eta e^{i\varphi}Y(t-1) + Y - \sqrt{1-\eta^2}Y_0\right).\end{aligned} \tag{B.79}$$

Up to zeroth order the nonlinear part reads

$$N = \frac{8i}{(1+\delta^2)^2}|Y|^2 Y + \mathcal{O}(\epsilon). \tag{B.80}$$

With this Eq. (B.79) reads

$$\begin{aligned}Y =&\frac{1-i\delta}{1+i\delta}\eta e^{i\varphi}Y\left(t-1\right)-\epsilon\frac{d}{dt}\frac{Y+\eta e^{i\varphi}Y\left(t-1\right)}{1+i\delta}+\sqrt{1-\eta^2}Y_0\\ &+\epsilon^3\frac{8i}{\left(1+\delta^2\right)^2}\left|Y\right|^2Y+\mathcal{O}\left(\epsilon\right).\end{aligned} \tag{B.81}$$

Comparing Eqs. (B.41) and (B.81) reveals that they are identical up to a scaling of the field of $\frac{1+i\delta}{2}$. Hence, the normal form for $Y$ is identical to the one of $E$ (up to the mentioned scaling). In fact, this scaling can be derived from Eq. (B.36) as well. Solving for $Y$ yields $Y=\frac{1+i\delta}{2}E+\mathcal{O}\left(\epsilon\right)$, where we set $h=2$.

Equivalently one can derive a normal form for the output $O$ which is in the good cavity limit

$$O=E-Y=\frac{1-i\delta}{2}E. \tag{B.82}$$

Consequently, we find $\left|O\right|^2=\left|Y\right|^2=\frac{1+\delta^2}{4}\left|E\right|^2$.

### B.2.2. Normal Form via a Functional Mapping Approach

The linear operator of the normal form can also be computed using the functional mapping approach. We start at the NDDE representation from Eq. (B.38). Following Section 2.3.2, we find the coefficients $\mathcal{A}=-\left(1+i\delta\right)$ and $\mathcal{B}=\eta e^{i\varphi}\left(1-i\delta+i\omega\epsilon\right)$ where we replaced the temporal derivatives by their Fourier-transformed equivalent. According to Eq. (2.37), the linear operator reads

$$\mathcal{L}=\ln\left[\eta e^{i\varphi}\frac{1-i\delta+i\omega\epsilon}{1+i\delta-i\omega\epsilon}\right] \tag{B.83}$$

$$=\ln\left(\eta e^{i\left(\varphi-2\arctan\delta\right)}\right)+\ln\left[\frac{1-\frac{-i\omega\epsilon}{1-i\delta}}{1+\frac{-i\omega\epsilon}{1+i\delta}}\right] \tag{B.84}$$

$$=\left(\eta-1+i\tilde{\varphi}\right)-\frac{2}{1+\delta^2}\left(-i\omega\epsilon\right)-\frac{2i\delta}{\left(1+\delta^2\right)^2}\left(-i\omega\epsilon\right)^2+\frac{2}{3}\frac{3\delta^2-1}{\left(1+\delta^2\right)^3}\left(-i\omega\epsilon\right)^3+\mathcal{O}\left(\epsilon^4\right), \tag{B.85}$$

which is the linear operator we found via the multiple time scale approach (cf. Eq. (B.72)). Next, we consider again Eq. (B.38) and find the nonlinearity in the map[22]

$$N=i\frac{\left|E_n\right|^2E_n+\eta e^{i\varphi}\left|E_{n-1}\right|^2E_{n-1}}{1+i\delta+i\epsilon\omega}. \tag{B.86}$$

[22]The injection $\frac{2\sqrt{1-\eta^2}}{1+i\delta-i\epsilon\omega}Y_0$ is another nonlinearity. But the $-i\epsilon\omega$ can be dropped because $Y_0$ is a constant. Hence, it results in an additive term of $\frac{2\sqrt{1-\eta^2}}{1+i\delta}Y_0$.

Here, we note that the nonlinearity in Eq. (B.38) is $\mathcal{O}\left(\epsilon^2\right)$ such that we need to compute the nonlinearity also up to $\mathcal{O}\left(\epsilon^2\right)$ such that the error is in $\mathcal{O}\left(\epsilon^4\right)$ as for the linear operator in Eq. (B.85). In Eq. (B.85), we choose $(\eta - 1 + i\tilde{\varphi})$ to be $\mathcal{O}\left(\epsilon^2\right)$ (as we did in the multiple time scale approach) such that $\mathcal{L}_1 \sim \partial_z$ and we can use Eq. (2.48) to compute the shift of the nonlinearity

$$\Rightarrow N_{n-1} = i\frac{1 + \epsilon\mathcal{L}_1 + \frac{1+i\delta}{1-i\delta}}{1 + i\delta - i\epsilon\omega} \left|E_{n-1}\right|^2 E_{n-1} + \mathcal{O}\left(\epsilon^2\right) \tag{B.87}$$

$$= i\left[\frac{1}{1+i\delta} - \frac{-i\epsilon\omega}{(1+i\delta)^2}\right]\left[\frac{2}{1-i\delta} + iv\epsilon\omega\right] \left|E_{n-1}\right|^2 E_{n-1} + \mathcal{O}\left(\epsilon^2\right) \tag{B.88}$$

$$= iv\left[1 + \frac{2}{1+i\delta}\epsilon i\omega\right] \left|E_{n-1}\right|^2 E_{n-1} + \mathcal{O}\left(\epsilon^2\right), \tag{B.89}$$

where we used the shortcut $v = \frac{2}{1+\delta^2}$. The nonlinearity in the final PDE is then according to Eq. (2.49)

$$\mathcal{N}_{n-1} = e^{-\mathcal{L}} N_{n-1} + \mathcal{O}\left(\epsilon^2\right) \tag{B.90}$$

$$= iv\left[1 - \epsilon\mathcal{L}_1\right]\left[1 + \frac{2}{1+i\delta}\epsilon i\omega\right] \left|E_{n-1}\right|^2 E_{n-1} + \mathcal{O}\left(\epsilon^2\right) \tag{B.91}$$

$$= v\left(i + v\delta\epsilon i\omega\right) \left|E_{n-1}\right|^2 E_{n-1} + \mathcal{O}\left(\epsilon^2\right), \tag{B.92}$$

which corresponds to the nonlinearity found via the multiple time scale approach (cf. Eq. (B.72)).

### B.2.3. The "Intuitive" Normal Form

After going through the lengthy derivation of the normal form for the LLE via the multiple time scale and functional mapping approach, we want to present a short derivation based on the intuition we gained along the way. The central idea here is to simply include the nonlinearity in the phase shift. We rewrite the NDDE in Eq. (B.41) as map assuming $|E(t-1)|^2 = |E|^2 + \mathcal{O}(\epsilon)$ and using the effective detuning $\theta = \delta - |E|^2$, such that we obtain

$$E = \eta e^{i(\varphi - 2\arctan\theta)} E(t-1) + 2\frac{\sqrt{1-\eta^2}}{1+i\theta} Y_0 + \mathcal{O}(\epsilon). \tag{B.93}$$

As we are operating the reference frame of the injection, our wave packet is centered around the frequency $\omega_0$. That is, considering a plane wave close to $\omega_0$, it gains a (frequency and state dependent) phase shift of

$$\beta(E,\omega) = \varphi - 2\arctan\left(\omega_c - \omega - |E|^2\right) \tag{B.94}$$

in each round-trip, where we explicitly write out the detuning $\delta = \omega_c - \omega_0$. The operator in the normal form is then the logarithm of the coefficient of $E(t-1)$ in the map:

$$\begin{aligned}\partial_\xi \hat{E}(\xi,\omega) &= \ln\left(\eta e^{i\beta(\hat{E},\omega)}\right)\hat{E}(\xi,\omega) + 2\frac{\sqrt{1-\eta^2}}{1+i\theta}Y_0 \qquad &(B.95)\\ &= i\beta\left(\hat{E},\omega\right)\hat{E}(\xi,\omega) - (1-\eta)\hat{E} + 2\frac{\sqrt{1-\eta^2}}{1+i\theta}Y_0. &(B.96)\end{aligned}$$

Now, we expand the phase shift $\beta\left(\hat{E},\omega\right)$ around the carrier frequency $\omega_0$

$$\beta(\omega) = \beta(\omega_0) + \left.\frac{\partial\beta}{\partial\omega}\right|_{\omega_0}\Delta\omega + \frac{1}{2}\left.\frac{\partial^2\beta}{\partial\omega^2}\right|_{\omega_0}(\Delta\omega)^2 + \frac{1}{6}\left.\frac{\partial^3\beta}{\partial\omega^3}\right|_{\omega_0}(\Delta\omega)^3 + \ldots, \tag{B.97}$$

where we defined $\Delta\omega = \omega - \omega_0$. Finally, we perform an inverse Fourier transform $\hat{E}(\xi,\omega) \to E(\xi,z)$ which defines the fast time scale as $-i\Delta\omega \to \partial_z$. Hence, we obtain

$$\begin{aligned}\partial_\xi E(\xi,z) = &\left[i\beta(\omega_0) - \partial_z\left.\frac{\partial\beta}{\partial\omega}\right|_{\omega_0} - i\partial_z^2\frac{1}{2}\left.\frac{\partial^2\beta}{\partial\omega^2}\right|_{\omega_0} + \frac{1}{6}\partial_z^3\left.\frac{\partial^3\beta}{\partial\omega^3}\right|_{\omega_0} + \ldots\right]E\\ &- (1-\eta)E + 2\frac{\sqrt{1-\eta^2}}{1+i\theta}Y_0.\end{aligned} \tag{B.98}$$

Here, we can identify the dispersive properties of the setup as the phase constant, group velocity, group velocity dispersion (second order dispersion) and third-order dispersion which are defined as derivatives of $\beta(E,\omega)$ with respect to the frequency $\omega$ evaluated at the carrier frequency $\omega_0$. Further, we expand the nonlinearities for small $|E|^2$ which gives all correct nonlinear contributions:

- Phase constant & nonlinearity:

$$\beta\left(\omega_0\right)=\varphi-2\arctan\left(\delta-|E|^2\right) \tag{B.99}$$

$$=\varphi-2\arctan\left(\delta\right)+\frac{2}{1+\delta^2}|E|^2+\mathcal{O}\left(|E|^4\right); \tag{B.100}$$

- Group velocity & self-steepening:

$$\left.\frac{\partial\beta}{\partial\omega}\right|_{\omega_0}=\frac{2}{1+\left(\delta-|E|^2\right)^2} \tag{B.101}$$

$$=\frac{2}{1+\delta^2}+\frac{4\delta}{\left(1+\delta^2\right)^2}|E|^2+\mathcal{O}\left(|E|^4\right); \tag{B.102}$$

- Group velocity dispersion (GVD):

$$\beta_2=\left.\frac{\partial^2\beta}{\partial\omega^2}\right|_{\omega_0}=\frac{4\left(\delta-|E|^2\right)}{\left(1+\left(\delta-|E|^2\right)^2\right)^2} \tag{B.103}$$

$$=\frac{4\delta}{\left(1+\delta^2\right)^2}+\mathcal{O}\left(|E|^2\right); \tag{B.104}$$

- Third-order dispersion (TOD):

$$\beta_3=\left.\frac{\partial^3\beta}{\partial\omega^3}\right|_{\omega_0}=\frac{4\left(3\left(\delta-|E|^2\right)^2-1\right)}{\left(1+\left(\delta-|E|^2\right)^2\right)^3} \tag{B.105}$$

$$=\frac{4\left(3\delta^2-1\right)}{\left(1+\delta^2\right)^3}+\mathcal{O}\left(|E|^2\right). \tag{B.106}$$

For GVD and TOD, we did not calculate the corresponding nonlinear terms here, because we cannot check them as we did not calculate these terms with any other method. But all terms included in the above listing are equivalent to those obtained by the mapping or multiple time scale method. Even though this derivation is not completely rigorous, the idea to simply include the nonlinearity into the phase (i.e. to define the effective detuning $\theta$) seems to be enough to capture the nonlinear terms in the normal form PDE.

# C. Derivation of the Equations of Motion

In this Appendix, we present the complete derivation of the equations of motion (EOM) for the dynamics of phases and positions in a passively mode-locked laser that is used in Chapter 5. The derivation follows the lines of the Appendix in [126].

## Definitions

We define the scalar product in the vector space of real functions of periodicity $T$ as

$$\langle w|v\rangle = \int_0^T w\left(z\right) v\left(z\right) dz. \tag{C.1}$$

In what follows, we will deal with complex functions which we define as vectors with the real and imaginary parts as components. Then the scalar product reads

$$\langle w|v\rangle = \int_0^T \left[w_x\left(z\right) v_x\left(z\right) + w_y\left(z\right) v_y\left(z\right)\right] dz, \tag{C.2}$$

where the indices $x, y$ denote the real and imaginary parts, respectively. Now considering a linear operator $\mathcal{L}$, one can define the adjoint operator $\mathcal{L}^\dagger$ as

$$\langle w|\mathcal{L}v\rangle = \left\langle \mathcal{L}^\dagger w|v\right\rangle. \tag{C.3}$$

As an example, we consider the operator $\mathcal{L} = i$ (multiplication with imaginary unit) it corresponds to a matrix and we have

$$i\begin{pmatrix} v_x \\ v_y \end{pmatrix} = \begin{pmatrix} -v_y \\ v_x \end{pmatrix} = \begin{pmatrix} 0 & -1 \\ 1 & 0 \end{pmatrix}\begin{pmatrix} v_x \\ v_y \end{pmatrix}, \tag{C.4}$$

$$i^\dagger\begin{pmatrix} v_x \\ v_y \end{pmatrix} = \begin{pmatrix} v_y \\ -v_x \end{pmatrix} = \begin{pmatrix} 0 & 1 \\ -1 & 0 \end{pmatrix}\begin{pmatrix} v_x \\ v_y \end{pmatrix}, \tag{C.5}$$

such that the scalar product is preserved

$$\langle w|\mathcal{L}v\rangle = w_x\left(-v_y\right) + w_y\left(v_x\right), \tag{C.6}$$

$$\left\langle \mathcal{L}^\dagger w|v\right\rangle = \left(w_y\right) v_x + \left(-w_x\right) v_y. \tag{C.7}$$

## Preliminaries

We consider a nonlinear complex valued partial differential equation (PDE) with periodic boundaries of the form[23]

$$M\partial_\xi \psi = \mathcal{L}\psi + \mathcal{N}(\psi) + \eta e^{i\Omega} M\psi(z - \tau_f) \,. \tag{C.8}$$

Here, $\mathcal{L}$ is a linear operator, $\mathcal{N}(\psi)$ is a nonlinear function and $\eta e^{i\Omega} M\psi(x - \tau_f, s)$ a non-local term describing time-delayed feedback with the feedback delay time $\tau_f$, feedback strength $\eta$, feedback phase $\Omega$. Further, $M$ is the mass matrix and $M = \mathrm{diag}(1, 1, 0, 0)$ for the HME (3.155)–(3.157). Furthermore, $\psi = \psi(z, \xi)$ is a four-component real-valued vector function, and $z$ and $\xi$ denote the fast and slow time scales which describe the evolution within one round-trip and from one round-trip to the next one, respectively. The first two components of $\psi$ correspond to the real and imaginary parts of the electric field $E$ and the third and fourth components are the gain $g$ and absorber $q$,

$$\psi = \begin{pmatrix} \psi_x \\ \psi_y \\ \psi_g \\ \psi_q \end{pmatrix} = \begin{pmatrix} \mathrm{Re}(E) \\ \mathrm{Im}(E) \\ g - g_0 \\ q - q_0 \end{pmatrix}. \tag{C.9}$$

Here, $g_0$ is the pumping rate and $q_0$ is the value of the unsaturated losses that determines the modulation depth of the saturable absorber. For convenience and to account for the explicit form of the mass matrix $M$, we also define the the field and carrier components as two-component vector functions

$$\psi_f = (\psi_x, \psi_y, 0, 0)^T, \quad \psi_c = (0, 0, \psi_g, \psi_q)^T \tag{C.10}$$

such that $\psi = \psi_f + \psi_c$.

Next, we assume that the PDE (C.8) has a stationary single-pulse solution $\psi_s(z)$ and two neutral modes corresponding to the phase invariance (only for the field components) and translation invariance. Hence, every shifted and rotated version of $\psi_s$ is a solution of Eq. (C.8) as well. Hence, we define the one pulse solution $\psi_j = \psi_j(\xi, z)$ as

$$\psi_j = e^{i\varphi_j(\xi)}\psi_{s,f}(z - z_j(\xi)) + \psi_{s,c}(z - z_j(\xi)) \tag{C.11}$$

$$= R(\varphi_j(\xi))\,\psi_s(z - z_j(\xi)) \,, \tag{C.12}$$

where $\varphi_j(\xi)$ and $z_j(\xi)$ are the phase and position of the pulse which depend on the slow time, and $\psi_{s,f}$ and $\psi_{s,c}$ are the field and carrier components of the stationary

[23] We explicitly use the Haus master equation Eqs. (3.155)–(3.157).

solution. Further, $R(\varphi)$ is a rotation matrix

$$R(\varphi) = \begin{pmatrix} \cos\varphi & -\sin\varphi & 0 & 0 \\ \sin\varphi & \cos\varphi & 0 & 0 \\ 0 & 0 & 1 & 0 \\ 0 & 0 & 0 & 1 \end{pmatrix} \tag{C.13}$$

for the field components. Next, we employ a superposition ansatz to describe solutions $\Psi$ that consist of $N$ pulses

$$\Psi = \sum_{j=1}^{N} \psi_j + \delta\psi, \tag{C.14}$$

where $\delta\psi$ accounts for a small deviation from the simple summation. The aim of the following derivation is to determine how multiple pulses $\psi_j$ interact in the cavity. This can be expressed as dynamical *equations of motion* for $\varphi_j(\xi)$ and $z_j(\xi)$, respectively.

## Linearization

Inserting the superposition ansatz (C.14) into Eq. (C.8) yields (here the dot operators on the RHS denote the derivatives with respect to slow time: $\partial_\xi$)

$$M\partial_\xi\Psi = \sum_{j=1}^{N} \left[-\left(M\partial_z\psi_j\right)\dot{z}_j + \left(M\partial_\varphi\psi_j\right)\dot{\varphi}_j\right] + M\dot{\delta\psi} \tag{C.15}$$

$$= \sum_{j=1}^{N} \mathcal{L}\psi_j + \mathcal{L}\delta\psi + \mathcal{N}\left(\sum_{j}^{N}\psi_j + \delta\psi\right) + \eta M R(\Omega)\sum_{j=1}^{N}\psi_j(x-\tau_f) \tag{C.16}$$

$$\begin{aligned} &= \sum_{j=1}^{N} \mathcal{L}\psi_j + \mathcal{N}\left(\sum_{j=1}^{N}\psi_j\right) + \eta M R(\Omega)\sum_{j=1}^{N}\psi_j(z-\tau_f) + \\ &\qquad \left(\mathcal{L} + \left(\frac{\partial\mathcal{N}}{\partial\psi}\right)\bigg|_{\psi=\sum_j\psi_j}\right)\delta\psi, \end{aligned} \tag{C.17}$$

where in the last step, we expanded the nonlinearity around $\delta\psi = 0$. Further, we can identify the Jacobian defined as

$$\mathcal{J} = \mathcal{L} + \left(\frac{\partial\mathcal{N}}{\partial\psi}\right)\bigg|_{\psi=\sum_j\psi_j}. \tag{C.18}$$

Around a single pulse, one of the $\psi_j$ is dominant and governs the dynamics. Hence, the Jacobian around a pulse $\psi_m$ is approximately

$$\mathcal{J} \approx \mathcal{J}_m = \mathcal{L} + \left(\frac{\partial\mathcal{N}}{\partial\psi}\right)\bigg|_{\psi_m}. \tag{C.19}$$

Further, we can expand the nonlinearity in Eq. (C.17) around the same pulse

$$\mathcal{N}\left(\sum_{j=1}^{N}\psi_j\right)=\mathcal{N}\left(\psi_m\right)+\left.\frac{\partial\mathcal{N}}{\partial\psi}\right|_{\psi_m}\sum_{j\neq m}\psi_j, \tag{C.20}$$

such that one obtains

$$\sum_{j=1}^{N}\mathcal{L}\psi_j+\mathcal{N}\left(\sum_{j=1}^{N}\psi_j\right)=\left(\mathcal{L}+\left.\frac{\partial\mathcal{N}}{\partial\psi}\right|_{\psi_m}\right)\sum_{j\neq m}\psi_j=\mathcal{J}_m\sum_{j\neq m}\psi_j\,,$$

where we used $\mathcal{L}\psi_m+\mathcal{N}\left(\psi_m\right)=0$ as $\psi_m$ solves Eq. (C.8) in the absence of the feedback term. With these shortcuts, we can rewrite Eq. (C.17) as

$$\begin{aligned}\left(M\partial_\xi-\mathcal{J}_m\right)\delta\psi=&\sum_{j=1}^{N}M\partial_z\psi_j\dot{z}_j-M\partial_\varphi\psi_j\dot{\varphi}_j+\mathcal{J}_m\sum_{j\neq m}\psi_j+\\&\eta MR\left(\Omega\right)\sum_{j=1}^{N}\psi_j\left(z-\tau_f\right),\end{aligned} \tag{C.21}$$

which is valid around pulse $\psi_m$. The Jacobian $\mathcal{J}_m$ possess eigenvalues $\lambda_i^{(m)}$ corresponding to eigenfunctions $v_i^{(m)}$, which are defined by the generalized eigenvalue problem

$$\mathcal{J}_m v_i^{(m)}=\lambda_i^{(m)}Mv_i^{(m)}. \tag{C.22}$$

We know that two (neutral) eigenvalues are zero due to the rotational and translation symmetry in Eq. (C.17). The corresponding neutral eigenfunctions $v_t^{(m)}$ and $v_p^{(m)}$ read

$$v_t^{(m)}=\partial_z\psi_m, \tag{C.23}$$

$$v_p^{(m)}=\partial_\varphi\psi_m=iM\psi_m\,, \tag{C.24}$$

where the indices $t,p$ stand for *translation* and *phase*, respectively. Note that we can also define Eqs. (C.23), (C.24) in terms of the eigenfunctions of the stationary solutions $\psi_s$ which we simply define as $v_t$ and $v_p$ as $v_t^{(m)}=R\left(\varphi_m\right)v_t\left(z-z_m\right)$ and $v_p^{(m)}=R\left(\varphi_m\right)v_p\left(z-z_m\right)$. In the next step, we can now decompose $\delta\psi$ in Eq. (C.21) in the basis of eigenfunctions $v_i^{(m)}$

$$\delta\psi=\sum_j\beta_j^{(m)}\left(\xi\right)v_j^{(m)}\,, \tag{C.25}$$

where the $\beta_j^{(m)}\left(\xi\right)$ are the time-dependent coefficients.

Next, we consider the corresponding adjoint eigenvalue problem defined by the adjoint operator $\mathcal{J}_m^\dagger$ which has eigenfunctions $w_i^{(m)}$ and eigenvalues that are the complex conjugated of the eigenvalues of $\mathcal{J}_m$, i.e.,

$$\mathcal{J}_m^\dagger w_i^{(m)} = \bar{\lambda}_i^{(m)} M w_i^{(m)}, \tag{C.26}$$

where we used that $M^\dagger = M$ for the HME. At this point it is instructive to clarify important properties of the eigenfunctions. First, $\left(v_i^{(m)}, w_i^{(m)}\right)$ form a biorthogonal set, i.e.,

$$\left\langle w_i^{(m)} | M v_j^{(m)} \right\rangle = 0, \;\forall i \neq j. \tag{C.27}$$

This property can be easily shown when computing $\left\langle w_i^{(m)} | \mathcal{J}_m v_j^{(m)} \right\rangle$ in two ways:

$$\left\langle w_i^{(m)} | \mathcal{J}_m v_j^{(m)} \right\rangle = \lambda_j^{(m)} \left\langle w_i^{(m)} | M v_j^{(m)} \right\rangle, \tag{C.28}$$

$$\begin{aligned} \left\langle w_i^{(m)} | \mathcal{J}_m v_j^{(m)} \right\rangle &= \left\langle \mathcal{J}_m^\dagger w_i^{(m)} | v_j^{(m)} \right\rangle \\ &= \bar{\lambda}_i^{(m)} \left\langle M^\dagger w_i^{(m)} | v_j^{(m)} \right\rangle \\ &= \bar{\lambda}_i^{(m)} \left\langle w_i^{(m)} | M v_j^{(m)} \right\rangle. \end{aligned} \tag{C.29}$$

As this must hold for all $i, j$, in general $\lambda_j^{(m)} \neq \bar{\lambda}_i^{(m)}$, $\forall i \neq j$ and hence $\left\langle w_i^{(m)} | M v_j^{(m)} \right\rangle = 0$. Further, as the solutions $\psi_m$ are localized around $z_m$, so are the $v_i^{(m)}$ and $w_i^{(m)}$. As we assume well separated pulses, we obtain

$$\left\langle w_i^{(k)} | M v_j^{(m)} \right\rangle \approx 0, \;\forall k \neq m, \;\forall i, j. \tag{C.30}$$

## Projection on Adjoint Eigenmodes

We insert the expansion of $\delta\psi$ in the eigenfunctions defined in Eqs. (C.25) into (C.21) and identify the eigenfunctions defined in Eqs. (C.23), (C.24) to obtain

$$\begin{aligned} \sum_i \left(\partial_\xi - \lambda_i^{(m)}\right) \beta_i^{(m)} M v_i^{(m)} = &\sum_{j=1}^{N} \left[ M v_t^{(m)} \dot{z}_j - M v_p^{(m)} \dot{\varphi}_j \right] + \\ &\mathcal{J}_m \sum_{j \neq m} \psi_j + \eta M R\left(\Omega\right) \sum_{j=1}^{N} \psi_j \left(z - \tau_f\right). \end{aligned} \tag{C.31}$$

Projecting this equation onto an adjoint eigenmode $w_k^{(m)}$ corresponding to the same pulse and using the properties in Eqs. (C.27) and (C.30) yields

$$\sum_i \left(\partial_\xi - \lambda_i^{(m)}\right) \beta_i^{(m)} \left\langle w_k^{(m)} | M v_i^{(m)} \right\rangle = \left(\partial_\xi - \lambda_k^{(m)}\right) \beta_k^{(m)} \left\langle w_k^{(m)} | M v_k^{(m)} \right\rangle. \tag{C.32}$$

Inserting this into Eq. (C.31) gives

$$\partial_\xi \beta_k^{(m)} = \lambda_k^{(m)} \beta_k^{(m)} + C_k^{(m)} \,, \qquad \text{where} \quad C_k^{(m)} = \frac{\left\langle w_k^{(m)} | \text{RHS (C.31)} \right\rangle}{\left\langle w_k^{(m)} | M v_k^{(m)} \right\rangle}. \tag{C.33}$$

When projecting on the all eigenmodes except for $w_t^{(m)}$ and $w_p^{(m)}$, the $\beta_k^{(m)}$ will not diverge as the corresponding eigenvalues $\lambda_k^{(m)}$ are negative since $\psi_m$ is a stable stationary solution. For $w_{t,p}^{(m)}$, we assume the $\beta_{t,p}^{(m)}$ to evolve slowly such that $\partial_\xi \beta_{t,p}^{(m)} \approx 0$. Therefore we obtain

$$\overset{C_{t,p}^{(m)}=0}{\Rightarrow} \quad 0 = \left\langle w_{t,p}^{(m)} | \text{RHS (C.31)} \right\rangle \,. \tag{C.34}$$

Finally, we explicitly project onto $w_t^{(m)}$ and $w_p^{(m)}$ and use again the properties of the eigenfunctions defined in Eqs. (C.23), (C.24), such that we obtain the EOM for the phases and positions

$$N_t^{(m)} \dot{z}_m = \sum_{j \neq m} \left\langle w_t^{(m)} | \mathcal{J}_m \psi_j \right\rangle + \eta \sum_{j=1}^{N} \left\langle w_t^{(m)} | M R\left(\Omega\right) \psi_j \left(z - \tau_f\right) \right\rangle, \tag{C.35}$$

$$N_p^{(m)} \dot{\varphi}_m = \sum_{j \neq m} \left\langle w_p^{(m)} | \mathcal{J}_m \psi_j \right\rangle + \eta \sum_{j=1}^{N} \left\langle w_p^{(m)} | M R\left(\Omega\right) \psi_j \left(z - \tau_f\right) \right\rangle \,, \tag{C.36}$$

where the normalization constants read

$$N_t^{(m)} = - \left\langle w_t^{(m)} | M v_t^{(m)} \right\rangle, \tag{C.37}$$

$$N_p^{(m)} = \left\langle w_p^{(m)} | M v_p^{(m)} \right\rangle. \tag{C.38}$$

### Alternative Approach using the Fredholm Alternative

In fact, we can also use the Fredhom alternative to get to this result faster. It states that for an inhomogeneous linear equation $Ax = b$, one can project onto the kernel eigenmode $w$ of the corresponding adjoint homogeneous equation $A^\dagger w = 0$ to obtain

$$\langle w | b \rangle = \langle w | Ax \rangle = \left\langle A^\dagger w | x \right\rangle = 0. \tag{C.39}$$

Hence, we consider again Eq. (C.21) and use as before that the perturbation $\delta\psi$ evolves slowly (i.e., $\partial_\xi \delta\psi \ll 1$):

$$-\mathcal{J}_m \delta\psi = \text{RHS (C.31)}. \tag{C.40}$$

As $w_{t,p}^{(m)}$ are the kernel eigenmodes of $\mathcal{J}_m^\dagger$, we directly obtain

$$0 = \left\langle w_{t,p}^{(m)} | \text{RHS (C.31)} \right\rangle . \tag{C.41}$$

## C.1. The Explicit Form of the EOM

In the next step, we want to evaluate the scalar products in Eqs. (C.35),(C.36) to find the explicit form of the EOM.

### Non-local Feedback Term

First, we need to evaluate the scalar product containing the non-local term $\psi_j(z-\tau_f)$ in Eqs. (C.35), (C.36). We write the nonlocal term in terms of the stationary solution $\psi_s$ as

$$MR(\Omega)\psi_j(z-\tau_f) = MR(\Omega+\varphi_j)\psi_s(z-z_j-\tau_f) \tag{C.42}$$

and use that we are dealing with period functions such that we can shift the argument in functions of the scalar product by $z_m$:

$$\begin{aligned}\left\langle w_{t,p}^{(m)} | MR(\Omega)\psi_j(z-\tau_f)\right\rangle &= \langle R(\gamma) w_{t,p} | MR(\Omega+\varphi_j)\psi_s(z-z_j+z_m-\tau_f)\rangle \quad &\text{(C.43)}\\ &= \langle R(\gamma) w_{t,p} | MR(\Omega+\varphi_j)\psi_s(z-\Delta_{jm}-\tau_f)\rangle \, , \quad &\text{(C.44)}\end{aligned}$$

where we define $\Delta_{jm} = z_j - z_m$ and $\gamma$ is some rotation of the $m$-th adjoint eigenfunction $w_{t,p}^{(m)}$ with respect to the stationary state eigenfunction $w_{t,p}$. Next, we also consider the normalization factors $N_{t,p}^{(m)}$ on the LHS of Eqs. (C.35), (C.36), which depend on the eigenfunctions $v_{t,p}^{(m)}$ of the $m$-th pulse but can be shifted to depend only on the stationary modes $v_{t,p}$:

$$\left\langle w_{t,p}^{(m)} | M v_{t,p}^{(m)} \right\rangle = \langle R(\gamma) w_{t,p} | MR(\varphi_m) v_{t,p}\rangle \, . \tag{C.45}$$

For solving Eqs. (C.35), (C.36) for $z_m$ and $\varphi_m$, one needs to divide the expression in Eq. (C.44) with Eq. (C.45). We can multiply the ket-vectors with $R(-\varphi_m)$ and bra-vectors with $R(-\gamma)$ to remove the phase dependence from the denominator:

$$\frac{\langle R(\gamma) w_{t,p} | MR(\Omega+\varphi_j)\psi_s(z-\Delta_{jm}-\tau_f)\rangle}{\langle R(\gamma) w_{t,p} | MR(\varphi_m) v_{t,p}\rangle} = \frac{\langle w_{t,p} | MR(\Omega+\theta_{jm})\psi_s(z-\Delta_{jm}-\tau_f)\rangle}{\langle w_{t,p} | M v_{t,p}\rangle} \, , \tag{C.46}$$

where we define the phase difference $\theta_{jm} = \varphi_j - \varphi_m$. Next, we consider the action of the rotation operator $R(\alpha)$ which acts as

$$MR(\alpha)\,\psi_s(z) = [\cos(\alpha) + i\sin(\alpha)]\,\psi_{s,f}(z)\ , \tag{C.47}$$

where the imaginary unit $i$ can be understood as the operator defined in Eq. (C.4). Plugging this into the RHS of Eq. (C.46) gives

$$\begin{aligned}\langle w_{t,p}|MR(\Omega+\theta_{jm})\,\psi_s(z-\Delta_{jm}-\tau_f)\rangle = &\cos(\Omega+\theta_{jm})\,\langle w_{t,p}|\psi_{s,f}(z-\Delta_{jm}-\tau_f)\rangle + \\ &\sin(\Omega+\theta_{jm})\,\langle w_{t,p}|i\psi_{s,f}(z-\Delta_{jm}-\tau_f)\rangle\,.\end{aligned} \tag{C.48}$$

We write out the scalar products explicitly (here the index $i$ denotes $p$ or $t$, respectively) and assign names to them:

$$\begin{aligned}l_{1,i}(\Delta_{jm}) &:= \langle w_i|\psi_{s,f}(z-\Delta_{jm})\rangle \\ &= \int \big[w_{i,x}\psi_{s,x}(z-\Delta_{jm}) + w_{i,y}\psi_{s,y}(z-\Delta_{jm})\big]dz,\end{aligned} \tag{C.49}$$

$$\begin{aligned}l_{2,i}(\Delta_{jm}) &:= \langle w_i|i\psi_{s,f}(z-\Delta_{jm})\rangle \\ &= \int \big[-w_{i,x}\psi_{s,y}(z-\Delta_{jm}) + w_{i,y}\psi_{s,x}(z-\Delta_{jm})\big]dz,\end{aligned} \tag{C.50}$$

$$\Rightarrow l_i(\Delta_{jm}) := \sqrt{l_{1,i}^2(\Delta_{jm}) + l_{2,i}^2(\Delta_{jm})}. \tag{C.51}$$

Further, we define a phase $u_i$ as

$$u_i := \arctan\left(\frac{l_{1,i}}{l_{2,i}}\right), \tag{C.52}$$

$$\text{such that } \sin(u_i) = \frac{l_{1,i}}{l_i}, \quad \cos(u_i) = \frac{l_{2,i}}{l_i}. \tag{C.53}$$

With all these shortcuts, we rewrite Eq. (C.48) to obtain

$$\langle w_{t,p}|MR(\Omega+\theta_{jm})\,\psi_s(z-\Delta_{jm}-\tau_f)\rangle = l_{t,p}(\tau_f+\Delta_{jm})\sin[\Omega+\theta_{jm}+u_{t,p}(\tau_f+\Delta_{jm})]\,. \tag{C.54}$$

### Tail Terms

Next, we evaluate the remaining terms in Eqs. (C.35),(C.36). First, we express all modes in terms of the stationary modes and separate into field and carrier components using $\psi_s = \psi_{s,f} + \psi_{s,c}$:

$$\frac{\left\langle w_{t,p}^{(m)} | \mathcal{J}_m \psi_j \right\rangle}{\left\langle w_{t,p}^{(m)} | M v_{t,p}^{(m)} \right\rangle} = \frac{\langle w_{t,p} | \mathcal{J}_s R\left(\theta_{jm}\right) \psi_{s,f}\left(z - \Delta_{jm}\right)\rangle}{\langle w_{t,p} | M v_{t,p}\rangle} + \frac{\langle w_{t,p} | \mathcal{J}_s \psi_{s,c}\left(z - \Delta_{jm}\right)\rangle}{\langle w_{t,p} | M v_{t,p}\rangle}, \quad \text{(C.55)}$$

where $\mathcal{J}_s$ is the Jacobian evaluated at the stationary solution. Here, we can already identify the phase-independent term

$$b_{t,p}\left(\Delta_{jm}\right) := \langle w_{t,p} | \mathcal{J}_s \psi_{s,c}\left(z - \Delta_{jm}\right)\rangle . \quad \text{(C.56)}$$

In fact, we can compute this force analytically (cf. Sec. C.3). The phase dependent term can be handled analogously to the non-local term (cf. Sec. C.1):

$$\begin{aligned} \langle w_{t,p} | \mathcal{J}_s R\left(\theta_{jm}\right) \psi_{s,f}\left(z - \Delta_{jm}\right)\rangle = &\cos\left(\theta_{jm}\right) \langle w_{t,p} | \mathcal{J}_s \psi_{s,f}\left(z - \Delta_{jm}\right)\rangle + \\ &\sin\left(\theta_{jm}\right) \langle w_{t,p} | \mathcal{J}_s i \psi_{s,f}\left(z - \Delta_{jm}\right)\rangle . \end{aligned} \quad \text{(C.57)}$$

Again, we assign names to the integrals[24]

$$a_{i,1}\left(\Delta_{jm}\right) := \langle w_i | \mathcal{J}_s \psi_{s,f}\left(z - \Delta_{jm}\right)\rangle , \quad \text{(C.58)}$$

$$a_{i,2}\left(\Delta_{jm}\right) := \langle w_i | \mathcal{J}_s i \psi_{s,f}\left(z - \Delta_{jm}\right)\rangle , \quad \text{(C.59)}$$

$$a_i\left(\Delta_{jm}\right) = \sqrt{a_{1,i}^2\left(\Delta_{jm}\right) + a_{2,i}^2\left(\Delta_{jm}\right)} \quad \text{(C.60)}$$

and the corresponding phase

$$r_i := \arctan\left(\frac{a_{1,i}}{a_{2,i}}\right), \quad \text{(C.61)}$$

$$\text{such that } \sin\left(r_i\right) = \frac{a_{1,i}}{a_i}, \quad \cos\left(r_i\right) = \frac{a_{2,i}}{a_i}, \quad \text{(C.62)}$$

such that we can write Eq. (C.57) as

$$\langle w_{t,p} | \mathcal{J}_s R\left(\theta_{jm}\right) \psi_{s,f}\left(z - \Delta_{jm}\right)\rangle = a_{t,p}\left(\Delta_{jm}\right) \sin\left[\theta_{jm} + r_{t,p}\left(\Delta_{jm}\right)\right] . \quad \text{(C.63)}$$

[24]When evaluating the integral numerically, it should only be calculated in the vicinity of $\psi_s$, as $\mathcal{J}_s$ is a local linear approximation.

### The Final Equations of Motion

Finally, we can combine the results from the previous sections (importantly Eqs. (C.54), (C.56) and (C.63)) to obtain the EOM:

$$\begin{aligned}\dot{z}_m = \sum_{j\neq m} \big[ & A_t\left(\Delta_{jm}\right)\sin\left[\theta_{jm}+r_t\left(\Delta_{jm}\right)\right]+B_t\left(\Delta_{jm}\right)+ \\ & \eta L_t\left(\tau_f+\Delta_{jm}\right)\sin\left[\Omega+\theta_{jm}+u_t\left(\tau_f+\Delta_{jm}\right)\right]\big],\end{aligned} \tag{C.64}$$

$$\begin{aligned}\dot{\varphi}_m = \sum_{j\neq m} \big[ & A_p\left(\Delta_{jm}\right)\sin\left[\theta_{jm}+r_p\left(\Delta_{jm}\right)\right]+B_p\left(\Delta_{jm}\right)+ \\ & \eta L_p\left(\tau_f+\Delta_{jm}\right)\sin\left[\Omega+\theta_{jm}+u_p\left(\tau_f+\Delta_{jm}\right)\right]\big],\end{aligned} \tag{C.65}$$

where the capital letters stand for the normalized forces

$$A_{t,p}=\frac{a_{t,p}}{N_{t,p}},\quad L_{t,p}=\frac{l_{t,p}}{N_{t,p}},\quad B_{t,p}=\frac{b_{t,p}}{N_{t,p}}$$

with the normalization factors[25]

$$N_t=-\left\langle w_t|Mv_t\right\rangle,\quad N_p=\left\langle w_p|Mv_p\right\rangle. \tag{C.66}$$

All terms in Eqs. (C.64),(C.65) can be understood intuitively: $A_{t,p}$ are the amplitudes of the phase dependent force (tail interaction), $B_{t,p}$ is the amplitude of the phase independent force (interaction via carriers), and $L_{p,t}$ are the amplitude of the force stemming from the (phase dependent) time-delayed feedback.

## C.2. Special Cases and Simplifications

Next, we consider certain special cases and simplifications of the EOM (C.64), (C.65).

### C.2.1. Nearest Neighbor Interactions

First, due to exponentially decaying tails it is sufficient to consider only nearest neighbor interactions, i.e., the sum $\sum_{j\neq m}$ reduces to $j=m\pm 1$. However, while the interaction via time-delayed feedback is only with a single other pulse (for a single time delay), the interaction must not necessarily be with the nearest neighbor but depends on the relation of the time delay $\tau$ and the length of the feedback loop $\tau_f$, i.e., $j=\lfloor\frac{\tau_f}{\tau}N\rfloor$ (or $j=\lceil\frac{\tau_f}{\tau}N\rceil$, depending on what is closer). This enables interesting scenarios, as one can create a synthetic second dimension by a proper choice of $\tau_f$, where pulses are coupled in one dimension via overlapping tails and in the other dimension via time-delayed

[25]The different signs for $N_{t,p}$ stem from the fact that we chose different signs for $z_j$ and $\varphi_j$ in the ansatz in Eq. (C.11).

feedback. However, here we remain with nearest neighbor interaction and choose $\tau_f$ in the vicinity of $\frac{\tau}{N}$ such that $j = m-1$,

$$\begin{aligned}\dot{z}_m =& A_t\left(z_{m+1}-z_m\right)\sin\left[\varphi_{m+1}-\varphi_m+r_t\left(z_{m+1}-z_m\right)\right]+B_t\left(z_{m+1}-z_m\right)+\\ &A_t\left(z_{m-1}-z_m\right)\sin\left[\varphi_{m-1}-\varphi_m+r_t\left(z_{m+1}-z_m\right)\right]+B_t\left(z_{m-1}-z_m\right)+\\ &\eta L_t\left(\tau_f+z_{m-1}-z_m\right)\sin\left[\Omega+\varphi_{m-1}-\varphi_m+u_t\left(\tau_f+z_{m-1}-z_m\right)\right], \qquad \text{(C.67)}\\ \dot{\varphi}_m =& A_p\left(z_{m+1}-z_m\right)\sin\left[\varphi_{m+1}-\varphi_m+r_p\left(z_{m+1}-z_m\right)\right]+B_p\left(z_{m+1}-z_m\right)+\\ &A_p\left(z_{m-1}-z_m\right)\sin\left[\varphi_{m-1}-\varphi_m+r_p\left(z_{m+1}-z_m\right)\right]+B_p\left(z_{m-1}-z_m\right)+\\ &\eta L_p\left(\tau_f+z_{m-1}-z_m\right)\sin\left[\Omega+\varphi_{m-1}-\varphi_m+u_p\left(\tau_f+z_{m-1}-z_m\right)\right]. \qquad \text{(C.68)}\end{aligned}$$

In this context, we need to define the boundary conditions (i.e., what does $\varphi_{N+1}$, $z_{N+1}$, $\varphi_0$ and $z_0$ mean). For the positions we need to be careful and add/subtract $\tau$, i.e.,

$$\begin{aligned}&z_{N+1}=z_1+\tau, \quad z_0=z_N-\tau,\\ &\varphi_{N+1}=\varphi_1, \quad \varphi_0=\varphi_N\,.\end{aligned}$$

### C.2.2. Damped Translational Mode

Depending on the cavity geometry, the dynamics of the phases and positions can occur on different time scales. In particular, in short cavities, interaction via carriers, namely repulsion via gain, is dominant, such that the translational mode is damped and the pulses are in an equidistant configuration $z_m - z_{m-1} = \frac{\tau}{N}\,\forall m$. Hence, the coefficients of the phase dependent terms and the phase $r_p$ in Eqs. (C.64), (C.65) become constants:

$$A_+ = A_p\left(-\frac{\tau}{N}\right),\, A_- = A_p\left(\frac{\tau}{N}\right) \tag{C.69}$$

$$\psi_+ = r_p\left(-\frac{\tau}{N}\right),\, \psi_- = r_p\left(\frac{\tau}{N}\right). \tag{C.70}$$

Inserting these relations in Eqs. (C.67), (C.68) and neglecting the effects of time-delayed feedback (TDF) for a moment, we obtain a set of Kuramoto equations for the phase interaction:

$$\dot{\varphi}_m = A_+\sin\left(\varphi_{m-1}-\varphi_m+\psi_+\right)+A_-\sin\left(\varphi_{m+1}-\varphi_m+\psi_-\right)+\omega_0\,, \tag{C.71}$$

where

$$\omega_0 = B_p\left(-\frac{\tau}{N}\right)+B_p\left(\frac{\tau}{N}\right) \tag{C.72}$$

is a common phase rotation that can be scaled out by using a comoving reference frame.

On the other hand, when the effects of TDF are dominant, we obtain

$$\dot{\varphi}_m = \eta L_p \left(\tau_f - \frac{\tau}{N}\right) \sin\left[\Omega + \varphi_{m-1} - \varphi_m + u_p \left(\tau_f - \frac{\tau}{N}\right)\right]. \tag{C.73}$$

An interesting special case occurs, when choosing resonant feedback, i.e., $\tau_f = \frac{\tau}{N}$. First, we notice, that the normalization factor $N_p$ defined in Eq. (C.66) is equal to the overlap integral $l_{2,p}(0)$ (cf. Eq. (C.50)). Consequently, we find

$$L_p(0) = \frac{l_p(0)}{l_{2,p}(0)} = \frac{1}{\cos u}, \tag{C.74}$$

where we used Eq. (C.52) and defined $u = u_p(0)$. This leads to an effective EOM with a single free parameter $u$:

$$\dot{\varphi}_m = \frac{\eta}{\cos u} \sin\left(\Omega + \varphi_{m-1} - \varphi_m + u\right). \tag{C.75}$$

### C.2.3. Interaction of Two Pulses

The situation with only two pulses is special because right and left interaction go to the same pulse. Here, we define $\theta = \varphi_2 - \varphi_1$ and $\Delta = z_2 - z_1$ as the corresponding phase and position difference, respectively,

$$\begin{aligned}\dot{\Delta} =& A_t(-\Delta)\sin\left[-\theta + r_t(-\Delta)\right] + B_t(-\Delta) + \\ & \eta L_t(\tau_f - \Delta)\sin\left[\Omega - \theta + u_t(\tau_f - \Delta)\right] - \\ & A_t(\Delta)\sin\left[\theta + r_t(\Delta)\right] - B_t(\Delta) - \\ & \eta L_t(\tau_f + \Delta)\sin\left[\Omega + \theta + u_t(\tau_f + \Delta)\right],\end{aligned} \tag{C.76}$$

$$\begin{aligned}\dot{\theta} =& A_p(-\Delta)\sin\left[-\theta + r_p(-\Delta)\right] + B_p(-\Delta) + \\ & \eta L_p(\tau_f - \Delta)\sin\left[\Omega - \theta + u_p(\tau_f - \Delta)\right] - \\ & A_p(\Delta)\sin\left[\theta + r_p(\Delta)\right] - B_p(\Delta) - \\ & \eta L_p(\tau_f + \Delta)\sin\left[\Omega + \theta + u_p(\tau_f + \Delta)\right].\end{aligned} \tag{C.77}$$

We note that the forces are periodic functions, i.e., $A_{p,t}(-\Delta) = A_{p,t}(\tau - \Delta)$. From Eqs. (C.76), (C.77), it is easy to see that the equations are antisymmetric in $\theta$ and $\Delta$, i.e., we have

$$\dot{\Delta}(\Delta, \theta) = -\dot{\Delta}(-\Delta, -\theta), \tag{C.78}$$

$$\dot{\theta}(\Delta, \theta) = -\dot{\theta}(-\Delta, -\theta). \tag{C.79}$$

This symmetry corresponds to the permutation of the pulses. Now, we can immediately identify two steady state $(\Delta^*, \theta^*) = \left(\frac{\tau}{2}, 0\right)$ and $(\Delta^*, \theta^*) = \left(\frac{\tau}{2}, \pi\right)$ corresponding to a symmetric configuration. However, the more interesting symmetry is the one around the steady states at $\frac{\tau}{2}$. Therefore, we consider $\Delta = \frac{\tau}{2} \pm \delta$ and $\theta = \pi \pm \alpha$ to obtain

$$\dot{\Delta}\left(\frac{\tau}{2} - \delta, \pi - \alpha\right) = -\dot{\Delta}\left(\frac{\tau}{2} + \delta, \pi + \alpha\right), \tag{C.80}$$

$$\dot{\theta}\left(\frac{\tau}{2} - \delta, \pi - \alpha\right) = -\dot{\theta}\left(\frac{\tau}{2} + \delta, \pi + \alpha\right). \tag{C.81}$$

### C.2.4. Linear Stability Analysis of $N$ Equidistant Pulses

In the absence of time-delayed feedback, we can consider a set of $N$ pulses, which interact solely via gain repulsion in a unidirectional way (left to right), i.e.,

$$\dot{z}_n = B_t\left(z_{n-1} - z_n\right) \tag{C.82}$$

with the boundary conditions $z_0 = z_N - \tau$ and $z_{N+1} = z_1 + \tau$. The stable steady state is the equidistant configuration $z_n^* = n\frac{\tau}{N} + v_0\xi$, where $v_0 = B_t\left(-\tau/N\right)$. To analyze its linear stability, we consider $z_n = z_n^* + \delta_n$. Then one obtains

$$\dot{\delta}_n = B_t'\left(-\frac{\tau}{N}\right)\left(\delta_{n-1} - \delta_n\right) \tag{C.83}$$

with the periodic boundary condition $\delta_0 = \delta_N$ and $\delta_{N+1} = \delta_1$. We expand the perturbations in Fourier modes

$$\delta_n = \sum_p a_p e^{\lambda_p \xi + i q_p n}, \tag{C.84}$$

where due to boundary conditions, the wave number satisfies

$$e^{i q_p N} \stackrel{!}{=} 1 \tag{C.85}$$

$$\Leftrightarrow q_p = \frac{2\pi}{N}p, \quad p = 0, \ldots, N-1. \tag{C.86}$$

Using this expansion in Eq. (C.83) yields

$$\sum_p a_p \lambda_p e^{\lambda_p \xi + i q_p n} = B_t'\left(-\frac{\tau}{N}\right)\sum_p a_p e^{\lambda_p \xi + i q_p n}\left[e^{-i q_p} - 1\right]. \tag{C.87}$$

This has to be fulfilled for each element of the sum individually because the modes are linearly independent. Therefore, we find

$$\lambda_p = B_t'\left(-\frac{\tau}{N}\right)\left(e^{-iq_p}-1\right) \tag{C.88}$$

$$= B_t'\left(-\frac{\tau}{N}\right)\left[\left(\cos\left(q_p\right)-1\right)-i\sin\left(q_p\right)\right]. \tag{C.89}$$

We know that $B_t\left(\Delta\right)$ is exponentially recovering with $\Delta$ (cf. Sec. C.3) so its derivative is positive: $B_t'\left(-\tau/N\right) > 0$. Hence, we see that the steady states is indeed stable as $\cos\left(q_p\right)-1 \leq 0\ \forall p$. However, the imaginary part does not vanish for $N > 2$ and therefore leads to a convergence to the steady states in spirals. Calculating the eigenvalues explicitly yields:

- For $N = 2$ we have $q_p = \pi p$. The corresponding eigenvalues are:

$$\lambda_0 = 0,$$
$$\lambda_1 = -2B_t'\left(-\frac{\tau}{N}\right).$$

- For $N = 3$ we have $q_p = \frac{2\pi}{3}p$. The corresponding eigenvalues read:

$$\lambda_0 = 0,$$
$$\lambda_1 = B_t'\left(-\frac{\tau}{N}\right)\left[-\frac{3}{2}+i\frac{\sqrt{3}}{2}\right],$$
$$\lambda_2 = B_t'\left(-\frac{\tau}{N}\right)\left[-\frac{3}{2}-i\frac{\sqrt{3}}{2}\right].$$

## C.3. Analytical Approaches to Carrier Interaction

We want to characterize the interaction forces further. In particular, the phase independent force reads

$$B_{t,p}\left(\Delta\right) = \frac{1}{N_{t,p}}\left\langle w_{t,p}\middle|\mathcal{J}_s\psi_{s,c}\left(z-\Delta\right)\right\rangle. \tag{C.90}$$

As $\Gamma_g \ll \Gamma_q$, we can neglect the effect of the saturable absorber and only consider the impact of the gain. We define $z_0$ as the position where the pulse has decayed sufficiently such that one can assume exponential recovery. For $z > z_0$ the gain recovers as

$$\psi_{s,g}\left(z\right) = \left(g_s-g_0\right)e^{-\Gamma\left(z-z_0\right)} = Te^{-\Gamma z}, \tag{C.91}$$

$$\text{where}\quad T = \left(g\left(z_0\right)-g_0\right)e^{\Gamma z_0}. \tag{C.92}$$

We remember that this function is $\tau$ periodic. Hence, for $z < z_0$ the gain component reads

$$\psi_{s,g}(z) = \left(Te^{-\Gamma\tau}\right)e^{-\Gamma z}. \tag{C.93}$$

That is, in total one obtains

$$\psi_{s,g}(z) = T\begin{cases} e^{-\Gamma z} & z > z_0\,, \\ e^{-\Gamma(z+\tau)} & z < z_0\,. \end{cases} \tag{C.94}$$

With that in mind, one can find $\psi_{s,g}(z-\Delta)$. It reads

$$\psi_{s,g}(z-\Delta) = Te^{\Gamma\Delta}\begin{cases} e^{-\Gamma z} & z > z_0+\Delta\,, \\ e^{-\Gamma(z+\tau)} & z < z_0+\Delta\,. \end{cases} \tag{C.95}$$

However, we remember that for the overlap integrals, we integrate over $[z_p - a, z_p + a]$, where $a \ll \tau$ (because the Jacobian is a local linear approximation) and $z_p < z_0$ is the position of the pulse. As long as $\Delta > a$ (as should be the case for well-separated pulses), we can use

$$\psi_{s,g}(z-\Delta) = Te^{\Gamma\Delta}e^{-\Gamma(z+\tau)}. \tag{C.96}$$

Hence, we can calculate the force

$$B_{t,p}(\Delta) = C_{t,p}e^{\Gamma\Delta}\,, \tag{C.97}$$

$$\text{where}\quad C_{t,p} = \frac{T}{N_{t,p}}\left\langle w_{t,p}\middle|\mathcal{J}_s\left(e^{-\Gamma(z+\tau)}e_g\right)\right\rangle. \tag{C.98}$$

Here, $e_g$ is a unit vecor with a component in the gain part.

## C.4. Obtaining the Eigenmodes of the Direct and Adjoint System

For a successful numerical implementation of the EOM, it is crucial to have access to the eigenmodes of the direct ($v_{t,p}$) and adjoint ($w_{t,p}$) system respectively. While the direct modes can be simply obtained using Eqs. (C.23) and (C.24), it is more difficult for the adjoint modes. First, we compute the direct operator $\mathcal{J}$. For a simulation based on $N_z$ grid points, it is a $(4N_z \times 4N_z)$ matrix as the state vector $\psi_s$ is composed of the four fields $\mathrm{Re}(E)$, $\mathrm{Im}(E)$, $g - g_0$ and $q - q_0$. The $k$-th column of $\mathcal{J}$ can be obtained by integrating the full PDE in Eqs. (3.155)–(3.157) for a perturbed state $\psi_s + \delta_k$ for $k = 1, \ldots 4N_z$. Then the adjoint operator is simply the transposed (because all fields are real):

$$\mathcal{J}^{\dagger}_{(4N_z \times 4N_z)} = \left(\mathcal{J}_{(4N_z \times 4N_z)}\right)^T . \tag{C.99}$$

The kernel of $\mathcal{J}^{\dagger}$ is spanned by two vectors, namely $w_t$ and $w_p$. If we numerically compute the kernel-eigenvectors of $\mathcal{J}^{\dagger}$, the result will be two vectors $w_{1,2}$ which are an (arbitrary) superposition of $w_t$ and $w_p$:

$$w_1 = a w_t + b w_p, \tag{C.100}$$

$$w_2 = c w_t + d w_p, \tag{C.101}$$

where $a, b, c, d \in \mathbb{R}$ are random coefficients. To obtain $w_{t,p}$ themselves, we can use the biorthogonality, i.e.,

$$\langle w_t | v_p \rangle = \langle w_p | v_t \rangle = 0. \tag{C.102}$$

With that, we can linearly combine $w_{1,2}$ with particularly chosen coefficients to obtain the modes $w_{t,p}$

$$\langle w_2 | v_t \rangle w_1 - \langle w_1 | v_t \rangle w_2 = \langle w_t | v_t \rangle \left(bc - ad\right) w_p, \tag{C.103}$$

$$\langle w_2 | v_p \rangle w_1 - \langle w_1 | v_p \rangle w_2 = \langle w_p | v_p \rangle \left(ad - bc\right) w_t. \tag{C.104}$$

## C.5. Extracting Steady States from Phase Space

When performing the parameter study in Section 5.3, we show many times phase spaces (e.g., in Fig. 5.20), from which we infer bifurcation diagrams (e.g., Fig. 5.22). Here, we want to detail how we extract the steady states from the phase space and how we compute their stability.

To obtain the steady states, one can consider the nullclines of $\dot{\Delta}$ and $\dot{\theta}$, respectively. These can be computed numerically by, e.g., the `contour`-function in `Matlab`. In the next step, one has to calculate numerically the intersections between the nullclines using, e.g., the `Matlab`-function `polyxpoly` to obtain the steady state $\left(\tilde{\Delta}^*, \tilde{\theta}^*\right)$. Note that this steady state is numerically computed and therefore not exact, i.e., is does not necessarily fulfill exactly $\dot{\Delta}\left(\tilde{\Delta}^*, \tilde{\theta}^*\right) = 0 = \dot{\theta}\left(\tilde{\Delta}^*, \tilde{\theta}^*\right) = 0$. Therefore we define

$$\tilde{\Delta}^* = \Delta^* + \epsilon_{\Delta}, \quad \tilde{\theta}^* = \theta^* + \epsilon_{\theta} \tag{C.105}$$

where $(\Delta^*, \theta^*)$ is the analytical steady state and $\epsilon_{\Delta,\theta}$ are small perturbations to that. In the next step, we want to compute the corresponding stability information, i.e., the eigenvalues of the Jacobian

$$\mathcal{J} = \begin{pmatrix} \frac{\partial\dot{\Delta}}{\partial\Delta} & \frac{\partial\dot{\Delta}}{\partial\theta} \\ \frac{\partial\dot{\theta}}{\partial\Delta} & \frac{\partial\dot{\theta}}{\partial\theta} \end{pmatrix}\Bigg|_{(\Delta^*,\theta^*)}. \tag{C.106}$$

To obtain the derivatives, we apply another perturbation $\pm\delta_{\Delta,\theta}$. Using the central difference method, we obtain

$$\begin{aligned} \frac{\dot{\Delta}\left(\tilde{\Delta}^* + \delta_\Delta, \tilde{\theta}^*\right) - \dot{\Delta}\left(\tilde{\Delta}^* - \delta_\Delta, \tilde{\theta}^*\right)}{2\delta_\Delta} &= \frac{\partial\dot{\Delta}}{\partial\Delta}\bigg|_{(\tilde{\Delta}^*,\tilde{\theta}^*)} + \mathcal{O}\left(\delta_\Delta^2\right) \\ &= \frac{\partial\dot{\Delta}}{\partial\Delta}\bigg|_{(\Delta^*,\theta^*)} + \mathcal{O}\left(\epsilon_\Delta\partial_\Delta^2\dot{\Delta}, \epsilon_\theta\partial_\theta\partial_\Delta\dot{\Delta}, \delta_\Delta^2\right). \end{aligned}$$

The same procedure can be repeated for the other entries of the Jacobian.

## C.6. Extract Phase-Interaction-Parameters via Perturbation Approach

We present an approach to extract the parameters $A_\pm$, $\psi_\pm$ from the phase model in Eq. (5.7). We established the steady states as (cf. Eq. (5.72))

$$\varphi_j^{(p)} = j\Delta\varphi_p + \omega_p t. \tag{C.107}$$

Now, we consider a solution, where one of the phases is perturbed from the steady state. Let this be the $k$-th phase, i.e., $\varphi_k = \varphi_k^{(p)} + \delta$. The neighboring phases $k \pm 1$ now evolve as

$$\dot{\varphi}_{k+1} = A_+ \sin\left(\psi_+ - \Delta\varphi_p + \delta\right) + A_- \sin\left(\psi_- + \Delta\varphi_p\right) \tag{C.108}$$
$$= \omega_p + \delta \cdot k_+^{(p)} + \mathcal{O}\left(\delta^2\right), \tag{C.109}$$
$$\dot{\varphi}_{k-1} = A_+ \sin\left(\psi_+ - \Delta\varphi_p\right) + A_- \sin\left(\psi_- + \Delta\varphi_p + \delta\right) \tag{C.110}$$
$$= \omega_p + \delta \cdot k_-^{(p)} + \mathcal{O}\left(\delta^2\right), \tag{C.111}$$

where we used the definition of the common phase rotation of the splay state $\omega_p$ from Eq. (5.73). Further, $k_\pm^{(p)}$ are the same as in Eq. (5.76), but we explicitly use the upper index $p$ here to emphasize that the value depends on the splay state, i.e.,

$$\begin{aligned} k_+^{(p)} &= A_+ \cos\left(\psi_+ - \Delta\varphi_p\right), \\ k_-^{(p)} &= A_- \cos\left(\psi_- + \Delta\varphi_p\right). \end{aligned} \tag{C.112}$$

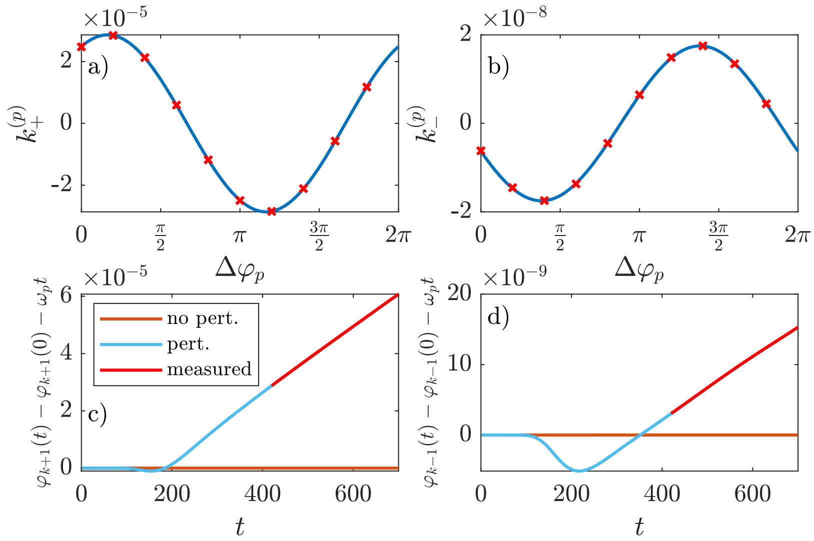


**Figure C.1:** Extracting parameter from the HME (3.155)–(3.157). Same parameters as in Figs. 5.5 and 5.6. (a),(b) Fits of $k_\pm^{(p)}$, which are measured using Eq. (C.115). (c),(d) Measurement for the $p = 9$-case. Due to the initial nonlinear response, we only use the last half of the simulation for the data. We use a perturbation of $\delta = 10^{-2}$. The fit parameters are $A_+ = 2.86 \times 10^{-5}$, $A_- = 1.75 \times 10^{-8}$, $\psi_+ = 0.165\pi$ and $\psi_- = -1.382\pi$.

Now we integrate $\dot{\varphi}_{k\pm1}$ over an interval $[0, T]$ which gives

$$\int_0^T \dot{\varphi}_{k+1} dt = \varphi_{k+1}(T) - \varphi_{k+1}(0) = \left(\omega_p + \delta k_+^{(p)}\right) T, \tag{C.113}$$

$$\int_0^T \dot{\varphi}_{k-1} dt = \varphi_{k-1}(T) - \varphi_{k-1}(0) = \left(\omega_p + \delta k_-^{(p)}\right) T. \tag{C.114}$$

We can simply solve for $k_\pm^{(p)}$:

$$\begin{aligned} k_+^{(p)} &= \frac{\varphi_{k+1}(T) - \varphi_{k+1}(0) - \omega_p T}{\delta \cdot T} \\ k_-^{(p)} &= \frac{\varphi_{k-1}(T) - \varphi_{k-1}(0) - \omega_p T}{\delta \cdot T} \end{aligned} \tag{C.115}$$

Therefore, we can find $N$ values for $k_\pm^{(p)}$ for $p = 1, \ldots, N$. We know from Eq. (C.112) that these values form a cosine. That is, we can simply fit the values and extract $A_\pm$, $\psi_\pm$ from the fit data. Therefore, it makes sense to use a high harmonic number such that there are more points to fit (one could even combine the results from different harmonic numbers to have more data to fit). Note that the results are independent of which $\text{HML}_N$ is used (of course $\tau$ needs to be adapted such that the pulse separation remains the same).

The scheme is presented in Fig. C.1 for an $\text{HML}_{10}$ state. We use the same parameters

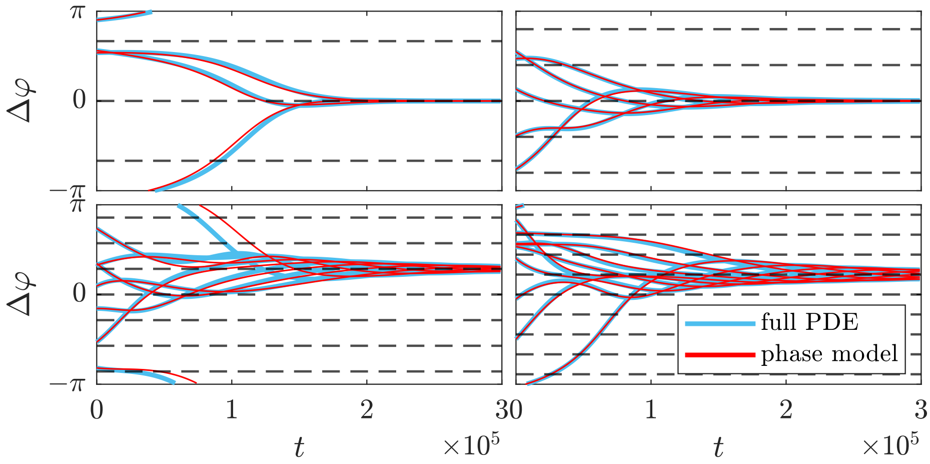


**Figure C.2:** Comparison of simulations of the HME (3.155)–(3.157) and the phase model in Eq. (5.7) for $N = 3, 5, 7, 9$ and randomized initial conditions. The parameters $A_\pm$, $\psi_\pm$ for the phase model are given in Fig. C.1.

as in Figs. 5.5 and 5.6. Panels (a),(b) show the result of fitting $k_\pm^{(p)}$. For each red cross, we consider a diagram as in panels (c),(d) (which are shown exemplary for the $p = 9$-case). The orange line shows the result of an unperturbed simulation from which we can extract $\omega_p$ as the average phase velocity: $\omega_p = \frac{1}{N}\sum_j \frac{\varphi_j(T)-\varphi_j(0)}{T}$. The blue line is from the perturbed simulation. We can see that for the first round-trips the simulation does not follow the prediction in Eqs. (C.109) and (C.111). We assume, that is because we "forced" the perturbation on the pulse $k$ (i.e., we multiplied $1/N$-th of the field – centered around the $k$-th pulse – with $\exp(i\delta)$). Therefore, discontinuities are created, which lead to a nonlinear response. However, after this has settled, we can observe the expected linear behavior. Hence, for the measurement of both $\omega_p$ and $k_\pm^{(p)}$, we only consider half of the simulation, which is marked by the red line. This shows a difficulty of the method as there is no universal recipe on which perturbation $\delta$ and integral range $T$ should be used. However, as long as they are chosen in way that simulations as in Fig. C.1 (c),(d) exhibit linear behavior, the result should be independent of $\delta$ and $T$.

Finally, we can test the fit parameters by comparing simulations of the HME (3.155)–(3.157) with results of the phase model (5.7) with fit parameters $A_\pm$, $\psi_\pm$ defined in Fig. C.1. This comparison is shown in Fig. C.2 for $N = 3, 5, 7, 9$ and random initial phases[26]. We can observe very good (yet not perfect) agreement.

[26] We first simulate the $p = 0$ solution (which is stable in this case). Then, we "force" the initial phases onto each section of the field. Because of that, small discontinuities are created. Hence, we let the simulation settle for $\sim 10^3$ steps before starting the comparison.

# List of Publications

The following publications originated from the work on this thesis and contain results presented here:

- T. G. Seidel, S. V. Gurevich, and J. Javaloyes. "Conservative Solitons and Reversibility in Time Delayed Systems". In: *Phys. Rev. Lett.* 128 (2022), p. 083901. DOI: 10.1103/PhysRevLett.128.083901, cited as [98]
- T. G. Seidel, J. Javaloyes, and S. V. Gurevich. "A normal form for frequency combs and localized states in Kerr–Gires–Tournois interferometers". In: *Opt. Lett.* 47.12 (2022), pp. 2979–2982. DOI: 10.1364/OL.457777, cited as [99]
- T. G. Seidel, J. Javaloyes, and S. V. Gurevich. "Normal dispersion Kerr cavity solitons: beyond the mean-field limit". In: *Opt. Lett.* 49.24 (2024), pp. 7008–7011. DOI: 10.1364/OL.538135, cited as [100]
- T. G. Seidel, A. Bartolo, A. Garnache, M. Giudici, M. Marconi, S. V. Gurevich, and J. Javaloyes. "Multistable Kuramoto Splay States in a Crystal of Mode-Locked Laser Pulses". In: *Phys. Rev. Lett.* 134 (2025), p. 033801. DOI: 10.1103/PhysRevLett.134.033801, cited as [125]
- T. G. Seidel, J. Javaloyes, and S. V. Gurevich. "Coherent pulse interactions in mode-locked semiconductor lasers". In: *Chaos, Solitons and Fractals* 195 (2025), p. 116244. DOI: 10.1016/j.chaos.2025.116244, cited as [126]

The following publications were produced in the course of this thesis but do not contain results discussed here:

- A. Bartolo, T. G. Seidel, N. Vigne, A. Garnache, G. Beaudoin, I. Sagnes, M. Giudici, J. Javaloyes, S. V. Gurevich, and M. Marconi. "Manipulation of temporal localized structures in a vertical external-cavity surface-emitting laser with optical feedback". In: *Opt. Lett.* 46.5 (2021), pp. 1109–1112. DOI: 10.1364/OL.414353, cited as [44], the authors AB and TGS contributed equally
- T. G. Seidel, J. Javaloyes, and S. V. Gurevich. "Influence of time-delayed feedback on the dynamics of temporal localized structures in passively mode-locked semiconductor lasers". In: *Chaos: An Interdisciplinary Journal of Nonlinear Science* 32.3 (2022), p. 033102. DOI: 10.1063/5.0075449, cited as [45]
- E. R. Koch, T. G. Seidel, S. V. Gurevich, and J. Javaloyes. "Square-wave generation in vertical external-cavity Kerr–Gires–Tournois interferometers". In: *Opt. Lett.* 47.17 (2022), pp. 4343–4346. DOI: 10.1364/OL.468236, cited as [122]

- E. R. Koch, T. G. Seidel, J. Javaloyes, and S. V. Gurevich. "Temporal localized states and square-waves in semiconductor micro-resonators with strong time-delayed feedback". In: *Chaos: An Interdisciplinary Journal of Nonlinear Science* 33.4 (2023), p. 043142. DOI: 10.1063/5.0143562, cited as [123]
- T. Lohmann, T. G. Seidel, J. Javaloyes, and S. V. Gurevich. *Dynamics of localized states in the anomalous dispersion regime of an injected Kerr–Gires–Tournois interferometer*. (in preparation), based upon [107]
- M. Hunkemöller, T. G. Seidel, J. Javaloyes, and S. V. Gurevich. *Influence of phase modulation on the dynamics of temporal localized structures in injected Kerr microcavities*. (in preparation), based upon [142]
- Y. Fleck, T. G. Seidel, J. Javaloyes, and S. V. Gurevich. *Spatio-Temporal Localized States in an Injected Kerr–Gires–Tournois Interferometer*. (in preparation), based upon [91]

# Bibliography

[1] A. Einstein. “Zur Quantentheorie der Strahlung”. In: *Physikalische Zeitschrift* 18 (1917), pp. 121–128. DOI: 10.1515/9783112596609-016.

[2] J. P. Gordon, H. J. Zeiger, and C. H. Townes. “Molecular Microwave Oscillator and New Hyperfine Structure in the Microwave Spectrum of $NH_3$”. In: *Phys. Rev.* 95 (1954), pp. 282–284. DOI: 10.1103/PhysRev.95.282.

[3] T. H. Maiman. “Stimulated Optical Radiation in Ruby”. In: *Nature* 187 (1960), pp. 493–494. DOI: 10.1038/187493a0.

[4] G. P. Agrawal. *Fiber-Optic Communication Systems*. 4th. Wiley, 2010. DOI: 10.1002/9780470918524.

[5] T. Vo-Dinh. *Biomedical Photonics Handbook*. 2nd. CRC Press, 2014. DOI: 10.1201/b17289.

[6] W. M. Steen and J. Mazumder. *Laser Material Processing*. 4th. Springer, 2010. DOI: 10.1007/978-1-84996-062-5.

[7] T. W. Hänsch. “Nobel Lecture: Passion for precision”. In: *Rev. Mod. Phys.* 78 (2006), pp. 1297–1309. DOI: 10.1103/RevModPhys.78.1297.

[8] A. D. Ludlow, M. M. Boyd, J. Ye, E. Peik, and P. O. Schmidt. “Optical atomic clocks”. In: *Rev. Mod. Phys.* 87 (2015), pp. 637–701. DOI: 10.1103/RevModPhys.87.637.

[9] I. Coddington, N. Newbury, and W. Swann. “Dual-comb spectroscopy”. In: *Optica* 3.4 (2016), pp. 414–426. DOI: 10.1364/OPTICA.3.000414.

[10] M. T. Murphy et al. “High-precision wavelength calibration of astronomical spectrographs with laser frequency combs”. In: *Monthly Notices of the Royal Astronomical Society* 380.2 (2007), pp. 839–847. DOI: 10.1111/j.1365-2966.2007.12147.x.

[11] E. Meron, E. Gilad, J. von Hardenberg, M. Shachak, and Y. Zarmi. “Vegetation patterns along a rainfall gradient”. In: *Chaos, Solitons & Fractals* 19.2 (2004). Fractals in Geophysics, pp. 367–376. DOI: 10.1016/S0960-0779(03)00049-3.

[12] P. W. Anderson. “Absence of Diffusion in Certain Random Lattices”. In: *Phys. Rev.* 109 (1958), pp. 1492–1505. DOI: 10.1103/PhysRev.109.1492.

[13] N. N. Rosanov and G. V. Khodova. "Diffractive autosolitons in nonlinear interferometers". In: *J. Opt. Soc. Am. B* 7.6 (1990), pp. 1057–1065. DOI: 10.1364/JOSAB.7.001057.

[14] M. Tlidi, P. Mandel, and R. Lefever. "Localized structures and localized patterns in optical bistability". In: *Phys. Rev. Lett.* 73 (1994), pp. 640–643. DOI: 10.1103/PhysRevLett.73.640.

[15] W. J. Firth and A. J. Scroggie. "Optical Bullet Holes: Robust Controllable Localized States of a Nonlinear Cavity". In: *Phys. Rev. Lett.* 76 (1996), pp. 1623–1626. DOI: 10.1103/PhysRevLett.76.1623.

[16] L. Lugiato. "Introduction to the feature section on cavity solitons: An overview". In: *IEEE Journal of Quantum Electronics* 39.2 (2003), pp. 193–196. DOI: 10.1109/JQE.2002.807195.

[17] S. Barland et al. "Cavity solitons as pixels in semiconductor microcavities". In: *Nature* 419.6908 (2002), pp. 699–702. DOI: 10.1038/nature01049.

[18] F. Leo et al. "Temporal cavity solitons in one-dimensional Kerr media as bits in an all-optical buffer". In: *Nat Photon* 4.7 (2010), pp. 471–476. DOI: 10.1038/nphoton.2010.120.

[19] J. K. Jang, M. Erkintalo, S. Coen, and S. G. Murdoch. "Temporal tweezing of light through the trapping and manipulation of temporal cavity solitons". In: *Nat Commun* 6 (2015). DOI: 10.1038/ncomms8370.

[20] P. Camelin, J. Javaloyes, M. Marconi, and M. Giudici. "Electrical addressing and temporal tweezing of localized pulses in passively-mode-locked semiconductor lasers". In: *Phys. Rev. A* 94 (2016), p. 063854. DOI: 10.1103/PhysRevA.94.063854.

[21] M. Marconi, J. Javaloyes, S. Balle, and M. Giudici. "How Lasing Localized Structures Evolve out of Passive Mode Locking". In: *Phys. Rev. Lett.* 112 (2014), p. 223901. DOI: 10.1103/PhysRevLett.112.223901.

[22] N. Akhmediev and A. Ankiewicz. *Dissipative Solitons: From Optics to Biology and Medicine Series*. Vol. 751. Lecture Notes in Physics. Springer Berlin Heidelberg, 2008. ISBN: 978-3-540-23373-2. DOI: 10.1007/978-3-540-78217-9.

[23] S. M. Link, D. J. H. C. Maas, D. Waldburger, and U. Keller. “Dual-comb spectroscopy of water vapor with a free-running semiconductor disk laser”. In: *Science* (2017). DOI: `10.1126/science.aam7424`.

[24] T. Herr et al. “Temporal solitons in optical microresonators”. In: *Nature Photonics* 8.2 (2014), pp. 145–152. DOI: `10.1038/nphoton.2013.343`.

[25] H. A. Haus. “Mode-locking of lasers”. In: *IEEE Journal of Selected Topics in Quantum Electronics* 6.6 (2000), pp. 1173–1185.

[26] J. Tu and J. Kutz. “Pulse Formation, Harmonic Mode-Locking, and Stability in Actively Mode-Locked Laser Cavities”. In: *Quantum Electronics, IEEE Journal of* 45.3 (2009), pp. 282–291. DOI: `10.1109/JQE.2009.2013143`.

[27] C. Cuadrado-Laborde, A. Diez, M. Delgado-Pinar, J. L. Cruz, and M. V. Andrés. “Mode locking of an all-fiber laser by acousto-optic superlattice modulation”. In: *Opt. Lett.* 34.7 (2009), pp. 1111–1113. DOI: `10.1364/OL.34.001111`.

[28] D. Kopf, F. X. Kärtner, K. J. Weingarten, and U. Keller. “Pulse shortening in a Nd:glass laser by gain reshaping and soliton formation”. In: *Opt. Lett.* 19.24 (1994), pp. 2146–2148. DOI: `10.1364/OL.19.002146`.

[29] C. Peng et al. “Theoretical analysis of actively mode-locked fiber ring laser with semiconductor optical amplifier”. In: *Optics Communications* 209.1 (2002), pp. 181–192. DOI: `10.1016/S0030-4018(02)01620-6`.

[30] K. Zoiros, T. Houbavlis, and M. Moyssidis. “Complete theoretical analysis of actively mode-locked fiber ring laser with external optical modulation of a semiconductor optical amplifier”. In: *Optics Communications* 254.4 (2005), pp. 310–329. DOI: `10.1016/j.optcom.2005.06.003`.

[31] D. J. Derickson et al. “Suppression of multiple pulse formation in external-cavity mode-locked semiconductor lasers using intrawaveguide saturable absorbers”. In: *IEEE photonics technology letters* 4.4 (1992), pp. 333–335.

[32] S. Hoogland et al. “Passively mode-locked diode-pumped surface-emitting semiconductor lasers”. In: *IEEE Photonics Technology Letters* 12 (2000), pp. 1135–1137. DOI: `10.1109/68.874213`.

[33] R. Haring et al. "Picosecond surface-emitting semiconductor laser with $> 200$ mW average power". In: *Electronics Letters* 37.12 (2001), pp. 766–767. DOI: 10.1049/el:20010546.

[34] R. Häring et al. "High-power passively mode-locked semiconductor lasers". In: *Quantum Electronics, IEEE Journal of* 38 (2002), pp. 1268–1275. DOI: 10.1109/JQE.2002.802111.

[35] A. C. Tropper, H. D. Foreman, A. Garnache, K. G. Wilcox, and S. H. Hoogland. "Vertical-external-cavity semiconductor lasers". In: *Journal of Physics D: Applied Physics* 37.9 (2004), R75. DOI: 10.1088/0022-3727/37/9/R01.

[36] J. Mulet and S. Balle. "Spatiotemporal optical model of VCSELs in the presence of polarization effects". In: *Quantum Electronics, IEEE Journal of* 38 (2002), pp. 291–305. DOI: 10.1109/3.985571.

[37] I. V. Babushkin, N. A. Loiko, and T. Ackemann. "Eigenmodes and symmetry selection mechanisms in circular large-aperture vertical-cavity surface-emitting lasers". In: *Phys. Rev. E* 69 (2004), p. 066205. DOI: 10.1103/PhysRevE.69.066205.

[38] U. Keller and A. C. Tropper. "Passively modelocked surface-emitting semiconductor lasers". In: *Physics Reports* 429.2 (2006), pp. 67–120. DOI: 10.1016/j.physrep.2006.03.004.

[39] F. Kartner, I. Jung, and U. Keller. "Soliton mode-locking with saturable absorbers". In: *IEEE Journal of Selected Topics in Quantum Electronics* 2.3 (1996), pp. 540–556. DOI: 10.1109/2944.571754.

[40] R. Bonifacio and L. Lugiato. "Superfluorescence in a cavity". In: *Optics Communications* 47.1 (1983), pp. 79–83. DOI: 10.1016/0030-4018(83)90342-5.

[41] A. G. Vladimirov and D. Turaev. "Model for passive mode locking in semiconductor lasers". In: *Phys. Rev. A* 72 (2005), p. 033808. DOI: 10.1103/PhysRevA.72.033808.

[42] A. G. Vladimirov. "Short- and long-range temporal cavity soliton interaction in delay models of mode-locked lasers". In: *Phys. Rev. E* 105 (2022), p. 044207. DOI: 10.1103/PhysRevE.105.044207.

[43] A. G. Vladimirov. “Temporal Cavity Soliton Interaction in Passively Mode-Locked Semiconductor Lasers”. In: *Optics* 4.3 (2023), pp. 433–446. DOI: 10.3390/opt4030031.

[44] A. Bartolo et al. “Manipulation of temporal localized structures in a vertical external-cavity surface-emitting laser with optical feedback”. In: *Opt. Lett.* 46.5 (2021), pp. 1109–1112. DOI: 10.1364/OL.414353.

[45] T. G. Seidel, J. Javaloyes, and S. V. Gurevich. “Influence of time-delayed feedback on the dynamics of temporal localized structures in passively mode-locked semiconductor lasers”. In: *Chaos: An Interdisciplinary Journal of Nonlinear Science* 32.3 (2022), p. 033102. DOI: 10.1063/5.0075449.

[46] L. Jaurigue, B. Krauskopf, and K. Lüdge. “Multipulse dynamics of a passively mode-locked semiconductor laser with delayed optical feedback”. In: *Chaos: An Interdisciplinary Journal of Nonlinear Science* 27.11 (2017), p. 114301. DOI: 10.1063/1.5006743.

[47] C. Otto, K. Lüdge, A. G. Vladimirov, M. Wolfrum, and E. Schöll. “Delay-induced dynamics and jitter reduction of passively mode-locked semiconductor lasers subject to optical feedback”. In: *New Journal of Physics* 14.11 (2012), p. 113033. DOI: 10.1088/1367-2630/14/11/113033.

[48] R. Arkhipov, A. Amann, and A. Vladimirov. “Pulse repetition-frequency multiplication in a coupled cavity passively mode-locked semiconductor lasers”. In: *Applied Physics B* 118 (2015). DOI: 10.1007/s00340-015-6030-3.

[49] V. S. Ilchenko, A. A. Savchenkov, A. B. Matsko, and L. Maleki. “Nonlinear Optics and Crystalline Whispering Gallery Mode Cavities”. In: *Phys. Rev. Lett.* 92 (2004), p. 043903. DOI: 10.1103/PhysRevLett.92.043903.

[50] L. Maleki and A. Matsko. “Lithium niobate whispering gallery resonators: applications and fundamental studies”. In: *Ferroelectric Crystals for Photonic Applications: Including Nanoscale Fabrication and Characterization Techniques*. Springer, 2014, pp. 337–383. DOI: 10.1007/978-3-642-41086-4_13.

[51] T. J. Kippenberg, A. L. Gaeta, M. Lipson, and M. L. Gorodetsky. “Dissipative Kerr solitons in optical microresonators”. In: *Science* 361.6402 (2018), eaan8083. DOI: 10.1126/science.aan8083.

[52] Q. Xu, V. R. Almeida, and M. Lipson. “Micrometer-scale all-optical wavelength converter on silicon”. In: *Opt. Lett.* 30.20 (2005), pp. 2733–2735. DOI: 10.1364/OL.30.002733.

[53] N. Matsuda, R. Shimizu, Y. Mitsumori, H. Kosaka, and K. Edamatsu. “Observation of optical-fibre Kerr nonlinearity at the single-photon level”. In: *Nature Photonics* 3 (2009), pp. 95–98. DOI: 10.1038/nphoton.2008.292.

[54] R. L. Carman, R. Y. Chiao, and P. L. Kelley. “Observation of Degenerate Stimulated Four-Photon Interaction and Four-Wave Parametric Amplification”. In: *Phys. Rev. Lett.* 17 (1966), pp. 1281–1283. DOI: 10.1103/PhysRevLett.17.1281.

[55] C. Schelte, A. Pimenov, A. G. Vladimirov, J. Javaloyes, and S. V. Gurevich. “Tunable Kerr frequency combs and temporal localized states in time-delayed Gires-Tournois interferometers”. In: *Opt. Lett.* 44.20 (2019), pp. 4925–4928. DOI: 10.1364/OL.44.004925.

[56] F. Gires and P. Tournois. “Interferometre utilisable pour la compression d’impulsions lumineuses modulees en frequence”. In: *C. R. Acad. Sci. Paris* 258 (1964), pp. 6112–6115.

[57] C. Schelte et al. “Third Order Dispersion in Time-Delayed Systems”. In: *Phys. Rev. Lett.* 123 (2019), p. 043902. DOI: 10.1103/PhysRevLett.123.043902.

[58] L. A. Lugiato and R. Lefever. “Spatial Dissipative Structures in Passive Optical Systems”. In: *Phys. Rev. Lett.* 58 (1987), pp. 2209–2211. DOI: 10.1103/PhysRevLett.58.2209.

[59] A. Pasquazi et al. “Micro-combs: A novel generation of optical sources”. In: *Physics Reports* 729 (2018), pp. 1–81. DOI: 10.1016/j.physrep.2017.08.004.

[60] Y. K. Chembo, D. V. Strekalov, and N. Yu. “Spectrum and Dynamics of Optical Frequency Combs Generated with Monolithic Whispering Gallery Mode Resonators”. In: *Phys. Rev. Lett.* 104 (2010), p. 103902. DOI: 10.1103/PhysRevLett.104.103902.

[61] Y. K. Chembo and N. Yu. “Modal expansion approach to optical-frequency-comb generation with monolithic whispering-gallery-mode resonators”. In: *Phys. Rev. A* 82 (2010), p. 033801. DOI: 10.1103/PhysRevA.82.033801.

[62] Y. K. Chembo and C. R. Menyuk. “Spatiotemporal Lugiato-Lefever formalism for Kerr-comb generation in whispering-gallery-mode resonators”. In: *Phys. Rev. A* 87 (2013), p. 053852. DOI: 10.1103/PhysRevA.87.053852.

[63] S. Coen, H. G. Randle, T. Sylvestre, and M. Erkintalo. “Modeling of octave-spanning Kerr frequency combs using a generalized mean-field Lugiato–Lefever model”. In: *Opt. Lett.* 38.1 (2013), pp. 37–39. DOI: 10.1364/OL.38.000037.

[64] L. Columbo et al. “Unifying Frequency Combs in Active and Passive Cavities: Temporal Solitons in Externally Driven Ring Lasers”. In: *Phys. Rev. Lett.* 126 (2021), p. 173903. DOI: 10.1103/PhysRevLett.126.173903.

[65] K. Ikeda. “Multiple-valued stationary state and its instability of the transmitted light by a ring cavity system”. In: *Optics Communications* 30.2 (1979), pp. 257–261. DOI: 10.1016/0030-4018(79)90090-7.

[66] T. Hansson and S. Wabnitz. In: *Nanophotonics* 5.2 (2016), pp. 231–243. DOI: doi:10.1515/nanoph-2016-0012.

[67] T. Hansson and S. Wabnitz. “Frequency comb generation beyond the Lugiato–Lefever equation: multi-stability and super cavity solitons”. In: *J. Opt. Soc. Am. B* 32.7 (2015), pp. 1259–1266. DOI: 10.1364/JOSAB.32.001259.

[68] M. Anderson et al. “Coexistence of Multiple Nonlinear States in a Tristable Passive Kerr Resonator”. In: *Phys. Rev. X* 7 (2017), p. 031031. DOI: 10.1103/PhysRevX.7.031031.

[69] S. H. Strogatz. *Nonlinear Dynamics and Chaos with Student Solutions Manual: With Applications to Physics, Biology, Chemistry, and Engineering.* CRC Press, 2018. ISBN: 9780429399640. DOI: 10.1201/9780429399640.

[70] S. Yanchuk and G. Giacomelli. “Spatio-temporal phenomena in complex systems with time delays”. In: *Journal of Physics A: Mathematical and Theoretical* 50.10 (2017), p. 103001. DOI: 10.1088/1751-8121/50/10/103001.

[71] M. Wolfrum, S. Yanchuk, P. Hövel, and E. Schöll. "Complex dynamics in delay-differential equations with large delay". In: *The European Physical Journal Special Topics* 191.1 (2010), pp. 91–103. DOI: `10.1140/epjst/e2010-01343-7`.

[72] M. C. Mackey. "Commodity price fluctuations: Price dependent delays and nonlinearities as explanatory factors". In: *Journal of Economic Theory* 48.2 (1989), pp. 497–509. DOI: `10.1016/0022-0531(89)90039-2`.

[73] A. Keane, B. Krauskopf, and C. M. Postlethwaite. "Climate models with delay differential equations". In: *Chaos: An Interdisciplinary Journal of Nonlinear Science* 27.11 (2017).

[74] M. t. Vrugt, J. Jeggle, and R. Wittkowski. "Jerky active matter: A phase field crystal model with translational and orientational memory". In: *New Journal of Physics* 23 (2021). DOI: `10.1088/1367-2630/abfa61`.

[75] A. Otto, D. Müller, and G. Radons. "Universal Dichotomy for Dynamical Systems with Variable Delay". In: *Phys. Rev. Lett.* 118 (2017), p. 044104. DOI: `10.1103/PhysRevLett.118.044104`.

[76] A. Otto, W. Just, and G. Radons. "Nonlinear dynamics of delay systems: an overview". In: *Philosophical Transactions of the Royal Society A: Mathematical, Physical and Engineering Sciences* 377.2153 (2019), p. 20180389. DOI: `10.1098/rsta.2018.0389`.

[77] J. Rombouts, L. Gelens, and T. Erneux. "Travelling fronts in time-delayed reaction–diffusion systems". In: *Philosophical Transactions of the Royal Society A: Mathematical, Physical and Engineering Sciences* 377.2153 (2019), p. 20180127. DOI: `10.1098/rsta.2018.0127`.

[78] J. Doyne Farmer. "Chaotic attractors of an infinite-dimensional dynamical system". In: *Physica D: Nonlinear Phenomena* 4.3 (1982), pp. 366–393. DOI: `10.1016/0167-2789(82)90042-2`.

[79] G. Giacomelli and A. Politi. "Relationship between Delayed and Spatially Extended Dynamical Systems". In: *Phys. Rev. Lett.* 76 (1996), pp. 2686–2689. DOI: `10.1103/PhysRevLett.76.2686`.

[80] F. Marino and G. Giacomelli. "Spatiotemporal representation of long-delayed systems: An alternative approach". In: *Phys. Rev. E* 102 (2020), p. 052217. DOI: `10.1103/PhysRevE.102.052217`.

[81] F. T. Arecchi, G. Giacomelli, A. Lapucci, and R. Meucci. "Two-dimensional representation of a delayed dynamical system". In: *Phys. Rev. A* 45 (1992), R4225–R4228. DOI: 10.1103/PhysRevA.45.R4225.

[82] S. Yanchuk, S. Ruschel, J. Sieber, and M. Wolfrum. "Temporal Dissipative Solitons in Time-Delay Feedback Systems". In: *Phys. Rev. Lett.* 123 (2019), p. 053901. DOI: 10.1103/PhysRevLett.123.053901.

[83] J. K. Hale. *Theory of Functional Differential Equations*. Applied Mathematical Sciences. Springer, 1977. ISBN: 9780387902036.

[84] M. Lichtner, M. Wolfrum, and S. Yanchuk. "The spectrum of delay differential equations with large delay". In: *SIAM journal on mathematical analysis* 43.2 (2011), pp. 788–802. DOI: 10.1137/090766796.

[85] S. Heiligenthal et al. "Strong and Weak Chaos in Nonlinear Networks with Time-Delayed Couplings". In: *Phys. Rev. Lett.* 107 (2011), p. 234102. DOI: 10.1103/PhysRevLett.107.234102.

[86] J. A. Murdock. *Normal Forms and Unfoldings for Local Dynamical Systems*. Theoretical and Mathematical Physics. Springer, 2003. ISBN: 978-0-387-95464-6. DOI: 10.1007/b97515.

[87] C. Schelte, J. Javaloyes, and S. V. Gurevich. "Functional mapping for passively mode-locked semiconductor lasers". In: *Opt. Lett.* 43.11 (2018), pp. 2535–2538. DOI: 10.1364/OL.43.002535.

[88] C. Schelte, D. Hessel, J. Javaloyes, and S. V. Gurevich. "Dispersive Instabilities in Passively Mode-Locked Integrated External-Cavity Surface-Emitting Lasers". In: *Phys. Rev. Applied* 13 (2020), p. 054050. DOI: 10.1103/PhysRevApplied.13.054050.

[89] E. R. Koch, J. Javaloyes, and S. V. Gurevich. "Thermo-optical spiking and mixed-mode oscillations in injected Kerr microcavities". In: *arXiv preprint arXiv:2412.02510* (2024). DOI: 10.48550/arXiv.2412.02510.

[90] J. Mulet and S. Balle. "Mode locking dynamics in electrically-driven vertical-external-cavity surface-emitting lasers". In: *Quantum Electronics, IEEE Journal of* 41.9 (2005), pp. 1148–1156. DOI: 10.1109/JQE.2005.853355.

[91] Y. Fleck. "Spatio-Temporal Localized States in an Injected Kerr–Gires–Tournois Interferometer". MA thesis. Universität Münster, 2024.

[92] W. W. Chow, S. W. Koch, and M. S. III. *Semiconductor Laser Physics.* Berlin: Springer-Verlag, 1994. ISBN: 978-3-642-64752-9. DOI: 10.1007/978-3-642-61225-1.

[93] G. P. Agrawal and N. A. Olsson. "Amplification and compression of weak picosecond optical pulses by using semiconductor-laser amplifiers". In: *Opt. Lett.* 14.10 (1989), pp. 500–502. DOI: 10.1364/OL.14.000500.

[94] A. M. Perego et al. "Coherent master equation for laser modelocking". In: *Nat. Commun.* 11.1 (2020), p. 311. DOI: 10.1038/s41467-019-14013-4.

[95] J. Hausen, K. Lüdge, S. V. Gurevich, and J. Javaloyes. "How carrier memory enters the Haus master equation of mode-locking". In: *Opt. Lett.* 45.22 (2020), pp. 6210–6213. DOI: 10.1364/OL.406136.

[96] M. Nizette and A. G. Vladimirov. "Generalized Haus master equation model for mode-locked class-$B$ lasers". In: *Phys. Rev. E* 104 (2021), p. 014215. DOI: 10.1103/PhysRevE.104.014215.

[97] T. Seidel. "Influence of Time Delayed Feedback on the Dynamics of Temporal Localized Structures". MA thesis. Universität Münster, 2020.

[98] T. G. Seidel, S. V. Gurevich, and J. Javaloyes. "Conservative Solitons and Reversibility in Time Delayed Systems". In: *Phys. Rev. Lett.* 128 (2022), p. 083901. DOI: 10.1103/PhysRevLett.128.083901.

[99] T. G. Seidel, J. Javaloyes, and S. V. Gurevich. "A normal form for frequency combs and localized states in Kerr–Gires–Tournois interferometers". In: *Opt. Lett.* 47.12 (2022), pp. 2979–2982. DOI: 10.1364/OL.457777.

[100] T. G. Seidel, J. Javaloyes, and S. V. Gurevich. "Normal dispersion Kerr cavity solitons: beyond the mean-field limit". In: *Opt. Lett.* 49.24 (2024), pp. 7008–7011. DOI: 10.1364/OL.538135.

[101] V. Kolmanovskii and A. Myshkis. *Applied theory of functional differential equations.* Vol. 85. Springer Science & Business Media, 2012.

[102] M. Marconi, J. Javaloyes, S. Balle, and M. Giudici. "Passive Mode-Locking and Tilted Waves in Broad-Area Vertical-Cavity Surface-Emitting Lasers". In: *IEEE J. Sel. Top. Quantum Electron.* 21.1 (2015), pp. 85–93. DOI: 10.1109/JSTQE.2014.2346614.

[103] P. Camelin et al. "Temporal localized structures in mode-locked vertical external-cavity surface-emitting lasers". In: *Opt. Lett.* 43.21 (2018), pp. 5367–5370. DOI: 10.1364/OL.43.005367.

[104] N. N. Akhmediev and A. Ankiewicz. *Solitons: nonlinear pulses and beams.* Chapman & Hall, 1997.

[105] K. Engelborghs, T. Luzyanina, and D. Roose. "Numerical bifurcation analysis of delay differential equations using DDE-BIFTOOL". In: *ACM Trans. Math. Softw.* 28.1 (2002), pp. 1–21. DOI: 10.1145/513001.513002.

[106] J. S. Lamb and J. A. Roberts. "Time-reversal symmetry in dynamical systems: A survey". In: *Physica D: Nonlinear Phenomena* 112.1 (1998). Proceedings of the Workshop on Time-Reversal Symmetry in Dynamical Systems, pp. 1–39. DOI: 10.1016/S0167-2789(97)00199-1.

[107] T. Lohmann. "Dynamics of localized states in the anomalous dispersion regime of an injected Kerr–Gires–Tournois interferometer". MA thesis. Universität Münster, 2024.

[108] P. Parra-Rivas. "Dynamics of dissipative localized structures in driven nonlinear optical cavities". PhD thesis. Vrije Universiteit Brussel, 2017.

[109] Wolfram Research, Inc. *Mathematica, Version 14.0.* Champaign, IL, 2024.

[110] S. Yanchuk. "Properties of stationary states of delay equations with large delay and applications to laser dynamics". In: *Mathematical Methods in the Applied Sciences* 28.3 (2005), pp. 363–377. DOI: 10.1002/mma.584.

[111] J. Sieber, K. Engelborghs, T. Luzyanina, G. Samaey, and D. Roose. *DDE-BIFTOOL Manual - Bifurcation analysis of delay differential equations.* 2016. DOI: 10.48550/arXiv.1406.7144.

[112] D. A. W. Barton, S. Terrien, D. Hessel, S. V. Gurevich, and J. Javaloyes. *DDE-BIFTOOL – Methods and parts of implementation for neutral DDEs and demo.* sourceforge.net/projects/ddebiftool/. 2019.

[113] Y.-P. Ma, J. Burke, and E. Knobloch. "Defect-mediated snaking: A new growth mechanism for localized structures". In: *Physica D: Nonlinear Phenomena* 239.19 (2010), pp. 1867–1883. DOI: 10.1016/j.physd.2010.06.014.

[114] J. Burke and E. Knobloch. "Localized states in the generalized Swift-Hohenberg equation". In: *Phys. Rev. E* 73 (2006), p. 056211. DOI: 10.1103/PhysRevE.73.056211.

[115] P. Glendinning and C. Sparrow. "T-points: a codimension two heteroclinic bifurcation". In: *Journal of Statistical Physics* 43 (1986), pp. 479–488. DOI: 10.1007/BF01020649.

[116] V. V. Bykov. "The bifurcations of separatrix contours and chaos". In: *Physica D: Nonlinear Phenomena* 62.1-4 (1993), pp. 290–299. DOI: 10.1016/0167-2789(93)90288-C.

[117] J. Knobloch, J. S. Lamb, and K. N. Webster. "Using Lin's method to solve Bykov's problems". In: *Journal of Differential Equations* 257.8 (2014), pp. 2984–3047. DOI: 10.1016/j.jde.2014.06.006.

[118] M. Stöhr, E. R. Koch, J. Javaloyes, S. V. Gurevich, and M. Wolfrum. "Square waves and Bykov T-points in a delay algebraic model for the Kerr–Gires–Tournois interferometer". In: *Chaos: An Interdisciplinary Journal of Nonlinear Science* 33.11 (2023), p. 113105. DOI: 10.1063/5.0173320.

[119] A. Hariz et al. "Swift-Hohenberg equation with third-order dispersion for optical fiber resonators". In: *Phys. Rev. A* 100 (2019), p. 023816. DOI: 10.1103/PhysRevA.100.023816.

[120] P. Parra-Rivas, D. Gomila, and L. Gelens. "Coexistence of stable dark- and bright-soliton Kerr combs in normal-dispersion resonators". In: *Phys. Rev. A* 95 (2017), p. 053863. DOI: 10.1103/PhysRevA.95.053863.

[121] E. R. Koch. "Square-waves and pulsating dynamics in time-delayed active micro-cavities". MA thesis. Universität Münster, 2022.

[122] E. R. Koch, T. G. Seidel, S. V. Gurevich, and J. Javaloyes. "Square-wave generation in vertical external-cavity Kerr–Gires–Tournois interferometers". In: *Opt. Lett.* 47.17 (2022), pp. 4343–4346. DOI: 10.1364/OL.468236.

[123] E. R. Koch, T. G. Seidel, J. Javaloyes, and S. V. Gurevich. "Temporal localized states and square-waves in semiconductor micro-resonators with strong time-delayed feedback". In: *Chaos: An Interdisciplinary Journal of Nonlinear Science* 33.4 (2023), p. 043142. DOI: 10.1063/5.0143562.

[124] M. Conforti and F. Biancalana. “Multi-resonant Lugiato–Lefever model”. In: *Opt. Lett.* 42.18 (2017), pp. 3666–3669. DOI: 10.1364/OL.42.003666.

[125] T. G. Seidel et al. “Multistable Kuramoto Splay States in a Crystal of Mode-Locked Laser Pulses”. In: *Phys. Rev. Lett.* 134 (2025), p. 033801. DOI: 10.1103/PhysRevLett.134.033801.

[126] T. G. Seidel, J. Javaloyes, and S. V. Gurevich. “Coherent pulse interactions in mode-locked semiconductor lasers”. In: *Chaos, Solitons and Fractals* 195 (2025), p. 116244. DOI: 10.1016/j.chaos.2025.116244.

[127] C. Schelte, J. Javaloyes, and S. V. Gurevich. “Dynamics of temporally localized states in passively mode-locked semiconductor lasers”. In: *Phys. Rev. A* 97 (2018), p. 053820. DOI: 10.1103/PhysRevA.97.053820.

[128] D. Hessel, S. V. Gurevich, and J. Javaloyes. “Wiggling instabilities of temporal localized states in passively mode-locked vertical external-cavity surface-emitting lasers”. In: *Opt. Lett.* 46.10 (2021), pp. 2557–2560. DOI: 10.1364/OL.428182.

[129] A. Gordon and B. Fischer. “Phase Transition Theory of Many-Mode Ordering and Pulse Formation in Lasers”. In: *Phys. Rev. Lett.* 89 (2002), p. 103901. DOI: 10.1103/PhysRevLett.89.103901.

[130] R. Weill, A. Rosen, A. Gordon, O. Gat, and B. Fischer. “Critical Behavior of Light in Mode-Locked Lasers”. In: *Phys. Rev. Lett.* 95 (2005), p. 013903. DOI: 10.1103/PhysRevLett.95.013903.

[131] L. Leuzzi, C. Conti, V. Folli, L. Angelani, and G. Ruocco. “Phase Diagram and Complexity of Mode-Locked Lasers: From Order to Disorder”. In: *Phys. Rev. Lett.* 102 (2009), p. 083901. DOI: 10.1103/PhysRevLett.102.083901.

[132] L. Munsberg, J. Javaloyes, and S. V. Gurevich. “Topological localized states in the time delayed Adler model: Bifurcation analysis and interaction law”. In: *Chaos* 30.6 (2020), p. 063137. DOI: 10.1063/5.0002015.

[133] A. B. Grudinin and S. Gray. “Passive harmonic mode locking in soliton fiber lasers”. In: *J. Opt. Soc. Am. B* 14.1 (1997), pp. 144–154. DOI: 10.1364/JOSAB.14.000144.

[134] A. Haboucha, H. Leblond, M. Salhi, A. Komarov, and F. Sanchez. "Coherent soliton pattern formation in a fiber laser". In: *Opt. Lett.* 33.5 (2008), pp. 524–526. DOI: 10.1364/OL.33.000524.

[135] F. Amrani, M. Salhi, P. Grelu, H. Leblond, and F. Sanchez. "Universal soliton pattern formations in passively mode-locked fiber lasers". In: *Opt. Lett.* 36.9 (2011), pp. 1545–1547. DOI: 10.1364/OL.36.001545.

[136] J. A. Acebrón, L. L. Bonilla, C. J. Pérez Vicente, F. Ritort, and R. Spigler. "The Kuramoto model: A simple paradigm for synchronization phenomena". In: *Rev. Mod. Phys.* 77 (2005), pp. 137–185. DOI: 10.1103/RevModPhys.77.137.

[137] R. Berner, S. Yanchuk, Y. Maistrenko, and E. Schöll. "Generalized splay states in phase oscillator networks". In: *Chaos: An Interdisciplinary Journal of Nonlinear Science* 31.7 (2021), p. 073128. DOI: 10.1063/5.0056664.

[138] C. W. Gardiner. *Handbook of stochastic methods*. Springer-Verlag, 1994. ISBN: 3540156070.

[139] P. Parra-Rivas, D. Gomila, L. Gelens, and E. Knobloch. "Bifurcation structure of localized states in the Lugiato-Lefever equation with anomalous dispersion". In: *Phys. Rev. E* 97 (2018), p. 042204. DOI: 10.1103/PhysRevE.97.042204.

[140] E. Fermi, J. Pasta, and S. M. Ulam. *Studies of nonlinear problems. I.* Technical Report LA-1940. 1955, p. 22.

[141] Y. Sun, S. Wabnitz, and P. Parra-Rivas. "Multimode resonance transition to collapsed snaking in normal dispersive Kerr cavities: bright versus dark solitons". In: *Opt. Lett.* 48.20 (2023), pp. 5403–5406. DOI: 10.1364/OL.499907.

[142] M. Hunkemöller. "Temporal Localized States in Injected Microcavities: The Influence of Phase Modulation". MA thesis. Universität Münster, 2024.

[143] N. D. Mermin and H. Wagner. "Absence of Ferromagnetism or Antiferromagnetism in One- or Two-Dimensional Isotropic Heisenberg Models". In: *Phys. Rev. Lett.* 17 (1966), pp. 1133–1136. DOI: 10.1103/PhysRevLett.17.1133.

[144] S. Yanchuk and G. Giacomelli. “Pattern Formation in Systems with Multiple Delayed Feedbacks”. In: *Phys. Rev. Lett.* 112 (2014), p. 174103. DOI: 10.1103/PhysRevLett.112.174103.

[145] L. Yuan, Q. Lin, M. Xiao, and S. Fan. “Synthetic dimension in photonics”. In: *Optica* 5.11 (2018), pp. 1396–1405. DOI: 10.1364/OPTICA.5.001396.

[146] R. J. LeVeque. *Finite Difference Methods for Ordinary and Partial Differential Equations: Steady-State and Time-Dependent Problems.* Philadelphia, PA: Society for Industrial and Applied Mathematics, 2007. DOI: 10.1137/1.9780898717839.

[147] H. Uecker, D. Wetzel, and J. D. M. Rademacher. “pde2path - A Matlab Package for Continuation and Bifurcation in 2D Elliptic Systems”. In: *Num. Math.: Theory, Methods and App.* 7.1 (2014), pp. 58–106. DOI: 10.1017/S1004897900000295.

[148] S. Hartmann. *BICE: A numerical path continuation software written in Python.* Available at https://zivgitlab.uni-muenster.de/s_hart20/bice, accessed 23 Jan 2025.

[149] D. A. W. Barton, B. Krauskopf, and R. E. Wilson. “Collocation schemes for periodic solutions of neutral delay differential equations”. In: *Journal of Difference Equations and Applications* 12.11 (2006), pp. 1087–1101. DOI: 10.1080/10236190601045663.

# Acknowledgments

Completing this PhD thesis has been a challenging journey, which I could not have accomplished without the help and support of many individuals to whom I would like to express my deepest gratitude. In particular, I want to thank ...

... my supervisors Svetlana Gurevich and Julien Javaloyes not only for your guidance, patience and encouragement in the last years, but also for caring about your students and having an open ear for their problems.

... my colleagues (both former and current) in Münster for all the great time we shared either running around the Kleinwalsertal, exploring conference cities or simply enjoying long coffee breaks. But also for many helpful discussions which contributed to this thesis.

... my office mates at the UIB for warmly welcoming me on multiple stays in Palma.

... our co-workers in Nice for many valuable discussions, which helped me to see various aspects of this thesis from an experimental point of view.

... my girlfriend Vivi for the never-ending support and love.

... my friends and family for all the encouragement and support.

... the *Studienstiftung des deutschen Volkes* for their financial support without which I would not have had the privilege to conduct this thesis.

# Curriculum Vitae

## Personal Data

| | |
|---|---|
| Name | Thomas Georg Seidel |
| Date of birth | 04.01.1996 |
| Birthplace | Göttingen, Germany |
| Nationality | German |

## Academic Education

| | |
|---|---|
| since 10/2020 | **PhD candidate** at the Institute for Theoretical Physics at the University of Münster, supervised by Prof. Svetlana Gurevich and Prof. Julien Javaloyes (Universitat de les Illes Balears, Palma, Spain) |
| 10/2018 – 09/2020 | **Master of science** in physics at the University of Münster, grade 1.0, Master thesis: *"Influence of Time Delayed Feedback on the Dynamics of Temporal Localized Structures"* |
| 09/2017 – 01/2018 | **Erasmus stay** at the University of Strathclyde, Glasgow, UK |
| 10/2015 – 09/2018 | **Bachelor of science** in physics at the University of Münster, grade 1.1, Bachelor thesis: *"Dynamics of discrete light bullets in passively mode-locked semiconductor lasers"* |
| 06/2014 | **Abitur** at the Städtisches Gymnasium Haan, grade 1.5 |
| 2006 – 2014 | Städtisches Gymnasium Haan |
| 2003 – 2006 | Grundschule Bollenberg, Haan |
| 2002 – 2003 | Lohbergschule, Göttingen |

## Scholarships & Awards

| | |
|---|---|
| since 10/2021 | **Doctoral scholarship** of the foundation *Studienstiftung des deutschen Volkes* |
| 07/2021 | **Infinion Master Award** for the best master thesis at the department of physics at the University of Münster |
| 07/2016 – 09/2020 | **Scholarship** of the foundation *evangelischen Studienwerks Villigst* |

## Engagement

| | |
|---|---|
| 09/2014 – 08/2015 | **Voluntary service** with the foundation *IN VIA Köln e.V.* at the Holy Childhood Pre- and Primaryschool, Himo, Tanzania |

## Work Experiences

since 10/2020 **Research**

- Author of 10 articles (8 as first author) published in peer-reviewed journals
- International collaboration with, e.g., researchers from Spain and France
- Speaker at (inter)national conferences and workshops

since 10/2018 **Teaching**

- Co-supervisor of four master and two bachelor thesis
- Organization of the bachelor course *Physics III: Waves and Quanta*
- Tutor for master courses *Numerical Methods for Complex Systems I & II*
- Tutor for various bachelor courses

## Conferences, Workshops and Research Stays

| | |
|---|---|
| 12/2020 | *Workshop* European Semiconductor Laser workshop, *(online)* |
| 03/2021 | *Conference* DPG Spring Meeting, *(online)* |
| 06/2021 | *Conference* CLEO Europe, *(online)* |
| 06/2021 | *Workshop* Nonlinear Dynamics in Semiconductor Lasers, *(online)* |
| 07–08/2021 | *Research Stay* at the Universitat de les Illes Balears in Palma, Spain |
| 08/2021 | *Conference* Dynamics Days in Nice, France |
| 04/2022 | *Conference* SPIE in Straßburg, France |
| 07/2022 | *Conference* ENOC in Lyon, France |
| 09/2022 | *Workshop* Self-organisation and Complexity in Mittelberg, Austria |
| 09/2022 | *Conference* DPG Spring Meeting in Regensburg, Germany |
| 11/2022 | *Conference* International Conference on Control of Self-Organizing Nonlinear Systems in Potsdam, Germany |
| 11–12/2022 | *Research Stay* at the Universitat de les Illes Balears in Palma, Spain |
| 06/2023 | *Project Meeting* KOGIT in Nice, France |
| 06/2023 | *Conference* CLEO Europe in München, Germany |
| 07/2023 | *Workshop* Nonlinear Dynamics in Semiconductor Lasers in Berlin, Germany |
| 09/2023 | *Workshop* Self-organisation and Complexity in Mittelberg, Austria |
| 10/2023 | *Research Stay* at the Universitat de les Illes Balears in Palma, Spain |
| 06/2024 | *Project Meeting* KOGIT in Münster, Germany |
| 09/2024 | *Workshop* Self-organisation and Complexity in Mittelberg, Austria |